Measurement of the Neutrino-Oxygen Neutral Current Quasi-elastic Interaction Cross-section by Observing Nuclear De-excitation γ-rays in the T2K Experiment

Huang Kunxian

December 18, 2015

Department of Physics, Graduate School of Science
Kyoto University

Measurement of the Neutrino-Oxygen Neutral Current Quasi-elastic Interaction Cross-section by Observing Nuclear De-excitation γ-rays in the T2K Experiment

A dissertation
submitted in partial fulfillment of the requirements
for the Degree of Doctor of Science
in the Graduate School of Science, Kyoto University

Kunxian Huang

Department of Physics, Graduate School of Science
Kyoto University
December, 2015

Dissertation Committee:
Tsuyoshi Nakaya
Atsuko K. Ichikawa
Akihiro Minamino
Toru Tanimori
Takahiro Kawabata

Abstract

The T2K (Tokai to Kamioka) experiment is a long baseline neutrino oscillation experiment. A 30 GeV proton beam is used to produce the intense muon neutrino beam at J-PARC, and the average energy of neutrinos is 630 MeV. The Super-Kamiokande detector serves as a far detector of the T2K experiment, and it observe the neutrino events induced by the T2K beam neutrinos at a distance of 295 km from the J-PARC.

This thesis reports the measurement of neutrino-oxygen neutral current quasi-elastic (NCQE) interaction cross-section $\sigma_{\nu,NCQE}$ by observing the de-excitation γ-rays at Super-Kamiokande with the T2K neutrino beam. The study of the de-excitation γ-rays from the NCQE reactions has two motivations. First, a disappearance of neutral current (NC) events can be used to provide an evidence for the existence of sterile neutrinos, as the sterile neutrino does not interact with a nucleus via weak interactions. Therefore, the disappearance of γ-ray events induced by NCQE interactions at the far detector is a good tool to probe active neutrino to sterile neutrino oscillations in T2K. Second, for the supernova relic neutrino (SRN) search at Super-Kamiokande, the de-excitation γ-ray events from atmospheric neutrinos are one of the main backgrounds. Since there has been no previous measurement of the de-excitation induced by ν-O NCQE interactions, the T2K measurement can also be used to estimate the number of background events from atmospheric neutrinos.

As most nuclear de-excitation γ-ray events at the Super-Kamiokande detector with the T2K neutrino beam are expected to be induced by neutrino-oxygen NCQE interaction, the events are used as signal to measure the ν-O NCQE cross-section. We measure the cross-section value by comparing the expected number of events to the observed number of events.

In this thesis, the T2K data taken from Jan., 2010 to Jun., 2012 are firstly analyzed. Forty three de-excitation γ-ray candidate events are selected. We compare the observed number of events with an expectation number of 51.0. As a result, the flux-averaged NCQE cross-section is measured as $< \sigma^{obs}_{\nu,NCQE} >= 1.55 \times 10^{-38}\mathrm{cm}^2$ with the 68% confidence interval of $(1.08, 2.34)\times10^{-38}\mathrm{cm}^2$. The result is consistent with a recent theoretical calculation of $< \sigma^{theory}_{\nu,NCQE} >= 2.01\times10^{-38}\mathrm{cm}^2$. The p-value of the background-only hypothesis (no NCQE) is 4×10^{-8}, which corresponding to an evidence of the NCQE signal at 5.4σ significance. This is the first measurement of ν-O NCQE interaction cross-section. Secondly, we add data taken from Oct., 2012 to May, 2013 to improve the precision with more statistics. As a result, the the flux-averaged NCQE cross-section is updated as $< \sigma^{obs,updated}_{\nu,NCQE} >= 1.75 \times 10^{-38}\mathrm{cm}^2$ with the 68% confidence interval of $(1.33, 2.52)\times10^{-38}\mathrm{cm}^2$.

The results of the cross-section measurement are used to estimate the influences on the sterile neutrino search and the SRN search. For sterile neutrino search, the expected upper limit on θ_{34} shows that upper limit is 53.5° (59°) at 90% confidence level, with the true value of $\theta_{34} = 0^\circ$ (20°). The uncertainty of the de-excitation γ-rays induced by neutral current interactions is $\sim 60\%$ now. If the uncertainty is reduced to 10% in future, the SRN signal would be found at a 3σ level at SK-Gd (Gd-loaded Super-Kamiokande).

Acknowledgment

This thesis would not be finished without many people's help, and I would like to express my sincere appreciate to these marvelous people.

First of all, I want to appreciate my two advisors Tsuyoshi Nakaya and Atsuko K. Ichikawa. When I expressed the willing to have a research on the T2K experiment., Tsuyoshi Nakaya kindly accept me as a member of this excellent laboratory in Kyoto Univ. His guidence about the research is always pointing the right path, and I learned the keen sense of physics science from him. I also want to thank that he gave me so interesting research topic of de-excitation γ-ray by the T2K beam. It is so unique and very important for Super-Kamiokande future. Atsuko K. Ichikawa gave me many adivices about the MIZUCHE research and other physics analysis. Beside the directional guidance, she always shows willpower and perseverance to physics research, which inspires me a lot. I also want to express my gratitude to Akihiro Minamino. He gave me a lot of advices kindly, and he helped me to fix this thesis.

I have so many thanks to NCGamma analysis group people. I am grateful to work with Yusuke Koshio. His experience and fervour about Super-Kamiokande and neutrino experiments helped me a lot to analyze the data. He also gave me advice about how to organize a presentation, and I benefit from the concepts a lot. Alexander Himmel also gave me many advices kindly, and I want express my deeply grateful here. He always reminds me to make a concise presentation, and his coding has the concise philosophy which I was eager to learn. My work won't get so success if Koh Ueno did not make so much efforts before. He always answers my questions kindly and quickly, and I got the correct direction with his guidance. Corina Nantais is also a member of the analysis group. I am pleasure to work with her, and she sing so good at Karaoke. I also thank other people who helped me in the NCGamma analysis group including Akira Konaka, Hirohisa Tanaka, Tetuya Shirahige, Tsuyoshi Nakaya. I also thank to Arthur M. Ankowski, Makoto Sakuda and other members in cosmic physics laboratory of Okayama University, as they finished the theoretic work of the NCQE cross-section and the de-excitation branching ratios.

I give my gratitude to the MIZUCHE members, who helped me to study this interesting detector. I am grateful to Ken Sakashita for his guidance to MIZUCHE construction and the analysis work. He gave me many encourage and advice privately. Akira Murakami made most parts of MIZUCHE simulations. He can concentrate on every topic quickly, and I was impressed by his works. When MIZUCHE operates during neutrino time, Shota Takahashi worked with me all day along. He made a lot of efforts to construct MIUCHE, and we can not get operations without his great contributions. I am also grateful to other MIZUCHE members: Atsuko K. Ichikawa, Takashi Kobayashi, and Tsuyoshi Nakaya.

Masashi Yokoyama helped me to have Hyper-Kamiokande sensitivity study, and I am grateful to have my first time to have a good physics potential study.

I must thank to all members of T2K collaboration and members of Super-Kamiokande collaboration. Especially, I give the earnest grateful to members of Kamioka Observatory and members of KEK neutrino group, as the T2K experiment can not get so fruitful results without their endless efforts. The T2K-SK group of T2K collaboration gave me many valuable advices, and the three conveners of Kimihiro Okumura, Roger Wendall, and Mike Wiking organize the group progress very well. I would also thank the T2K-SK group and the three conveners especially.

The students and teachers at Kamioka Observatory are so kind and bright, and I had a good time there. I would like to thank Masayuki Nakahata, Masato Shiozawa, Yoshinari Hayato, Tomonobu Tomura, Kimihiro Okumura, Jun Kameda, Hidekazu Tanaka, Yusuhiro Nishimura, Ikki Iyogi, Tristan Irvine, Yuki Nakano, Osamu Takachio, Yusuke Suda, Yuji Okajima, Takahiro Suzuki, Ryosuke Akutsu, Konosuke Iwamoto, Shimpei Tobayama, Asato Oii, Masatoshi Kobayashi, Yang Zhang, Miwa Shimode.

When I worked on MIZUCHE at J-PARC, I lived in Ota Danchi together with Shota Takahashi, Tatsuya Kikawa, Kento Suzuki, Kei Ieki, Akira Murakami, Akihiro Minamino. I enjoyed the time staying with them. We always have some tough discussion about physics and a lot of nonsense chats which really make us relax after one day's work. After the collaboration meeting work, we usually have hot pot party, Okonomiyaki party, and TV game. Takahiro Hiraki, Motoyasu Ikeda, Ryosuke Ohta, and Megan Friend were also staying Tokai with me, and I also want to thank their accompany.

I appreciate the excellent laboratory of high energy physics at Kyoto University. Not only neutrino members, but also K0T0 members and ATLAS members gave me stimulus of particle physics, and I benefit a lot from the discussions with them. Shota Takahashi, Tatsuya Kikawa, and Kento Suzuki are my classmates. I will never forget the days with you, and wish that we can get together sometimes. I also want to thank Seiko Hirota and Kiseki Nakamura. We have many discussion about physics and other interests which broaden my vision. Cao van Son, Patel Nikhul, Benjamin Quilain helped me to finish this thesis even they were very busy, I have to thank their kindness. I want to thank to the other members of my laboratory: Masaya Ishino, Hajime Nanjo, Toshi Sumida, Motoyasu Ikeda, Yasuhiro Nakajima, Hajime Kubo, Masashi Otani, Koji Shiomi, Takahiko Masuda, Naoki Kawasaki, Daichi Naito, Yosuke Maeda, Takahiro Yamauchi, Shigeto Seki, Takuya Tashiro, Tokio Nagasaki, Kohei Goda, Naoyuki Kamo, Shinichi Akiyama, Takaaki Hineno, Tatsuya Hayashino, Yuki Ishiyama, Keigo Nakamura, Kota Nakakiri, Ichinori Kamiji, Takuto Kunigo, Miao Jiang, Keisuke Kondo, Matoshi Shinohara, Saori Yanagita, Sei Ban, Mika Yamamoto, Ryutaro Monden, Kento Haneda.

I also want to thanks Japan Student Service Organization (JASSO) and the Global COE program give me the supports to finish the PhD degree. I give a immense gratitude to the Iwatani Naoji Foundation, which supports me and also take my life. Taipei Economic and Cultural office in Osaka also gives me and other Taiwanese students in Kyoto a help, and I want to express my appreciation.

I also want to thank my elders and my friends in Kyoto. I got so many warming and courages from all of you.

At the end, I give greatest thanks and for my family at Taiwan. My two sisters gave me so many supplies and warming, and I wish both you have a happy life. I always want to say sorry and thanks to my parents, and they gave all themselves to me without any preservation. I wish that I can be a responsible person as you are.

黃坤賢

Kyoto, Japan
Dec., 2015

Hope this thesis make people of Taiwan and Japan understand each other.

Contents

Chapter 1

Introduction

1.1 Neutrinos in the Standard Model of particle physics

In 1960's, Sheldon Lee Glashow, Abdus Salam and Steven Weinberg developed the electroweak theory which completes the unification of weak interaction and electromagnetic interaction[1–3]. The theory satisfies $\mathrm{SU}(2)_L \otimes \mathrm{U}(1)_Y$ symmetry, a left-handed neutrino ν_l and its corresponding left-handed charge lepton l^- form a isospin doublet as

$$\Psi_L = \begin{pmatrix} \nu_l \\ l^- \end{pmatrix}_L \tag{1.1}$$

Since no right-handed neutrino is found until now, the right-hand field only consists of l_R singlet. Salam and Weinberg also introduced the Higgs field ϕ, that is coupling to leotons (Yukawa coupling) to lead a mass term for lepton as below

$$\mathcal{L}_Y = -f_e[\overline{\Psi_L} \begin{pmatrix} \phi^+ \\ \phi^0 \end{pmatrix} e_R^-] + h.c.^1 \tag{1.2}$$

As shown in the above equation, the neutrino mass term is zero. The Glashow-Weinberg-Salam (GWS) theory predicts a neutral current boson Z^0 that exchanges momentum in weak interaction. In 1970's, many experiments confirmed the quark model, and QCD (quantum color dynamics) theories are proposed. The Standard Model is completed with electroweak and QCD theories. In 1983, Z^0 boson is discovered in UA1 experiment. The resonance width of Z^0 is the sum of individual width of lepton and quark decay mode, and the width measurements at LEP shows that the number of flavors of neutrino is $N_\nu = 2.99 \pm 0.01$ [4]. Thus, there are three and only three flavor types of neutrinos in the Standard Model. Nowadays, the third generation leptons and quarks are found, the particles in fermion section are shown as Table 1.1. In the boson section, the H^0 boson was found in the ATLAS and the CMS experiment at LHC in 2012 [5, 6]. The bosons are listed in Table 1.2. Here, some neutrino properties in the Standard Model are as follow:

1. Three flavor neutrinos ν_e, ν_μ, and ν_τ are corresponding to their charge lepton e, μ, τ in weak charge current interactions.

2. Only left-handed neutrino and right-handed anti-neutrino exist.

3. Neutrinos have zero mass.

Table 1.1: Fermion particles in the Standard Model. The mass values are from Reference [21].

Fermion section (spin=1/2)				
	generation	*I*	*II*	*III*
Quark	name	u	c	t
	charge	+2/3	+2/3	+2/3
	mass(MeV)	$2.3^{+0.7}_{-0.5}$	1275 ± 25	$(173.21 \pm 0.51 \pm 0.71) \times 10^3$
	name	d	s	b
	charge	-1/3	-1/3	-1/3
	mass(MeV)	$4.8^{+0.5}_{-0.3}$	95 ± 5	$(4.18 \pm 0.03) \times 10^3$
Lepton	name	e	μ	τ
	charge	-1	-1	-1
	mass(MeV)	$0.5109 \pm 1.1 \times 10^{-8}$	105.658 ± 3.5^{-6}	1776.82 ± 0.16
	name	ν_e	ν_μ	ν_τ
	charge	0	0	0
	mass(MeV)	$< 2 \times 10^{-6}$(tritium decay)		

Table 1.2: Boson particles in the Standard Model. The mass values are from Reference [21].

Boson section					
name	γ	$W^\pm$	Z^0	g	H^0
force	EM	weak	weak	strong	
charge	0	± 1	0	0	0
spin	1	1	1	1	0
mass(GeV)	0	80.385 ± 0.015	91.1876 ± 0.0021	0	125.7 ± 0.4

The Standard Model assumes zero mass of neutrino, but the neutrino oscillation experiments show the proof against the prediction [7]. The detail of neutrino mass theories are described in Appendix A.1.

1.2 Neutrino Interactions

1.2.1 Weak Interactions

In 1934, Enrico Fermi proposed the theory to explain β-decay with angular momentum conservation $\Delta J = 0$, and that is known as "Fermi interaction". Fermi described that the β-decay is similar with electromagnetic (E.M.) interaction. The β-decay has some difference with E.M. interaction such as the coupling constant G_β is much smaller than the constant of E. M.. The interaction is referred to as "weak interaction". Later, George Gamow and Edward Teller made an extension of Fermi's theory to describe the β-decay with angular momentum transition $\Delta J = \pm 1$, which is called as "Gamow-Teller"

[1] h.c.: hermitian conjugate

transition. Yang and Lee used Kaon decay to propose a parity violation in weak interaction. In 1957, Wu Chien-Shiung used ^{60}Co to examine the parity conservation in the β-decay reaction, the result shows that the parity is violated in the β decay reactions[8]. In the same year of Wu's experiment, Rober Marshak and George Sudarshan proposed the V-A theory for weak interactions, while later the V-A theory is also presented by Richard Feynman and Nurray Gell-Mann. Beside to β-decay, the decay rate of pion decay and muon decay also obey the calculation of the V-A theory. For example, the Lagrangian for muon decay $\mu \to e + \nu_\mu + \overline{\nu}_e$ is written as below

$$\mathcal{L} = -(G_\mu/\sqrt{2})[\overline{\nu}_\mu \gamma^\mu (1-\gamma^5)\mu][\overline{e}\gamma_\mu(1-\gamma^5)\nu_e] \tag{1.3}$$

where G_μ is the coupling constant of weak interaction and $\gamma_\mu(1-\gamma^5)$ denotes the V-A form in weak interaction.

The V-A theory predicts that the cross-section of neutrino-quark scattering is proportion to center-of-mass energy squared $\sigma_{\nu,d\to e^- u} \propto s$. If the energy exceeds 300 GeV, the reaction probability exceed unity. There is a contradiction for the V-A theory and the unity of reaction probability. Glashow, Weinberg, and Salam accommodated particles W^+, W^-, W^0, and B that are interacting particles with nonzero mass. The Higgs mechanism is involved to give a mass to the interacting bosons.

Let us focus on the neutrino-nucleus interaction in the following paragraphs.

1.2.2 Neutrino-nucleus interactions

Here, the discovery of neutrino-nucleus charge current scattering and neutral current scattering are described. Then, some neutrino-nucleus interactions are described. The details of the neutrino-nucleus quasi-elastic scattering are described in Chapter 4.3.

Discovery of Charge Current interaction In 1950's, the success of Fermi's theory about β-decay leads the research of neutrino existence. The detection of neutrinos through CC interaction is achieved by Cowan and Reines using $\overline{\nu}_e + p \to e^+ + n$ reaction [9]. They made a water tank with dissolved $CdCl_2$ surround by two liquid scintillators, and they used anti-neutrinos produced from a nuclear reactor. They detected the annihilation 0.51 MeV γ-ray and the delayed γ-ray from neutron capture reaction to prove the existence of neutrino by neutrino-nucleus charge current scattering.

Discovery of Neutral Current interaction The existence of weak neutral current reaction is predicted by GWS theory at 1960's. In 1973, the Gargamelle experiment used a bubble chamber to observe neutrino interactions[10]. Since the experiment used ν_μ beam, the neutral current (NC) events are expected to be detected as hadronic events without muon track. The 102(63) $\nu(\overline{\nu})$ NC candidate events exceed the expected numbers of neutron background events which are estimated from CC events with neutron cascade. The results provide a convincing proof of the neutral current interaction that is leading the Z boson existence.

Nuclear excitation induced NC inelastic scattering The ν-nucleus neutral current inelastic scattering induces a nuclear excitation as below

$$\nu + A \to \nu + A^* \,(\mathsf{NC\ inelastic}) \tag{1.4}$$

where A is a target nucleus, and A^* is an excited nucleus. After the NC inelastic interaction, the excited nucleus emits a γ-ray, which is observed as a signal event. The NC inelastic events dominate all neutral current events if the neutrino energy is less than 100 MeV. As the supernova neutrinos have energy lower than 100 MeV, the NC inelastic interactions are used to detector the supernova explosion neutrinos ν_e, ν_μ, ν_τ.

Quasi-elastic scattering If neutrino energy is in subGeV region $\mathcal{O}(0.1 \sim 1$ GeV), the quasi-elastic scattering dominates in neutrino-nucleus events. The neutral current quasi-elastic (NCQE) scattering and charge current quasi-elastic (CCQE) scattering are written as below

$$\begin{array}{rcl} \nu + A & \rightarrow & \nu + (A-1)^* + N\,(\mathsf{NCQE}) \\ \nu_l + A & \rightarrow & l^- + (A-1)^* + p\,(\mathsf{CCQE}) \end{array} \tag{1.5}$$

where l^- is the charge lepton, p is a proton, and A is the target nucleus, N is a knockout nucleon. We use an impulse approximation theory to simulate the NCQE scattering as described in Chapter 4.3.

Resonance pion production If neutrino energy exceeds $\mathcal{O}(300$ MeV), there are chances to have a baryon resonance in neutrino-nucleus scattering. On the intermediate state, an intermediate baryon N^* is produced, then it decays to a nucleon and a meson m in the final state as follows:

$$\begin{array}{rcl} \nu_l + N \rightarrow l^- & + & N^* \\ & & N^* \rightarrow N' + m \end{array} \tag{1.6}$$

For T2K neutrino flux, the most of intermediate baryons are $\Delta(1232)$, which decays to a nucleon and a meson for neutrino-nucleus resonance interaction as below

$$\begin{array}{rcl} \nu_l + N & \rightarrow & l^- + \Delta \rightarrow l^- + N' + \pi\,(\mathsf{CC1}\pi\mathsf{res}) \\ \nu + N & \rightarrow & \nu + \Delta \rightarrow \nu + N' + \pi\,(\mathsf{NC1}\pi\mathsf{res}) \end{array} \tag{1.7}$$

The produced meson has a chance to be absorbed by a nucleus in final state interaction (FSI), and two nucleons are knocked out of the nucleus. Then, the remained nucleus also have a chance to emit a de-excitation γ-ray, this is a background source in NCQE measurement by observing γ-ray signal.

1.2.3 Previous research of neural current quasi-elastic interaction with de-excitation γ-ray

The de-excitation γ-rays are a useful tool to detecting the weak neutral current interaction, when the energy of neutrino is at $\mathcal{O}$(MeV) to $\mathcal{O}$(subGeV) region. The KARMEN experiment [18] produces ν_μ beam with energy of 28 MeV, then a liquid scintillator array is used as a carbon target. The de-excitated γ-rays from the carbon nuclei are observed to make a research of neutral current (NC) inelastic scattering firstly [19]. This opens a door to study on neutrino neutral current (NC) interaction by observing the de-excitated γ-rays.

Beside ν-^{12}C NC inelastic reaction, the K2K experiment studied de-excitation γ-rays induced by ν-water NCQE interaction [20]. K2K is a long-baseline neutrino oscillation experiment, and the ν_μ neutrino beam with average energy of 1.3 GeV is produced at KEK, Tsukuba City. The K2K experiment used a 1 kton water Cherenkov detector at the near site in KEK, and the detector is shown in Figure 1.1. The de-excitation

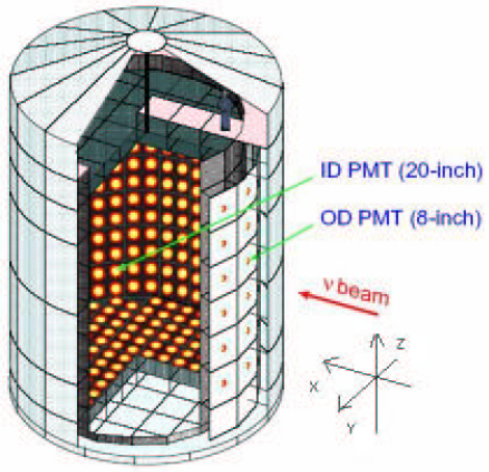

Figure 1.1: Schematic view of 1 kton water Cherenkov detector at near site of the K2K experiment from Ref. [20]

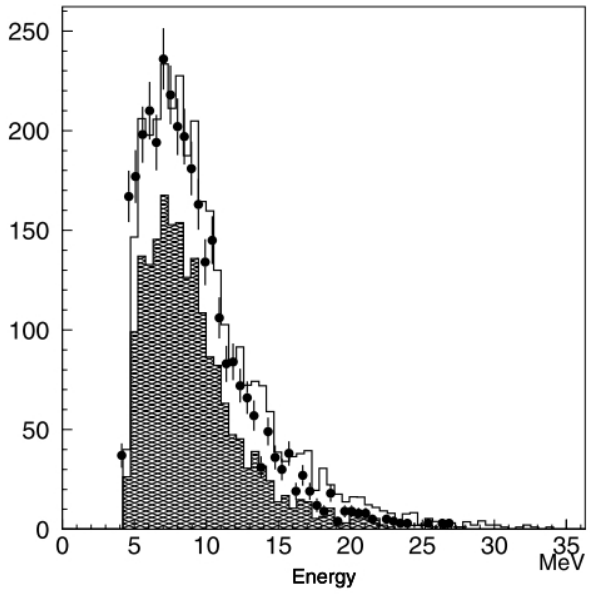

Figure 1.2: The energy distribution of de-excitation γ-ray events from Ref. [20]. The dots represent the data. Histogram shows the distribution of the expected γ-ray events, and the hatched histogram shows the expected γ-ray events that are induced from ν-water NCQE interactions.

γ-rays induced by ν-water NCQE reactions are expected to be observed at the 1 kton water Cherenkov detector. The K2K uses data taken from Oct. 2003 to Dec. 2003 for the analysis, and the accumulative proton-on-target of the used data is 9.69×10^{18}. The selection procedures are as follows: select event timing located at bunch structure, single interaction in a spill, the number of hit PMTs, the number of photoelectrons, the number of effective hit PMTs, multi particle events, and reconstructed vertex inside fiducial volume. As a result, 3291 γ-ray candidate events are selected. The energy distribution of the events is shown in Figure 1.2, there is a peak near 6 MeV. This is the first observation of de-excitation γ-ray induced by ν-water NCQE interaction. However, the details of NCQE cross-section theory and nuclear de-excitation were not studied yet, the K2K experiment did not give a result of NCQE cross-section measurement.

The K2K results give us a chance to measure the NCQE cross-section by observing de-excitation γ-rays at Super-Kamikande with the T2K high intensity neutrino beam.

1.3 Neutrino Oscillation

1.3.1 Theory

The theory of neutrino oscillation is mentioned here briefly, and the details of neutrino mass and neutrino oscillation theory are in Appendix A.1. The idea of neutrino oscillation is proposed by B. Pontecorvo to explain the possible lepton number violation reactions [12, 13]. In 1962, the neutrino mixing is proposed by Z. Maki, M. Nakagawa, and S.

Sakata [11]. Now, the neutrino mixing of flavor eigenstate and mass state is written as below

$$\nu_L^l = U_{l,i}\nu_L^{'i} \tag{1.8}$$

where $\nu^l = (\nu_e, \nu_\mu, \nu_\tau)$ is the weak "flavor" states, and three "mass" neutrino eigenstates is $\nu^i = (\nu_1, \nu_2, \nu_3)$. The unitary matrix $U_{l,i}$ is referred as to Pontecorvo-Maki-Nakagawa-Sakata (PMNS) matrix, which describes the neutrino mixing. The PMNS matrix has three mixing angles and one CP violation phase, and the matrix is given by [14]

$$U = \begin{pmatrix} c_{12}c_{13} & s_{12}c_{13} & s_{13}e^{-i\delta} \\ -s_{12}c_{23} - c_{12}s_{23}s_{13}e^{i\delta} & c_{12}c_{23} - s_{12}s_{23}s_{13}e^{i\delta} & s_{23}c_{13} \\ s_{12}s_{23} - c_{12}c_{23}s_{13}e^{i\delta} & -c_{12}s_{23} - s_{12}c_{23}s_{13}e^{i\delta} & c_{23}c_{13} \end{pmatrix} \tag{1.9}$$

where $s_{ij} = \sin\theta_{ij}$ and $c_{ij} = \cos\theta_{ij}$. Three θ_{ij} are the mixing angles, δ is the CP violating phase for Dirac neutrino. The Schrodinger equation is used to describe the neutrino propagation in time as below.

$$i\frac{d}{dt}|\nu_i(\vec{x},t)\rangle = \mathcal{H}|\nu_i(\vec{x},t)\rangle \tag{1.10}$$

The mass eigenstates $|\nu_i\rangle$ are stationary states. After a time interval t the mass states are given by

$$|\nu_i(\vec{x},t)\rangle = e^{-iE_it}|\nu_i(\vec{x},t=0)\rangle \tag{1.11}$$

The flavor states $|\nu_\alpha(\vec{x},t)\rangle$ are the linear combination of mass states $|\nu_i(\vec{x},t=0)\rangle$

$$|\nu_\alpha(\vec{x},t)\rangle = \sum_i U_{\alpha,i}e^{-iE_it}|\nu_i(\vec{x},t=0)\rangle = \sum_{i,\beta} U_{\alpha,i}U^*_{\beta,i}e^{-iE_it}|\nu_\beta(\vec{x},t=0)\rangle \tag{1.12}$$

Because the neutrino momentum p is much larger than its mass m_i, the energy of mass eigenstate E_i is approximated as below

$$E_i = \sqrt{m_i^2 + p^2} \simeq p + m_i^2/2p \simeq p + m_i^2/2E_i \tag{1.13}$$

Then, Equation 1.12 is written as below

$$|\nu_\alpha(\vec{x},t)\rangle = \sum_{i,\beta} U_{\alpha,i}U^*_{\beta,i}e^{-ipt}e^{-im_i^2t/2E}|\nu_\beta(\vec{x},t=0)\rangle \tag{1.14}$$

Now, the oscillation probability $P(\nu_\alpha \to \nu_\beta) = |\langle\nu_\beta|\nu_\alpha\rangle|^2$ is derived as follows:

$$\begin{aligned} P(\nu_\alpha \to \nu_\beta)(L) &= |\langle\nu_\beta|\nu_\alpha\rangle|^2 \\ &= \sum_i\sum_j U_{\alpha i}U^*_{\alpha j}U^*_{\beta i}U_{\beta j}exp(-i\frac{(m_i^2 - m_j^2)L}{2E}) \\ &= \sum_{i,j}|U_{\alpha i}U^*_{\beta i}|^2 + 2Re\sum_{j>i}U_{\alpha i}U^*_{\alpha j}U^*_{\beta i}U_{\beta j}exp(-i\frac{(\Delta m_{ij}^2)L}{2E}) \end{aligned} \tag{1.15}$$

where the $\Delta m_{ij}^2 = m_i^2 - m_j^2$ is mass-squared splitting between mass state i, j.

The scenario of three-flavor oscillation is considered here. Under the limit of $|\Delta m_{32}^2| >> |\Delta m_{21}^2|$, the probability of $\nu_\mu \to \nu_\mu$ oscillation is

$$P(\nu_\mu \to \nu_\mu) \simeq 1 - 4c_{13}^2s_{23}^2(1 - c_{13}^2s_{23}^2)\sin^2(\Delta_{32}) \tag{1.16}$$

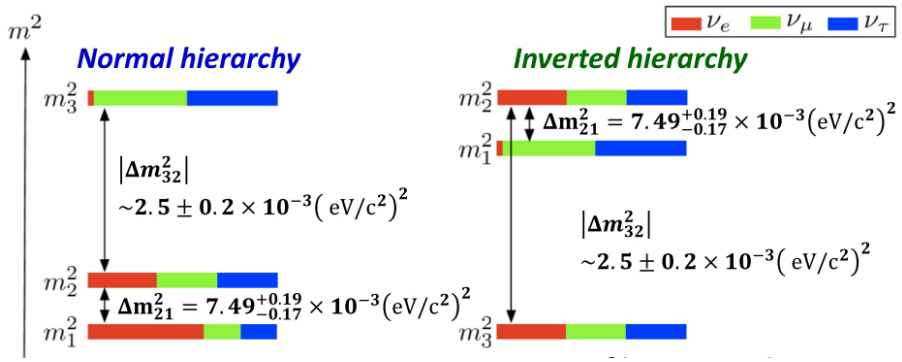

Figure 1.3: The neutrino mass hierarchy plot. The left figure shows normal hierarchy, where the $m_3 > m_2, m_1$. The right figure shows the inverted hierarchy, where the $m_2, m_1 > m_3$.

where the phase factor is written as

$$\Delta_{ij} = \frac{\Delta m_{ij}^2 L}{4E_\nu} = 1.27\frac{\Delta m_{ij}^2[eV^2]L[km]}{E_\nu[GeV]} \tag{1.17}$$

The $\nu_\mu \to \nu_e$ oscillation is measured by accelerator experiment. If the mass effect appears in the long-baseline oscillation experiment, the ν_e appearance from a ν_μ beam is obtained from a probability given by

$$\begin{aligned} P(\nu_\mu \to \nu_e) &= 4c_{13}^2 s_{13}^2 s_{23}^2 \sin^2\Delta_{31} \\ &+ 8c_{13}^2 s_{12}s_{13}s_{23}(c_{12}c_{23}\cos\delta - s_{12}s_{13}s_{23})\cos\Delta_{32}\sin\Delta_{31}\sin\Delta_{21} \\ &- 8c_{13}^2 c_{12}c_{23}s_{12}s_{13}s_{23}\sin\delta\sin\Delta_{32}\sin\Delta_{31}\sin\Delta_{21} \\ &+ 4s_{12}^2 c_{13}^2(c_{12}^2 c_{23}^2 + s_{12}^2 s_{23}^2 s_{13}^2 - 2c_{12}c_{23}s_{12}s_{23}s_{13}\cos\delta)\sin^2\Delta_{21} \\ &+ 8c_{13}^2 s_{13}^2 s_{23}^2(1-2s_{13}^2)(\frac{a}{\Delta m_{31}^2}\sin^2\Delta_{31} - \frac{a\cdot L}{4E_\nu}\cos\Delta_{32}\sin\Delta_{31}) \end{aligned} \tag{1.18}$$

where the last term in the above equation due to the matter effect for long base-line oscillation, and the coefficient a is $a[\mathrm{eV}] = 7.56\times10^{-5}\rho[\mathrm{g/cm^3}]E_\nu[\mathrm{GeV}]$. The corresponding probability for $\overline{\nu}_\mu \to \overline{\nu}_e$ transition is obtained by replacing the delta term $\delta \to -\delta$ and mass effect term $a \to -a$ in Equation 1.18. The CP violation phase δ is found by comparing the probabilities between $\nu_\mu \to \nu_e$ and $\overline{\nu}_\mu \to \overline{\nu}_e$. The CP violation in lepton sector may have a key to solve the matter-antimatter asymmetry in University. The future accelerator experiments have high potential to measure the CP phase δ.

mass hierarchy As mentioned previously, the neutrino oscillation probability depends on the mass-squared splitting Δm_{ij}^2. Super-Kamiokande uses $\nu_\mu \to \nu_\mu$ oscillation of atmospheric neutrinos to measured $|\Delta m_{32}^2| \sim 2.5\times10^{-3}$ eV^2. On the other hand, reactor neutrino experiments and solar neutrino experiments measure the $\Delta m_{21}^2 \sim 7.5\times10^{-5}$ eV^2, which is smaller than $|\Delta m_{32}^2|$. Since the sign of Δm_{31}^2 is not known yet, there are two possible mass order for three mass eigenvalues: $m_3 > m_2, m_1$ or $m_2, m_1 > m_3$. The former is referred to as normal hierarchy (NH), and the later one is referred to as inverted hierarchy (IH). The two hierarchies are as shown in Figure 1.3.

The sign of Δm_{31}^2 is expected to be determined using the matter effect in future neutrino oscillation experiments. For example, the Super-Kamiokande experiment has a

Table 1.3: Sensitivity of different neutrino oscillation experiments from Reference [21].

Source	Type of ν	$\overline{E}_\nu$[MeV]	L[km]	min(Δm^2)[eV^2]
Reactor	$\overline{\nu}_e$	~ 1	1	$\sim 10^{-3}$
Reactor	$\overline{\nu}_e$	~ 1	100	$\sim 10^{-5}$
Accelerator	$\nu_\mu, \overline{\nu}_\mu$	$\sim 10^3$	1	~ 1
Accelerator	$\nu_\mu, \overline{\nu}_\mu$	$\sim 10^3$	$100 \sim 1000$	$\sim 10^{-3}$
Atmospheric ν	$\nu_{\mu,e}, \overline{\nu}_{\mu,e}$	$\sim 10^3$	10^4	$\sim 10^{-4}$
Solar	ν_e	~ 1	1.5×10^8	$\sim 10^{-11}$

plan to measure the oscillation probability difference between $\nu_\mu \to \nu_e$, $\overline{\nu}_\mu \to \overline{\nu}_e$, $\nu_\mu \to \nu_\mu$ and $\overline{\nu}_\mu \to \overline{\nu}_\mu$ using the atmospheric neutrinos, and that difference is resulted from the matter effect [147].

1.3.2 Measurements of neutrino oscillation parameters

The oscillation parameters $\theta_{ij}, \Delta m^2_{ij}$ are measured by neutrino experiments, which use various sources of neutrinos, such as solar, atmosphere, nuclear reactor, accelerator. The sensitivities of each source and baseline distance for the oscillation parameters are summarized in Table 1.3. Each mixing angle and each mass-squared splitting are described as the following paragraphs.

Measurements of θ_{23} and Δm^2_{23} If the neutrino has energy E_ν at energy region of $(0.1, 100)$ GeV, the probability of ν_μ disappearance for traveling distance of 10km$\sim 10^4$km is mainly dependent on θ_{32} and Δm^2_{32}. Atmospheric neutrinos are a useful neutrino source to study θ_{32} and Δm^2_{32}. Cosmic rays produce pions via nuclear interactions, then the pion decays to $\pi^\pm \to \mu^\pm + \nu_\mu(\overline{\nu}_\mu)$, and the muon decays $\mu^\pm \to e^\pm + \nu_e(\overline{\nu}_e) + \overline{\nu}_\mu(\nu_\mu)$. The flux ratio of ν_μ to ν_e is $\Phi(\nu_\mu + \overline{\nu}_\mu) : \Phi(\nu_e + \overline{\nu}_e) \approx 2 : 1$. Super-Kamiokande (SK) gave the first evidence of neutrino oscillations by observing the upward-going ν_μ disappearance, and the oscillation parameters with two-flavor oscillation model are obtained as $\sin^2 2\theta > 0.82$ and 5×10^{-4} eV$^2 < \Delta m^2 < 6 \times 10^{-3}$ eV^2 [24].

The accelerator experiment with a long baseline $L \sim$ several hundred km measures the ν_μ disappearance. The MINOS experiment produces ν_μ-dominated beam or $\overline{\nu}_\mu$-enhanced beam via changing the current direction of focus horn. The disappearance probability of $\nu_\mu(\overline{\nu}_\mu)$ is obtained by detecting the decreased number of $\nu_\mu(\overline{\nu}_\mu)$ events at the far detector with distance 735 km away from the target. By combining of measured data using atmospheric neutrinos in MINOS, the MINOS measured $|\Delta m^2| = 2.41^{+0.09}_{-0.10} \times 10^{-3}$ eV^2 and $\sin^2(2\theta) = 0950^{+0.035}_{-0.036}$ under the hypothesis of identical parameters for ν_μ and $\overline{\nu}_\mu$. The results of $|\Delta\overline{m}^2| = 2.50^{+0.23}_{-0.25} \times 10^{-3}$ eV^2 and $\sin^2(2\overline{\theta}) = 097^{+0.03}_{-0.08}$ are obtained by the only $\overline{\nu}_\mu$ oscillation data [25].

The T2K experiment also measured the ν_μ disappearance probability, and the measured parameter results is $\sin^2\theta_{23} = 0.514^{+0.055}_{-0.056}(0.511 \pm 0.055)$ and $\Delta m^2_{32} = (2.51 \pm 0.10) \times 10^{-3}$ eV^2/c^4 (2.48 ± 0.10) for normal (inverted) hierarchy. The allowed region of the T2K $(\sin^2\theta_{23}, \Delta m^2_{23})$ results are as shown in Figure 1.4[26].

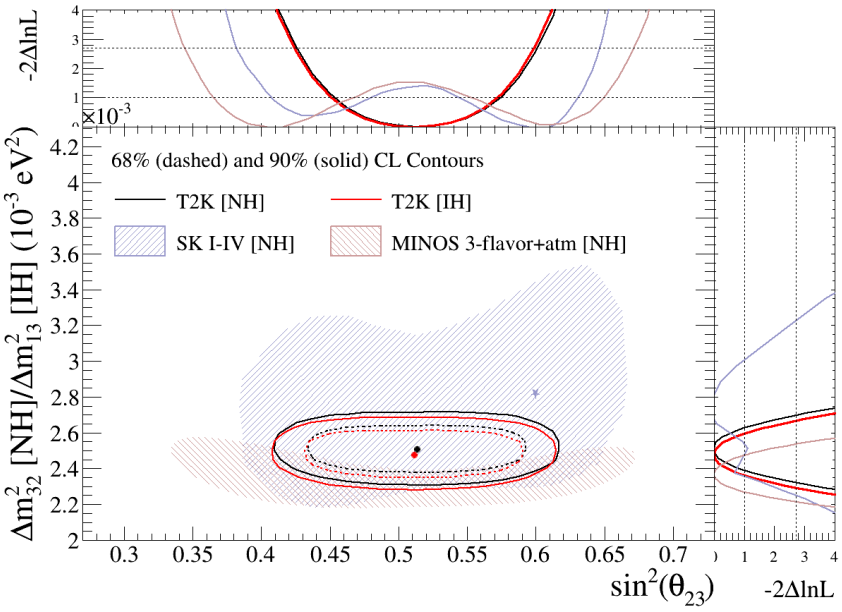

Figure 1.4: The measured 68% and 90% confidence level regions for $\sin^2\theta_{23}$ and Δm_{32}. The SK and MINOS 90% C.L. regions for normal hierarchy are also shown for comparison. The two profiles of likelihoods for $\sin^2\theta_{23}$ and Δm^2_{32} are shown separately at the top and the right overlaid.

Measurements of θ_{12} and Δm^2_{12} To obtain θ_{12} value and Δm^2_{12} value, the $\nu_e(\overline{\nu}_e)$ disappearance probability is measured using neutrinos from nuclear reactor or solar. The ν_e neutrino flux from sun is predicted by solar standard model (SSM), the recent calculation of SSM is in [27]. Because of the MSW effect inside the sun [16, 17], the ν_e flux at earth is significantly smaller than the expectation of the SSM. This deficit is referred to as "solar neutrino problem". The Super-Kamiokande experiment uses elastic reactions $\nu_e + e^- \rightarrow \nu_e + e^-$ to measure the ^{8}B ν_e flux from the sun [86, 87]. By comparison between the expected event rate and the observed event rate, the oscillation parameters are obtained by including the MSW effect and oscillation effect from solar to earth. The best fit of parameter set is $(\sin\theta_{12}, \Delta m^2_{21}) = (0.30^{+0.02}_{-0.01}, 7.6 \pm 0.2 \times 10^{-5}\ \text{eV}^2)$. Recently, the day-night asymmetry of the solar neutrino event rate $A_{DN} = 2(R_D - R_N)/(R_D + R_N)$ was reported, and the results gave a hint of MSW effect by the earth. The analysis gave a 68% confidence level allowed range of $4 \times 10^{-5}\ \text{eV}^2 \leq \Delta m^2_{21} \leq 7 \times 10^{-5}\ \text{eV}^2$.

The SNO experiment uses heavy water (D_2O) as the target of neutrino-nucleus reactions. The ^{8}B solar neutrinos are measured by the following reactions

$$\begin{aligned} \nu_e + d &\rightarrow e^- + p + p\,(\mathsf{CC}). \\ \nu + d &\rightarrow \nu + p + n\,(\mathsf{NC}) \\ \nu + e^- &\rightarrow \nu + e^-\,(\text{elastic scattering}, \mathsf{ES}) \end{aligned} \tag{1.19}$$

While the rates of CC events and ES events have a depletion comparing to expected event rate, the NC events do not change by flavor transitions. The analysis result with a two-flavor neutrino oscillation yield $\Delta m^2_{21} = (5.6^{+1.9}_{-1.4}) \times 10^{-5}\text{eV}^2$ and $\tan^2\theta_{12} = 0.427^{+0.033}_{-0.029}$[22].

Neutrinos from nuclear reactor are also used to study $(\theta_{12}, \Delta m^2_{21})$ by measuring $\overline{\nu}_e$ disappearance probability. The KamLAND experiment observes $\overline{\nu}_e$ with energies of few MeV from nuclear reactors averaged 180 km away. KamLAND compares the event rate during the period of nuclear reactor on and the period of nuclear reactor off, then they

subtract the two event rates to remove the background from geo ν or other background sources. The best fit result of Kamland is obtained as $\tan\theta_{12} = 0.436^{+0.029}_{-0.025}$ and $\Delta m^2_{21} = (7.53^{+0.18}_{-0.18}) \times 10^{-5}$ eV^2 with $\sin^2\theta_{13} = 0.023^{+0.0020}_{-0.002}$ [23].

Measurements of θ_{13} To obtain the θ_{13} value, there are two useful flavor transition modes which are used for prove θ_{13}. First, the probability of $\nu_\mu \to \nu_e$ is as shown in Equation 1.18, that has a leading term dependent on θ_{13}. The T2K experiment gave the first hint of $\theta_{13} > 0$ at 2.5σ significance in 2011[59]. Recently, the T2K experiment reported the observation of 28 ν_e events at the far detector. That is leading to a measurement of $\sin^2 2\theta_{13} = 0.140^{+0.038}_{-0.032}(0.170^{+0.045}_{-0.037})$ for normal (inverted) hierarchy at $\delta = 0$[61].

Second, reactor experiments with a short baseline ($\mathcal{O}(1km)$) have a high potential to measure θ_{13} via $\overline{\nu}_e$ disappearance. The $\overline{\nu}_e$ signal is detected via inverse beta decay reaction. The Daya Bay experiment reported the first evidence of nonzero of $\sin^2 2\theta_{13}$ at 5.2σ significance in 2012 [60], and the best fit of θ_{13} is $\sin^2 2\theta_{13} = 0.092 \pm 0.016(stat.) \pm 0.005(syst.)$ in three-flavor neutrino framework. There are other reactor experiments such as RENO[29], and Double Chooz[30]. The RENO experiment measured $\theta_{13} > 0$ exceeding 5σ significance. Currently, the results of measurement from Daya Bay gave the most precise measurement of $\sin^2 2\theta_{13} = 0.090^{+0.008}_{-0.009}$ [28].

Measurements of δ If neutrinos are Dirac particles, there is a CP violation phase δ in PMNS matrix. The δ term appear in the $\nu_\mu \to \nu_e$ oscillation probability as shown in Eqn. 1.18. The T2K experiment used the ν_e appearance probability combing with the results of reactor θ_{13} measurement to give the first CP phase measurement which prefer $\delta_{CP} = -\pi/2$. The constrains of δ_{CP} by T2K results are as follows: if the neutrino mass ordering is normal (inversed) hierarchy, the excluded region at 90% is $0.19\pi \sim 0.80\pi$ ($-0.04\pi \sim 1.03\pi$) [61].

1.3.3 Sterile neutrino search

As mentioned previously, the three-flavor neutrino mixing scenario is studied in many oscillation experiments, and two mass-squared splittings Δm^2_{ij} are measured as < 0.01 eV^2. In some neutrino experiments with a short baseline, the ν_e appearance probability (or disappearance) probability exceeds the expected probability with three-flavor neutrino mixing scenario. The anomalies are explained with the existence of additional one or more non-active neutrino states that have mass of $\mathcal{O}(1eV)$. The non-active neutrino states (ν_s or ν_{s1}, ν_{s2}...) are referred to as "sterile neutrino". Some experimental hints or negative results of sterile neutrinos will be mentioned in the following paragraphs.

The LSND experiment used stop pions to produce $\overline{\nu}_\mu$ with energy $E_{\overline{\nu}} < 52.8$ MeV. Then, a liquid scintillator detector is located 30 meter downstream from the beam stop, and it observed $\overline{\nu}_e$ signal[31]. The LSND measured the oscillation $\overline{\nu}_\mu \to \overline{\nu}_e$ using the reaction $\overline{\nu}_e p \to e^+ n$, and a e^+ signal and a delayed 2.2 MeV γ-ray signal from neutron capture are detected. LSND reported that an excess of $87.9 \pm 22.4(stat.) \pm 6.0(sys.)$ $\overline{\nu}_e$ events above the expected background events are observed, and the observed number exceeds the expected background events. The best fit of $(\sin^2\theta, \Delta m^2)$ for the oscillation is at $(\sin^2\theta, \Delta m^2) = (0.003, 1.2\ \text{eV}^2)$, and LSND suggests the oscillation with the parameter Δm^2 within the range of $0.2 \sim 10\text{eV}^2$. The results gave the first hint of the light sterile neutrino.

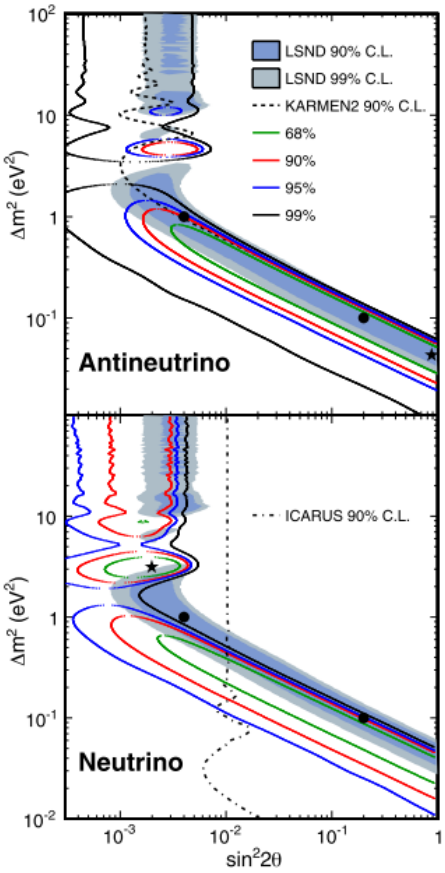

Figure 1.5: The allowed regions in the anti-neutrino (upper) mode and the neutrino (lower) mode using a two-neutrino oscillation model of the MiniBooNE measurement are shown. The limits from KARMEN and ICARUS are also shown in the plots. The two stars show the MiniBooNE best fit points.[33]

Next, the MiniBooNE experiment used the pion decays to produce $\overline{\nu}_\mu$ beam with the mean energy of 600 MeV. The mineral oil detector locates 541 meter downstream of the target, and the distance is chosen to satisfy L[m]/E[MeV]$\sim$ 1 [32], so the L/E is similar with that of LSND. The mineral oil detector measures $\overline{\nu}_e$ signal via the CCQE reactions. An excess of 78.4 ± 28.5 $\overline{\nu}_e$ events above the expected backgrounds are observed. To reproduce the result of LSND, the MiniBooNE experiment uses two-neutrino oscillation model to obtain the best fit of oscillation parameters at $(\sin^2\theta, \Delta m^2) = (0.88, 0.043$ eV^2), but the region at 68% confidence level distributes over a broad region up to $(\sin^2\theta, \Delta m^2) = (0.004, 0.8$ eV^2) [33] as shown in the upper plot of Figure 1.5. The results indicate an signal region at 99% confidence level (C.L.) that is consistent with some part of the LSND 99% C.L. The MiniBooNE experiment also measured the oscillation of $\nu_\mu \to \nu_e$ using the ν_μ beam. An excess of 162.0 ± 47.8 events above the expected background is observed, and the best fit of parameters is at $(\sin^2\theta, \Delta m^2) = (0.002, 3.14$ eV^2) as shown in the bottom plot of Figure 1.5.

Reactor experiments with the reactor-detector distance < 100 meter show that the ratio of observed flux to expected flux N_{obs}/N_{exp} is less than unity, and the average ratio is 0.943 ± 0.023 with a deviation from unity at 99.2% confidence level (C.L.) [38]. This $\overline{\nu}_e$ flux depletion is referred to as "reactor anti-neutrino anomaly". One possible solution for the anomaly is the existence of a sterile neutrino ν_s with a large m^2 value. A scenario

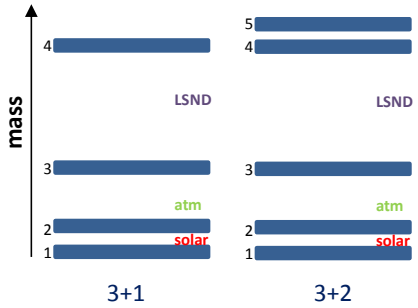

Figure 1.6: The mass hierarchy of "3+1" and "3+2" model, the situation of $m_4 >> m_{1\sim3}$, and $m_5, m_4 >> m_{1\sim3}$ are shown in the figure. The "LSND" denotes the mass difference suggested by LSND experiment and MiniBooNE.

of one sterile neutrino mixing with three active neutrinos is used for the analysis, and the combined results of reactor experiments with baseline $<$ 2km are used to calculate the oscillation parameters of $\sin^2 2\theta = 0.14 \pm 0.08(95\%)$ and $|\Delta m^2| > 1.5$ eV^2 [38].

Some negative results for $\nu_\mu \to \nu_s$ oscillation were obtained in the following experiments: KARMEN 2, NOMAD[36], ICARUS[37], and Super-Kamiokande atmospheric neutrino[35]. The KARMEN 2 experiment used stop muons to produce $\overline{\nu}_\mu$ beam, which is used to measure the $\overline{\nu}_\mu \to \overline{\nu}_e$ oscillation probability[34]. The inverse beta decay $\overline{\nu}_e + p \to n + e^+$ reactions are used to detect the $\overline{\nu}_e$ appearance, and 15 $\overline{\nu}_e$ candidate events are observed. The expected number of background events is $N_{BG}^{exp} = 15.8 \pm 0.5$. Therefore, there are no obvious deviations from the expectation of background. As a result, the exclusive upper limits of the oscillation parameters are obtained as $\sin^2 2\theta < 1.7 \times 10^{-3}$ for $\Delta m^2 \geq 100$ eV^2 and $\sin^2 2\theta = 1.0$ for $\Delta m^2 < 0.055$ eV^2 at 90% confidence level. The allowed oscillation mass parameter of LSND (0.2$\sim$10 eV^2) are not confirmed by KARMEN 2, and some allowed area in oscillation parameters ($\sin^2 2\theta$, Δm^2) plot are excluded by 90% C.L. Figure 1.5 (from Ref. [33]) shows the exclusion regions (area right to the dotted line) by KARMEN and ICARUS in the oscillation parameter plots.

To explain the anomalies in LSND and MiniBooNE, two simple models with light sterile neutrinos are proposed. They are called "$3+1$" and "$3+2$" corresponding to one (ν_4) sterile neutrino and two sterile (ν_4, ν_5) neutrinos. Therefore, the neutrino mixing matrix expands to 4×4 elements for "3+1" model, and the matrix expands to 5×5 elements for the "3+2" model. Figure 1.6 shows possible mass hierarchy of the two models. A recent global fit including all oscillation experiments obtain the combined results for the two models[39]. For the "3+1" scenario, the best fit of the oscillation parameters is at $\Delta m^2_{41} = 0.93$ eV^2 for $|U_{e4}| = 0.15$ and $|U_{\mu4}| = 0.17$, and the χ^2 for the best fit is $\chi^2_{3+1} = 87.9/66$. For the "3+2" scenario, the best fit of the oscillation parameters is at $\Delta m^2_{41} = 0.47$ eV^2, $\Delta m^2_{51} = 0.87$ eV^2 for $|U_{e4}| = 0.13$, $|U_{\mu4}| = 0.15$, $|U_{e5}| = 0.14$ and $|U_{\mu5}| = 0.13$, and the χ^2 for the best fit is $\chi^2_{3+2} = 72.7/63$. The fitting result of "3+2" for active-to-sterile oscillation is slightly better than that of "3+1" model.

For accelerator neutrino experiments and atmospheric neutrino experiments, charged current (CC) reactions induced by ν_τ do not occur or the CC event induced by ν_τ is not simple to analyze. It is not simple to study the active-to-sterile neutrino oscillation with CC reaction signal. The neutral current (NC) reaction is a useful tool to measure the active-to-sterile oscillation, as the rates of NC reaction events for three active neutrinos

are the same. The MINOS experiment compares the event rate of neutral current reactions with hadrons between near detector and far detector [40, 41]. MINOS assumes $m_4 >> m_3$ for "3+1" model and a mass-squared splitting Δm^2_{43} with magnitude $\mathcal{O}(1$ eV$^2)$. There is no oscillation leading the depletion at near detector, while rapid oscillations are predicted at far detector. The expected number of NC events at far detector is calculated based on the observed number of NC events at near detector. As a result, 802 NC candidate events are observed at far detector, while the expected number of events is $754 \pm 28(stat.) \pm 37(sys.)$. Therefore, no evidence for depletion of NC events is obtained at the far detector.

The T2K experiment [58] has a potential to measure active neutrino disappearance by detecting NC events at the far detector Super-K. The de-excitation γ-ray events induced by NCQE reactions dominate in all NC events at Super-K. Except for the $\overline{\nu}_\mu \rightarrow \overline{\nu}_e$ measurement at the near detector, the detection of NCQE reaction events at Super-K opens a door to active-to-sterile neutrino oscillation search in the T2K experiment.

1.4 Supernova relic neutrino search at Super-Kamiokande

Supernova neutrino If a star with its weight heavier than eight times of solar mass comes its live end, the nuclear fusion in the star does not sustain its own gravity. The outer matter in the star accelerates toward its center with speed of ~ 0.23c, and this is referred to as a "core collapse"[42] of the star. Since the matter density inside is very high, electrons start to be captured by their nucleus as the following reaction.

$$e^- + p \rightarrow n + \nu_e \,(\text{electron capture}) \tag{1.20}$$

where ν_e is emitted in the reaction. If electrons disappear inside the star, electron degeneracy pressure become smaller, this cause the collapse velocity faster. The produced neutrinos at the inner core may be trapped in the core if the density of the innere core reaches $10^{10} \sim 10^{11}$ g/cm^3. The collapse continues until the neutron degeneracy pressure and neutron-neutron interaction appearing, then the collapsing matter bounce outward referred to as an explosion. The re-bounce leads an expanding shock wave which accelerates heavy nuclei to high energy, then the heavy nuclei dissociates into free protons and neutrons at outer core. The free protons catch the electrons to generate a large amount of electron-neutrinos (electron capture) on the time scale of the order of 10 ms, and this is called "deleptonisation burst". In the same time, the shock wave interacted with the trapped neutrinos, the equal numbers of the three flavors of neutrino-antineutrino pairs $(\nu - \overline{\nu})$ are produced. After the shock wave going out, the hot core releases neutrino pairs $(\nu - \overline{\nu})$ which are called as "thermal neutrino", and the time scale of the emission is ~ 10 sec.

The core collapse and explosion cause enormous heat of $\mathcal{O}(10^{46}$ J) produced, and only 1% fraction of heat are carried by light, and the 99% fraction of energy is expected to be released by neutrinos.

Supernova relic neutrino The frequency of supernova explosion in the galaxy is predicted as 2 or 3 times per century[43]. Although no neutrinos from supernova are observed after the last observation from supernova 1987A. The past supernova neutrinos diffuse over Universe space, and the diffusing neutrinos are called as "Supernova Relic Neutrino" (SRN) or "Diffuse Supernova Neitrino Background" (DSNB). The flux of SRNs

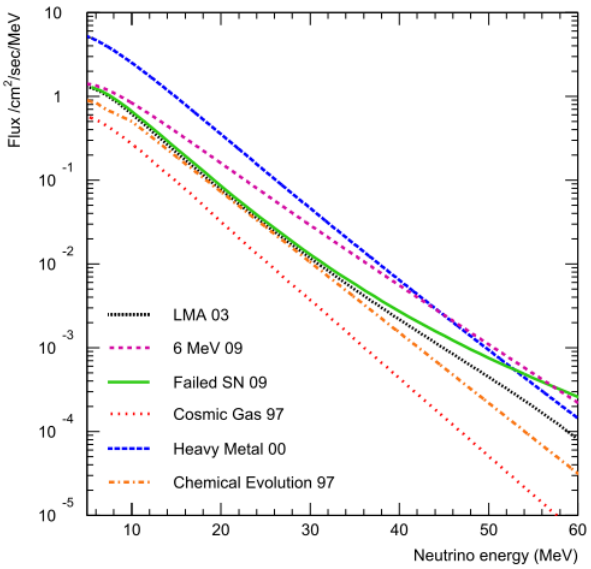

Figure 1.7: Some predictions of SRN flux spectrum from Ref. [56]. As the inverse beta decay is used for detecting signal, the flux is only plotted with only $\overline{\nu}_e$.

is a function of supernova burst rate, and the energy spectrum of SRN is redshifted as $E_\nu/(1+z)$, where z is the redshift constant coming from the expansion of the universe.

The flux of SRN is predicted by many models [44–55], and Figure 1.7 shows some predicted flux at energy region of $5 \sim 60$ MeV. The detection of SRNs is a important calibration for supernova models, as there is one neutrino sample of SN 1987A. The detection also reveal important information such as supernova rate, or cosmic star formation rates, and the redshift parameter z.

SRN observation at Super-K Super-K has potential to observe the SRN $\overline{\nu}_e$ via inverse beta decay $\overline{\nu}_e + p \to e^+ + n$. In 2013, Super-K reported the result of SRN search during the period of SK I (1497 days livetime), SK II(794 days livetime), and SK III (562 days livetime)[56]. The Cherenkov light signal from e^+ is observed as a SRN event, as the annihilation γ-ray has too low energy to be detected. The background sources are muon spallation, radioactive impurities at the detector wall, and the dark noise of PMT. The SRN analysis applies several selections to search for the SRN candidate events. There are still some background events remaining in the candidate events as shown in Figure 1.8, which shows the Cherenkov angle distribution of observed events. The reconstruction of Cherenkov angle of an event is described in Appendix B.3. The remaining background sources are explained in the next paragraph.

Remaining background For SRN research at Super-K, there are four remaining background sources. First, some $\nu_\mu(\overline{\nu}_\mu)$ CC reaction from atmospheric neutrino ν_μ produces a low energy μ which does not emit Cherenkov light. If its decayed electron has energy within the energy region of (10 MeV, 30 MeV), this decay-e event is remained. Second, the CC reactions from atmospheric neutrino ν_es are another source of background, if the energy of produced e is within the energy region of (10 MeV, 30 MeV). Third, NCπ reaction from atmospheric neutrino produces π^+ with energy $E_\pi > 200$ MeV that emits Cherenkov light. Besides, some decayed muons also emit Cherenkov light so the event is

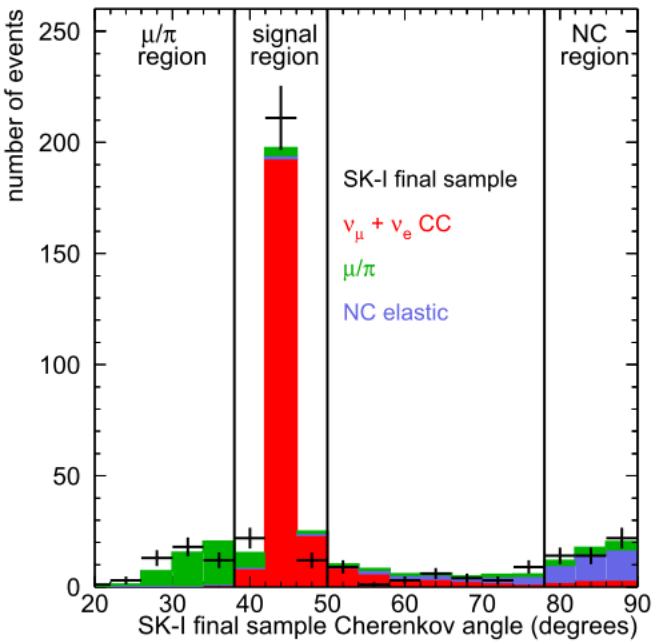

Figure 1.8: Cherenkov angle distribution (the reconstruction of Cherenkov angle of an event is described in Appendix B.3) of the observed events and the expected events during SK I period from Ref. [56]. Since the NCQE (NC elastic) events from atmospheric neutrinos have multiple γ-rays, the most angles of the NCQE events are reconstructed to be larger than 78 degree. The SRN analysis uses angle cut ($38.0 \leq \theta \leq 50.0$) to select the SRN signal.

selected as a candidate event. The π and the μ emit Cherenkov light, and the Cherenkov angle is $\theta_c \leq 38$ degree as described in Appendix B.3. The background events are removed by selecting events with $\theta_c \geq 38$ degree. Forth, the de-excitation γ-ray induced by the NCQE interaction from atmospheric neutrino is a background source. The energy spectrum of NCQE events is similar with that of the SRN, but the angles of the most NCQE events with $E_{rec} \geq 16$ MeV are multi-gamma events as mentioned in Chapter 5.3.4. The multi-gamma events are reconstructed to be larger than 78 degree as mention in Appendix B.3, so the most NCQE background events are removed by selecting events with angle $\theta \leq 50$ degree.

To remove the background events, the SRN signal is selected by the angle cut that is within the angle region of $38^o \leq \theta_c \leq 50^o$. There are still relevant background events than SRN events as shown in Figure 1.8. The combined SRN flux upper limit is measured as between 2.8 and 3.0 $\overline{\nu}_e$ cm^{-2}s^{-1} $>$ 16 MeV.

SRN search using neutron tagging method Super-K uses a neutron tagging method to observe the neutron produced in the inverse beta decay reaction $\overline{\nu}_e + p \rightarrow e^+ + n$ recently [57]. The delayed γ-rays from neutron capture are used to have a coincidence with the primary signal of e^+. By using the coincidence, about 80% fraction of atmospheric ν CC background events are removed, if there is no neutron produced (or more than one neutrons) at the reaction. But, the NCQE events induced by the atmospheric neutrinos are not removed by the neutron tagging method, as neutron is produced at the NCQE reaction.

As a result, Super-K reported the 13 inver-se-beta-decay candidates in the range of $E_{\overline{\nu}_e}$

between 13.3 MeV and 31.3 MeV, and all the observed candidate events are attributed to background. In the future, Super-K has a plan to lower the energy threshold to 10 MeV, and the new threshold allows more NCQE events with Cherenkov angle in tha range of $38 \leq \theta_c \leq 50$ to be selected as the candidate events. It is important to have a precise estimation for the number of NCQE events for future SRN search.

1.5 Overview of this thesis

This thesis reports the measurement of the $\nu-$oxygen neutral current quasi-elastic (NCQE) cross section by observing de-excitation γ-rays with the T2K neutrino beam. The study of the NCQE reaction has the following two motivations: First, the de-excitation γ-rays induced by the NCQE interaction from atmospheric neutrinos are one background source in supernova relic neutrino (SRN) searches as shown in Section 1.4. However, there is no previous experimental result to measure $\sigma_{\nu,NCQE}$. Because the average energy of T2K neutrino beam is 630 MeV which is the same order with the average energy of atmospheric neutrinos. The measurement of NCQE cross-section by T2K neutrino beam can be used to reduce the uncertainty of SRN search. Second, the de-excitation γ-ray events provide a tool for active-to-sterile neutrino oscillation search $\nu_\mu \rightarrow \nu_s$ at T2K experiment. The most de-excitation γ-ray events are induced by the NCQE reactions, so the disappearance of the number of the events is used to measure the active-to-sterile neutrino oscillation.

In this these, the overviews of the T2K experiment and the Super-Kamiokande detector are mentioned in Chapter 2. An overview of the NCQE cross-section analysis is described in Chapter 3. Chapter 4 describes the simulation processes of de-excitation γ-ray events induced by the T2K neutrino beam. The simulation is used to predict the expected number of beam-related events. In Chapter 5, the selection procedure for the observed number of de-excitation γ-ray events is described. The event information of energy, timing, vertex, direction, Cherenkov angle, and pre-activity are used to select γ-ray candidate events from the T2K spill data. After the selection, the comparisons between the observed events and the expected events are described. In Chapter 6, the uncertainty of the NCQE cross-section measurement is described. As a result, the measurement results of NCQE cross-section are mentioned in Chapter 7. In Chapter 8, we consider the influence of the de-excitation γ-ray observation on the sterile neutrino search at T2K and the supernova relic neutrino search at Super-K. Chapter 9 describes the conclusions of this thesis.

Chapter 2

T2K experiment

2.1 Overview

The T2K (Tokai to Kamioka) experiment[58] is a long baseline neutrino oscillation experiment. A 30 GeV proton beam is used to produce the intense muon neutrino beam in J-PARC, Tokai Village, Ibaraki. The near detector complex, located at 280 meter downstream of target, detects the neutrino beam properties and measures the neutrino-nucleus cross-sections. The Super-Kamiokande detector serves as a far detector of the T2K experiment, and observes neutrino events at a distance of 295 km from J-PARC. The numbers of neutrino events before oscillation and the number of neutrino events after oscillation are measured respectively at the near and far detectors. The neutrino oscillation probabilities are obtained by comparing the two numbers of events. Figure 2.1 shows the schematic of the T2K experiment.

2.2 Goals of T2K experiment

The main goal of the T2K experiment is to measure the neutrino oscillation parameters. The goals can be divided into:

ν_e appearances from ν_μ beam for θ_{13} and δ phase research

Before 2012 Feb., the main physics goal was the measurement of $\sin^2 2\theta_{13}$ using $\nu_\mu \rightarrow \nu_e$ appearance since only an upper limit was known ($\frac{1}{2}\sin^2\theta_{13} > 0.004$ at 90% C.L). In June, 2011, T2K gave the first indication of ν_e appearance: $0.03 < \sin^2 2\theta_{13} < 0.28$ which lead to a nonzero θ_{13} significance of 2.5σ [59]. The Daya Bay reactor experiment measured the first evidence of nonzero θ_{13} with 5.2σ significance and gave $\sin^2 2\theta_{13} =$

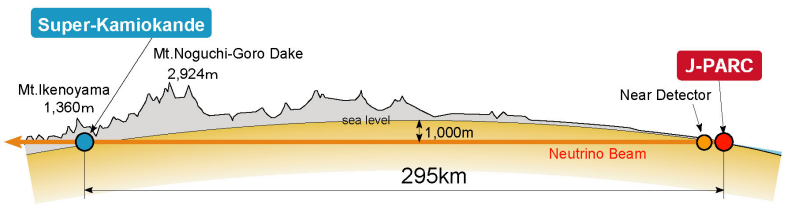

Figure 2.1: The T2K experiment schematic [58].

$0.092 \pm 0.016 \pm 0.005$ in 2012, Feb through $\overline{\nu_e}$ disappearance [60]. From then on, the measurement of lepton CP violation angle δ_{CP} became T2K goal and can be achieved by precisely measuring the ν_e ($\overline{\nu_e}$) appearance probability. Currently, the first constrain of δ_{CP} angles at 90% C.L. are observed by combining the T2K and reactor results in Ref. [61].

ν_μ disappearance for precise measurement of Δm^2_{32} and θ_{23}

The other goal of T2K is the precise measurement of the —Δm^2_{32}— mass difference and the mixing angle $\sin^2\theta_{23}$ via ν_μ disappearance. A recent measurement from Super-Kamiokande using atmospheric neutrino [62] shows that the mixing angle θ_{23} is $\sim \frac{1}{4}\pi$. But the sign of $\sin^2\theta_{23} - 0.5$ is not still determined due to the remaining large uncertainty. The uncertainty of $\sin^2\theta_{23}$ affects the precision of the δ_{CP} measurement. Nowadays, the T2K experiment gave the most precise result of $\sin^2\theta_{23} = 0.514 \pm 0.082$ in Ref. [63]. T2K aims to measure $\sin^2 2\theta_{23}$ and Δm^2_{32} with a precision wihthin 1% and 3% respectively.

Others

The intense neutrino beam produced in J-PARC has a narrrow energy distribution with a peak near 600 MeV. The neutrino-nucleus interactions are studied at the near detectors using the neutrino beam. At the far site, there is a study of NCQE interaction using solar neutrino analysis method. Besides the neutrino interaction studies, there are rich physics topics such as sterile neutrino (Sec. 8.1), dark matter [64, 65], Lorentz violation [66, 67], etc.

2.3 J-PARC neutrino beam

off-axis method

Given the designed baseline, the energy of neutrino beam is tuned to maximize the oscillation. T2K uses the "off-axis" method to obtain the desired energies of neutrinos as detailed in the following paragraph.

If a neutrino is produced from pion decay with an off-axis angle θ_{OA} with respect to the pion direction, the energy of the neutrino is derived as below:

$$E_\nu = \frac{m_\pi^2 - m_\mu^2}{2(E_\pi - p_\pi \cos\theta_{OA})} = \frac{m_\pi^2 - m_\mu^2}{2p_\pi(1/\beta_\pi - \cos\theta_{OA})} \tag{2.1}$$

where m_π and m_μ are the pion mass and the muon mass respectively, and p_π is the pion momentum. By adjusting the off-axis angle, the desired energies of neutrinos could be obtained. The T2K beam axis is intentionally shifted by 2.5 degree from the direction of the Super-Kamiokande (Super-K) detector. The off-axis angle is selected to be 2.5^o to tune the energy spectrum of neutrinos to be a narrow distribution peaked at 600 MeV as shown in Figure 2.4. For a neutrino energy of 600 MeV, the oscillation is maximal at a distance of 295 km.

2.3.1 J-PARC proton beam

The proton accelerator J-PARC consists of three accelerators: a linear accerator (LINAC), a rapid-cycling synchrotron (RCS) and a main ring (MR) synchrotron. The

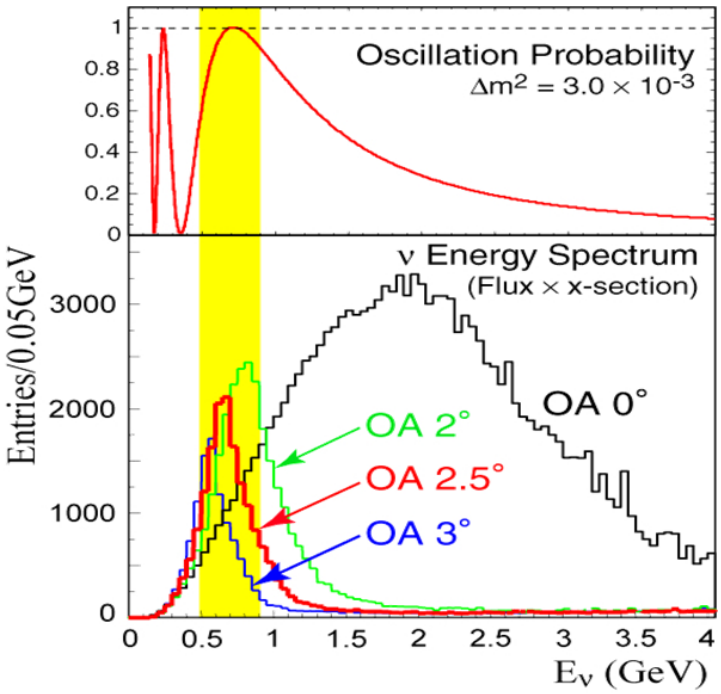

Figure 2.2: The lower plot shows the energy spectrum of neutrinos with the different off-axis angles at distance of 295 Km. The upper plot shows the oscillation probability $\nu_\mu \rightarrow \nu_e$ is maximum at $\sim$ 600 MeV, and the off-axis angle of 2.5 degree at distance of 295 Km. The energy spectrum of neutrino has a narrow distribution peaked at 600 MeV.

overview of the proton beam accelerators is as shown in Figure 2.4. The H^- ions are accelerated to 400 MeV in LINAC, then they are converted to H^+ beam by charge-stripping foils before the injection to RCS. RCS accelerates the proton beam to 3 GeV, and RCS supplies about 5% of proton beam to MR. In MR, the protons are accelerated to 30 GeV with repetition cycling time of $\sim$ 2.48 sec. In a single spill (one cycling), the harmonic number of MR is nine, and eight buckets are filled with proton beam from injection of RCS. The last backet is empty for the rise-time (1104 ns) of extraction to neutrinobeam-line. Therefore, a beam spill have eight bunches.

The bunch structure of proton beam is the feature that distinguishes the ν beam signal from the beam-unrelated backgrounds. A summary of the proton beam properties in MR is as shown in Table 2.1.

2.3.2 primary beamline

The neutrino beamline is composed of two sequential sections: primary beamline and secondary beamline. In the primary beamline, the proton beam is extracted from MR and the beam-line transports beam towards the proper direction.

The primary beamline consists of the preparation section (54 m), the arc section (147 m) and the final focusing section (37 m). Figure 2.4 shows each part of the primary beamline. In the preparation section, the extracted proton beam is tuned with a series of 11 normal conducting magnets. In the arc section, 14 doublets of superconducting combined function magnets (SCFMs) bend the proton beam toward the direction of the Super-K detector by 80.7 degree. In the focusing section, ten normal magnets guide and focus the proton beam onto the target. Here, the proton beam is guided downward by

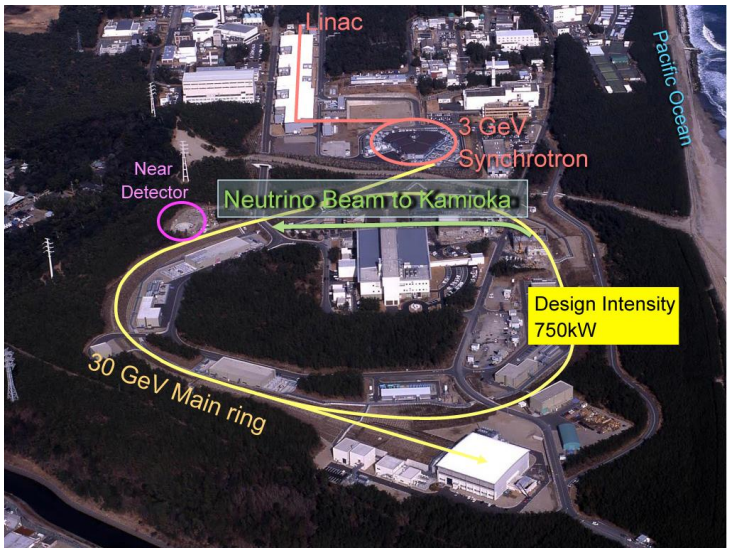

Figure 2.3: A bird eye view of J-PARC.

Table 2.1: The properties of the MR proton beam. The parameter values are the operating values in Mar, 2015.

Parameters	Present value (Mar. 2015)
beam energy	30 GeV
beam power	310 kW
repetition cycle time	2.48 sec
proton per spill	$\sim 1.6 \times 10^{14}$/spill
bunch per spill	8/spill
bunch interval	581 ns
bunch width	58 nsec

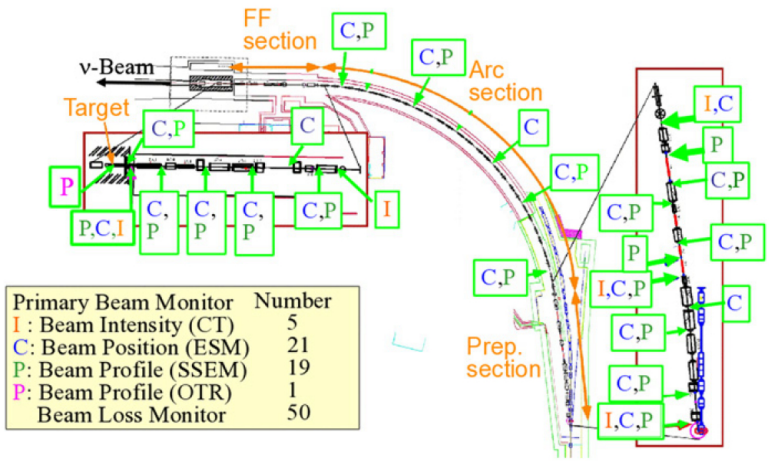

Figure 2.4: The primary beamline. The locations of the monitors are marked as the arrows [58].

3.637 degree with respect to the horizontal.

To ensure the stability of the neutrino beam, the monitors in primary beam measure the following proton beam properties: the intensity, the position, the profile ,and the loss rate.

- Current transfer (CT): Five current transfers measure the proton beam intensity and the beam timing. Each CT monitor is a 50-turns coil of a copper wire around a ferromagnetic core. It measures currents induced by the proton beam bunches, and the signal is recorded by a 160 MHz FADC. The precision of the proton beam intensity measurement is 2%. The timing of beam is measured with precision better than 10 ns.

- Electro-static monitor (ESM): Twenty-one electro-static monitors measure the center position of the proton beam non-destructively. Each ESM consists of four round-rectangular electrodes, and the electrodes are located around the proton beam orbit. The induced currents of the four electrodes are compared to measure the beam position. The measurement precision of the beam center position is less than 450 μm, while the required precision for beam steady is 500 μm.

- Segmented secondary emission monitor (SSEM): Nineteen segmented secondary emission monitors measure the profile of proton beam. Each SSEM consists of two thin titanium foil strips and an anode HV foil between the two foil strips. The foil strip are oriented horizontaly, while the anode HV foil is oriented vertically. If the proton beam passes through the strips, electrons are emitted from the strips in proportion to the beam intensity. The electrons drift along the electric field to the anode foil, and this drift process induces currents on the strips. The beam profile is reconstructed from the corrected charge distributions. The uncertainty of the beam width measurement by SSEM is 700 μm.

- Beam loss monitor (BLM): Fifty beam loss monitors detect leaks of the proton beam near the beam pipes. Each BLM is a wire proportional counter filled with an Ar-CO_2 mixture. The signal is integrated during the spill. If the signal exceeds the threshold, a beam abort interlock signal is fired. The BLMs have sensitivity down to a 16 mW beam loss.

2.3.3 secondary beam-line

The secondary beam-line (Figure 2.5) consists of three sections: the target station, the decay volume, and the beam dump. The target station is composed of the following devices: first, a baffle which is a collimator to protect the magnetic horns from a damage by the deviation of proton beam. Second, an optical transition radiation monitor (OTR) which measures the proton beam profile. The proton beam hits a carbon target and produces hadrons which are focused by three magnetic horns. The produced hadrons then enter the decay volume, and most of them are pions which decay into muons and muon neutrinos. All the non-decaying hadrons and muons below ~ 5 GeV/c are stopped by the beam dump. The muons with energies $E_\mu > 5$ GeV are detected by a array of ion chamber detectors and silicon photodiode detectors located after the beam dump. The detectors monitor the beam profile of each spill by detecting the penerated muons, and we call the muon detectors as “MUMON”. The secondary beamline facilities are filled

with helium gas (1 atm) to reduce the pion absorptions and to suppress the tritium and NO_x production by radiation.

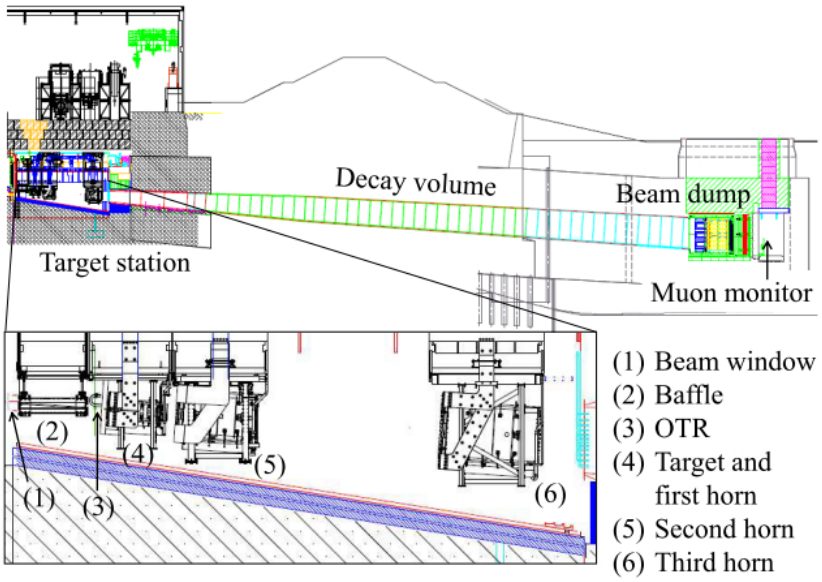

Figure 2.5: The side-view of the secondary beam-line from Ref. [58]. The decay volume is 96 meter long.

optical transition radiation monitor

The optical transition radiation monitor (OTR) is located in front of the target, and measures the proton beam profile [68]. The OTR has a thin titanium-alloy foil, which is placed at 45° from the incident proton beam. As the beam passes through the foil, visible light is produced in a narrow cone around the beam. The light at the entrance transition is reflected at 90^o from the beam direction, and the light is directed away from the target. Then, the lights are detected by the CCD camera.

target

The target core is a 1.9 interaction-length long (91.4cm long), 2.6cm diameter and 1.8g/cm^3 graphite rod. The core and a surrounding 2 mm thick graphite tube are sealed inside a titanium case which is 0.3 mm thick. Hadrons are produced inside the graphite target.

horn

The electromagnetic horn consists of two coaxial (inner and outer) conductors which encompass a closed volume [69, 70]. The two conductors are loaded with pulsed currents. A toroidal magnetic field is generated inside the closed volume, and the field varies with $1/r$, where the r is distance to the beam axis. Three horns in serial are designed to focus the charged hadrons to the forward direction.

In the first horn, the pions with relatively large angle are collected to forward direction as shown in Figure 2.6. The second and the third horns focus the pions after the first horn.

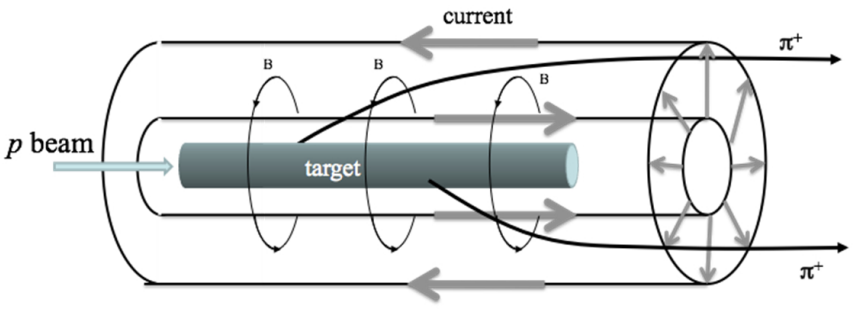

Figure 2.6: The schematic of the first horn and the target. The proton beam hits the graphite target and produces pions. The toroidal magnetic field inside the horn focuses these pions towards the forward direction.

The neutrino beam flux at Super-K increases by a factor of ∼16 because of the horn focus. The accuracy of the magnetic field intensity is ∼ 2% for the first horn and less than 1% for the second and third horn.

decay volume

The decay volume is a 96 m long steel tunnel, which is surrounded by a 6m thick reinforced concrete shielding. Inside the decay volume, the hadrons (pions, kaons) decay into neutrinos and muons.

Beam dump

The beam dump is located at the end of the decay volume. The core of the beam dump is made of 75 tons of graphite, and the core is surrounded by the helium vessel. Five iron plates are placed outside the helium vessel, and two iron plates are placed downstream the core. The total thickness of the 7 plates is 2.40 meter. The beam dump stops the muons with an energy lower than 5 GeV.

2.3.4 MUMON monitor

The intensity, profile and direction of the neutrino beam are monitored by measuring the muons which cross the beam dump by using the muon monitor, MUMON. The monitoring is done on a spill-by-spill basis [71, 138].

Figure 2.7 shows the picture of MUMON. MUMON has two kinds of detector array: ionization chamber (IC) and silicon PIN photo-diodes [138]. There are seven ionization chambers filled with a gas mixture which consists of 98% Ar and 2% N_2. Each IC contains seven sensors in a aluminum gas tube. The $75 \times 75 \times 3$ mm^3 active volume of each sensor is made by two parallel plate electrodes, and a high voltage of 200 V is applied between the two electrodes. The silicon PIN photodiode (Hamamtsu S3590-08) has an active area 10×10 mm^2 and a depletion layer thickness of 300 μm. To fully deplete the silicon layer, a high voltage of 80 V is applied to the sensors.

In the physical operation period from Jan., 2010 to May 2013, the MUMON measured the most spill of beam direction within a 0.30 mrad deviation from zero as shown in Figure 2.22, which is less than the requirement of 1 mrad. The total collected charge, which is proportional to the beam intensity, has a RMS fraction less than 1.0% for most of the

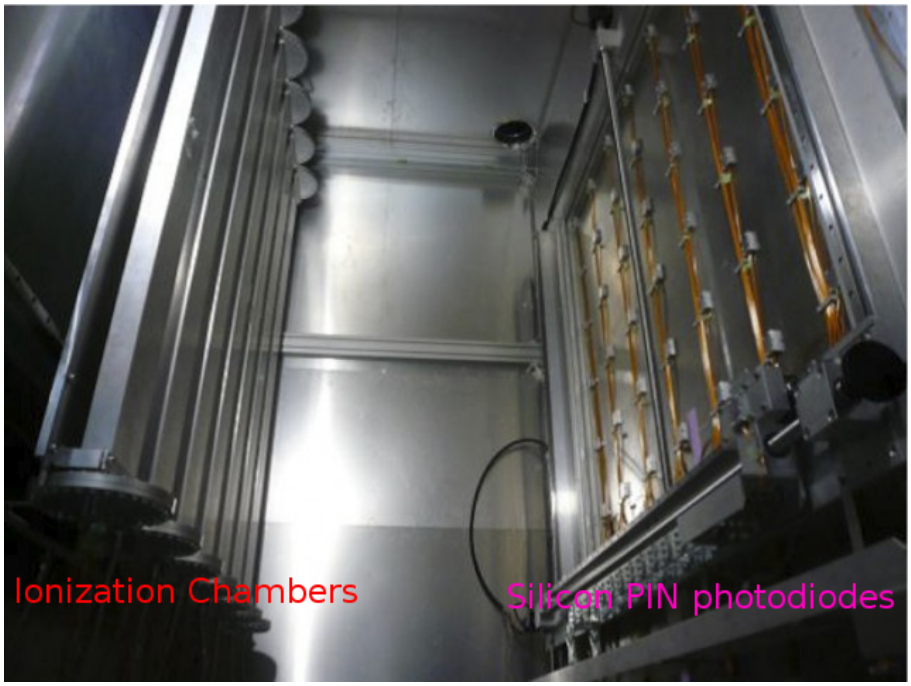

Figure 2.7: A picture of MUMON. The left detectors are ionization chamber arrays, and the right detectors are the silicon PIN photo-diode arrays. The muon direction is from the right side to left side in the picture [58].

operation, which means that MUMON has a high stability that is compatible with the requirement of uncertainty within 3%.

2.4 Near Detectors

The neutrino energy spectrum, beam profile, the beam flavor content, and the interaction rates of neutrino beam are measured by a set of detectors located 280 meter from the target. The measured results are used to refine the prediction of the observable neutrino beam flux at Super-K. The detectors are installed in a pit inside the near detector hall as shown in Figure 2.8.

2.4.1 ND280

The ND280 detector is a complex composed of several subdetectors located inside a magnet as shown in Figure 2.9. It is located 2.5° off-axis from the beam center and is aligned with the target and Super-K.

Magnet The magnet is donated from CERN. It provides a dipole magnetic field of 0.2 Tesla which allows to measure the charge and the momentum of charged particles in the detectors.

PØD The pi-zero detector (PØD) [72], located the most upstream inside the magnet, consists of tracking planes of scintillator bars alternating with either water target/brass foils or lead foils. Signal of each bar is readed out by a wavelength shifting fibers (WLS

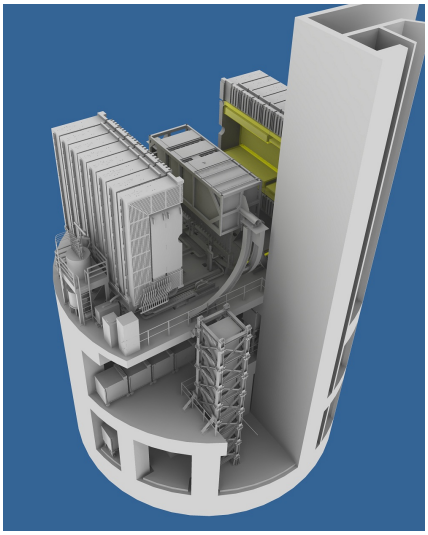

Figure 2.8: The near detector hall in J-PARC from Ref. [58]. The ND280 off-axis detectors are located at B1 floor (upper level here), and the magnet are opened in the figure. The horizontal INGRID modules are located at SS floor (middle level), while the vertical INGRID modules are arranged from the B2 (bottom) to B1 floor.

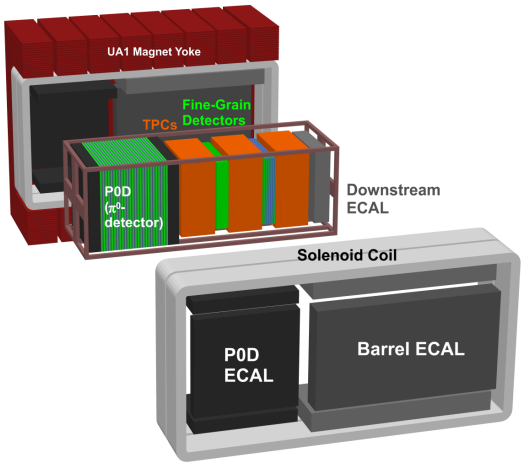

Figure 2.9: Schematic view of the ND280 detector from Ref. [58]. In the picture, the UA1 magnetic yoke is opened. In operation period, the detectors are closed inside the UA1 magnet yoke. The neutrino beam goes from left side to right in the figure.

fiber) and a Multi-Pixel Photon Counter (MPPC). It was designed to measure the neutral current pion production $\nu_\mu + N \to \nu_\mu + N + \pi^0 + X$ in the water target.

TPC Downstream of PØD, there are tracker detectors including three time projection chambers (TPC) and two fine grained detectors (FGD). Each TPC detector [74] has an inner box that holds an argon-based drift gas. The inner box is subdivided by the cathode located at its midpoint, and the inner box supports the micro-megas modules located in a plane parallel to the cathode. If a charged particle passes through the inner box, ionization electrons are produced along the particle track. The electrons drift away from the center cathode toward one of the readout planes. Particle identification is done with an energy loss of charged particles in the gas and momentum reconstructed from the track curvature.

FGD Two fine grained detectors (FGD) [73] use plastic scintillator bars to observe tracks of charge particles from the neutrino interactions. The first FGD detector consists of 30 layers of scintillator bars, and the second FGD consists of 7 layers of scintillator bars alternating with six 2.5 cm thick layers of water. The ratio of ν cross-section on carbon over water is measured by comparing the numbers of neutrino events of the two FGD detectors.

ECal The electro-magnetic calorimeter (ECal) [75] is a sampling electromagnetic calorimeter surrounding the inner detectors (PØD, TPCs, FGDs). The ECal consists of layers of

plastic scintillator bars, WLS fiber and MPPC readouts, and lead absorber sheets, and it is designed to measure electron produced from ν_e and γ-rays produced from π^0s.

SMRD The side muon range detectors (SMRD) [76] is composed of scintillation counters with embedded WLS fibers and MPPC readouts. A multiple layers of plastic scintillation counters are placed in the air gaps in between the iron plates. SMRD measures the momenta of muons produced from the neutrino reactions, and also identifies backgrounds from the beam neutrino interactions in the yoke or walls.

2.4.2 INGRID

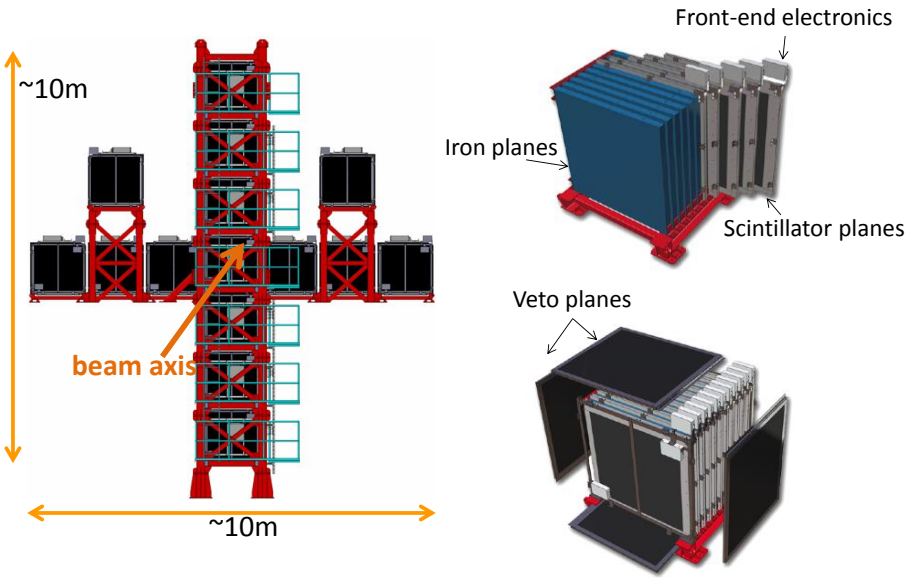

Figure 2.10: The INGRID detector [77]. The left graph shows the arrangement of 16 INGRID modules. The right upper graph shows the structure of a module which is a sandwich made of 9 iron target plates and 11 scintillator trackers. The front-end electronics boards are contained inside the aluminum box. The right bottom graph shows the module surrounded by the scintillator veto planes.

The INGRID (Interactive Neutrino GRID) detector [77] consists of 16 identical modules. As shown in Figure 2.10, the 14 modules are arranged as a cross of two identical groups along the horizontal and vertical axis, while two additional shoulder modules are located at off-axis directions outside the main cross. The center of the INGRID cross, with two overlapping modules, corresponds to the beam center (off-axis angle 0^o). Each INGRID module has 9 iron target planes and 11 tracking scintillator planes, which are arranged as a sandwich structure as shown in the right upper graph of Figure 2.10. The iron mass is 7.1 ton per module, and the iron serves as the main neutrino interacting target. The scintillator bars are made of polystyrene and are produced in a rectangular cross-section shape (1.0 cm$\times$5.0 cm) through extrusion. The scintillator light is collected and transported by WLS fibers to the attached MPPCs. Veto planes are installed around this sandwich structure in order to dispose of background events coming from the hall

walls or cosmic rays. Finally, the set of scintillators, fibers and photosensors is contained in a light-tight dark box while the front-end electronics boards are mounted outside the dark box.

The INGRID detector is designed to monitor the neutrino beam direction and the intensity using neutrino interactions with the modules. The neutrino event rates in each module are compared to obtain the profile of neutrino beam. The beam center is obtained from a fit of the beam profile with a Gaussian function which leads to a precision better than 10 cm. It corresponds to a 0.4 mrad precision on the beam angle.

2.5 Super-Kamiokande detector

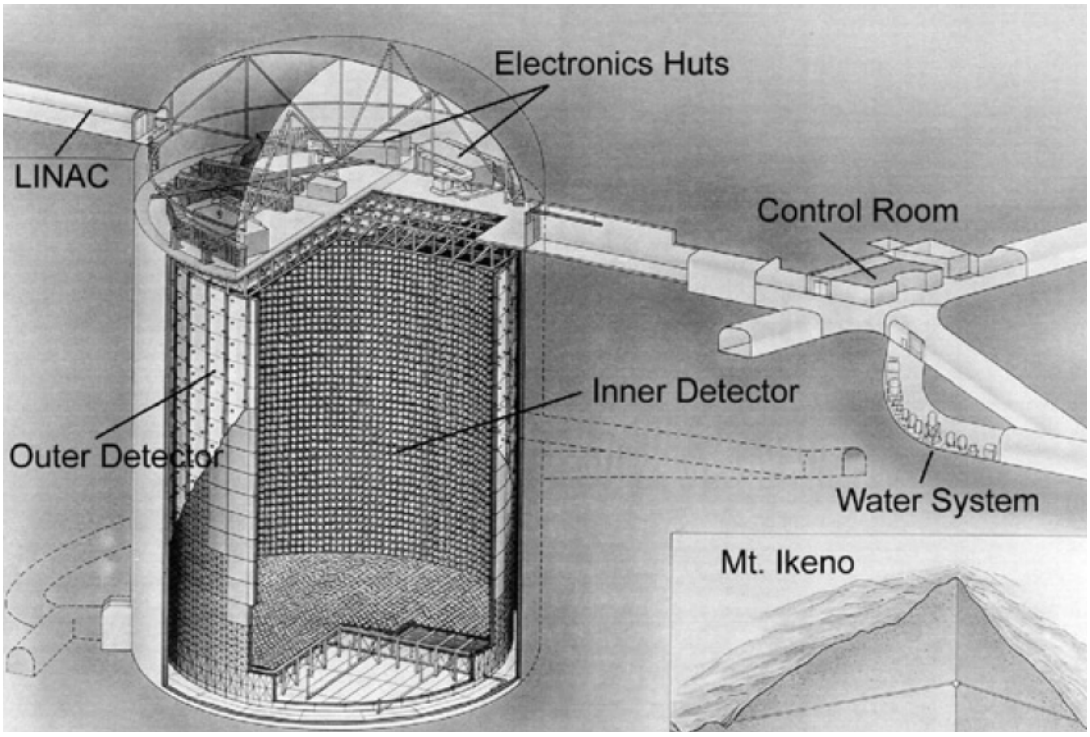

Figure 2.11: The sketch of the Super-K detector and electronics huts and control room, and etc from Ref. [78]. The detector cavity lies 1000 meter under the peak of Mt. Ikenoyama.

2.5.1 Overview

The Super-Kamiokande (Super-K or SK) detector is the world largest water Cherenkov detector [78], which is located in Kamioka-Cho Hida City, Gifu Prefecture, Japan. The Super-K detector is 295 km distant from J-PARC, and serves as the far detector for the T2K experiment. Besides accelerator neutrino, various topics such as proton decay and neutrinos from various sources such as atmosphere, solar, and supernova are studied at Super-K. The Super-K detector consists of a welded stainless-steel tank, 39m diameter and 42 m tall, and have a water capacity of 50,000 tons. The water tank and the other facilities are as shown in Figure 2.11. Inside the Super-K detector, a stainless-steel framework supports 11,146 inward-facing PMTs and 1,885 outward-facing PMTs.

Table 2.2: The measured background radiation rates of γ-rays and neutrons near super-K cavity dome from Ref. [78].

background	Energy range	Rate
γ rays	$E_\gamma \geq 0.5$MeV	$0.1\text{cm}^{-2}\text{s}^{-1}\text{sr}{-}1$
	$E_\gamma \geq 5$MeV	$2.7 \times 10^{-6}\text{cm}^{-2}\text{s}^{-1}\text{sr}{-}1$
neutron	$E_n \leq 5 \times 10^{-2}$eV	$1.4 \times 10^{-5}\text{cm}^{-2}\text{s}^{-1}$
	$5 \times 10^{-2}\text{eV} < E_n \leq 2.5$MeV	$2.5 \times 10^{-5}\text{cm}^{-2}\text{s}^{-1}$
	$2.5\text{MeV} < E_n \leq 25$MeV	$0.33 \times 10^{-5}\text{cm}^{-2}\text{s}^{-1}$

The volume surrounded by the 20 inch inward-facing PMTs is called the Inner Detector (ID), and the ID PMTs are used to observe the charge particle produced from neutrino interactions. The volume outside the framework serves as an active veto counter against incoming background particles, which is referred as the Outer Detector (OD).

The cavity which houses the facilities is located 1000 meter under the peak of Mt. Ikenoyama. Cosmic ray muons having an energy less than 1.3 TeV do not reach the cavity, and the muon flux is 6×10^{-8} $\text{cm}^{-2}\text{s}^{-1}\text{sr}^{-1}$, which does not represent a significant background for the experiment. The downward-going muons are observed with a net rate about 2 Hz. The other backgrounds in the Super-K cavity are shown in Table 2.2

Each ID PMT has a dynamic range from 1 photoelectron (p.e.) to $\sim$300 p.e. Super-K is able to detect events over a wide range of energy, from 4 MeV to over 1 TeV. The neutrinos from solar and supernova have lower energy values (from 4 MeV to 100 MeV), and are therefore called "low energy events". The energy of the "low energy event" is calculated using the number of hit PMTs as described in Appendix B. The atmospheric neutrinos have energy above $\mathcal{O}$(100 MeV), so the total charge of an event is used to calculate its energy.

phases of Superkamikande detector

The Super-Kamiokande started to taking data from April 1996. Until now, the Super-K operation is separated into four periods. From the first physical operation at 1996 to the maintenance in July 2001, this initial phase is called as "SK I". From October 2002 until the next shutdown in October 2005, the Super-K detector was operating with half of its ID PMTs due to an accident. The photo-coverage was only 19%, less than half of the design value of 40%. This phase is called "SK II". The Super-K detector started again operation with full number ID PMTs in July 2006, and stopped briefly for the electronics upgrade in September 2008. This phase is called as "SK III". The period from September 2008 to now is called "SK IV", and the T2K experiment started the operation within the SK IV period. In following sections, the Super-K detector during SK IV period is described in details.

2.5.2 Detector

As described previously, the Super-K detector has a stainless steel structure which supports the PMTs and optically separates the water tank between the inner (ID) and outer detectors (OD). The ID and OD are optically isolated using black sheets. The ID volume is a cylinder having a 33.8 diameter and a 36.2 m height, which represents a

capacity of 32 ktons of water. The 11,146 inward-facing PMTs are mounted on a 70 cm grid, and 7,650 of them are on the barrel (side walls), 1,748 PMTs are on the top cap and 1,748 PMTs are on the bottom round.

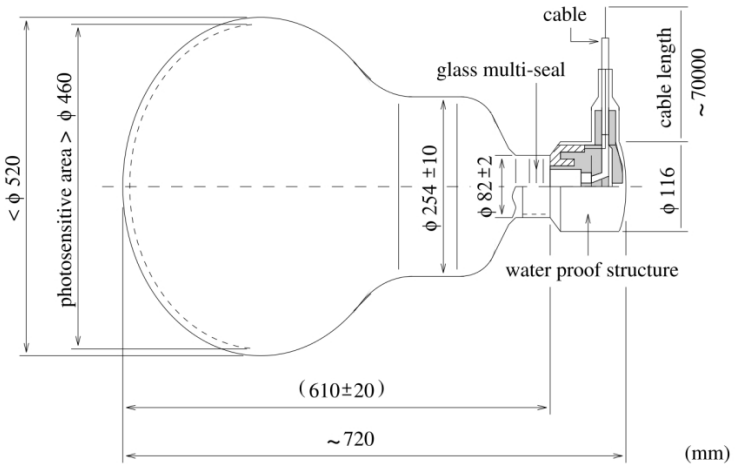

Figure 2.12: The schematic of 20 inch PMT from Ref. [78]. The inward-facing PMTs are installed in the stainless steel framework to detect the Cherenkov photons within the ID tank.

Figure 2.12 shows the schematic view of a 20 inch PMT. Each ID PMT has a diameter of 20 inch. The photo-cathode of ID PMT is made with bialkali (Sb-K-Cs) material, and the quantum efficiency of the photo-cathode has a peak about 21% at 360 $\sim$ 400 nm as shown in Fig. 2.13. The photo-sensitive area of each ID PMT has a diameter $\phi > 460$mm [79]. The design value of photo-coverage of the ID surface is 40%. The single photo-electron signal is clearly separated from the pedestal, and the transit-time spread for the signal is about 2.2 ns as shown on Figure 2.14. The dark noise rate of a PMT at the 0.25 p.e. threshold in Super-K is about 0.3kHz. The ID PMTs are operated with a gain of $\sim 10^7$ using a supply high voltage operated from 1600 V to 2000 V. The high voltage values are determined by the scintillator ball/Xe lamp calibration as described in Ref. [82]. To prevent the PMTs from cracking chain reaction, the ID PMTs are encased in fiber-reinforced plastic (FRP) cases with acrylic front windows.

All cables run up along the support structure to the top of the tank, then they are routed into the electronics huts. The black sheets cover the stainless steel framework except for the front window of ID PMTs as shown in Figure 2.15.

The 2.5 meter extension concentric to the support structure form the OD volume. The OD is designed to identify the incoming cosmic rays and atmospheric neutrino interactions with charge particles leaving the inner detector. Therefore, the requirements for the OD are not as stringent as those for the ID, *e.g.* the timing resolution is $\sim$ 15ns longer than the ID PMTs by 4 ns. The ID walls are covered with 8-inch PMTs, while 591 OD PMTs are recycled from the IMB experiment, and 1293 new PMTs are installed in the OD.

2.5.3 Electronics and data acquisition system

The T2K experiment started from 2010 during the SK IV phase. The electronics and DAQ system during SK IV period are described here.

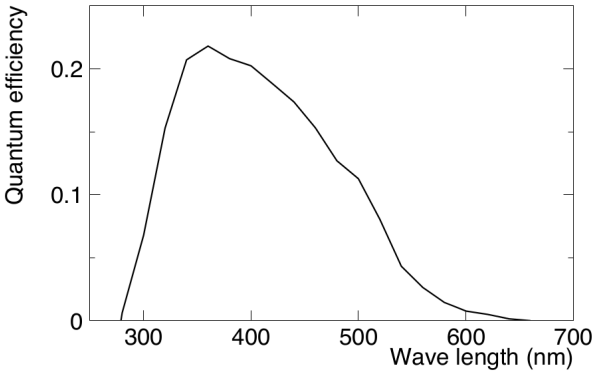

Figure 2.13: Quantum efficiency of photo-cathode of ID PMT from Ref. [79]. The quantum efficiency is a function of wavelength.

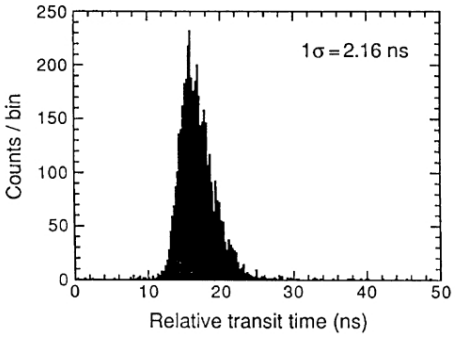

Figure 2.14: The relative transit time distribution for a typical ID PMT at the single photo-electron intensity level from Ref. [78].

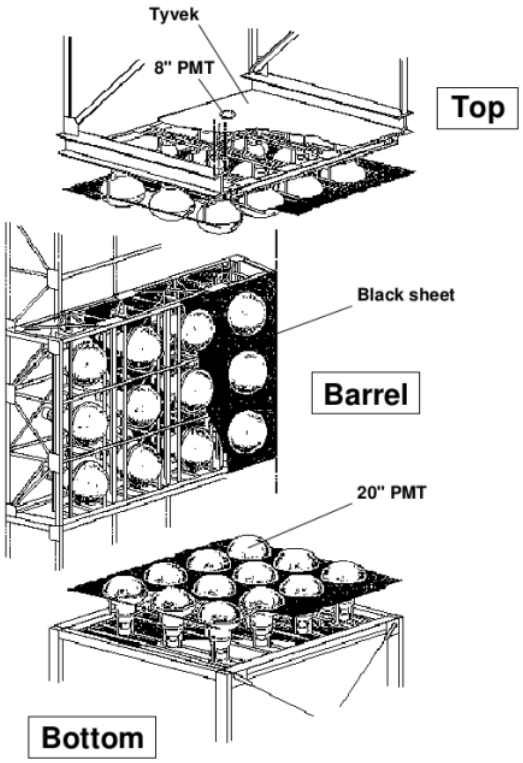

Figure 2.15: The schematic view of support structures for the inner detector [78].

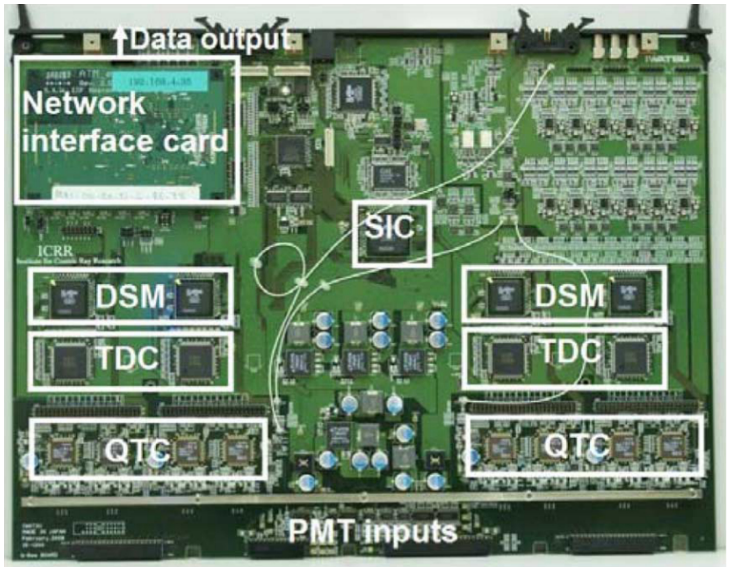

Figure 2.16: The QBEE board for the Super-K readout [83].

To ensure the stability of data-taking and improve the high-speed processing, the front-end electronics of Super-K was replaced in September, 2008. The front-end electronics board is QBEE [83], which is an abbreviation of "QTC (charge to time converter) Based Electronics with Ethernet" as shown in Figure 2.16. The discriminators on the QBEE boards vary the discriminator voltage level from -0.3 to -14 mV for the PMT signals. If a signal of a PMT exceeds the threshold of the discriminator, the PMT is referred to as one "hit PMT". There are eight QTC chips in a QBEE board, and QTC chip integrates the input charges and outputs pulses having width proportional to the amount of charge. A Time to Digital converter (TDC) receives the QTC output pulse, and the TDC chip digitizes the pulse width and arriving time information. Then, the charge, timing and the input channel information are stored in Fast-In-Fast-Out (FIFO) memory with size of 1.5 MB. A custom network interface card in QBEE transfers data to online PC by adopting Ethernet, and the data transfer for a QBEE board achieves 11.8 MB/s.

Data from the 550 QBEE boards are collected and saved into disk by the on-line system which is shown in Figure 2.17. The data digitized in QBEE are first transfered to 20 front-end PCs, then the software in front-end PCs sorts the data by time order, and finally, the data are sent to the Merge PCs. A manager PC receives the processed data report from the front-PCs, and the manager PC requests the data transfer to the specific Merge PC. After the confirmation of implementation from the Merge PC, the data flow manager computes the next request for transfer from the front-end PCs.

In the Merge PCs, data are sorted by timing order again. Then, the data are merged to blocks which contain the information of hit PMTs within 22 ms time window. The process software trigger searches if the signal exceed the trigger conditions. There are several triggers prepared for the different physical purpose, and the triggers are summarized in Table 2.3. Special High Energy (SHE) trigger, High Energy (HE) trigger, Low Energy (LE) trigger, Super Low Energy (SLE) trigger are basic triggers for different thresholds of numbers of hit PMTs. The after trigger (AFT) is designed to search a neutron tagging signal that is delayed 2.2 MeV γ-ray by a neutron capture. The AFT trigger save more than 500 μsec data after the SHE trigger. An outer detector (OD) trigger is searching the

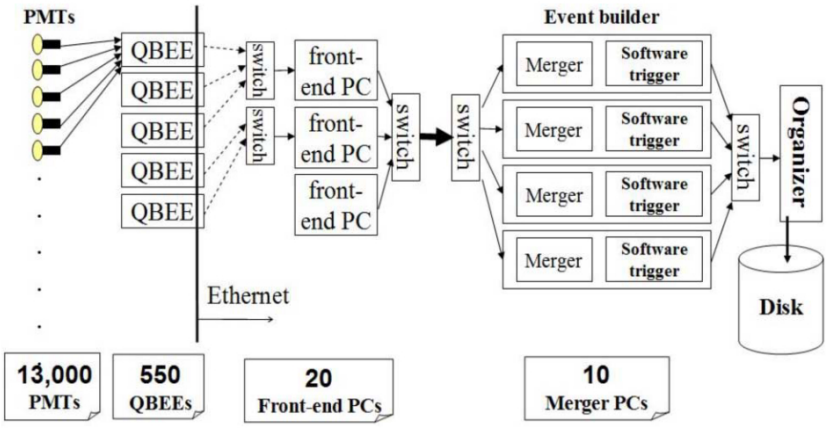

Figure 2.17: The block view of the data acquisition system for the Super-K [83]. The QBEE boards integrate the PMT charge signal, digitize the signals, and transfer them to front-end PCs by Ehthernet. In the right part of the figure, components of online system are drawn. The data are transferred from QBEE to the organizer PCs via Ethernet.

Table 2.3: Summary of the Super-K software trigger.

trigger type	hit number within 200ns	save event time range μsec
SHE (before Sep. 2011)	70	$-5 \sim +35$
SHE (after Sep. 2011)	58	$-5 \sim +35$
HE	50	$-5 \sim +35$
LE	47	$-5 \sim +35$
SLE	34	$-0.5 \sim +1.0$
AFT	SHE not OD	$+35 \sim 535$
OD	22	$-5 \sim +35$
T2K	–	$-500 \sim +535$

activities that in outer detector. The T2K trigger selects the T2K beam events around the GPS signal time.

The triggered data blocks are sent to the Organizer PC, and the Organizer PC sort the data block again and remove the overlapping parts in the neighboring blocks. Then, the data are saved into the hard disks for off-line physics analysis.

The electronics and DAQ of SK IV provide the high speed processing which is necessary to lower the detecting energy threshold of solar neutrino to 4 MeV, and they have the capacity to detect 8,000 events within 10 sec for supernova neutrino.

GPS based trigger for T2K on-timing events

Spill information for trigger In Super-K, the SK DAQ system (sukonh02) receives the T2K spill information from J-PARC, and the DAQ system produces a T2K software trigger to save the beam data. The transfer from the J-PARC beamline to the SK DAQ system is done via a dedicated network as shown in Figure 2.18. The L2 VPN in SINET3 is used to avoid having a pass through firewalls and routers. To eliminate the timing biases, the hit PMT information within ± 500 μsec near the beam arrival time

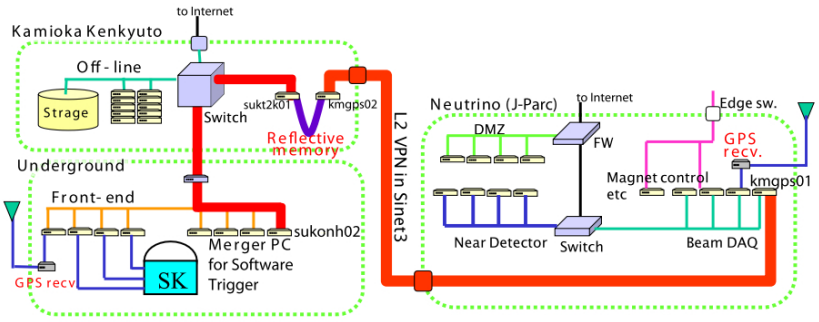

Figure 2.18: The schematic of T2K beam data acquisition at Super-K. Spill information is transferred from J-PARC to Super-K via a dedicated network shown as the red thick line.

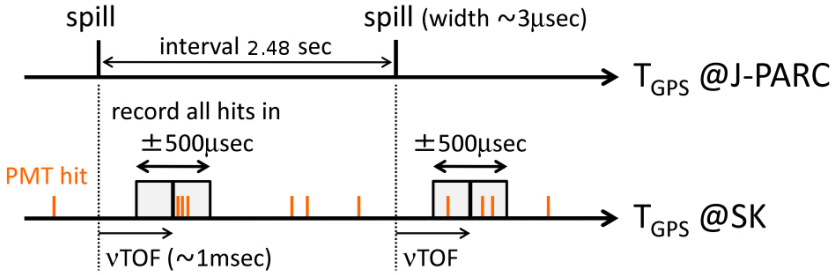

Figure 2.19: The hit PMT information within ± 500 μsec are saved as T2K beam data at Super-K. At Mar. 2015, the time intervals of spills are 2.48 sec.

are stored in disk as shown in Figure 2.19, while the spill duration is $(-2, 10)$ μs. The arrival timing at Super-K is calculated by the absolute spill time adding a neutrino time-of-flight (TOF), which is 295.336km$\div 2.997 \times 10^5$ km/sec= 985.134 msec. The absolute spill time is based on the J-PARC GPS system that uses the spill information. After Super-K receives the spill information, it is transfered back to J-PARC for checking data corruption.

GPS-based event timing at Super-K Super-K has two independent GPS modules and their receiver: GPS1, and GPS2. Each GPS receiver sends one pulse per second (1PPS) to a local time clock (LTC) inside the mine. On top of this, an auxiliary Rb atomic clock that is installed to provide the timing information when the two GPS are not consistent.

The validity of the event timing is checked by monitoring the timing difference between GPS1 and GPS2. If both GPS systems receive GPS satellite signals normally, the timing difference between two GPS systems is less than 200nsec ($|$T(GPS1)-T(GPS2)$| < 200$ ns). If only one satellite is available, the time difference may be large.

If the flag of both GPS1 and GPS2 are both error, so the spill data is flagged as a bad spill. After Jan. 2013, the restriction is changed to $|$T(GPS1)-T(GPS2)-offset$| < 100$ ns, otherwise the spill is classified as bad one. For T2K RUN1-4 spill data, only 0.05% fraction of the data are rejected by the GPS errors. The Rubidium clock is prepared for comparison of two GPS timing and give an auxiliary source of event timing if the two GPS are not consistent with Rb clock. The GPS2 has better stability than GPS1. During the T2K RUN1-3 period, GPS2 information is preferred than GPS1. During the T2K

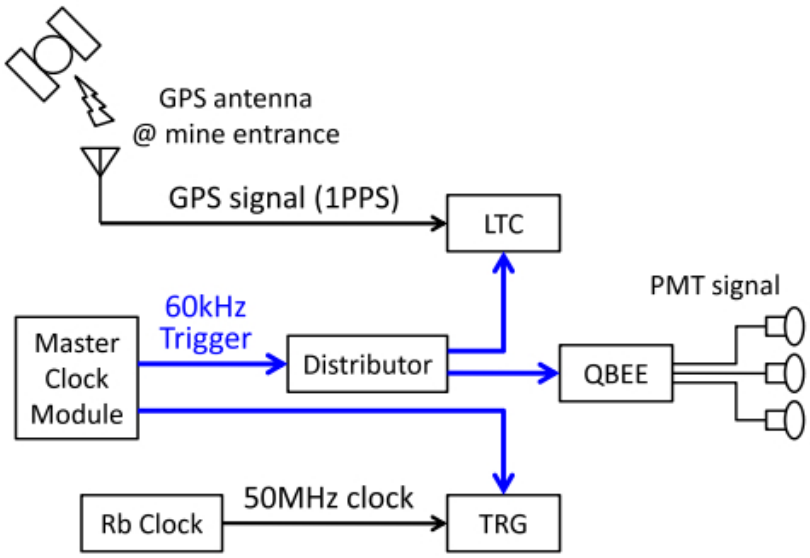

Figure 2.20: The schematic of the GPS system for the event timing information. The timing of each PMT hit and the 1PPS signal from the GPS clock are synchronized using a 60 kHz trigger signal. The GPS receiver is located at the entrance of the mine.

RUN4 period and after, the GPS2 is reliable in past tests, so only GPS2 information is used to determine the event timing. The summary of GPS selection for the event timing is in Table 2.4.

Table 2.4: Summary of clock selections for T2K- beam event timing.

T2K RUN	condition	selected time stamp
1-3	$\|$GPS1-GPS2$\|$ < 100 ns or $\|$GPS2-Rb$\|$ < 100 ns	GPS2
	$\|$GPS1-Rb$\|$ < 100ns	GPS1
	otherwise	Rb
4	all	GPS2

2.6 Beam Data Summary

In April 2009, the construction of the T2K neutrino beam-line finished, and the beam-line started its commissioning. The T2K experiment started to take data for physical analysis (physics RUN) from Jan. 2010. This thesis uses the T2K RUN1-4 data, and Figure 2.21 shows the history of delivered T2K RUN1-4 POT until May 2013. The accumulative POT of good spills is 6.57×10^{20}. During the T2K RUN1 period, the proton beam operated with only six bunches in single beam spill. In other T2K RUN, the proton beam operated with 8 bunches. The RUN2 period was stopped due to the Great East Japan earthquake. Thanks for the unremitting efforts of the J-PARC/KEK staff, the proton beam was renovated before the end of 2011. The data sets analyzed in this thesis are mentioned in Chapter 5.1 and Appendix G.

The MUMON and the INGRID checked the average beam profile and direction as shown in Figure 2.22. The stability of beam direction is much better than ±1 mrad. The

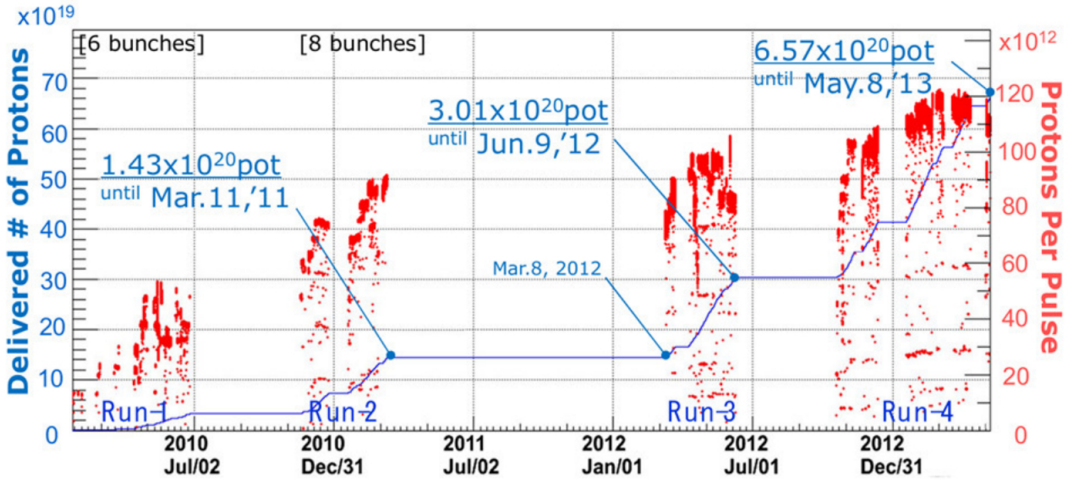

Figure 2.21: The history of neutrino beam in unit of delivered POT (proton on target) until May, 2013. The red points denote POT of corresponding spills. The blue line histogram represents the accumulated POT value.

event rates of INGRID for measuring the beam intensity have small fluctuation ($< 0.7\%$) except for the T2K RUN3b period. Since the horn currents in the T2K RUN3b period operated with only 205kA, the beam intensities by POT number are expected to be lower than for the other periods.

After T2K RUN4, J-PARC stopped to serve T2K beam for one year due to the Hadron Hall accident. Until now (Dec. 2015), the accumulated POT in neutrino mode is 7.09×10^{20} and the POT in anti-neutrino mode is 4.04×10^{20}. The T2K experiment achieved $\sim 14.2\%$ accumulated beam data out of the nominal 7.8×10^{21} POT goal.

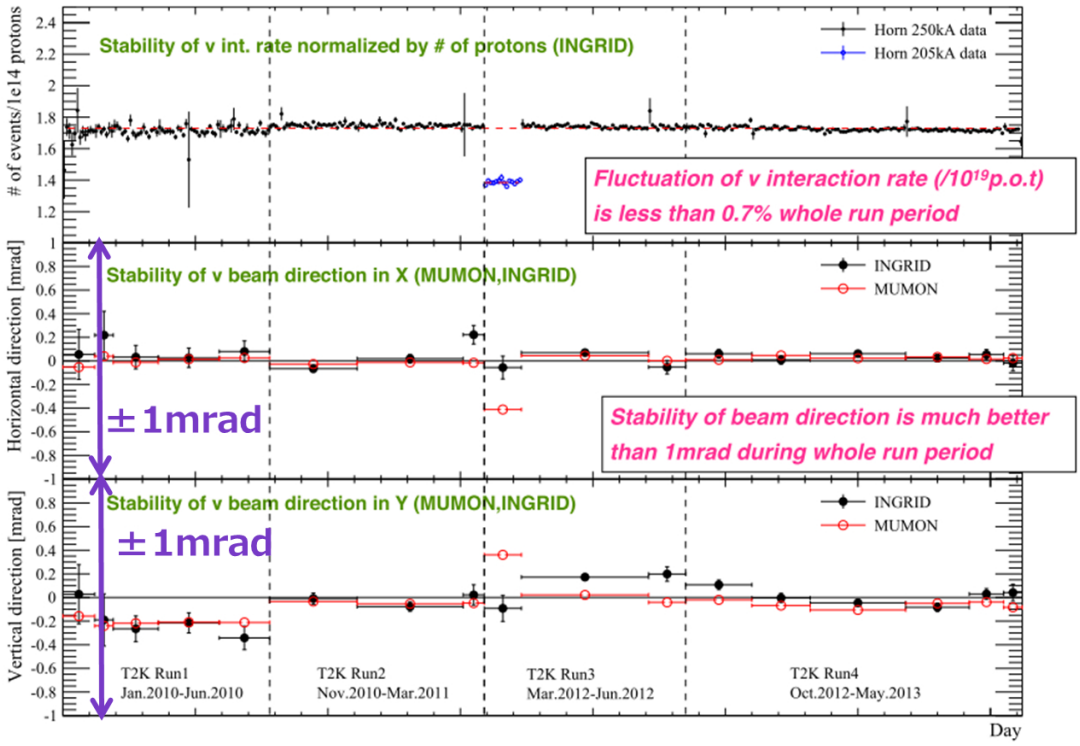

Figure 2.22: The top plot is the INGRID measurement of the neutrino beam intensity stability. The horizontal axis shows the day of T2K operaction period from Jan., 2010 to May, 2013, and the verticle dash lines show the boundaries of each T2K Run period. The vertical axis is the event rate of INGRID per 10^{14} POT. The fluctuations of event rates are smaller than 0.7% during the T2K RUN1-4 period, and interaction rates at the horn operated at 205kA are smaller than rates at other periods. The center and bottom plots are the beam direction measured by MUMON and INGRID. The vertical axis of center plot (bottom plot) shows the measured horizontal (vertical) direction of the beam. Each data point is the averaged direction of the beam for each main ring (MR) RUN. While the MUMON monitors the muon beam direction, INGRID measures the neutrino beam one, and its fluctuation are much better than ± 1 mrad.

Chapter 3

Analysis overview

In this chapter, the overview of ν-water neutral current quasi-elastic (NCQE) cross-section measurement is described. Figure 3.1 shows the overview of the analysis. To measure the ν-water NCQE cross-section, we scale up the theoretical prediction by the factor obtained from the comparison between the expected number of events and the observed number of candidate events.

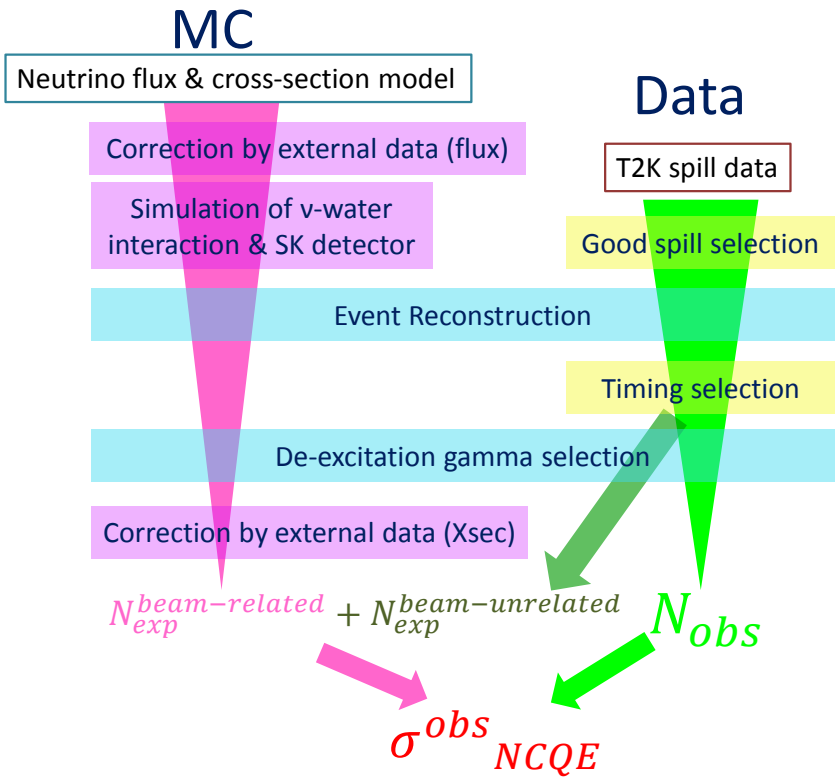

Figure 3.1: The flowing chart of the NCQE cross-section analysis.

The signal is de-excitation γ-ray induced by NCQE scattering. The T2K spill data events are reconstructed using fitting tools for the Super-K low energy event ($E_{rec} < 100$ MeV). After event reconstruction, we select the events with energy of $4 \sim 30$ MeV. The neutrino beam spill has a bunch structure, so we select the events with the timing within 100ns from the timing center of one of bunches. Then, the reconstructed variables such as the vertex position are used to remove most of beam-unrelated backgrounds. As a

result, the observed number of de-excitation γ-ray candidate events is obtained.

Second, the expected number of events is calculated separately for beam-related one and beam-unrelated one as

$$N_{exp} = N_{exp}^{beam-related} + N_{exp}^{beam-unrelated} \tag{3.1}$$

The beam-related events are neutrino reaction events induced by the T2K neutrino beam, and they include several kinds of ν-nucleus reactions: signal reaction of NCQE and other background such as NC1π, CCQE, etc. To predict the number of beam-related events, the T2K ν beam flux prediction at Super-K is used to simulate the events at Super-K. We select the events in the same way as the data analysis. The beam-unrelated events are from the radioactive impurities of detector wall and PMTs mainly. To estimate the number of beam-unrelated events, we use the "off-timing" events which are described in Appendix E.

The systematic uncertainties of the measurement comes from the following sources: flux, cross-section, primary γ-ray production, secondary γ-ray production, Super-Kamiokande detector response, and oscillation parameters. The uncertainty of neutrino beam flux is mainly from the hadron production on the target, and the main component of the uncertainty due to hadron production is estimated with the CERN NA61 results. The uncertainty of neutrino cross-section is mainly derived from results of MiniBooNE, SciBooNE, and NOMAD experiments. The uncertainty due to the primary γ-ray production is estimated by varying the MC parameters or by incorpolating the errors of external experiment data such as ^{16}O(e,e'p)^{15}N experiment in NIKHEF-K and ^{16}O(p,p'p)^{15}N at RCNP. The uncertainty due to the secondary γ-ray production is only estimated using two MC simulators, since there is no external experimental data. The uncertainty due to the detector response is estimated based on the Super-K calibration results. The expected number of CC events is affected by the oscillation parameters. The uncertainties of the oscillation parameters are used to estimate the variation of the expected number of CC events.

As a result, the ν-oxygen NCQE cross-section is measured with data in T2K RUN1-3 is described in Section 7.1. The new result including T2K RUN4 data until May 2013 is as described in Section 7.2.

Chapter 4

Prediction of observables at Super-K

4.1 Overview

This chapter describes the steps that lead to the expected observables at Super-K predicted with Monte Carlo (MC) simulations. The simulations are performed in three steps:

1. a neutrino beam simulation (Sec. 4.2)
2. a neutrino interaction simulation (Sec. 4.3)
3. a detector simulation (Sec. 4.4)

4.2 Neutrino beam simulation

The neutrino spectrum at Super-K is predicted in the following simulation steps: the simulation of proton beam hitting the target to produce hadrons, the propagation of these hadrons and their decay in the secondary beam-line that lead to the daugther neutrino.

First, the proton beam interactions and the hadronic chain productions in the target are simulated by FLUKA [99] Then, the produced particles in target are transferred to JNUBEAM which is a simulation code based on GEANT3[100]. JNUBEAM is designed to simulate propagation of the particle and its decay from the target to the decay tunnel and beam dump. Hadronic productions are corrected based on the data of external experiments such as the one by the CERN NA61/SHINE experiment (Ref. [90, 91]).

Figure 4.1 shows the expected neutrino beam flux at Super-K [89]. The fractions of ν_μ, $\overline{\nu}_\mu$, and ν_e in neutrino beam flux are respectively 94%, 6% and 1% assuming no neutrino oscillation, $\overline{\nu}_e, \nu_\tau, \overline{\nu}_\tau$ are not included in the simulation. The peak energy of the ν_μ flux is about 600 MeV, and the tail extends to several GeV.

4.3 Neutrino Interaction simulation

The NEUT simulation code[88] is developed to simulate neutrino-nucleus interactions with various material such as proton, carbon, oxygen, iron, etc. The following neutrino-nucleus interactions are included in NEUT:

Charged Current Quasi-elastic Scattering: $\nu + n \to l^- + p$

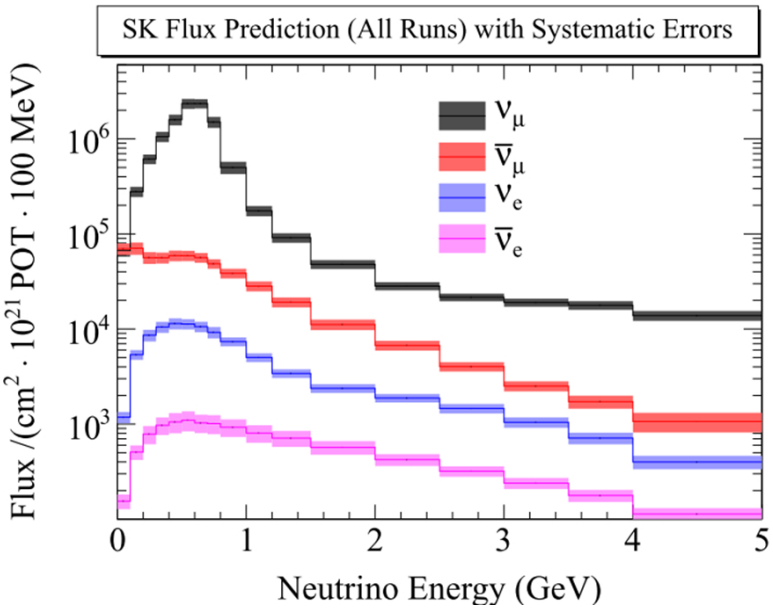

Figure 4.1: The T2K neutrino beam fluxes at Super-K without neutrino oscillations. The errors of neutrino flux are drawn as the color box in the figure.

Neutral Current Quasi-elastic Scattering:	$\nu + X \to \nu + (X-1) + N'$
CC Single π, K, η Resonance Production:	$\nu + N \to l^- + N' + \pi(\eta, K)$
NC Single π, K, η Resonance Production:	$\nu + N \to \nu + N' + \pi(\eta, K)$
CC Coherent π productions:	$\nu + X \to l^- + X + \pi$
NC Coherent π productions:	$\nu + X \to \nu + X + \pi$
CC Deep Inelastic Scattering:	$\nu + N \to l^- + N' + m\pi(\eta, K)$
NC Deep Inelastic Scattering:	$\nu + N \to \nu + N' + m\pi(\eta, K)$

where the l means the outgoing charged lepton, the $N(N')$ is a target (outgoing) nucleon, the X is a target nucleus, and the m is an integer number of produced pions. In practice, NEUT generates Monte Carlo simulation events as follows:

1. The total number of interaction at energy E_ν is calculated as $\phi(E) \times \sigma_{tot}(E)$, where $\phi(E_\nu)$ is the neutrino flux and $\sigma_{tot}(E)$ is the total neutrino cross-section at E_ν.

2. The rate of each interaction is predicted using the corresponding interaction cross-section.

3. Events are generated according to the rate. For each event, outgoing particles are generated depending on the selected interaction type.

4. Some produced particle such as pions interact with a nucleon inside nucleus. The possible interactions are inelastic scattering, absorption, and charge exchange. These interactions are simulated before the particles going out of nucleus.

The neutrino-nucleus cross-sections implemented in NEUT are shown in Figure 4.2. This section discusses the ν-oxygen NCQE interaction and the other background interactions such as CCQE, NC1π, etc.

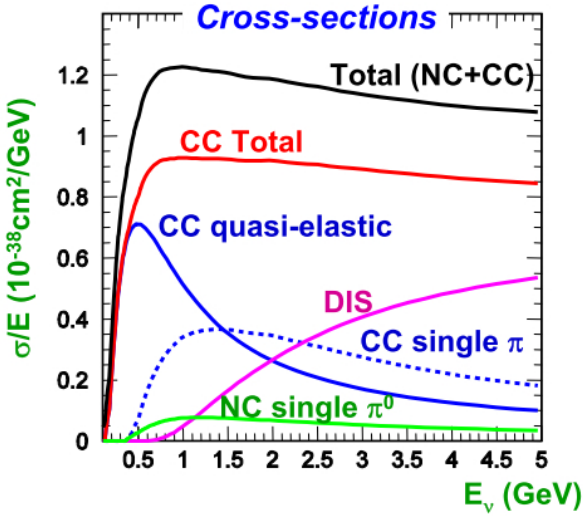

Figure 4.2: Neutrino-nucleus interaction cross-sections in NEUT simulation..

4.3.1 Neutral Current Quasi-elastic Interaction

If the energy of incoming neutrino is larger than 50 MeV,the neutrino-nucleon cross-section is reduced by form factors due to the inner structure of the nucleon. The NC elastic scattering describes that a neutrino interact with a free nucleon, and the differential NC elastic cross-section is written as Llewellyn-Smith formalism:[101, 102]

$$\begin{aligned}\frac{d\sigma}{d|q^2|}&\left[\begin{array}{l}\nu+N\rightarrow\nu+N\\ \overline{\nu}+N\rightarrow\overline{\nu}+N\end{array}\right]\\ &=\frac{G_F^2}{4\pi}\left[A(q^2)\frac{m_N^2}{2E_\nu^2}\pm B(q^2)\frac{(s-u)}{2E_\nu^2}+C(q^2)\frac{(s-u)^2}{2m_N^2E_\nu^2}\right],\end{aligned}\tag{4.1}$$

where E_ν is the energy of the incident neutrino, m_N is the nucleon mass, G_F is the Fermi coupling constant. The s, u are the Mandelstam variables. In Equation (4.1), the form factor terms of A, B and C are given by

$$\begin{aligned}A(q^2)&=\tfrac{-q^2}{m_N^2}\{(1+\tau)(F_A^Z)^2-(1-\tau)(F_1^Z)^2+\tau(1-\tau)(F_2^Z)^2+4\tau F_1^Z F_2^Z\},\\ B(q^2)&=4\tau F_A^Z(F_1^Z+F_2^Z),\\ C(q^2)&=\tfrac{1}{4}((F_A^Z)^2+(F_1^Z)^2+\tau(F_2^Z)^2),\end{aligned}\tag{4.2}$$

where $\tau=\frac{-q^2}{4m_N^2}$, the momentum of weak current is $q=p'-p$, and $q^2=-2m_NT_N$. T_N is the kinetic energy of the nucleon. F_i^Z is a form factor. F_1^Z, F_2^Z, and F_A^Z are the Dirac, the Pauli, and the axial vector nucleon weak neutral current form factors respectively, and they are written as follows:

$$\begin{aligned}F_1^Z&=\pm\tfrac{1}{2}F_1-2\sin^2\theta_W F_1^{EM,Z},\\ F_2^Z&=\pm\tfrac{1}{2}F_2-2\sin^2\theta_W F_2^{EM,Z},\\ F_A^Z&=\pm\tfrac{1}{2}(F_A^s\pm F_A)=\frac{\Delta s\pm g_A}{2(1-\frac{q^2}{M_A^2})^2},\\ F_P^Z&=\frac{2m_N^2F_A^Z}{m_\pi^2-q^2},\end{aligned}\tag{4.3}$$

where Z is p (proton) or n (neutron), the $+(-)$ sign corresponds to the proton (neutron) form factors, the angle θ_w is the weak mixing angle, and $\Delta s=-0.08$ is the strange quark

contribution, m_π is the mass of pion. Then, F_1, F_2 is defined as a function of electric form factor G_E^V and magnetic form factor G_M^V:

$$\begin{aligned} F_1(q^2) &= (1+\tau)^{-1}[G_E^V + \tau G_M^V], \\ F_2(q^2) &= (1+\tau)^{-1}[G_M^V - G_E^V], \end{aligned} \tag{4.4}$$

$F_V^{EM,Z}$ and $F_W^{EM,Z}$ are the Dirac and Pauli electromagnetic form factors respectively:

$$\begin{aligned} F_1^{EM,Z} &= (1+\tau)^{-1}[G_E^Z + \tau G_M^Z], \\ F_2^{EM,Z} &= (1+\tau)^{-1}[G_M^Z - G_E^Z], \end{aligned} \tag{4.5}$$

where a parameterization of G_E^V, G_M^V, which is called "BBBA05" is used in NEUT. The parameterization is based on recent experimental data at Jefferson Lab. [107], and the two dipole nucleon form factors are written as shown in Ref. [108].

$$G_E^V = G_E^p - G_E^n, \qquad G_M^V = G_M^p - G_M^n, \tag{4.6}$$

$$G_{E,M}^Z = \mu \frac{\sum_{k=0}^{2} a_k \tau^k}{1 + \sum_{k=1}^{4} b_k \tau^k} \tag{4.7}$$

This thesis uses a recent theoretical calculation of NCQE cross-section [115] with the simple parameterization of G_E^Z, G_M^Z from Ref. [109, 110].

$$G_{E,M}^Z = \mu \frac{\sum_{k=0}^{1} a_k \tau^k}{1 + \sum_{k=1}^{3} b_k \tau^k} \tag{4.8}$$

where the parameters μ, a_k, and b_k of $G_{E,M}^Z$ are summarized in Table 4.1 in which μ_p, (μ_n) is the anomalous magnetic moment of proton (neutron) in units of the nuclear magneton. But, G_E^n is given by [111].

$$G_E^n(Q^2) = \frac{A\tau}{1 + B\tau} G_D(Q^2), \tag{4.9}$$

where $G_D = (1 + Q^2/\Lambda^2)^{-2}$ with $\Lambda^2 = 0.71$ $(\mathrm{GeV}/c)^2$ is a dipole form factor, $Q^2 = -q^2$, $A = 1.70$, and $B = 3.30$.

Table 4.1: Summary of parameters for nucleon electromagnetic form factors $G_{E,M}^Z$ from Ref. [109]. The parameter a_0 is assigned to be 1.

Quantity	μ	a_1	b_1	b_2	b_3
G_E^p	1	-0.24	10.98	12.82	21.97
G_M^p	μ_p	0.12	10.97	18.86	6.55
G_M^n	μ_n	2.33	14.72	24.20	84.1

Impulse approximation

An impulse approximation (IA) method is adopted to obtain accurate quasi-elastic cross-section predictions on bound nucleons inside nucleus [112, 113]. First, let us consider the NCQE interaction as the following process

$$\nu + A \to \nu' + (A-1) + N, \quad N = p, n \tag{4.10}$$

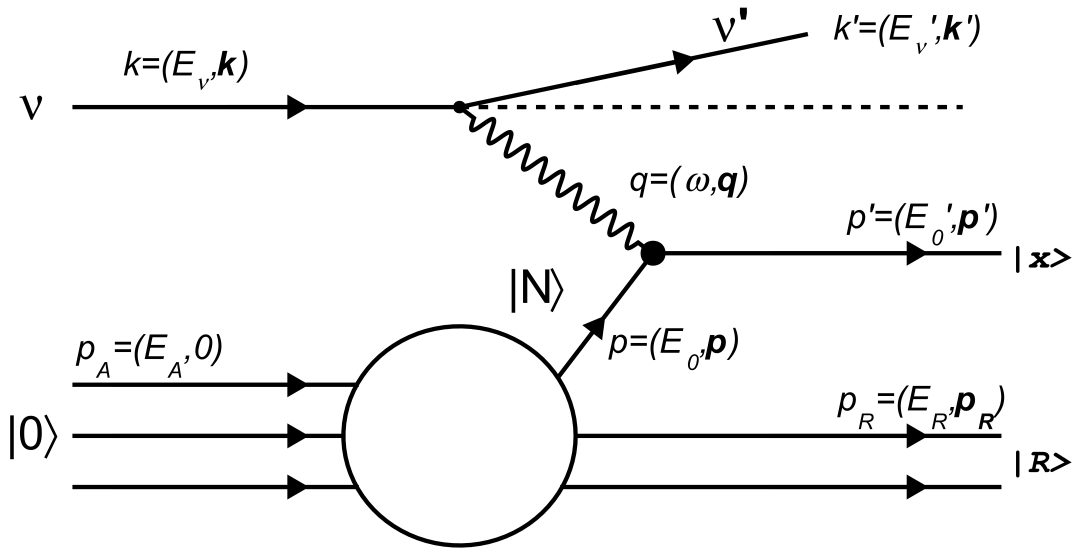

Figure 4.3: Diagram of impulse approximation of $\nu+A \to \nu+(A-1)+N$. The interaction is described as a collection of scattering with individual nucleons.

Figure 4.3 shows the feynman diagram of the impulse approximation model. The neutrino ν initially carries four momentum $k = (E_\nu, \mathbf{k})$. After scattering, the four momentum of $\nu^{'}$ becomes $k' = (E'_\nu, \mathbf{k}')$, and the momentum difference $q = k' - k = (\omega, \mathbf{q})$ is taken by the weak current. The bound nucleon has the initial four momentum $p = (E_0, \mathbf{p})$, then the nucleon $|x\rangle$ is knocked out with four momentum $p' = (E'_0, \mathbf{p}')$. On the other hand, the residual nucleus $|R\rangle$ has the final four momentum as $(E_R, \mathbf{p}_R)$ where $\mathbf{p}_R = \mathbf{q} - \mathbf{p}'$. The differential cross-section is written as follows into the Born approximation as follows. (Ref. [114])

$$\frac{d^2\sigma}{d\Omega dE_{\nu'}} = \frac{G_F^2}{8\pi^2}\frac{E'_\nu}{E_\nu}\frac{L_{\mu\nu}W^{\mu\nu}}{m_N E'_0}\delta(\omega + E_0 - E'_0) \tag{4.11}$$

where G_F is the Fermi constant, and m_N is the mass of nucleon. The lepton tensor $L_{\mu\nu}$ is given by the neutrino kinematics as below

$$L_{\mu\nu} = 2[k'_\mu k_\nu + k'_\nu k_\mu - g_{\mu\nu}(k \cdot k') - i\epsilon_{\mu\nu\alpha\beta}k^\alpha k'^\beta] \tag{4.12}$$

The hadronic tensor $W^{\mu\nu}$ contains the information of nucleus structure as follows: The initial state of hadronic is noted $|0\rangle$, and final state of all hadronic noted $|X\rangle$. J^μ is the nuclear weak neutral current operator. The hadronic tensor $W^{\mu\nu}$ is written as follows

$$W^{\mu\nu} = \sum_X \langle 0|J^\mu|X\rangle\langle X|J^\nu|0\rangle\delta(p_0 + q - p_X) \tag{4.13}$$

The IA scheme has two assumptions: (i) If the momentum of weak current $\mathbf{q}$ is large, the target nucleus is probed as a collection of individual nucleons. (ii) Then, the knocked out nucleon is treated independently with the residual (A-1) nucleus. The two assumptions mean that the IA model does not take into account of the Pauli blocking effect and the dynamical final state interactions (FSI).

Based on the assumption (i), the nuclear current operator is written as the sum of one nucleon currents

$$J^\mu \to \sum_i j_i^\mu \tag{4.14}$$

where the i-th current refers to the i-th individual bound nucleon which is knocked out of the nucleus. The final state $|X\rangle$ is separated to knockout nucleon $|x, \mathbf{p}'\rangle$ and the residual nucleus $|R, \mathbf{p}_R\rangle$.

$$|X\rangle \rightarrow |x, \mathbf{p}'\rangle \otimes \ |R, \mathbf{p}_R\rangle \tag{4.15}$$

The above equation is used to rewrite the hadronic tensor parts as

$$\sum_X |X\rangle\langle X| \rightarrow \sum_x \int d^3p' |x, \mathbf{p}'\rangle\langle \mathbf{p}', x| \sum_R d^3p_R |R, \mathbf{p}_R\rangle\langle \mathbf{p}_R, R| \tag{4.16}$$

A complete set of free nucleon states with momentum $\mathbf{p} = -\mathbf{p}_R$ is rewritten as

$$\int d^3p_R |N, -\mathbf{p}_R\rangle\langle -\mathbf{p}_R, N| \tag{4.17}$$

Equation 4.15 is then used to substitute $|X\rangle$ in the bracket $\langle 0|J^\mu|X\rangle$ (in Equation 4.13). Then, the above Equation 4.17 is inserted into the bracket.

$$\langle 0|J^\mu|X\rangle = \left(\frac{m_N}{\sqrt{\mathbf{p}_R^2 + m_N^2}}\right)^{\frac{1}{2}} \langle 0|R, \mathbf{p}_R\rangle |N, -\mathbf{p}_R\rangle \sum_i \langle -\mathbf{p}_R, N|j_i^\mu|x, \mathbf{p}'\rangle \tag{4.18}$$

The hadronic tensor becomes

$$\begin{aligned} W^{\mu\nu} = & \sum_{x,R} \int d^3p_R d^3p' |\langle 0|R, \mathbf{p}_R; N, -\mathbf{p}_R\rangle|^2 \frac{m_N}{E_{\mathbf{p}_R}} \\ & \times \sum_i \langle -\mathbf{p}_R, N|j_i^\mu|x, \mathbf{p}'\rangle\langle \mathbf{p}', x|j_i^\nu|N, -\mathbf{p}_R\rangle \\ & \times \delta^3(\mathbf{q} - \mathbf{p}_R - \mathbf{p}')\delta(\omega + E_0 - E_R - E_0') \end{aligned} \tag{4.19}$$

Because of the last delta function $\delta(\omega + E_0 - E_R - E_0')$ is re-written by identity

$$\delta(w + E_0 - E_R - E_0') = \int dE \delta(E - m_N + E_0 - E_R)\delta(\omega - E + m_N - E_0') \tag{4.20}$$

and another delta function $\delta^3(\mathbf{q} - \mathbf{p}_R - \mathbf{p}')$ is canceled by integral of $\int d^3p_R$. The $W^{\mu\nu}$ becomes

$$W^{\mu\nu} = \int d^3p_R .....\delta(\mathbf{q} - \mathbf{p}_R - \mathbf{p}') = 1 \times (.....), \tag{4.21}$$

Because of $\mathbf{p}_R = \mathbf{q} - \mathbf{p}' = -\mathbf{p}$, the spectral function of the target is defined as follow.

$$P(\mathbf{p}, E) = \sum_R |\langle 0|R, -\mathbf{p}\rangle|N, \mathbf{p}\rangle|^2 \delta(E - m_N + E_0 - E_R) \tag{4.22}$$

where E_0 is the ground energy-level of the target nucleon, and $E_R = E + E_0 - m_N$ is the energy of the residual nucleus. Later, the spectral function is predicted using a local density approximation (LDA) [116] that inserts the nucleon-nucleon interactions in a calculation. The hadronic tensor $W^{\mu\nu}$ in Equation (4.19) is written as

$$W^{\mu\nu}(\mathbf{q}, \omega) = \sum_i \int d^3p dE W_{i,N}^{\mu\nu}(\widetilde{\omega}) \frac{m_N}{E_{\mathbf{p}}} P(\mathbf{p}, E) \tag{4.23}$$

where $W^{\mu\nu}_{i,N}(\widetilde{\omega})$ describes the weak interactions of i-th nucleon in free space.

$$W^{\mu\nu}_{i,N}(\mathbf{q},\widetilde{\omega}) = \sum_x \langle N,-\mathbf{p}|j^\mu_i|x,\mathbf{p}+\mathbf{q}\rangle\langle \mathbf{p}+\mathbf{q},x|j^\nu_i|N,\mathbf{p}\rangle \times \delta(\widetilde{\omega}+\sqrt{\mathbf{p}^2+m_N^2}-E_0^{'}) \quad (4.24)$$

The nuclear binding effect appears in Equation 4.20, therefore the energy $\omega \to \widetilde{\omega}$ is replaced by

$$\begin{aligned}\widetilde{\omega} &= E_0^{'} - \sqrt{\mathbf{p}^2+m_N^2} \\ &= \omega + E_0 - E_R - \sqrt{\mathbf{p}^2+m_N^2} \\ &= \omega - E + m_N - \sqrt{\mathbf{p}^2+m_N^2} \end{aligned} \quad (4.25)$$

Here, the differential cross-section for a nucleus is written as

$$\frac{d\sigma_{\nu A}}{dE^{'}_\nu d\Omega} = \int d^3\mathbf{p}dEP(\mathbf{p},E)(\frac{m_N}{E_\mathbf{p}})\left[Z\frac{d^2\sigma_{\nu p}}{dE^{'}_\nu d\Omega} + (A-Z)\frac{d^2\sigma_{\nu n}}{dE^{'}_\nu d\Omega}\right] \quad (4.26)$$

The differential cross-section for a bound nucleon is written as

$$\frac{d^2\sigma_{\nu N}}{dE^{'}_\nu d\Omega} = \frac{G_F^2}{8\pi^2}\frac{E^{'}_\nu}{E_\nu}L_{\mu\nu}W^{\mu\nu}_{i,N} \quad (4.27)$$

The hadronic tensor of Equation (4.24) is written by the five structure functions W_j given by

$$W^{\mu\nu}_N = -g^{\mu\nu}W_1 + \widetilde{p}^\mu\widetilde{p}^\nu\frac{W_2}{m_N^2} + i\epsilon^{\mu\nu\alpha\beta}\widetilde{p}_\alpha\widetilde{p}_\beta\frac{W_3}{m_N^2} + \widetilde{q}^\mu\widetilde{q}^\nu\frac{W_4}{m_N^2} + (\widetilde{p}^\mu\widetilde{q}^\nu+\widetilde{p}^\nu\widetilde{q}^\mu)\frac{W_5}{m_N^2} \quad (4.28)$$

where $\widetilde{p} = (E_0,\mathbf{p})$ and $\widetilde{q} = (\widetilde{\omega},\mathbf{k}-\mathbf{k}')$. Now, a square of scattering matrix $|\mathcal{M}_{\nu N}|^2$ is the leptonic tensor multiplying the hadronic tensor as follows.

$$|\mathcal{M}_{\nu N}|^2 = L^{\mu\nu}W_{N,\mu\nu} = 16\sum_i W_i(\frac{A_i}{m_N^2}) \quad (4.29)$$

A_i function contains the kinematic factors as shown in Appendix B of Ref. [113],

$$\begin{aligned} A_1 &= m_N^2(k\cdot k') \\ A_2 &= (k\cdot\widetilde{p})(k'\cdot\widetilde{p}) - \tfrac{A_1}{2} \\ A_3 &= (k\cdot\widetilde{p})(k'\cdot\widetilde{q}) - (k\cdot\widetilde{q})(k'\cdot\widetilde{p}) \\ A_4 &= (k\cdot\widetilde{q})(k'\cdot\widetilde{q}) - \tfrac{\widetilde{q}^2}{2}\tfrac{A_1}{m_N^2} \\ A_5 &= (k\cdot\widetilde{p})(k'\cdot\widetilde{q}) + (k'\cdot\widetilde{p})(k\cdot\widetilde{q}) - (\widetilde{q}\cdot\widetilde{p})\tfrac{A_1}{m_N^2} \end{aligned} \quad (4.30)$$

The $A_{4,5}$ terms only contribute 4% to the cross-section, and the A_{1-3} terms dominate. The structure function W_j is written in terms of nucleon form factors F_i [115].

$$\begin{aligned} W_1 &= \tau(F_1^Z+F_2^Z)^2 + (1+\tau)(F_A^Z)^2 \\ W_2 &= (F_1^Z)^2 + \tau(F_2^Z)^2 + (F_A^Z)^2 \\ W_3 &= (F_1^Z+F_2^Z)F_A \\ W_4 &= \tfrac{1}{4}[(F_1^Z)^2 + \tau(F_2^Z)^2 - (F_1^Z+F_2^Z)^2 - 4F_P(F_A^Z-\tau F_P^Z)] \\ W_5 &= \tfrac{1}{2}W_2 \end{aligned} \quad (4.31)$$

where the $\tau = -\widetilde{q}^2/(4m_N^2)$. The form factor F_i^Z is assigned with Equation 4.3.

Figure 4.4 shows the comparison between the NCQE cross-section and the other NC cross-sections. The NCQE cross-section dominates in subGeV region, and most of the de-excitated γ-ray candidate events are expected from NCQE reactions.

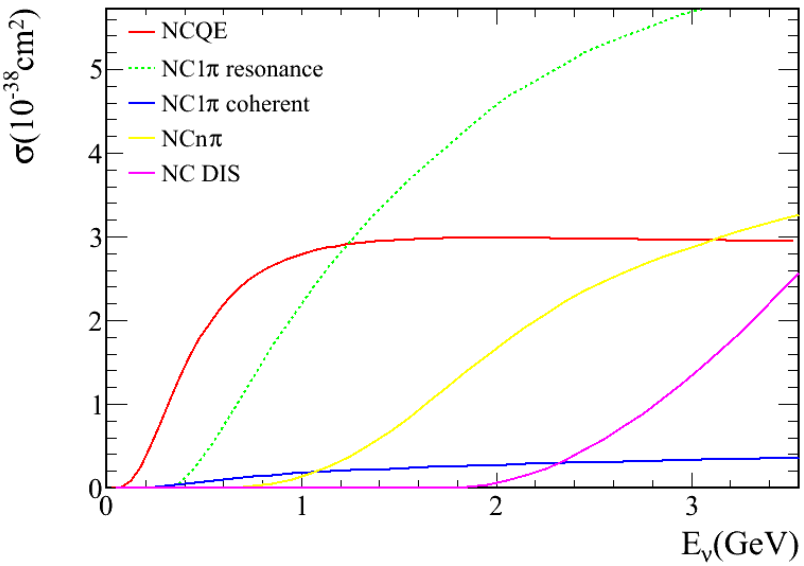

Figure 4.4: The cross-sections of neutrino-oxygen neutral current interactions [88, 115]. The NCQE cross-section dominates in all NC samples at subGeV region. If neutrino energy exceeds $\sim$ 1GeV, the NC1π resonance reaction dominates.

4.3.2 De-excitation gamma ray induced by NCQE interaction

NEUT simulates the nuclear de-excitation after ν-nucleus interaction. Here, the simulation of γ-ray de-excitation in the residual nucleus is described. The weak neutral current knocks out a nucleon, and the residual nucleus is excited with a nucleon hole state.

Not only single nucleon, but also multi-nucleons may be emitted in the NCQE reaction due to the final state interaction (FSI). The ν-oxygen NCQE scatterings are given by.

$$\begin{aligned} \nu + {}^{16}O &\rightarrow \nu + {}^{15}O^* + n \\ \nu + {}^{16}O &\rightarrow \nu + {}^{15}N^* + p \\ \nu + {}^{16}O &\rightarrow \nu + {}^{14}N^* + n + p \\ \nu + {}^{16}O &\rightarrow \nu + {}^{14}B^* + p + p \\ &\cdots\cdots \end{aligned} \tag{4.32}$$

If a low-lying nucleon is knocked out in NCQE scattering, the residual oxygen (nitrogen) nucleus is excited as shown in Figure 4.5. The residual nucleus could de-excite to the ground state by emitting a γ-ray with energy of 6 MeV$\sim$10 MeV. The de-excitation γ-rays are observed by the Super-K detector, and they are referred to as "primary" γ-rays.

If the knocked-out nucleon interacts with other oxygen nucleus in water, it could lead another emission of de-excitation γ. At the same time, the hadronic interaction may emit more nucleons, therefore more de-excitation γ-rays could be produced. The γ-rays is referred to as "secondary" γ-rays. The "secondary" γ-rays are observed and pile up with "primary" γ-rays in the Super-K detector. The whole schematic of neutrino-oxygen NCQE and the de-excitation γ-rays are shown in Figure 4.6.

The primary γ-ray production is discussed in this section, and secondary γ-ray production is discussed in Subsec. 4.4.1.

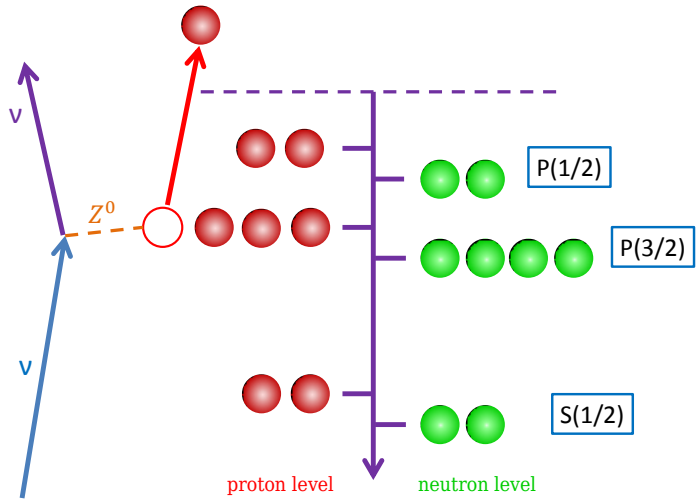

Figure 4.5: Neutrino-oxygen NCQE interaction schematic. In this figure, a proton in $p_(3/2)$ state is knocked out of oxygen nuclear, and the interaction leave a nucleon hole.

Spectral function and spectroscopic factor

NEUT adopted a fermi gas model for a description of the momentum distribution of nucleons $n(\mathbf{p}) = n(0)$ which is constant if $|\mathbf{p}| \leq p_F$, where p_F is the momentum of nucleons on the Fermi surface. The Pauli blocking effect restricts the the momentum value of the outgoing nucleon to $|p| > p_F$.p_F is assigned as 225 MeV for the oxygen nucleus in NEUT. The NCQE cross-section for bound nucleons is calculated in the Relativistic Fermi Gas (RFG) model which was proposed by Smith and Moniz [106].

Recently, the spectral function is added in NEUT for accurate prediction of neutrino cross-section. In Equation (4.26), the spectral function $P(\mathbf{p}, E)$ describes a probability of removing a nucleon $\phi(\mathbf{p})$ from the target with the removal energy E, where $\mathbf{p}$ is the momentum of nucleon. The spectral function of oxygen nucleus is derived using the local density approximation (LDA) module, which combines the electron scattering experimental data and the theoretical calculation for the nuclear matter [116, 117].

The LDA-based theoretical prediction is proved by the $(e, e'p)$ proton knocked-out experiment of E97-006 at Jefferson Lab.[118]. The spectral function is written in the factorized form as follows

$$P_N(\mathbf{p}, E) = \sum_{\alpha \in F} n_\alpha |\phi_\alpha(\mathbf{p})|^2 f_\alpha(E - E_\alpha) \tag{4.33}$$

where ϕ_α is the momentum-space wave function of single nucleon in a α-th shell model state (e.g. Woods-Saxon wave functions). $f_\alpha(E - E_\alpha)$ represents the energy width of the α-th state, and $-E_\alpha$ is the single binding energy of the α-state in mean field approximation. The occupation probability of the α-th state is $n_\alpha \leq 1$. If there is no nucleon-nucleon (NN) correction, $n_\alpha = 1$ and $f_\alpha = \delta(E - E_\alpha)$ are derived. All the states are summed up in the Fermi sea F.

Inside the nucleus, the nucleon-nucleon (NN) interaction induces virtual scattering processes. The virtual scattering processes excites the participating nucleons to energy states higher than the Fermi energy p_F. Virtual scattering processes also lead the contin-

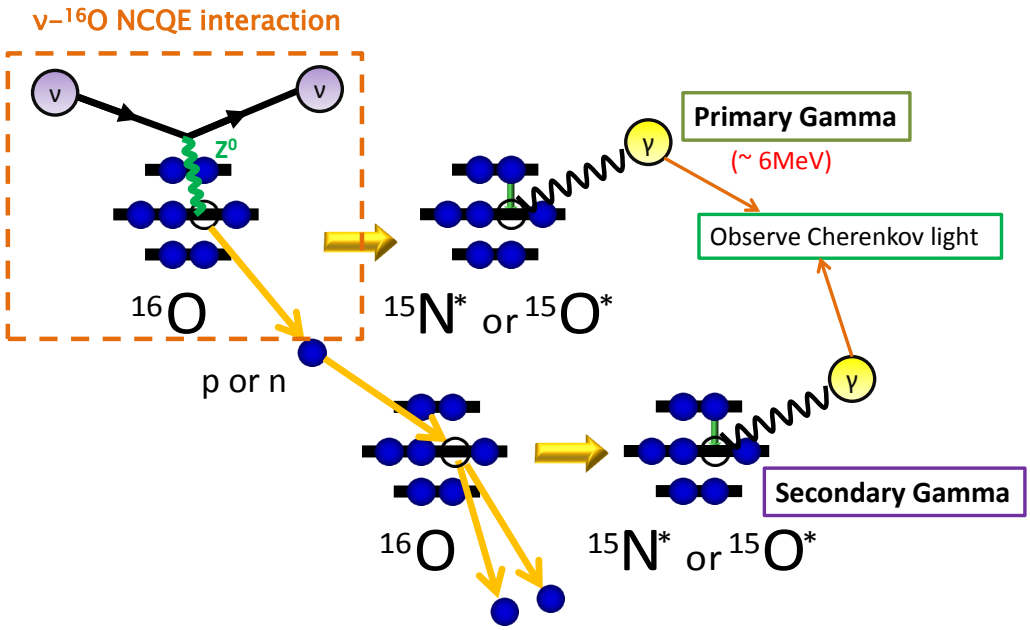

Figure 4.6: Neutrino-oxygen NCQE interaction and emission of de-excitation γ-rays schematic. The knocked out nucleon interacts with the other oxygen nucleus. Then, the hadronic interaction produces γ-rays which are called secondary γ-rays.

uum states with the larger removal energy E than e_F. The spectral function extends to the region $|\mathrm{p}| \gg p_F$ and $E \gg e_F$, where $p_F = 225$ MeV/c and $e_F \sim 30$ MeV for oxygen nucleus. As a result, the spectral function of the protons in oxygen nucleus is as shown in Figure 4.7 [112].

In a ${}^{16}_{8}\mathrm{O}$ nucleus, the probability of removing each nucleon depends on its removal energy E. For a simple shell model, the nucleons occupy three states: $1p_{1/2}$, $1p_{3/2}$ and $1s_{1/2}$ with a removal energy of 12.1, 18.4 and 42 MeV respectively. In the LDA model, the removal energy of nucleon state is not a single value. Figure 4.8 shows the integral of Equation (4.33) over nucleon momentum, and the red line in the figure represents the removal energy distribution of the protons in ${}^{16}_{8}\mathrm{O}$ [115]. There are two sharp peaks of $1p_{1/2}$ state and $1p_{3/2}$ state, while the peak of $1s_{1/2}$ state is distributed over a broad energy range.

In practice, the spectroscopic factor (strength) of α-th state represents the probability to remove a nucleon in α-th state. The spectroscopic factor of the α-state is calculated by integrating the removal energy distribution over the corresponding energy region of the α-th state. Here, the three spectroscopic factors of the proton states is calculated as the integral value over the removal energy range of $11.0 \leq E \leq 14.0$ MeV, $17.25 \leq E \leq 22.75$ MeV, and $22.75 \leq E \leq 62.25$ MeV respectively. The removal energy distribution of the neutrons in ${}^{16}_{8}\mathrm{O}$ is similar to the proton one, but the distribution of the neutrons is more strongly bound by 3.54 MeV than the proton one from Ref. [119]. The spectroscopic factors are expected be the same between the neutron and proton states.

Recently, a theoretical calculation for the spectroscopic factors and the NCQE cross-

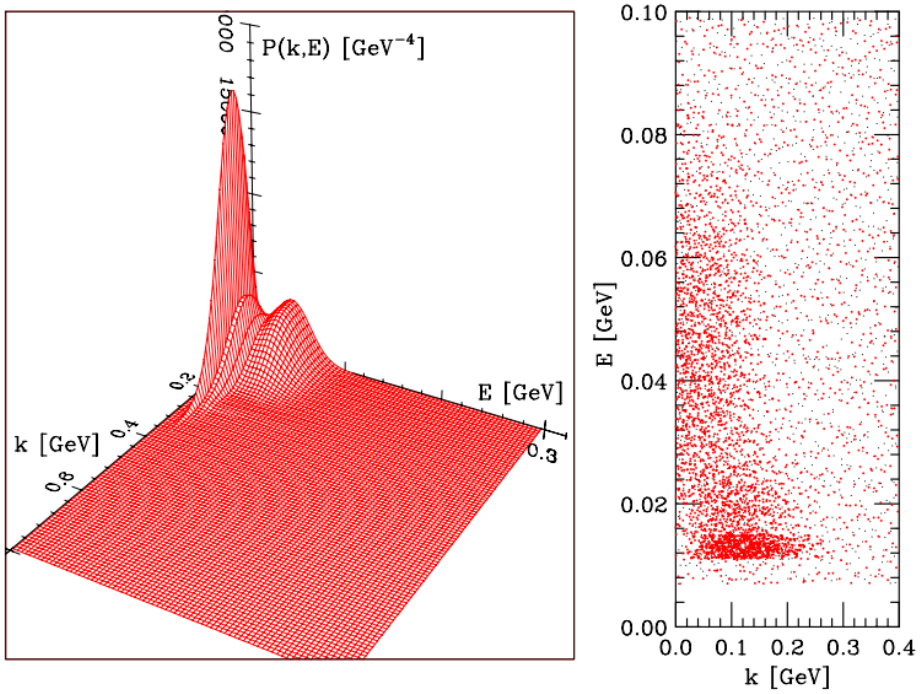

Figure 4.7: The spectral function $P(\mathbf{p}, E)$ of oxygen nucleus using LDA-based calculation from Ref. [112]. Left plot is the three dimensional plot of spectral function $P(k, E)$, where the absolute value of wave vector is $k = |\mathbf{k}| = |2\pi\mathbf{p}/h|$. The right plot is the scatter plot of $P(k, E)$. There are about 20 percent of $P(k, E)$ extend to the region $|\mathrm{p}| \gg p_F$ and $E \gg e_F$.

section has been published (Ref.[115]). Therefore, we update the spectroscopic factors (SFs) [1]in the NEUT simulation. The default value for NEUT spectroscopic factor [120] and the updates for SFs are summarized in Table 4.2.

Table 4.2: The spectroscopic factor (SF) of each nucleon state in $^{16}_{8}$O. Here, the SFs of the α-th shell state are listed. The NEUT default values are taken from previous calculation in Ref.[120]. This thesis uses the updated values in Ref. [115].

	residual nucleus	$1p_{1/2}$	$1p_{3/2}$	$1s_{1/2}$	others
NEUT	^{15}N	0.188	0.435	0.188	0.189
default	^{15}O	0.188	0.375	0.188	0.249
Update	^{15}N	0.158	0.3515	0.1055	0.385
	^{15}O	0.158	0.3515	0.1055	0.385

[1]Ref.[115] do not take account the degeneracy of the α-th state, and the listed spectroscopic factor in Ref.[115] represent a eight times of the knocked-out probability of single nucleon. In this thesis, the total knocked-out probability of nucleons in α-th state is listed. For example, $1p_{3/2}$ state has four protons, therefore we list the probability of single nucleon multiplied by four times as the probability of $1p_{3/2}$ state in Table 4.2.

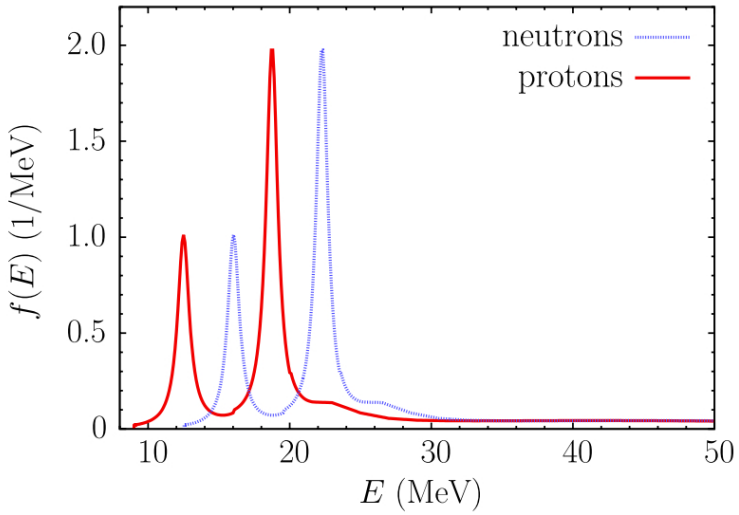

Figure 4.8: The spectral function integration over momentum for the protons and the neutrons in ^{16}O nucleus is a function of the removal energy (E) [115]. From Ref. [119], the neutrons are bound more strongly to the nucleus than those of protons, by 3.54 MeV. The spectroscopic factors (strength) is obtained integrating over the energy range $11.0 \leq E \leq 14.0$ MeV, $17.25 \leq E \leq 22.75$ MeV, and $22.75 \leq E \leq 62.25$ MeV, respectively.

Branching ratio of de-excitation γ-ray

In the NCQE cross-section measurement, the Super-K detector observes the de-excitation γ-ray events. If there were only primary γ-rays, the cross-section of γ-ray production induced by NCQE reactions would be written as below

$$\begin{aligned}\sigma_\gamma &\equiv \sigma(\nu + {}^{16}_{8}O \rightarrow \nu + \gamma + Y + N + ...) \\ &= \sum_\alpha \sigma(\nu + {}^{16}_{8}O \rightarrow \nu + \gamma + X^*_{i,\alpha} + N + ...) Br(X^*_{i,\alpha} \rightarrow \gamma + Y) \end{aligned} \quad (4.34)$$

where N is the knocked-out nucleon, and $X_{i,\alpha}$ is the residual nucleus with the α-th nucleon hole state, where the α-th state= $1p_{1/2}, 1p_{3/2}, 1s_{1/2}$ and the other continuum hole states. Y is the final system resulting from the electromagnetic decay of X_α, e.g., ${}^{15}_{8}$O,${}^{15}_{7}$N,${}^{14}_{7}$N+n, ${}^{14}_{6}$C+p. The $Br(X^*_{i,\alpha} \rightarrow \gamma + Y)$ denotes the γ-ray emission branching ratio for the α-th hole state of residual nucleus $X_{i,\alpha}$. The electron-oxygen scattering $^{16}\mathrm{O}(e,e'p)^{15}\mathrm{N}$ experiment provides the γ-ray emission branching ratios of $1p_{3/2}$, and proton-oxygen nucleus scattering $^{16}\mathrm{O}(p,p'p)^{15}\mathrm{N}$ experiment provides the branching ratios of $1s_{1/2}$ hole states.

There is no experimental data about the multi-hole de-excitation. We only assign the multi-hole state toto the same value as for single hole.

$1p_{1/2}$ hole state Since $1p_{1/2}$ hole state does not lead to a de-excitation, no γ-ray emissions are expected for the hole states.

$1p_{3/2}$ hole state Figure 4.9 (from Ref. [122]) shows that there are three possible energy levels for a nucleon to de-excitate into a $1p_{3/2}$ proton hole state: 6.32 MeV, 9.93 MeV and 10.70 MeV. The results of $^{16}\mathrm{O}(e,e'p)^{15}N$ experiment in NIKHEF-K[123] provide the three spectroscopic factors of the three energy levels. Therefore, we assign the the probabilities

Table 4.3: The summaries of the energy levels and the γ-ray emission branching ratios for the $1p_{3/2}$ nucleon hole state. The column of "Prob. of E.L." represents the probabilities of the three energy levels. The column of "B.R. in E.L." represents the γ-ray emission branching ratios of each energy level, and the column of "BR of $(X_\alpha \to \gamma + Y)$" represents the branching ratios of each de-excitation mode.

Residual nucleus	Energy level (MeV)	J_i^π	E_γ (MeV)	E_p (MeV)	Prob. of E.L.(%)	BR in E.L. (%)	BR of $(X_\alpha \to \gamma + Y)$ (%)
^{15}N	6.32	$\frac{3}{2}^-$	6.32	–	86.9	100	86.9
	9.93	$\frac{3}{2}^-$	9.93	–	4.9	77.6±1.9	3.8
			5.27+5.30	–		15.4±1.5	0.8
			6.32	–		4.9±1.2	0.24
			7.30	–		2.1±0.8	0.1
	10.70	$\frac{3}{2}^-$	–	0.5	8.2	–	–
^{15}O	6.18	$\frac{3}{2}^-$	6.18	–	86.9	100	86.9
	9.61	$\frac{3}{2}^-$	–	0.5	4.9	–	–
	10.48	$\frac{3}{2}^-$	–	0.5	8.2	–	–

of the three energy levels with the relative fractions of the three spectroscopic factors. The assigned probabilities are shown in the column of "prob. of E.L." in Table 4.3.

For each energy level of ^{15}N, a table in Ref. [124] provides the branching ratios of each de-excitation mode. The energy level of 6.32 MeV emits only single γ-ray with a 100% branching ratio. The energy level of 9.93 MeV emits single γ-ray with a 77.6% branching ratio and multi-γ rays with a $\sim$ 22% branching ration. The highest energy level of 10.7 MeV does not produce any γ-rays, but a free nucleon instead.

Since there is no experimental data of γ-ray emission from $1p_{3/2}$ neutron hole state, the spectroscopic factors of the three energy levels 6.18 MeV, 9.61 MeV and 10.48 MeV are set to the same values than the corresponding energy levels of proton hole state. From the Table of energy level ^{15}O in Ref. [124], the energy level of 9.61 MeV does not emit any γ-rays. Thus, only the energy level of 6.18 MeV produces γ-rays, with an energy > 5 MeV.

The γ-ray emission branching ratios of $1p_{3/2}$ nucleon hole state are summarized in Table 4.3. From the table, the proton hole state has a 91.8% probability to emit γ-rays, and the neutron hole state has a 86.9% probability to emit γ-rays. Most emitted γ-rays have energy of $\sim$ 6 MeV, which exceeds the threshold of 4 MeV for the analysis.

$1s_{1/2}$ hole state Table 4.4 summarizes the γ-ray emission branching ratios of $1s_{1/2}$ proton hole states from Ref. [125].

Here, we use data of $^{16}\mathrm{O}(p, p'p)^{15}\mathrm{N}$ experiment of E148 at the Research Center for Nuclear Physics (RCNP) [126–128] to assign the values of the γ-ray emission branching ratios for the $1s_{1/2}$ proton hole state. Then, the branching ratios to emit γ-rays with energy $E_\gamma > 6$ MeV and 3 MeV$< E_\gamma \leq 6$ MeV are estimated to be 15.6% and 27.9% respectively [125]. The E148 experiment does not observe the 15 MeV γ-ray emitted from $T = 1, 1^+$ state of ^{12}C, therefore we do not include the 15 MeV γ-ray in the simulation.

Since there is no experimental data of γ-ray emission from the $1s_{1/2}$ neutron hole

Table 4.4: The summaries of the energy levels and the γ-ray emission branching ratios for the $1s_{1/2}$ proton hole state from Ref. [125]. The column of "B.R. in E.L." represents the γ-ray emission branching ratios of each energy level, and the column of "BR of $(X_\alpha \to \gamma + Y)$" represents the branching ratios of each de-excitation mode.

Decay scheme	Energy level (MeV)	J^π	E_γ (MeV)	BR in E.L. (%)	BR of $(X_\alpha \to \gamma + Y)$ (%)
^{13}C+d	3.09	$\frac{1}{2}^+$	3.09	100	3.0
	3.68	$\frac{3}{2}^+$	3.68	99.3	4.2
	3.85	$\frac{5}{2}^+$	3.09	1.20	4.6
			3.68	36.3	
			3.85	62.5	
^{12}C+t	4.44	2^+	4.44	100.0	5.8
^{14}N+n	4.92	0^-	4.92	97	5.2
	5.11	2^-	5.11	79.9	<0.1
	5.69	1^-	3.38	63.9	4.5
			5.69	36.1	
	5.83	3^-	5.11	62.9	0.54
			5.83	21.3	
	6.20	1^+	3.89	76.9	<0.1
			6.20	23.1	
	6.45	3^+	5.11	8.1	2.8
			6.44	70.1	
	7.03	2^+	7.03	98.6	(6.7)
^{14}C+p	6.09	1^-	6.09	100.0	(<0.1)
	6.59	0^+	6.09	98.9	(<0.1)
	6.73	3^-	6.09	3.6	(0.43)
			6.73	96.4	
	6.90	0^-	6.09	100.0	(<0.1)
	7.01	2^+	6.09	1.4	(6.7)
			7.01	98.6	
	7.34	2^-	6.09	49.0	5.7
			6.73	34.3	
			7.34	16.7	

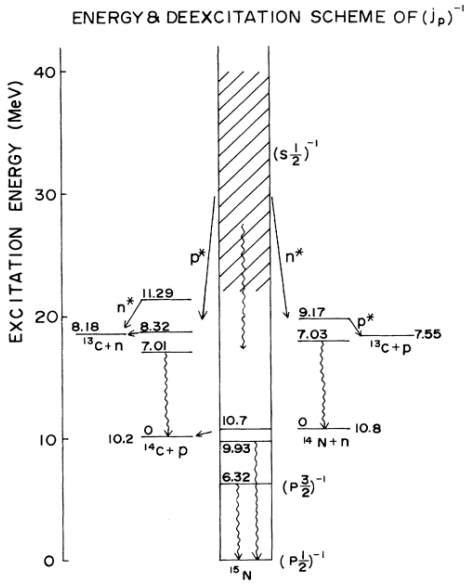

Figure 4.9: Energy level scheme of proton hole state in ^{15}N from Ref. [122]. The de-excitation modes are shown.

state, the branching ratio values of neutron hole states are assigned to the same values than the proton hole state ones.

Other continuum hole states As shown in Figure 4.8, the removal energy distribution of ^{16}O extends to $E \sim 300$ MeV. The nucleon states with removal energy larger than 62 MeV are referred to as "continuum nucleon states", as there is no peak in the energy region in the figure. There is no experiment that observes γ-ray emission from these continuum states. In this thesis, we assume that no γ-ray is emitted from the states.

Summary

The expected energy distribution of primary γ-rays is shown in Figure 4.10. Most of γ-rays have energy of 6.18 MeV or 6.32 MeV, as they are de-excited from ~ 6 MeV energy level of $1p_{3/2}$ nucleon hole states. The other energy levels of $1p_{3/2}$ hole states and $s_{1/2}$ hole states have smaller branching ratios to emit γ-rays with $E_\gamma > 3$ MeV.

From Ref. [115], Figure 4.11 shows the comparison between the NCQE cross-section σ_{NCQE} and the γ-ray production cross-section with only primary γ-rays σ_γ. The shape of $\sigma_\gamma(E_\nu)$ is similar to the shape of $\sigma_{NCQE}(E_\nu)$.[2] The ratio of $\sigma_\gamma/\sigma_{NCQE}$ is $\sim$41% for neutrino energy of 600 MeV.

4.3.3 Other neutrino interactions

On top of the γ-rays produced in NCQE interactions, the γ-ray events coming from the other ν-oxygen interactions are introduced here.

[2]Because the $\sigma_\gamma(E_\nu)$ mainly depends on the removal energy of $1p_{3/2}$ nucleon state, and the $\sigma_{NCQE}(E_\nu)$ is dependent on the average value of the removal energy, the shapes of the two cross-sections are not identical.

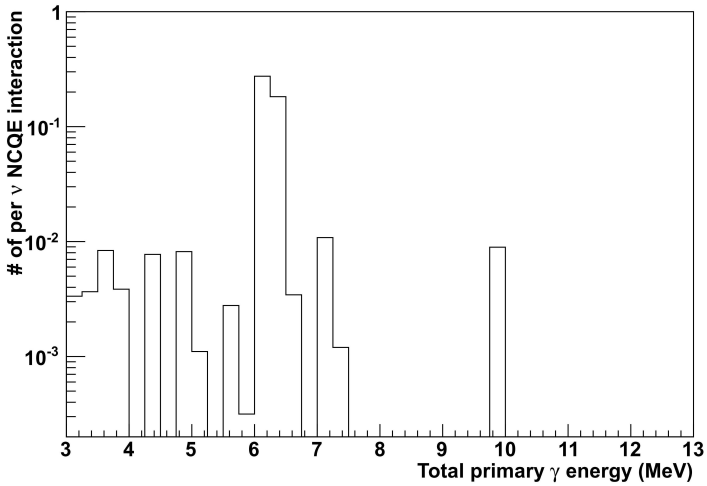

Figure 4.10: The energy distribution of primary γ-rays induced by NCQE reactions. The γ-rays with energy of 6.18 MeV and 6.32 MeV dominate in the energy distribution. The γ-rays with energy of 9.93 MeV are emitted from the 9.93 MeV energy level of $1p_{3/2}$ proton hole state.

NCothers interaction

NC inelastic The neutral current (NC) inelastic interaction, in which the target nucleus is excited, produces the de-excitation γ-rays. Therefore, the NC inelastic interaction is a background source for NCQE interaction measurement. The processes of de-excitation γ-rays induced by NC inelastic interactions are given by

$$\nu +^{16} O \rightarrow \nu +^{16} O^* \rightarrow^{15} N^* + p \ (^{15}O^* + n) \tag{4.35}$$

If the neutrino has energy of $E_\nu \geq 200$ MeV, the NC inelastic cross-section $\sigma_{NCinelastic}(E_\nu)$ is predicted using an extrapolation method [130, 131]. Then, the extrapolation result is calculated as $\sigma_{NCinelastic}(E_\nu$=500 MeV)$\simeq 4.8 \times 10^{-40}$cm^2, which is much smaller than the cross-section of NCQE reaction $\sigma_{NCQE}(E_\nu$=500 MeV). We assume that the γ-rays production for the NC inelastic reaction is similar to the NCQE-reaction one. As a result, the NC inelastic reaction contributes $< 3\%$ fraction of the de-excitation γ-ray events.

NC1π The NC1π interaction has two kinds of production mechanisms: The first one is via a delta (Δ) resonance. The second one is a coherent interaction with the entire nucleus. Since the γ-rays events induced by NC1π Δ resonance dominate, we focus on the NC1π Δ resonance reactions here. The neutrino with energy of around 1 GeV excites a Δ resonance in the scattering, which then decays into a nucleon and a pion as below:

$$\nu + N \rightarrow \nu + \Delta \rightarrow \nu + N^{'} + \pi \tag{4.36}$$

If the produced pion is absorbed before going out of the nucleus or if it is absorbed by the other oxygen nucleus in water, a de-excitation γ-ray is produced as below.

$$\pi^{\pm} +^{16} O \ \rightarrow \ X^*_\alpha + N^{'} + ... \rightarrow Y + \gamma + ... \tag{4.37}$$

where the residual nucleus X^*_α emits γ-rays, and the produced nucleon $N^{'}$ induces the secondary γ-ray production.

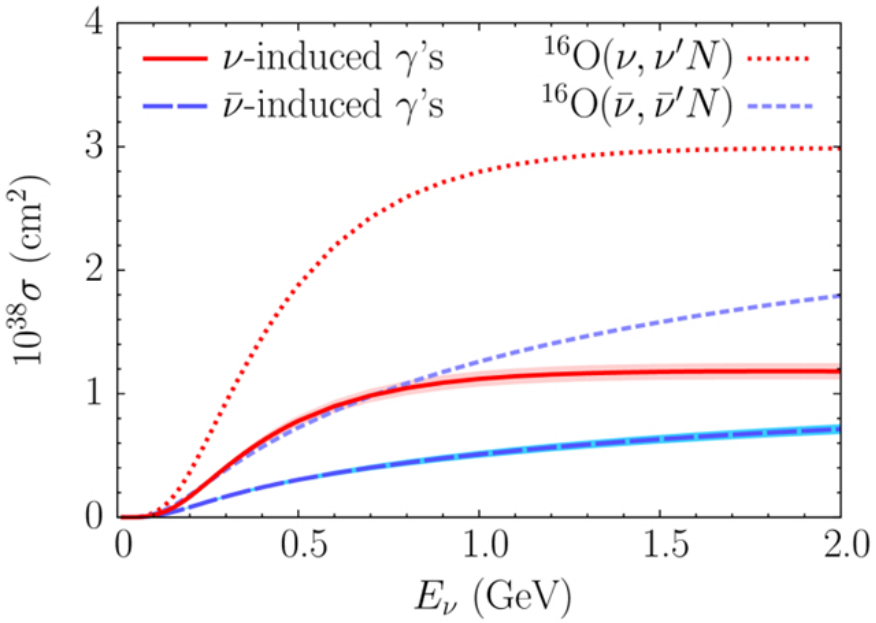

Figure 4.11: The cross-section of neutrino-oxygen (anti-neutrino-oxygen) NCQE reaction $\sigma_{NCQE}(E_\nu)$ is plotted as the red dashed line (blue dashed line). The cross-section of primary γ-ray production induced by neutrino-oxygen (anti-neutrino-oxygen) NCQE reaction $\sigma_\gamma(E_\nu)$is plotted as the red line (blue line).[115]

In NEUT, the pion absorption in the nuclear medium is simulated using the pion scattering data from Ref. [132–134]. Then, the branching ratio of γ-ray emission for each residual nucleus X^*_α are assigned using the experimental results of π^- absorption at rest in water at CERN [136]. In this experiment, the γ-rays are emitted from the residual excited nuclei such as $^{16}O^*$, $^{15}N^*$, $^{14}N^*$, $^{14}C^*$, $^{13}N^*$, $^{12}C^*$, and $^{10}B^*$. The residual nuclei and the γ-ray emission branching ratios are summarized in Table 4.5. The sum of γ-ray emission branching ratios for each residual nucleus is less than 6.1%.

The expected number of NC1π Δ resonance events is $\sim$ 20% fraction of the de-excitation γ-ray events at energy of the T2K neutrino.

CC interaction

If the neutrino-nucleus charge current (CC) interaction produces a charge lepton with a low momentum, the CC interaction might be a background source. There are two possible situations leading to a γ-ray candidate event induced by CC interaction: First, the charged lepton signal with a mis-identified Cherenkov angle is selected as a γ-ray event. Second, a nucleon is knocked out of the nucleus in a CCQE interaction, and a de-excitation γ-ray is emitted from the excited nucleus. The expected number of CC events is $\sim$ 4% fraction of the de-excitation γ-ray events.

Background reaction cross-section correction by external data

The T2K experiment uses a series of external experiments and on-situ measurements to correct the prediction of neutrino interaction cross-sections [129]. The external experiments such as MiniBooNE[92–95], SciBooNE[97, 98], and NOMAD[96] measure the neutrino cross-sections for a neutrino energy from subGeV to few GeV. In the NCQE

Table 4.5: The γ-ray emission branching ratios of the excited nucleus produced by pion absorption are summarized. The nucleus emits a γ-ray with a branching ratio less than 6.1%.

residual nucleus	Energy level (MeV)	J^π	E_γ (MeV)	BR of $(X_\alpha \to \gamma + Y)$ (%)
^{16}O	6.13	3^-	6.13	1.7
^{15}N	5.270	$\frac{5}{2}^+$	5.27	0.5
^{14}N	2.313	0^+	2.31	0.3
	3.945	1^+	1.63+2.31	4.8
	5.106	2^-	5.11	0.7
		2^-	2.79+2.31	0.2
^{14}C	6.728	3^-	6.72	< 0.2
^{13}C	3.684	$\frac{3}{2}^-$	3.68	1.9
	3.854	$\frac{5}{2}^+$	3.85	1.0
^{12}C	4.439	2^+	4.44	4.0
^{10}B	0.717	3^+	0.72	1.3

cross-section measurement, they are used to constrain the simulation model for the background neutrino interactions, such as CCQE, CC1π, and NC1π.

The cross-section models in NEUT have some input parameters, that are replaced using external experimental results. In the analysis, the used parameters are listed as follows:

- M_A^{QE} : the axial mass for axial vector form factor of CCQE cross-section model.
- M_A^{RES} : the axial mass for axial vector form factor of CC1π Δ resonance(res) reaction model or NC1π Δ resonance(res) reaction model.
- Three normalization parameters (norm) for CCQE, CC1π res, and NC1π res that are empirical and control the overall normalization of the cross-section.

Table 4.6 summarizes the parameters of the background cross-section models.

4.4 Detector Simulation

Super-K has developed a GEANT3-based[100] package (SKDETSIM) which is designed to simulate the propagation and interaction of the particles produced by the neutrino interaction. The package also simulates the Cherenkov light production by the charge particles, the photon absorption and scattering in water, the photon detection by the PMTs, and the signal digitization by SK DAQ.

4.4.1 Secondary gamma ray production

Here, the simulation of secondary γ-ray production is described. Unlike primary γ-ray production, there is no experimental data about the secondary γ-ray production. We only use some simulators in hand to predict the production without a data correction from external experiments.

Table 4.6: The parameters for the cross-section models. The values of the parameters are used to correct the cross-sections in the simulation.

Parameter name	Value	Contents
M_A^{QE}	1.21 GeV/c^2	axial mass for axial vector form factor of CC quasi-elastic
M_A^{RES}	1.41 GeV/c^2	axial mass for axial vector form factor of CC1π (res) or NC1π (res)
CCQE norm. $E_\nu < 1.5$GeV	1.0	normalization value for CCQE, $E_\nu < 1.5$GeV
CC1π(res) norm. $E_\nu < 2.5$GeV	1.15	normalization value for CC1π (res), $E_\nu < 2.5$GeV
NC1π(res) norm.	0.96	normalization value for NC1π (res)

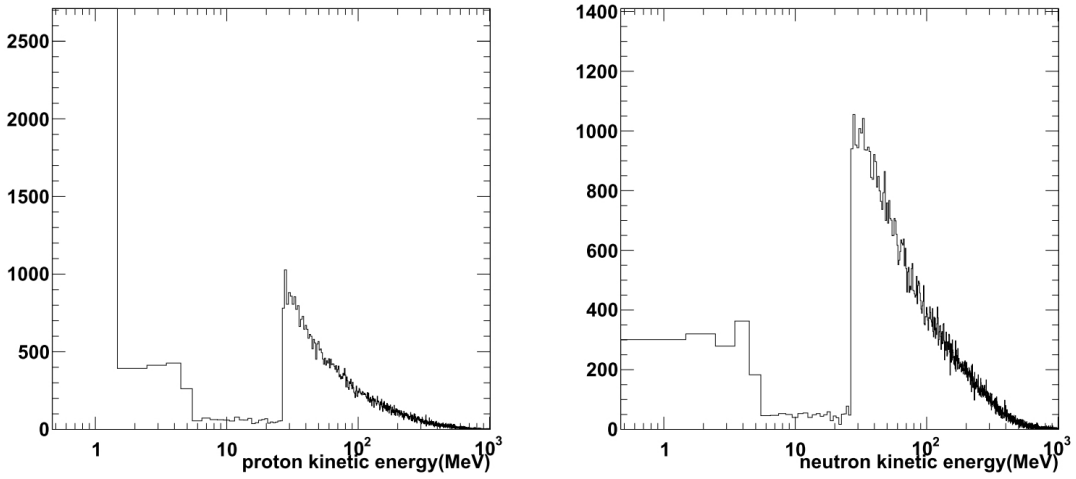

Figure 4.12: The kinetic energy T_N distribution of free nucleons escaped from oxygen nucleus by NCQE reactions. The vertical axes of the two plots are given in arbitrary units.

Table 4.7: Summary of the simulators used for the nucleon hadronic reactions.

hadron particle	$T_n < 20$MeV	20MeV$\leq T_n < 3.5$GeV
neutron	MICAP	NMTC
proton	NMTC	NMTC

As seen in Figure 4.6, the secondary γ-rays are induced by hadronic reactions. The hadronic reactions are simulated using GCALOR [135] of GEANT3. GCALOR is completed by four simulators: FLUKA, SCALE, NMTC, and MICAP. FLUKA and SCALE simulate the hadronic reactions of nucleons having a kinetic energy $T_N > 10$GeV and 10GeV$> T_N \leq 3$GeV respectively. While the NMTC and MICAP are used for hadronic reactions of nucleons with a relatively low kinetic energy. Figure 4.12 shows the kinetic energy T_N distribution of free nucleons escaping from the oxygen nucleus by NCQE reactions. In the left plot, the protons with $T_N \leq 1$ MeV come from the de-excitation of the specific energy levels[3] for $1p_{3/2}$ nucleon hole state. The protons with 1 MeV$\leq T_N \leq 5$ MeV comes from the three body decay of $1s_{1/2}$ nucleon state. The protons with 25 MeV$\leq T_N$ are the knocked out protons in the NCQE reactions. In the figure, the most free nucleons induced by NCQE reactions have kinetic energy lower than 2.5 GeV. Thus, MICAP[137] is used to simulate the neutron reactions having a kinetic energy T_n below 20 MeV. Table 4.7 shows the summary of the simulators used for nucleon hadronic reactions.

The secondary γ-ray energy versus the incident nucleon kinetic energy (E_γ-T_N) distributions are shown in Figure 4.13. In the neutron plot of the figure, there is a discontinuity in the borderline of two simulators. The discontinuity shows that the two simulators have different predictions at boundary kinetic energy of $T_N = 20$ MeV. We suppose that a single nucleon should be knocked out by the hadronic reactions, then de-excitation γ-ray with 6 MeV should be produced. But, there is no peak at $E_\gamma = 6$ MeV at region of neutron kinetic energy $T_N \geq 20$ MeV, where the hadronic reactions are simulated by NMTC.

Here, we focus on the multiplicity of secondary γ-rays since it affects the determination of Cherenkov angle as mentioned in Appendix B.3. Figure 4.14 shows the multiplicity of secondary γ-rays induced by neutrons. We expect that the multiplicity of secondary γ-rays is distributed continuously, but there is a gap for single γ-ray in the simulation by GEANT3.

We suppose that the GCALOR simulator in GEANT3 does not predict the secondary γ-ray production with the required accuracy. The details and the impact on systematic uncertainty of the simulation of secondary γ-ray production are in Section 5.3.4 and Section 6.3.

The total energy distribution of secondary γ-rays is shown in Figure 4.15. The peak of the distribution is located at 7 MeV, and the tail extends to high energy. Super-K observes de-excitation γ-ray events that consist of primary γ-rays and secondary γ-rays.

[3]The E.L. of 10.70 MeV for $1p_{3/2}$ nucleon hole state, the E.L. of 10.48 MeV and the E.L. of 9.61 MeV for $1p_{3/2}$ neutron hole state.

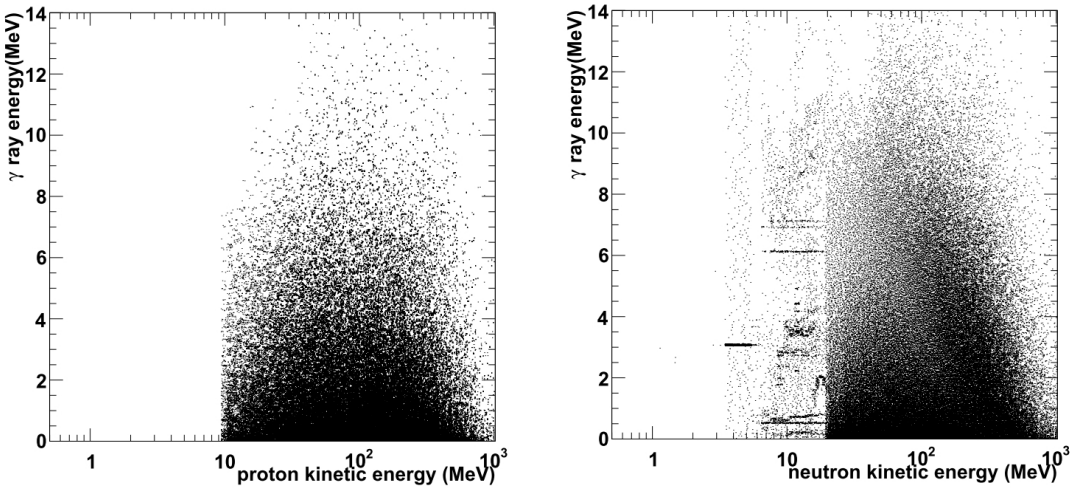

Figure 4.13: The secondary γ-ray energy versus nucleon kinetic energy (E_γ-T_N) distributions. The dots represent the γ-rays from the nucleon hadronic reactions. Left plot shows the γ-rays induced by protons. The right plot shows the γ-rays induced by neutrons, and there is a discontinuous boundary of $T_N = 20MeV$.

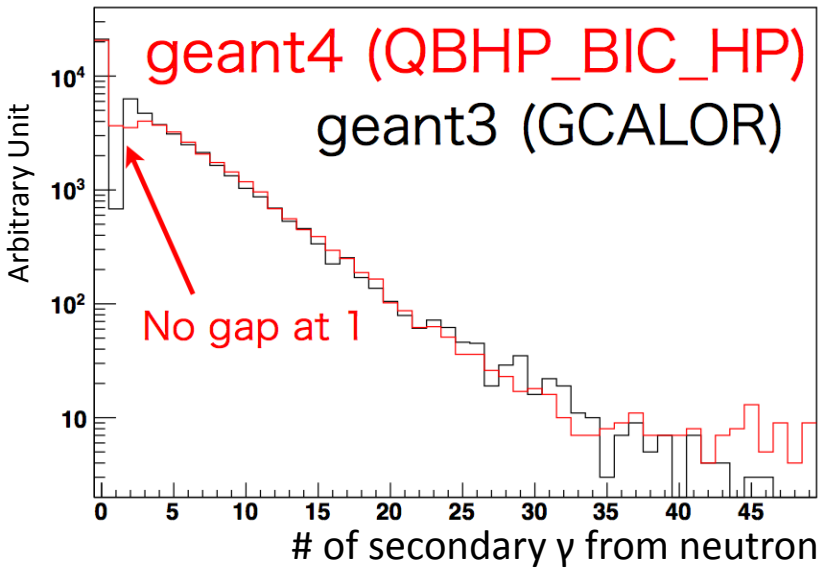

Figure 4.14: The multiplicity of secondary γ-rays induced by neutrons. The black line represent the secondary γ-ray simulated by GEANT3, and there is a gap at single γ-ray. The red line represents the result simulated by GEANT4.

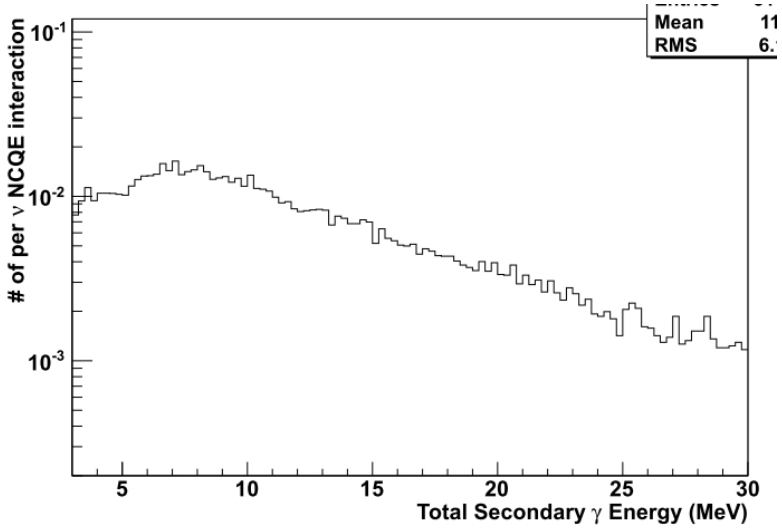

Figure 4.15: Distribution of total energy of secondary γ-rays. The peak of the distribution is at 7 MeV, and the tail extends to high energy.

4.5 Results of Monte Carlo simulation

The expected energy distribution of de-excitation γ-ray events in T2K Run1-3 is shown in Fig. 4.16, after having applied the selection described in Chapter 5. The reconstructed energy region is distributed from 4 MeV to 30 MeV. Table 5.8 shows that 68% of γ-ray events are expected to be induced by the NCQE reactions. The peak is located at $\sim$5 MeV because of the 6.18 MeV and 6.32 MeV primary γ-rays.

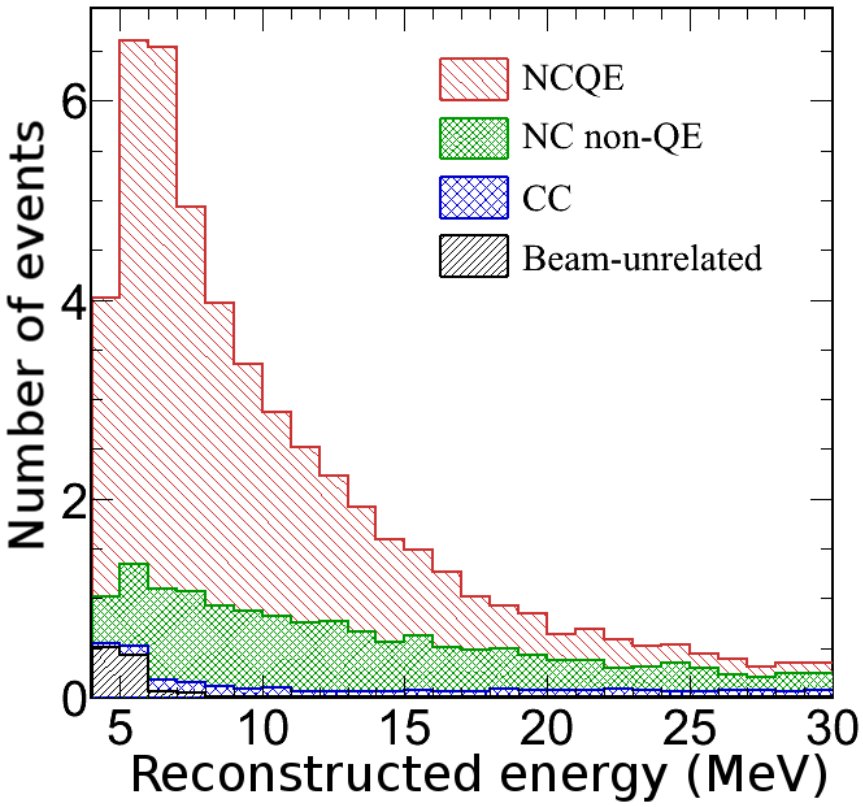

Figure 4.16: The expected energy distribution of de-excitation γ-ray events in T2K Run1-3. The red histogram is the NCQE events, the green histogram is the NCothers (or NC non-QE) events, and the blue histogram is the CC events. The black histogram is the beam-unrelated events which are discussed in Chapter 5.

Chapter 5

Event selection

This chapter discusses the selection of de-excitation γ-ray candidate events induced by the NCQE reactions from the T2K Run1-3 data. There are two background sources. First is the beam-related background events, which are induced by other interactions than NCQE such as NCothers interactions and CC interactions as mentioned in the previous chapter. Second, the radioactive impurities in the Super-K detector cause the beam-unrelated background events, and the rate is high at lower energy.

Comparisons between the observed candidate events and the expected candidate events are shown in this chapter.

5.1 Event selection

Several selections are applied to search the de-excitation γ-ray events in T2K spill data. Table 5.1 summarizes the used selections by sequence.

5.1.1 Data set

The de-excitation γ-ray caididate events are searched from the T2K beam spill data, which are taken during the following periods: RUN1(from Jan. 2010 to Jun. 2010), RUN2(from Nov. 2010 to Mar. 2011), RUN3(from Mar. 2012 to Jun. 2012). The analysis uses the data with the proton on target (POT) of 3.01×10^{20}. Normally, the

Table 5.1: Summary of event selections for the de-excitation γ-ray candidate events.

selection name	contents
Good beam spill	ν beam good + SK data quality
Reconstructed Energy	4 MeV$\leq E_{rec} \leq$ 30 MeV
Timing	ΔT_0 within $\pm$100 ns from bunch centers
Fiducial Volume	vertex distance to ID wall
DWall	vertex distance to ID wall
EffWall	vertex distance to ID wall
OvaQ	depend on vertex and hit pattern
Pre-activity	muon pre-activity
Cherenkov angle	$\theta_{rec} > 34.0^o$

horn was operated with 250kA configuration except the RUN3b, in which 200kA horn current configuration was applied. The T2K Run periods, corresponding the Super-K Run number, and other information are summarized in Table 5.2.

Table 5.2: Summary of the T2K Run1-3 data set. The total protons on target (POT) is 30.1×10^{19}.

T2K Run	MR Run	SK Run	POT($\times 10^{19}$)	Period: Start-End
	29-31	66251-66608	0.34	23, Jan.–25, Mar. ,2010
RUN1	32	66679-66727	0.76	14, Apr.–01, May., 2010
	33	66769-66902	1.21	09, May.–31, May., 2010
	34	66916-66945	0.93	07, Jun.–26, Jun., 2010
	36	67877-67977	4.16	18, Nov.–25, Dec., 2010
RUN2	37	68045-68175	5.67	19, Jan.–28, Feb., 2011
	38	68200-68208	1.26	04, Mar.–11, May., 2011
RUN3b	41	69542-69586	2.14	08, Mar.–21, Mar., 2012
RUN3c	42	69626-69720	11.24	08, Apr.–24, May., 2012
	43	69734-69753	2.41	27, May.–09, Jun., 2012
Total			30.10	

5.1.2 Good beam spill selection

As mentioned in Section 2.5.3, every spill information is sent from J-PARC to SK DAQ system. Information of every hit PMT within ± 500 μsec from the beam arrival time are stored.

The spill data falgged as "beam good spill" which is defined by the J-PARC beam-line status. The details of the flag are mentioned in Ref. [138].

Additional data quality flag is referred to as "SK data quality", which is based on the SK DAQ alive time and other SK data quality. The cuts for SK data quality are defined as follows:

1. SK DAQ alive: Due to the power failure and other SK DAQ failure, the deadtime fraction over all T2K spill data is 0.10%. The alive time of SK DAQ is the period without the mentioned DAQ failures.

2. Bad subrun cut: If a PMT has some discharges at dynode, a flasher noise is generated. The recorded 1 min data including the flash event is labeled as a "bad subrun". [1] This cut removes 0.31% fraction of the spill data.

3. GPS error: If both the GPS1 data and the GPS2 data have error flags, this spill is marked as bad spill. Until the end of T2K RUN3, there is no bad spill tagged by this cut.

4. Special data block: There are two special types of event blocks which are not recorded as normal data. The first block is "pedestal block", which is designed to save pedestal data of all channels on the front-end electronics. The second block

[1] A "SK subrun" is a unit of recorded data corresponding to about one minute of real time observation.

is "TDC reset block", which is reseting some counting in TDC chips. This cut removes 0.08% fraction of the all T2K spill data.

Table 5.3 shows the summary of good spills in each T2K RUN. Totally, the inefficiency of the "SK quality" is below 0.5%.

Table 5.3: Summary of good spill for T2K RUN1-3 data set. During all period, the Total POT is 65.70×10^{19}.

T2K Run	RUN1	RUN2	RUN3	Total	Inefficiency
# of good spill($\times 10^6$)	1.00	1.480	1.762	4.245	0.49%
Bunch # in per spill	6	8	8		

5.1.3 Event reconstruction

Super-K developed analysis tools to reconstruct the low energy event information such as vertex, direction, energy, and Cherenkov angle. Here, the reconstruction methods are described briefly [85, 86]. Details of the reconstruction method are in Appendix B.

Vertex reconstruction For neutrino events having energy less than 100 MeV, the charged particle produced from neutrino reaction does not travel so far from the position of neutrino interaction. The track of the charged particle can be viewed as the vertex of the neutrino event. Therefore, Cherenkov photons emitted from the charged particle are supposed to be generated at the same position and the same timing. The timing of each hit PMT t_i corresponds to the time-of-flight $t_{tof,i}$ from the vertex.

The vertex reconstruction of Super-K uses the timing information of hit PMTs to search the vertex [85]. First, for each possible vertex position, residual time $t_{res,i}$, which is a difference between the observed timing and the one expected from the assumed vertex position, is calculated for every hit PMTs. Second, a likelihood function is constructed from the residual times and is used to judge the most possible vertex candidates. A larger likelihood value of the vertex candidate represent that the residual times of hit PMTs distributed narrowly. The most procurable vertex is searched in the grid steps. The search process iss repeated with a finer length of step until the step is 1cm at last.

Energy reconstruction For low energy events, the average number of photo-electron of each hit PMT is one or two. It is hard to use the number of photoelectrons to reconstruct the energy value. The number of "effective hit PMTs" N_{eff} is used to reconstruct the energy of event [86]. The number of hit PMTs is corrected with information such as dark noise rate, PMT photo-cathode coverage correction, water transparency, quantum efficiency to obtain N_{eff}. As the reconstructed energy is a function of N_{eff}, a mono-energy electron calibration is used to define the function. If E_{rec} is less than 25 MeV, $E_{rec}(N_{eff})$ is given by

$$E_{rec} = 0.82 + 0.13N_{eff} - 1.11 \times 10^{-4}N_{eff}^2 + 1.25 \times 10^{-6}N_{eff}^3 - 3.42 \times 10^{-9}N_{eff}^4 \quad (5.1)$$

If the reconstructed energy is larger than 25 MeV, the fitting function of reconstructed energy is given by

$$E_{rec} = 25.0 + 0.138 \times (N_{eff} - 189.8) \quad (5.2)$$

Cherenkov angle reconstruction As a total number of photo-electrons of low energy event is below 200 p.e., it is not easy to fit a ring pattern to obtain the Cherenkov angle. A statistical method is introduced: any three hit PMTs and the reconstructed vertex compose a circular cone. The opening angle of the circular cone is taken account as an entry of the statics. All the possible opening angles are calculated, and the Cherenkov angle is chosen as the angle with most entries of in statics.

With the statistical method, the reconstructed Cherenkov angles θ_{rec} of electron event and muon event are 42 degree and less than 34 degree respectively, as their masses are different. Because the hit PMTs of multi-gamma event distribute widely as shown in Figure B.6, the Chenrenkov angle is reconstructed as 90 degree for such events.

5.1.4 Energy selection

As described in Section 2.5.3, we define the threshold of SLE software trigger as $N_{200} \geq 25$ to tag events with a reconstructed energy (total electron energy) above 4.0 MeV in the spill data, where the N_{200} is the number of hit PMTs within a 200 ns window. The tagged signals are referred to as very first event candidates, which are prepared to reconstruct their event information. Then, we remove the events which have the total number of hit PMTs larger than 400 ($N_{TOT} > 400$), which is corresponding to ~ 60 MeV electron signal before the reconstruction process to save CPU time.

The energy spectrum of the signal events is expected to have a peak near 6 MeV. We set the lower threshold for reconstructed energy to be 4 MeV, where the trigger efficiency is above 99.5%. We set the higher threshold to be 30 MeV, to eliminate the Michel electron background.

5.1.5 Timing cut

To remove the beam-unrelated background events, the GPS timing information is used. The timing of an event in spill is denoted as ΔT_0, in which the arrival time of the spill leading edge is used to be the zero point. First, the events are selected with "on-timing" criteria with the time interval of $-2\,\mu$s$< \Delta T_0 < 10\,\mu$s.

Second, the eight bunch structure of T2K beam provides a finer selection by the timing information. The de-excitation γ-ray events are distributed within either of the eight bunch timings. To determine the timing of the eight bunch centers, we use high-statistics fully contained (FC) events with high statistic, which have energy of $\mathcal{O}(100$ MeV). The timing ΔT_0 distribution of the FC events is shown in Figure 5.1, and the eight bunch centers are determinated by fitting the timing distribution. The fitted eight bunch centers are given by

$$\Delta T_0 = 99.5 + 581.0 \times (i-1) \ \ (ns) \tag{5.3}$$

where i is i-th bunch. The i is $1 \sim 6$ in RUN1, and i is $1 \sim 8$ in the other RUNs. The time interval of every bunch center is 581ns. The first bunch center has a offset of 99.5 ns.

After the determination, we define the second "on-timing" criteria that restricts the selection to be within $\pm$100 ns from the nearest bunch center.

Besides, an criteria of timing is used to estimate the number of beam-unrelated events $N_{exp}^{beam-unrelated}$: the events within $\Delta T_0 = (-5, -500)$ μsec are selected. This timing cut is referred to as "off-timing".

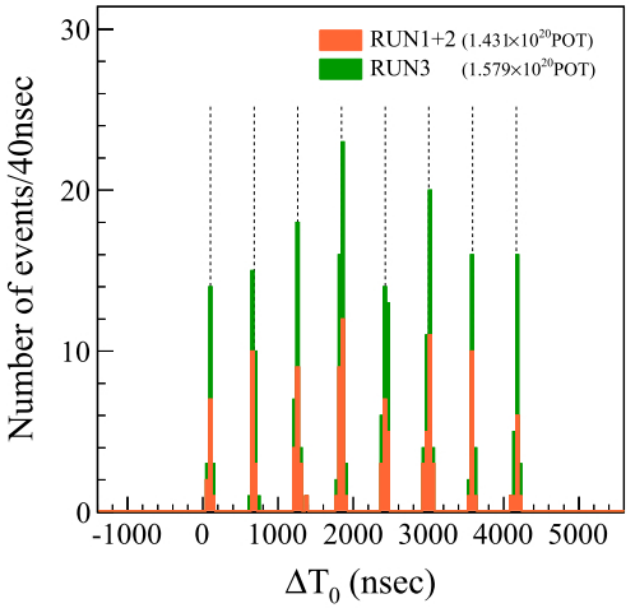

Figure 5.1: The ΔT_0 timing distribution of T2K FC events exhibits the eight bunch structure clearly. The eight dotted vertical lines represent the 581 nsec interval bunch center positions fitted to the observed FC event times. T2K Run1-2 and T2K RUN3 data are stacked.

5.1.6 Radioactivity background cut

The main contribution of beam-unrelated background events is from the radioactive impurities contained in the material of PMT and ID wall. The background events are expected to appear near ID wall frequently, so we remove the events with vertices near the ID wall to reduce the background event rate. However, the vertices of background events might be mis-reconstructed. To deal with this situation, the quality parameters of the event fit (reconstruct) are used to reduce the background rates.

Fiducial Volume

The beam-unrelated background events cluster near the inner detector wall, so we remove the events whose the vertices are within 2m from the ID wall. The used volume of the Super-K detector is inside 2 meter distance from the ID wall, fiducial volume (FV) as illustrated in Figure 5.2.

Distance to ID wall

To remove the background events entering FV from the ID wall, two parameters are used: dWall and effWall.

First, the dWall is defined as the distance from the reconstructed vertex to nearest ID wall. Second, the effWall is calculated as a distance from the reconstructed vertex along the backward of reconstructed direction to the ID wall. Figure 5.2 shows an instruction of FV, dWall and effWall. As the dWall cut and the effWall cut make stricter selections than FV volume cut, the threshold value of dWall and the threshold value of effWall are not shorter than 2 meter for event with vertex inside FV. We remove the events that have shorter dWall value or effWall value than corresponding threshold values, and most

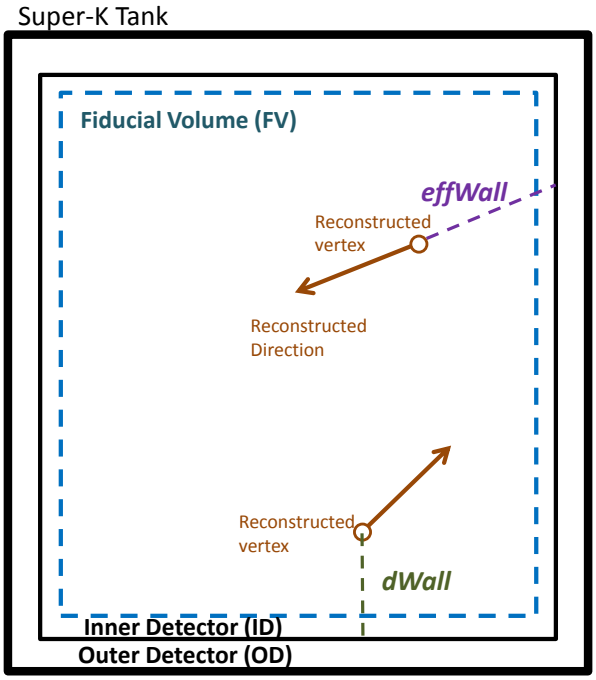

Figure 5.2: Illustration of FV, effWall and dWall in the Super-K tank. The dWall is the distance from the reconstructed vertex to nearest ID wall. The effWall is a distance from the reconstructed vertex along the backward of reconstructed direction to the ID wall.

of the removed events are backgrounds from the inner detector wall. In Appendix E, optimizations of the corresponding thresholds are discussed.

Goodness of the reconstruction

Although the vertex cuts remove most of backgrounds, there are remained background events with mis-reconstructed vertex. Here, two goodness parameters, that depend on the event reconstruction are introduced to remove such backgrounds.

For neutrino events, the residual timings of hit PMTs with a well-reconstructed vertex distributed narrowly. While for the radioactive background events, the residual timings distribute widely. A vertex goodness parameter G_V is a function of the residual timing distribution. If the residual timings $t_{res,i}$ of hit PMTs distribute narrowly, the value of G_V is larger.

For neutrino events, the positions of hit PMTs are expected to be located uniformly on azimuthal angle of the Cherenkov ring. While the hit PMTs of mis-reconstructed events do not distributed uniformly over the azimuthal angle, which is indicated as shown in Figure 5.3. From the figure, the azimuthal angle of the hit PMT depends on the reconstructed vertex and reconstructed direction. A direction goodness parameter G_A is used to check the quality the reconstruction. For well-reconstructed events, the intervals of azimuthal angles $\Delta\angle = \angle(i) - \angle(i-1)$ are expected to distribute similar to the uniform distribution, and they are close the average of the interval of azimuthal angles. The value of G_A is proportional to the largest difference between the intervals of azimuthal angles $\angle(i) - \angle(i)$ and the average interval $\Delta\angle_{avg} = 2\pi/N_{hit\,PMT}$, where $N_{hit\,PMT}$ is the number

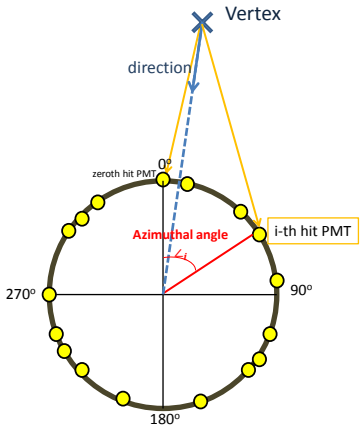

Figure 5.3: The azimuthal angle of i-th hit PMT in the Cherenkov ring.

of selected hit PMTs. Therefore, a small value of G_A represents that the hit PMTs are distributed uniformly.

The goodness of the event reconstruction is defined as ovaQ$\equiv$ $G_V^2 - G_A^2$ (one dimensional variable of the vertex and angular reconstruction qualities). For a well-reconstructed information of event, G_V is large and G_A is small. Events with the ovaQ value less than a certain threshold are removed, as most of them are backgrounds with mis-reconstructed vertex or direction. Details of the ovaQ parameter are described in Appendix D.

Optimization of the thresholds

To obtain the maximum signal-to-noise (S/N) ratio, we optimize threshold of dWall, threshold of effWall, and threshold of ovaQ. Here, introductions of the optimization of the the thresholds of dWall, effWall, and ovaQ are described. Details of the optimization and the results are in Appendix E.

A figure-of-merit (FOM) is used to an parameter which represent the S/N ratio. The FOM is given by

$$FOM \equiv \frac{N_{signal}}{\sqrt{N_{signal} + N_{background}}} \tag{5.4}$$

where N_{signal} ($N_{background}$) is the expected numbers of the beam-related (beam-unrelated) events. N_{signal} and $N_{background}$ are the functions of thresholds of (dWall, effWall, ovaQ). The expected number of beam-related events is obtained using the neutrino beam simulations, while the expected number of beam-unrelated events are obtained using "off-timing" events with the timing ΔT_0 $\in$(-500 μs, -5 μs). By scaling the number of off-timing events, we estimate the number of the beam-unrelated event occurring within the live-time of $N_{bunch} \times 200$ ns.

As the rate of background events depend on their energies, we search the threshold value which maximize the FOM for every 0.5 MeV- step energy within (4 MeV, 6.5 MeV). The cut thresholds of dWall, effWall and ovaQ are given as a function of energy as the linearly fitted lines to the obtained values. Those are shown in Fig. 5.4. An event with dWall, effWall or ovaQ less than the corresponding threshold is removed.

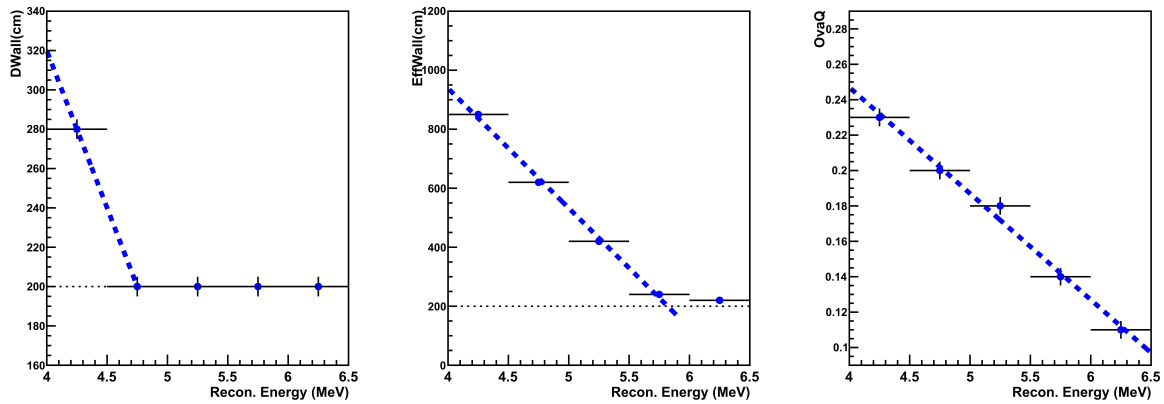

Figure 5.4: Cut thresholds of dWall, effWall and OvaQ for T2K RUN3. The blue points represent the optimization cut results for each energy bin. The blue dash lines are the fitting lines using the optimization points, and the fitting lines and their extrapolation are used for the thresholds of (dWall, effWall, ovaQ). The thresholds of dWall or effWall are not shorter than 200 cm, as the black dash lines denote the lines of 200 cm.

5.1.7 Pre-activity cut

Cosmic muons or induced muons from ν_μ charge current (CC) reactions with small momentum emit very little Cherenkov photons in water. Their decay electron signal from the muon passes the selection of reconstructed energy. To remove such events, we probe the pre-activity in the timing region $0.2 \sim 20\,\mu$s before.

We search the maximum number of hit PMTs in 30 ns window N_{30} among the 0.2–20 μs before the on-timing selected event. If N_{30} is larger than 22, there is likely the parent muon and the event candidate are considered as a decay electron event. The accidental dark noises might cause a signal of $N_{30} \geq 22$, and the pre-activity cut is expected to remove less than 0.1% of the de-excitation γ-ray signal events.

5.1.8 Cherenkov angle cut

In the beam-related backgrounds, some CC reactions or NCothers reactions produce a muon or a pion that emits Cherenkov light. The induced muons with momentum less than of 250 MeV/c remain after the reconstructed energy selection. The reconstructed Cherenkov angle is used to identify these background events. Since the mass of a muon or a pion is heavier than an electron. The Cherenkov opening angle distribution of the muon (or pion) events has a peak at $\sim 28^o$ which is much smaller than the maximum cherenkov angle of 34^0.

The Cherenkov angle distribution[2] of T2K ν beam MC simulation events are plotted in Figure 5.5. Most events with angles below 34 degree are CC events and NCothers events. Therefore, we remove the events with Cherenkov angle less than 34 degree.

[2]The method to reconstruct the Cherenkov angle value of an event is described in Appendix B.3.

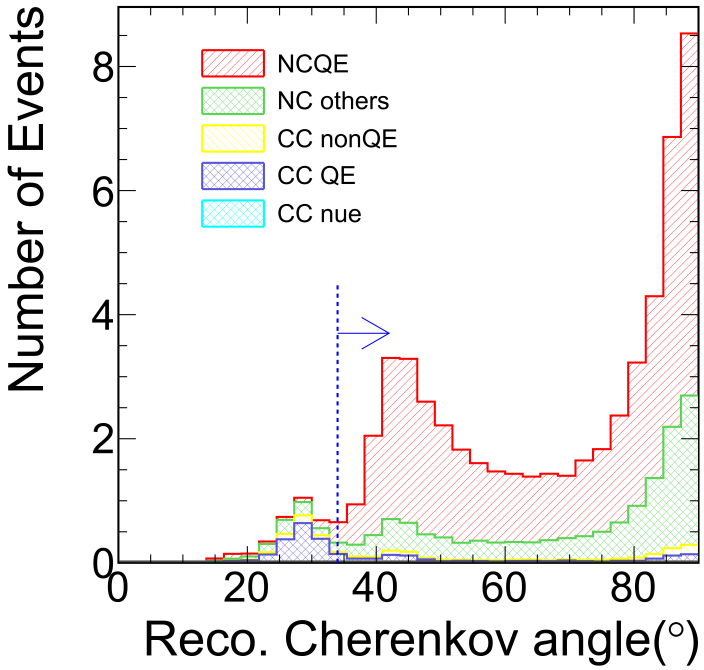

Figure 5.5: Reconstructed Cherenkov angle distribution of T2K RUN1-3 simulated events. The events are selected after the other selections. The red histogram represents the NCQE events, and the green histogram is the NCothers events including NC1π (res), NC1π (coh), etc. The yellow, blue, and light blue histogram show the CC events.

5.1.9 Efficiency of expected events

The ν beam-related events are estimated using the MC simulations, while the "off-timing" data events are used to estimate the beam-unrelated background events as described in Appendix E. Figure 5.6 shows the energy distributions of expected events in range of (4 MeV, 30 MeV) before and after the selections. The efficiency of signal (background) events is defined as efficiency= (the number of events after all the selections)/(the number of events after the energy selection). The number of the off-timing events is reduced to only 1.2 events, and the efficiency is below 0.1%. While the expected number of the beam-related events during the T2K RUN1-3 period is 49.8, and the efficiencies for each T2K run is $\sim$ 90% as shown in Table 5.4.

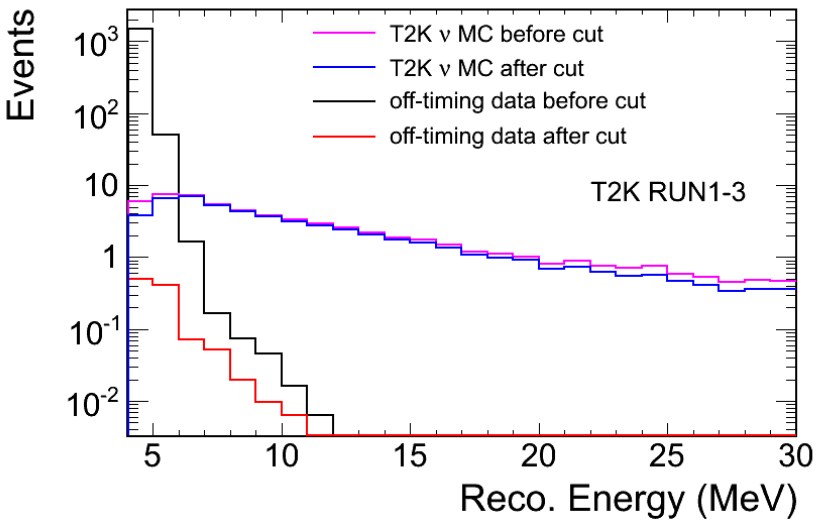

Figure 5.6: The reconstructed energy (Reco. energy) distribution of expected event from the T2K beam MC simulation and the off-timing data. The plot shows that the dWall, effWall and ovaQ cuts remove the radioactive background events effectively to less than 0.1%. After selections, the beam-unrelated events are expected to be only 1.2 events for T2K RUN1-3.

Table 5.4: The numbers of selected events at each selection procedure for T2K Run1-3. The expected numbers of selected event N_{exp} include beam-related MC simulation and off-timing (beam-unrelated). The expected numbers of selected event have good agreement with the numbers of observed data events N_{obs} in every procedure.

T2K RUN1-3	N_{obs}	N_{exp}		
Reduction cuts	On-timimg data	beam-related MC	off-timing	Total
energy & timimg	1582	55.85	1528.0	1583.9
dWall	273	55.49	154.3	209.8
effWall	159	54.58	69.78	124.4
ovaQ	49	53.17	1.19	54.4
angle & pre-activity	43	49.8	1.15	51.0
cut effiency	–	89.2%	0.07%	–

5.1.10 Summary of selection

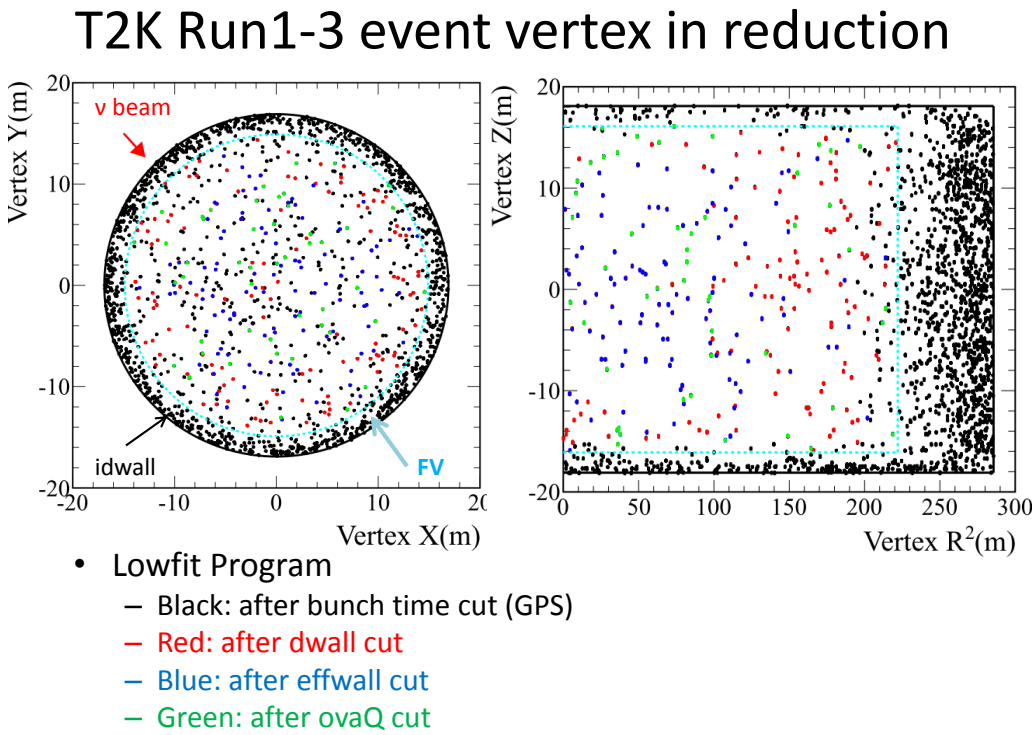

Figure 5.7: Vertex distribution of the selected γ-ray events at each selection process for the T2K Run1-3 data. The black lines are Super-K ID wall, and the blue dash lines are boundary of FV that is 2m distance inside the Super-K ID wall. X, Y, Z are the three orthogonal axises, and Z is the vertical axis. R^2 is distance from circle center, and that is equal to $X^2 + Y^2$.

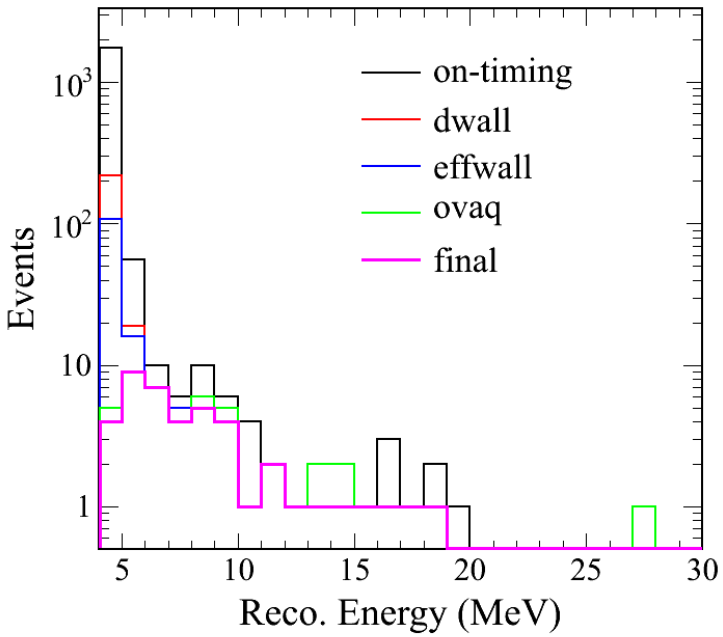

Figure 5.8: Reconstructed energy distribution of the selected events at each selection process for the T2K Run1-3 data..

Observed number of selected events Table 5.4 shows the summary of the event selecting of the T2K spill data. The vertex distributions of events in each selection process are shown in Figure 5.7. Figure 5.9 shows the selection parameters (dWall, effWall, ovaQ) distributions in each selection process. Figure 5.8 shows the energy distributions of selected events in each selection process. After the selections, 43 data events are selected as the de-excitation γ-ray candidates.

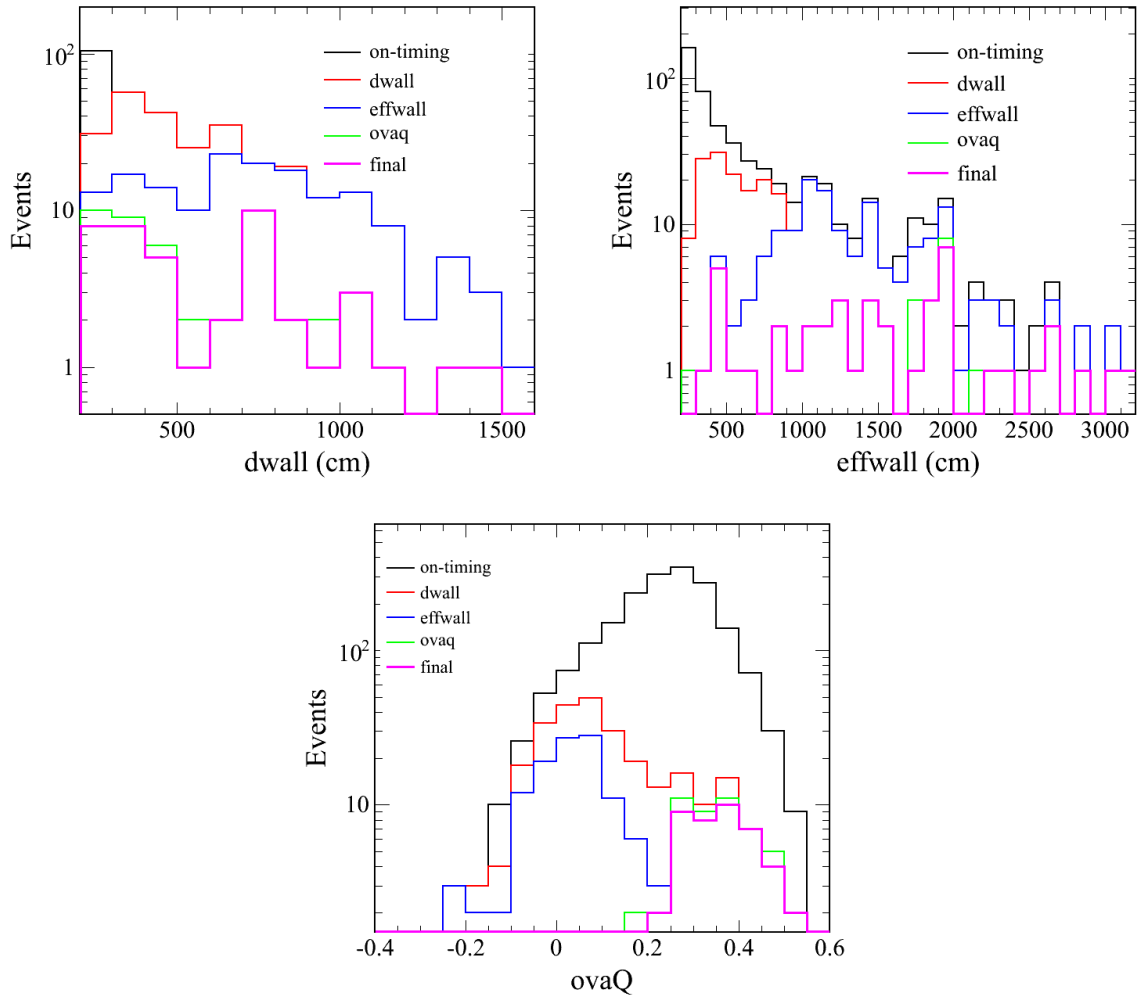

Figure 5.9: dWall (upper left) distribution, effWall (upper right) distribution and ovaQ (lower) distribution of the selected events at each selection process for the T2K Run1-3 data.

Comparison between expected events and observed events Table 5.4 shows the comparison between the numbers of events from the T2K spill data and the numbers of expected event at each selection process.

Table 5.5: Summaries of spectroscopic factors (SFs) of $1p_{3/2}$ hole state and γ-ray emission branching ratios (BRs) of the state. In the table, the values of NEUT default are listed in the row of "Before", and the values of the recent calculation are listed in the row of "Now".

	SF		γ-ray emission BR		SF×BR	
$1p_{3/2}$ nucleon hole	p	n	p	n	p	n
Before	0.435	0.375	93%	100%	0.40	0.38
Now	0.352	0.352	92%	87%	0.32	0.31
change ratio					-20%	-18%

5.2 Changes by updates of spectroscopic factors and branching ratio

As described in previous section, the spectroscopic factors (SFs) and the γ-ray emission branching rations (BRs) of $1p_{3/2}$ nucleon hole state are updated by the recent theoretical calculations [115]. Table 5.5 shows the SFs and BRs of the NEUT default (before) and the updated (now) in the simulation. The SF×BR of $1p_{3/2}$ decreases by 20% and 18% respectively for the proton and neutron hole states.

The NCQE events are separated into "primary γ-ray only", "secondary γ-ray only", and "both primary γ-ray and secondary γ-ray" as shown in Figure 5.20. The comparison of the reconstructed Cherenkov angle distributions of "primary γ only" events is shown in plot (i) of Figure 5.10. The expected number of "primary γ-ray only" events decreases by $\sim$ 23% after the updates. The expected number of "both primary γ-ray and secondary γ-ray" events decreases by $\sim$ 23% as shown in plot (iii) of Figure 5.10. Some of the primary γ-ray component in "both primary γ-ray and secondary γ-ray" events migrate into the "only secondary γ-ray" events after the updates. Then, the expected number of "secondary γ-ray only" increases $\sim$ 13% as shown in plot (ii) of Figure 5.10. As a result, the expected number of NCQE events decreases by 9.3% which is smaller than the decrease of the ratio of SF×BR by $\sim$18%.

Table 5.6: Summary of the expected numbers of events. In the table, the expected numbers using NEUT default and updated SR×BR are listed in the rows "Before" and "Now" respectively. The total events include the "NCQE" events and the "background" events.

	NCQE events	background events	total events
Before	38.4	17.3	55.7
Now	34.8	16.2	51.0
change ratio	-9.3%	-6%	-8.4%

We now check the changes of the total de-excitation γ-ray events, which include the NCQE events and the background events. Figure 5.11 shows the comparison of the Cherenkov angle distributions of total events. Since only the primary γ-rays production is updated, the multiplicity of γ-rays does not change significantly. The reconstruction of the Cherennkov angle depends on the multiplicity of γ-rays as described in Appendix

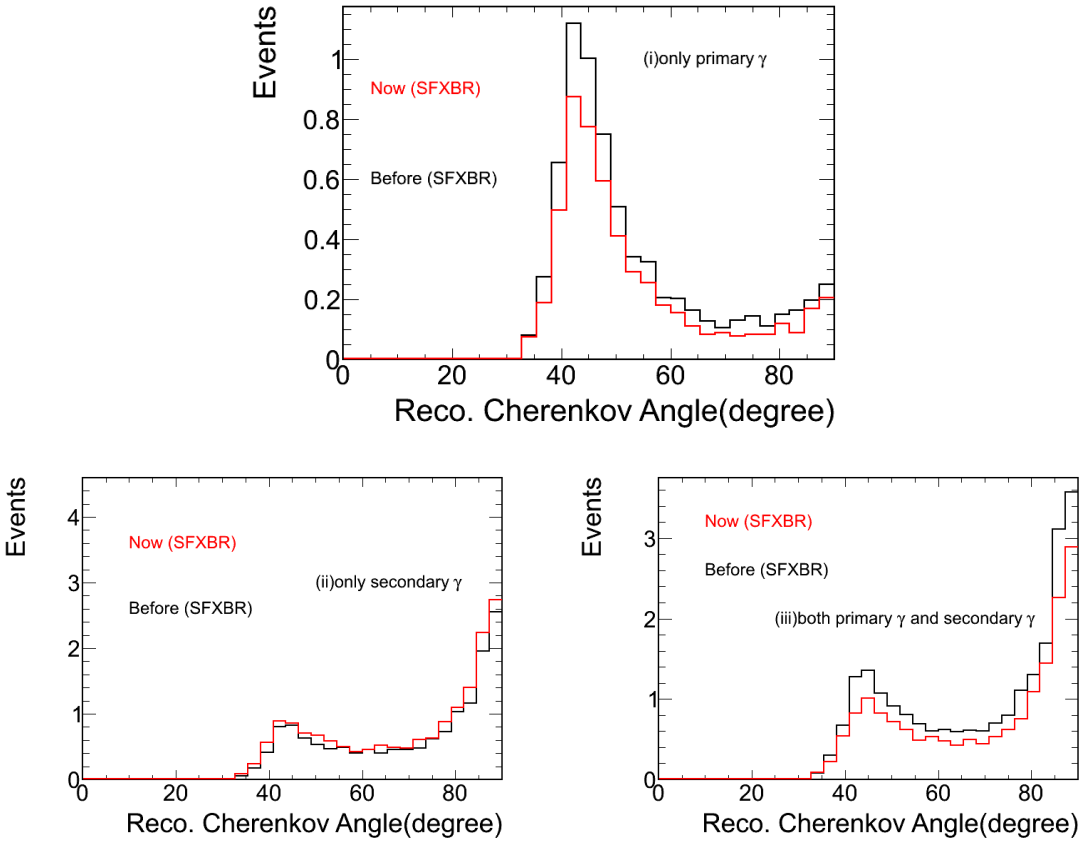

Figure 5.10: Cherenkov angle distributions of the NCQE events categorized by γ-rays. The black line shows the distribution using the NEUT default SR×BR (Before), and the red line shows the distribution applying the update SR×BR (Now). (i) The top plot is a Cherenkov angle distributions of "only primary γ-ray" events, which are from NCQE interactions. The main peak is located around 42°. The expected number of event decreases by $\sim$ 23% after the updates. (ii) The bottom left plot is a Cherenkov angle distributions of "only secondary γ-ray" events. The expected number of event increases by $\sim$ 13% after the updates. (iii) The bottom right plot is a Cherenkov angle distributions of "both primary γ-ray and secondary γ-ray" events. The expected number of event decreases by $\sim$ 23% after the updates.

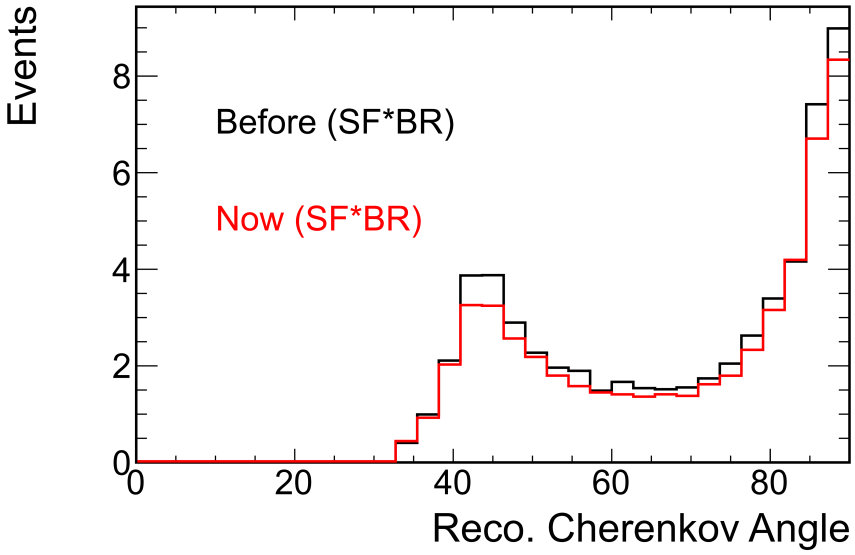

Figure 5.11: Cherenkov angle distributions of total events. The distribution using the NEUT default and updated SR×BR are indicated respectively by black (Before) and red (Now) lines. The expected number of total events decreases by 8% after the updates.

B.3. Therefore, the shape of the Cherenkov angle distribution is barely changed by the updates. Finally, the expected number of total events decreases by 8% after the updates as shown in Table 5.6.

5.3 Selection results

As shown in Table 5.4, 43 events are selected as the final de-excitation γ-ray candidates for the T2K RUN1-3 data, while the expected number of events is 51.0. Here, the comparisons between the data events and the expected events are described.

5.3.1 Vertex distribution

The vertex 2-D distributions of final candidate events inside the Super-K ID tank are shown in Figure 5.12. The vertex distribution is uniform inside fiducial volume.

5.3.2 Timing distribution

Figure 5.13 shows the ΔT_0 timing distribution of data events without the "on-timing" cut. It is clear that the event rates in the timing region of $\Delta T_0 \in (-2, 10)$ μsec are higher than the other off-timing region. We use the "on-timing" cut to remove the beam-unrelated backgrounds as mentioned previously.

Let us look at the details of the timing distribution, there is the clear structure of eight bunched as shown in Figure 5.14, where the timing region from -1μsec to $+5\mu$sec is shown. We expect that there are 3.6 events that outside the eight timing windows, and six events are found outside the eight timing windows, and the number is consistent with the expectations.

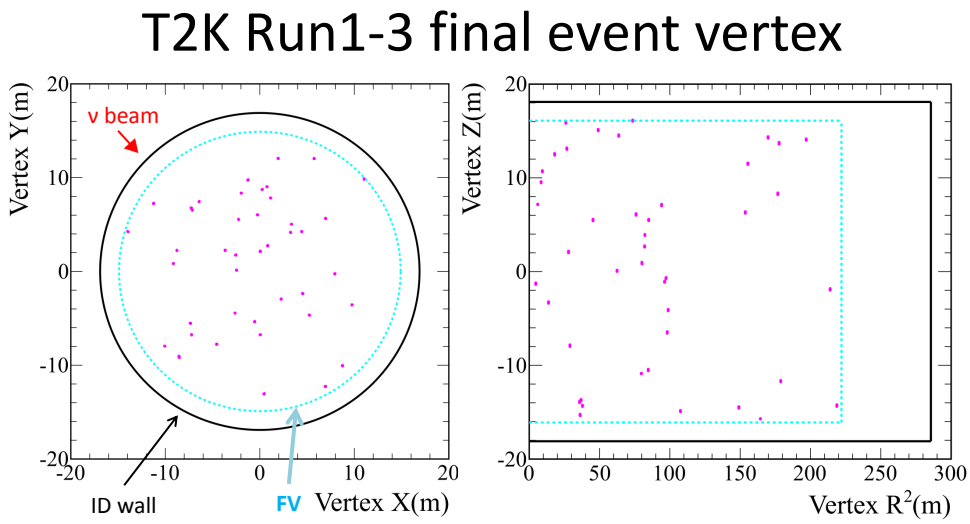

Figure 5.12: Vertex distribution of the de-excitation γ-ray candidate events inside the Super-K ID tank for T2K RUN1-3 data. The black lines are Super-K ID wall, and the blue dash lines are boundary of FV that is 2m distance inside the Super-K ID wall. X, Y, Z are the three orthogonal axises, and Z is the vertical axis. R^2 is distance from circle center, and that is equal to $X^2 + Y^2$.

Table 5.7: Summary of the numbers of the de-excitation γ-ray event candidates in every T2K RUN and the event rates per 10^{19} POT.

T2K Run	RUN1	RUN2	RUN3
Number of event	3	17	23
Event rate per 10^{19}POT	0.928	1.534	1.457

Now, we check the residual time of the event, that is the relative time to the nearest bunch center. Figure 5.15 shows that the selected events are distributed closely to the bunch centers, and the R.M.S. of the "on-timing" events is $\sim$ 25 ns.

5.3.3 Event rates

The event rates for every MR runs (main ring) and every T2K runs are shown in Figure 5.16, and the summary of the average rates of each T2K RUN is in Table 5.7. Forty three events are found with the accumulated POT of 30.1×10^{19}. Therefore, the average event rate is 1.43 event per 10^{19} POT.

Kolmogov-Smirnov test

The Kolmogov-Smirnov test (K-S test)[139, 141] is used to check the data event rate, which is supposed to be proportional to the T2K proton on target (POT). The cumulative distribution function (cdf) for the event rate is supposed to be a linear function increasing with the accumulative POT number. Figure 5.17 shows the number of γ-ray candidate events as a function of accumulative POT, and the red line is the cumulative probability

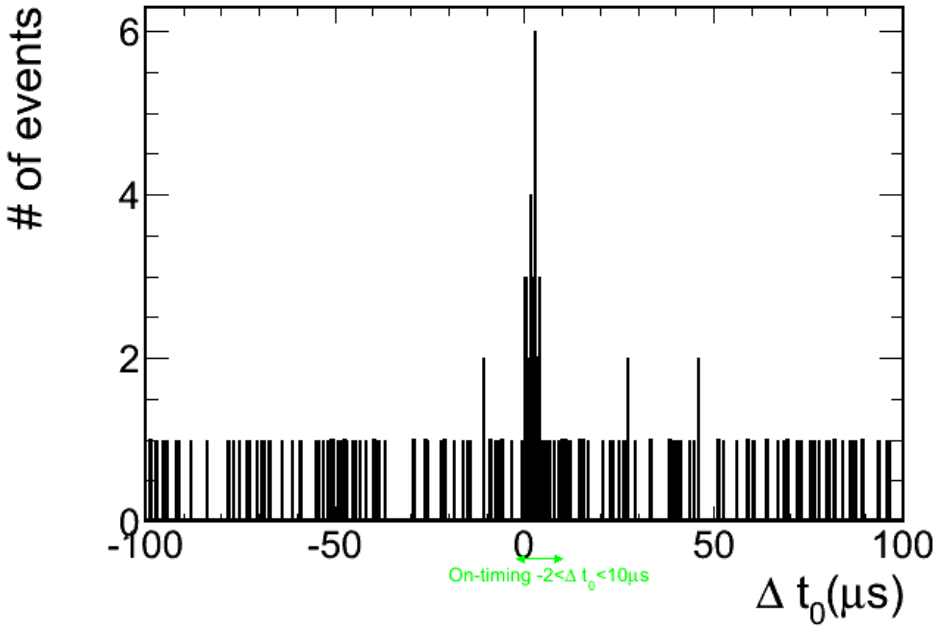

Figure 5.13: The timing distribution of events that are selected without "on-timing" cut for T2K RUN1-3 data example. The green arrow region is timing region of $\Delta T_0 \in (-2, 10)\mu$s.

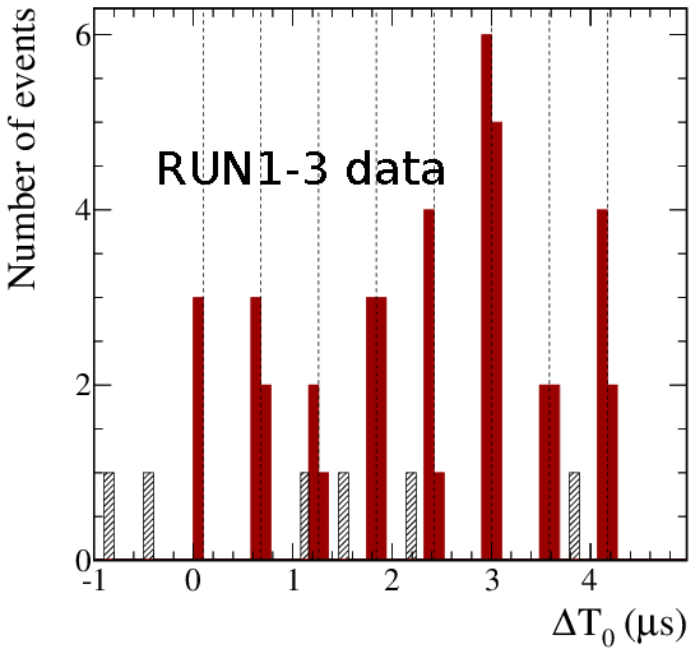

Figure 5.14: The ΔT_0 distribution of candidate events. The bunch centers are denoted as eight vertical dashed lines. The on-timing and off-timing events are shown in solid and hashed, respectively. Six off-timing events with hashed histogram is consistent with the expectation number of off-timing events which is 3.6 for the time integral of (-1 μs,5 μs).

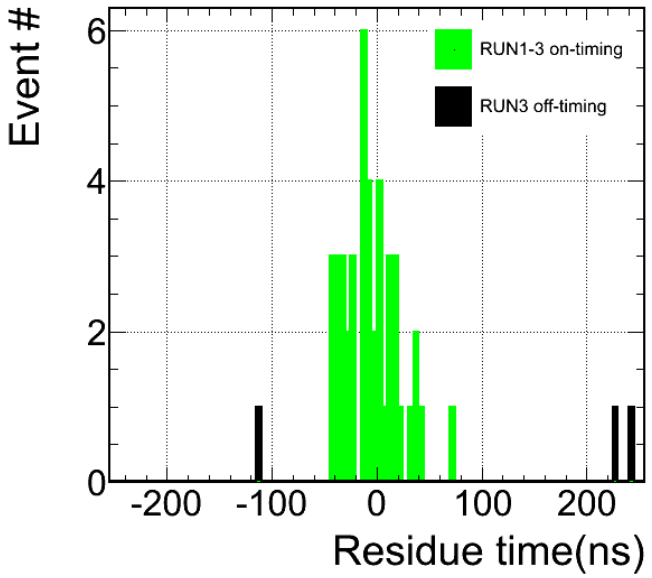

Figure 5.15: The residual timing distribution of events. The residual timings are relative to each nearest bunch center. T2K RUN1-3 candidate events are stacked within ±100 ns, and the RMS of all on-timing events are ∼25 ns. Three events with black soild are off-timing events, which is statistically consistent with 1.8 off-timing expected events for the time integral.

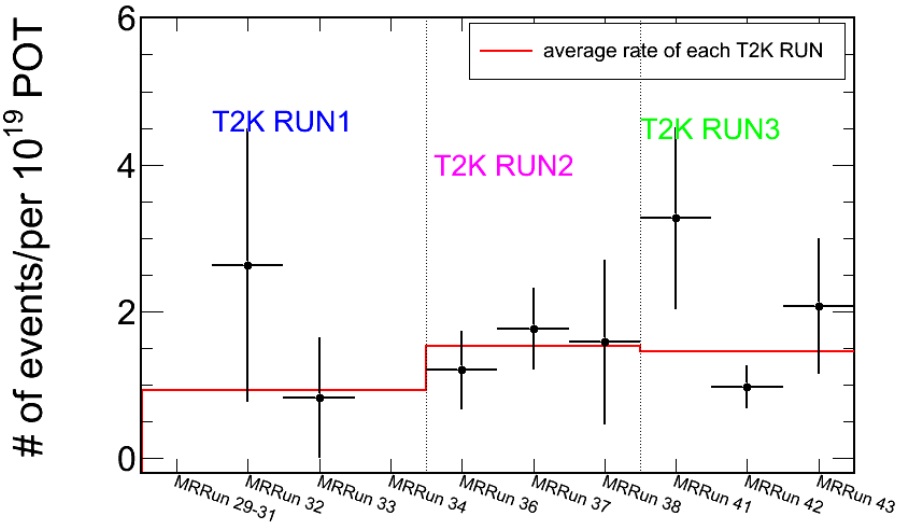

Figure 5.16: Event rate of each MR Run normalized by 10^{19} POT. The red histogram is representing the average event rates of each T2K RUN.

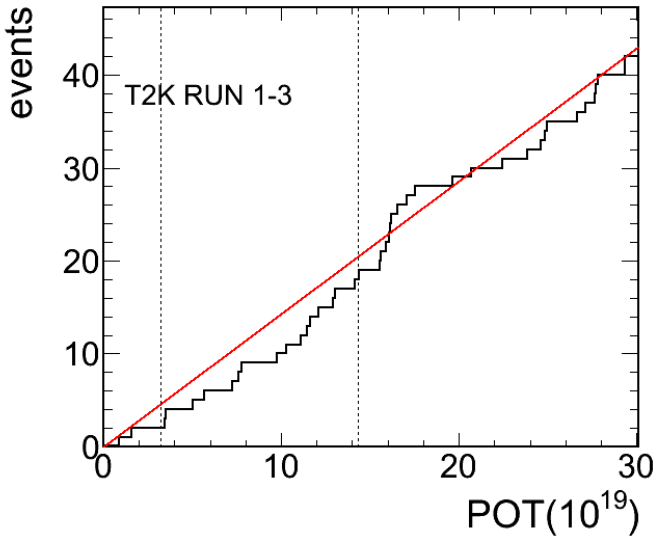

Figure 5.17: The de-excitation γ-ray candidates as a function of the accumulative POT for T2K RUN1-3. The red line is supposed as the cumulative probability distribution function for the uniform accumulative rate. The vertical dash lines are showing the boundaries of each T2K RUN.

distribution function for the uniform accumulative rate. After the normalization of the vertical axis by the number of candidate events, the D value[3] of K-S test for 43 candidates is calculated as 0.0924. As a result, the K-S probability (significance) is 0.839, which means we do not reject the uniform distribution hypothesis at the 83.9% level.

5.3.4 Energy and other parameters distributions

Table 5.8: Summary of the expected number of event of T2K RUN1-3. The NCQE signal is about $\sim$ 70% of the final event candidates.

T2K Run	RUN1-3	Fraction
NCQE	34.8	68.2%
NCothers	13.0	25.5%
CC	2.0	3.9%
Beam un-related	1.2	2.3%
Total	51.0	–

After all the selections, the numbers of expected events for each neutrino reactions are summarized in Table 5.8. The NCQE signal is expected to be $\sim$ 70% fraction of the total candidate events, while beam-unrelated background is only about 2%. The observed number of candidates events is 43 which is less than the expected number of candidate events of 51.0. The comparisons between data events and expected events are discussed as follows.

[3]D is the maximum value of absolute distance between two cumulative distribution functions.

Energy distribution The reconstructed energy distributions of the data candidate events and the expected candidate events is shown in Figure 5.18. The peak of the energy distribution is near 5 MeV, which is close to the expected 6 MeV prompt γ-ray. There are events with multiple γ-rays that originate from the contribution of secondary γ-rays overlapping with the primary γ-rays, and the tail in the reconstructed energy distribution extends to high energy region.

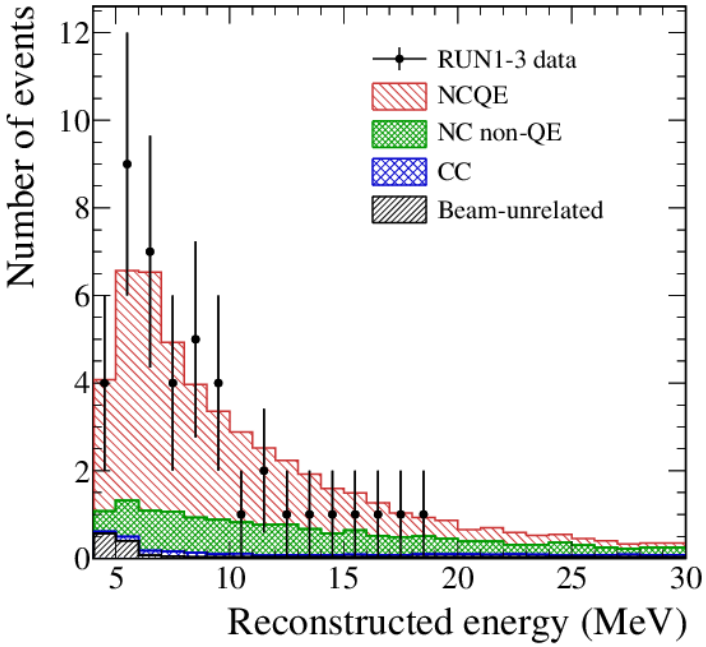

Figure 5.18: Comparison of the reconstructed energy spectrum between the expected events (histogram) and the data events(dots).

Cherenkov angle distribution Cherenkov angle distributions are shown in Figure 5.19. The expected number of candidate events of MC simulation is larger than that of data events near 90 degree, while the expected number of candidate events are smaller than that of data events near 42 degree. As mentioned previously, the Cherenkov angles of multi-gamma events are reconstructed near 90 degree. Because of de-excitation γ-ray production characteristics, most primary γ-rays after the NCQE reactions are produced as single γ-ray as discussed in Chapter 4.3.2. Most secondary γ-rays in GEANT3 simulation are produced as multiple γ-rays as shown in Figure 4.14. Figure 5.20 shows that the most events with angle near 90 degree have secondary γ-rays. The GCALOR simulator in GEANT3 is used to simulate the free nucleon-oxygen nucleus interactions that produce secondary γ-rays. However, there is no previous experiment data about γ-rays produced at neutron-water interactions. Therefore, we do not confirm the γ-ray multiplicities in GCALOR. There is an experiment proposal to observe the de-excitation γ-rays from water target using semi-monochromatic neutron beam in Research Center for Nuclear Physics (RCNP). The experiment proposal will be described in Appendix H. The secondary γ-ray multiplicities are expected to be confirmed in near future using the results of experiment at RCNP.

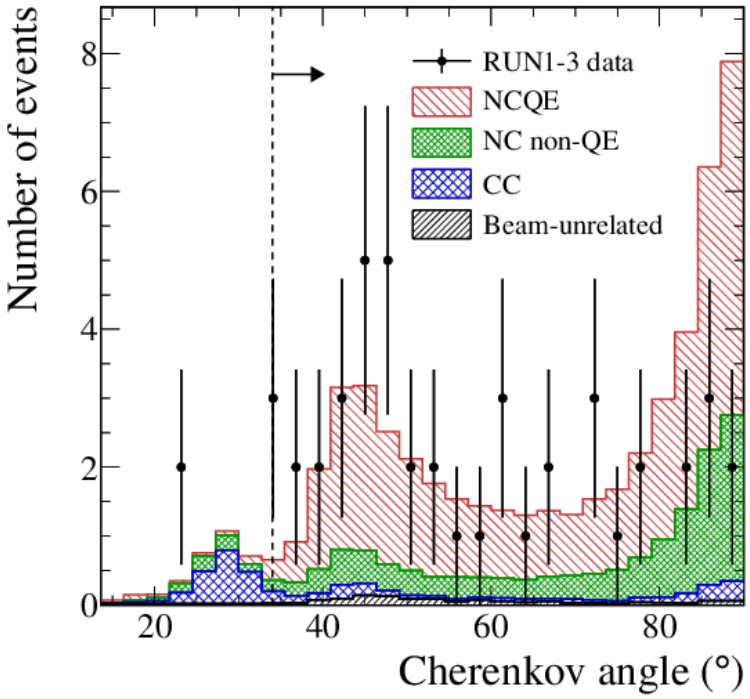

Figure 5.19: Comparison of Cherenkov angle distribution between the expected events and data events. The peak near 28^o is composed of CC background events, thus the events with the angle less than 34 degree are removed.

dWall, effWall and ovaQ distributions There is no statistically-significant difference in the distribution of the other parameters between the candidate events of the data events and those of the expected events as shown in Fig. 5.21.

5.3.5 Summary

This section describes the 43 observed events and the expected events as follows: The vertex distribution of the data candidate events is uniform. The event rate of T2K RUN1-3 is 1.43 events per 10^{19} POT, and the event rate is proportional to the T2K POT with 83.9% significance.

Comparing the events with the event prediction shows no statistically-significant difference between the data candidate events and the expected candidate events in most parameter distributions, except the Cherenkov angle distribution. The discrepancy in the Cherenkov angle distribution is supposed due to the the poor information about secondary γ-ray production, and a neutron-water experiment at RCNP is expected to correct the simulation in near future.

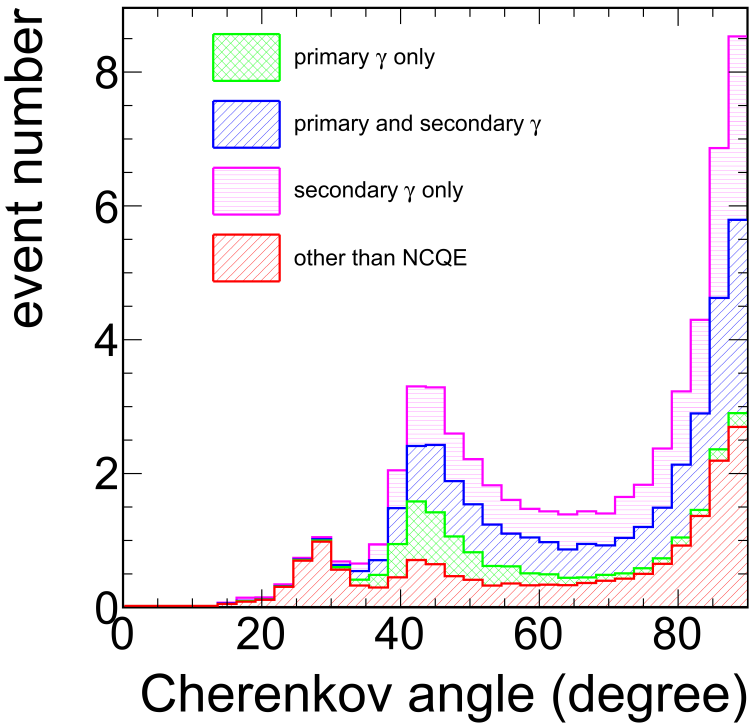

Figure 5.20: Cherenkov angle distribution of expected beam-related events, that is stacked by NCQE events and other reaction events. The green hatched histogram, blue hatched histogram and pink hatched histogram represent the NCQE events with "only primary γ-ray", "both primary γ-ray and secondary γ-ray", and "only secondary γ-ray" respectively. Near 90 degree, most of NCQE events have secondary γ-rays.

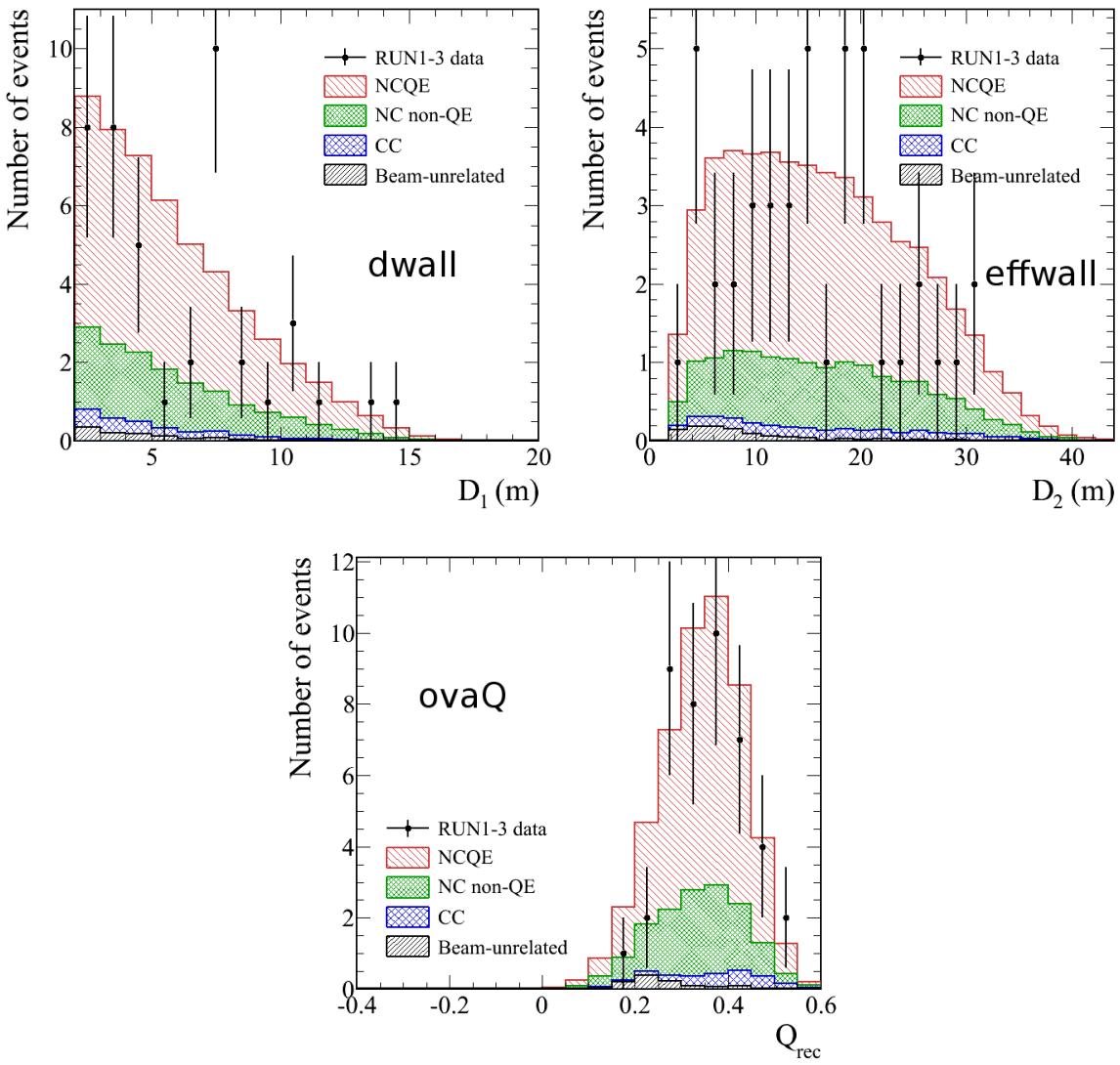

Figure 5.21: Comparison of the dWall, effWall and ovaQ distributions between the expected events (histogram) and the data events (dots) of T2K RUN1-3.

Chapter 6

Systematic Errors

In this chapter, the uncertainty on the NCQE cross-section measurement is described. The systematic uncertainties come from the following error sources: 1.Neutrino beam flux 2.Neutrino cross-section 3.Primary γ-ray production 4.Secondary γ-ray production 5.Detector response 6.Neutrino oscillation parameters. Table 6.1 summarizes the details for each error source. The statistical uncertainty is calculated using Poisson counting statistics. Finally, toy MC experiments are used to evaluate the combined uncertainty on the NCQE cross-section measurement.

Table 6.1: Summary of sources of systematic uncertainty.

Categories	Sources details	Prediction details
Neutrino beam flux	Hadronic interactions, proton beam alignment, off-axis angle, horn alignment, horn field, MC statistics	Sec. 4.2
Neutrino Cross-section	Parameters for background neutrino cross-section models: M_A^{QE}, M_A^{RES}, CCQE norm., CC1π res norm., NC1π res norm., etc.	Subsec. 4.3.3
Primary γ production	Spectroscopic factors, and γ-ray emission branching ratios	Subsec. 4.3.2 and Subsec. 4.4.1
Secondary γ production	Differences between simulators	Subsec. 4.4.1
Detector response	Energy resolustion, energy scale, trigger efficiency, dWall, effWall, ovaQ, Pre-activity, Cherenkov angle	Sec. 5.1 Appendix C, and Appendix D
Oscillation parameters	θ_{23} and Δm^2_{23}	Ref. [63]

In the following sections, the estimation of the uncertainties due to each source are described.

6.1 Neutrino beam flux and neutrino cross-sections

The sources of uncertainty due to flux are the hadron productions and the T2K beam parameters. The hadron productions include the production cross-sections, the pion and

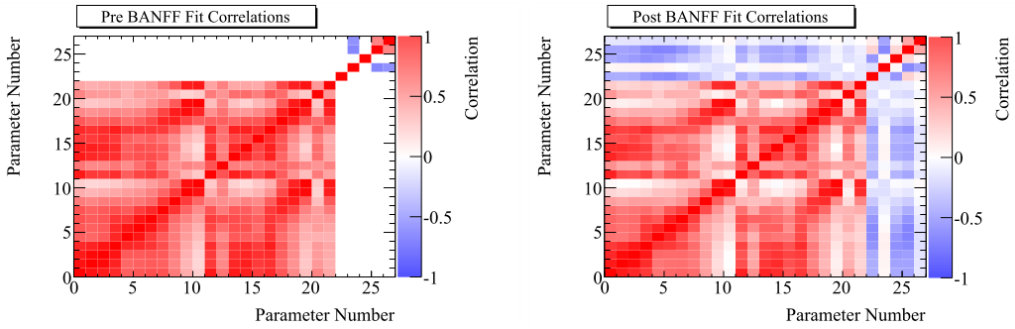

Figure 6.1: The left plot shows the correlation matrix for the flux and cross-section parameters with only constrains from the external experiments (non-ND280). The correlation matrix that includes a fit of the ND280 data is shown in the right plot [129]. The parameters are summarized in Table 6.2.

the kaon production multiplicities. As described in Sec. 4.2, the uncertainty on the hadron productions is corrected by the results of CERN NA61/SHINE experiment. The beam parameters include the proton beam position and direction, the horn current and alignment, the target alignment, and the neutrino beam intensity. The uncertainty due to the cross-sections of the background interactions from the uncertainties on the parameters of each cross-section model.

To get a precise prediction on the neutrino flux and on the neutrino interaction cross-sections for the neutrino oscillation analysis, the T2K experiment uses the ND280 measurement and the following set of external experimental results: CERN NA61/SHINE, MiniBooNE, SciBooNE, NOMAD. Hence the size of uncertainties is driven by these measurements. The prediction and the uncertainty of the neutrino flux are given in bins of neutrino energy in Table 6.2. Fourteen parameters for cross-section models which are used to predict the background interaction cross-sections such as CCQE, CC1π (res), CC1π coherent, NC1π (res), NC1π coherent etc. Table 6.2 shows the errors of the input parameters for the cross-section models, e.g axial mass, normalization parameters for each type of reactions, and W shape[1] [129]. Among the fourteen parameters, the five cross-section paramteres (M_A^{QE}, M_A^{RES}, CCQE norm., CC1π res norm., and NC1π res norm.) are also measured by ND280, and are summarized in Table 6.2. Figure 6.1 represents this correlation matrices obtained only with the external experiment constrains (left) and with ND280 data in addition to the external constrains (right). The correlations between flux and cross-section, after inclusion of ND280 data are negative, which means they are anti-correlated [129].

Since the ND280 detectors do not yet provide a measurement of the NCQE reaction, we use only the external experiment data to correct and constrain the flux and cross-section prediction. One observes that there is no correlation between fluxes and cross-sections. Table 6.2 summarizes the errors of the parameters for the flux and the cross-section models, and the errors are obtained from the non-ND280 matrix shown in the left plot of Figure 6.1.

In the measurement of the NCQE cross-section, we only assign the uncertainty due to flux for the NCQE events. For the background events, both the flux and cross-section

[1]The parameter "W shape" provides a way to modify the shape of the pion momentum distribution in NC1π (res) reaction, that shows a poor agreement with MiniBooNE data. This parameter represents the decay width of the resonant pion production.

Table 6.2: The matrix binning (0∼25) for the neutrino beam flux and the parameters for the cross-section models at Super-K. The error of the binning or parameters of the non-ND280 matrix are used to assign the uncertainties of the events. The bottom nine parameters for cross-section are not listed in the matrix, and the nominal values and errors of the parameters are listed.

Parameter name	bin No.	Error	Contents
neutrino beam flux ν_μ	$0 \sim 10$		bining: 0-0.4, 0.4-0.5, 0.5-0.6, 0.6-0.7, 0.7-1.0, 1.0-1.5, 1.5-2.5, 2.5-3.5 3.5-5.0, 5.0-7.0, 7.0-30.0, (GeV)
neutrino beam flux $\overline{\nu}_\mu$	$11 \sim 12$		bining: 0-1.5, 1.5-30.0 (GeV)
neutrino beam flux ν_e	$13 \sim 19$		bining: 0-0.5, 0.5-0.7, 0.7-0.8, 0.8-1.5 1.5-2.5, 2.5-4.0, 4.0-30.0, (GeV)
neutrino beam flux $\overline{\nu}_e$	$20 \sim 21$		bining: 0-2.5, 2.5-30.0, (GeV)
M_A^{QE}	22	0.45GeV	axial mass for axial vector form factor of CC quasi-elastic
M_A^{RES}	23	0.221GeV	axial mass for axial vector form factor of CC1π (res) or NC1π (res)
CCQE norm. ($E_\nu < 1.5$GeV)	24	0.11	normalization value for CCQE, $E_\nu < 1.5$GeV
CC1π(res) norm. ($E_\nu < 2.5$GeV)	25	0.32	normalization value for CC1π (res), $E_\nu < 2.5$GeV
NC1π(res) norm.	26	0.33	normalization value for NC1π (res)
Parameter name	normal value	Error (1σ)	Contents
CCQE norm. ($1.5 < E_\nu < 3.5$GeV)	1	30%	normalization value for CCQE, $1.5 < E_\nu < 3.5$GeV
CCQE norm. ($E_\nu > 3.5$GeV)	1	30%	normalization value for CCQE, $E_\nu > 3.5$GeV
CC1π(res) norm. ($E_\nu > 2.5$GeV)	1	40%	normalization value for CC1π (res) $E_\nu > 2.5$GeV
CC coherent norm.	1	100%	normalization value for CC coherent
CC other shape	0	40%	error for CC others σ =CC other shape/E_ν
CC ν_e norm.	1	6%	normalization value for ν_e CC interaction
NC coherent norm.	1	30%	normalization value for NC coh
NC other norm.	1	30%	normalization value for NC other
W shape	87.7 MeV	53%	decay width of resonance pion production

Table 6.3: The uncertainties due to the neutrino fluxes and cross-sections. The NCQE cross-section is the goal of this analysis, and therefore the uncertainty due to the NCQE cross-section is not assigned here.

Interaction	Flux	Cross-section
NCQE	11%	–
NCothers	10%	18%
CC	12%	24%

uncertainties are assigned. The uncertainties due to the flux and the cross-section for the neutrino interaction events are summarized in Table 6.3.

6.2 Primary Gamma Production

In the primary γ-ray production, the sources of uncertainty are the spectroscopic factors and the γ-ray emission branching ratios which are explained in Subsection 4.3.2 and Subsection 4.3.3 respectively.

6.2.1 NCQE interaction

In Subsection 4.3.2, four kinds of single hole states were mentioned for the ^{15}O nucleus: $1p_{1/2}$, $1p_{3/2}$, $1s_{1/2}$, and other continuum hole states. The removal energies of each single hole state is E($1p_{1/2}$) <E($1p_{3/2}$) <E($1s_{1/2}$) <E(continuum). Table 6.4 summarizes the uncertainties due to each single hole state, the multi-hole states, and the error due to the neglecting of the γ-rays having an energy E_γ <3 MeV are listed in the table.

For the NCQE events, the error sources of each hole state in $^{16}_{8}$O and E_γ <3 MeV simulation are discussed in the following paragraphs.

Table 6.4: The uncertainties for each source of primary γ-ray production. The uncertainty for NCQE events due to primary γ-ray production is 10%.

Source	Uncertainty (%)
$1p_{3/2}$	3
$1s_{1/2}$	1
continumm states	3
multi-holes	9
E_γ <3 MeV	1
total	10

$1p_{3/2}$ hole state Most primary γ-rays are produced from $1p_{3/2}$ hole states. The uncertainties on the probabilities for the three energy levels that make up the $1p_{3/2}$ nucleon hole state are quoted as 5.4%. This value is obtained from the ^{16}O(e,e'p)^{15}N experiment [123]. As mentioned in Table 4.3, the errors on the branching ratios for the four decay modes (9.93 MeV, 5.27+5.30 MeV, 6.32 MeV, 7.30 MeV) of the 9.93 MeV energy level are 1.9%, 1.5%, 1.2% and 0.8% respectively. If the probabilities for the 6.32

MeV and 9.93 MeV energy levels and BRs for the four decay modes in 9.93 MeV energy level are increased by the error size, the expected number of NCQE events increases by 3%. Thus, the uncertainty due to primary γ-ray production from the $1p_{3/2}$ nucleon hole state is set to $\pm$3%.

$1s_{1/2}$ hole state The γ-ray emission branching ratios of the $1s_{1/2}$ nucleon hole state are summarized in Table 4.4 [125]. The branching ratios to emit γ-rays with $E_\gamma > 6$ MeV and 3 MeV$\leq E_\gamma \leq$6 MeV are $15.6 \pm 1.3^{+0.6\%}_{-1.0\%}$ and $27.9 \pm 1.5^{+3.4\%}_{-2.6\%}$ respectively. If the branching ratios for γ-ray emission are increased by their error sizes, the expected number of NCQE events is increased by $\sim \pm 1\%$ with respect to the nominal number of events. The uncertainty due to the $1s_{1/2}$ hole state is therefore set to $\sim \pm 1\%$.

continuum hole states As mentioned in Subsection 4.3.2, the nominal simulation assumes that no γ-ray is produced from the hole states deeper than $1s_{1/2}$ (continuum states). To estimate the uncertainty due to the continuum hole states, we compare the expected number of NCQE events with zero branching ratios from such states (nominal) to the expected number of the events where the γ-ray emission branching ratio for the continuum states is assumed to be the same as the branching ratio of the $1s_{1/2}$ hole state. The comparison shows that the expected number of NCQE events changes by less than 3%. The uncertainty due to the continuum hole states is therefore set to $\pm$3%.

multi-holes states It is expected that about 40% of the NCQE events have multi-nucleons knocked out. Since there is no experimental data to measure the de-excitation γ-rays from the multi-hole states, we assume the simulation to be the same as the single hole case. To obtain the uncertainty due to the multi-hole states, we compare the expected number of events assuming the default single hole simulation with the expected number of events assuming that no γ-ray is produced from the multi-holes states. The difference between the two expected numbers of NCQE events is 9%, so the uncertainty due to the multi-hole states is taken to be 9%.

$E_\gamma < 3$ MeV Because the γ-rays with energy less than 3 MeV produced from $1s_{1/2}$ hole states do not pass the trigger, they do not affect the expected number of events. The de-excitation γ-rays with E_γ <3 MeV are not simulated. To estimate the uncertainty due to this neglected γ-rays, we compare the expected number of NCQE events removing the γ-rays with energy less than 3 MeV in simulation (nominal) to the expected number of events assuming the branching ratios from Table III in Ref. [140]. The change of the expected number of NCQE events is within 1%, so the uncertainty due to the γ-rays is set to 1%.

Summary of NCQE reaction The uncertainties of each source in primary γ-ray production are summarized in Table 6.4. Since the error sources are indenpendent with each other, they are summed up in quadrature to obtain the total uncertainty. As a result, the uncertainty of NCQE events due to the primary γ-rays production is determinated to be 10%. The uncertainty of multi-holes states dominates in the uncertainty due to the primary γ-ray production.

6.2.2 NC1π interaction

The de-excitation γ-rays are produced from the π absorption after NC1π reactions, where the γ-ray emission branching ratios for the default event estimation is listed in Table 4.5. To evaluate the uncertainty due to primary γ-ray production for NC1π events, we compare the expected number of events assuming the default branching ratios with the expected number of events under the following two scenarios: first, for zero γ-ray emission branching ratios in π absorption (calculated resulting in a 0.6% decrease from the default case); second, for γ-ray emission branching ratios set to the same values as these of NCQE interactions (the expected number of events increases by 2.5% from the default case). Hence, the uncertainty of NC background events due to primary γ-ray production is set to the maximum deviation which is equal to 3%.

6.3 Secondary Gamma Production

Table 6.5: Summary of the simulators used for the nominal expected events and the alternative expected events.

Nominal simulation		
neutron energy region	$T_n < 20$MeV	20MeV$\leq T_n < 3.5$GeV
simulator	MICAP	NMTC
Alternative simulation		
neutron energy region	$T_n < 30$MeV	30MeV$\leq T_n$
simulator	MICAP	NEUT

In Subsection 4.4.1, the simulation processes for secondary γ-ray production were described. In Table 4.7, the NMTC simulator and the MICAP simulator [137] are used to simulate the hadronic interactions induced by free nucleons. Since there are no experimental constrain on γ-rays induced by neutron-oxygen ($n-^{16}$O) interaction, the uncertainty due to secondary γ-rays is calculated by comparing the expected number of events using the different simulation models. Here, we make an alternative estimation of the expected number of events with different simulators. Table 6.5 summarizes the simulators used for the nominal (default) estimation and the simulators used for the alternative estimation.

Table 6.6: The percentage difference between the expected numbers of NCQE (NC1π) events for the default simulation and the alternative simulation. The uncertainty of NCQE (NC1π) events due to secondary γ-ray production is set to 12.6% (13.2%).

Interaction	$T_n < 30$MeV	$T_n > 30$MeV	Total
NCQE	2.8%	12.3%	12.6%
NC1π	2.9%	12.9%	13.2%

The resulting difference between the expected number of events with the nominal (default) simulation and the expected number of events with the alternative simulation are listed in Table 6.6. In the region where neutrons have a kinetic energy $T_n > 30$MeV, the average energy of the simulated secondary γ-rays by the NEUT simulator is higher

than the average energy of the secondary γ-rays using NMTC. The variation of the expected number of events induced by the neutron with $T_n > 30$ MeV is $\sim 12\%$, and this error dominates the uncertainty due to secondary γ-ray production.

6.4 Detector response

The uncertainty due to the detector response is based on the Super-K detector properties that include the following error sources: energy scale, energy resolution, trigger efficiency, dWall cut, effWall cut, ovaQ cut, pre-activity cut, and Cherenkov angle cut [86]. The error size is measured during the Super-K calibration as described in Appendix C. As a result, Table 6.7 shows the uncertainties due to each error source. The total uncertainty due to the detector response is calculated as 2.2%.

Table 6.7: Summary of the uncertainties of each source in the detector response. The uncertainty due to the detector is calculated to be 2.2%.

Source	Uncetainty (%)
Energy scale	0.4
Energy resolution	1
Trigger efficiency	1
dWall	1
effWall	0.5
ovaQ	0.5
Pre-activity	<0.1
Cherenkov angle	1
Total	2.2

6.5 Oscillation parameters

For the CC background events, there is an uncertainty due to the neutrino oscillation parameters. From the T2K ν_μ disappearance results [63], the oscillation parameters with 68% confidence level errors are $\Delta m^2_{32} = 2.443^{+0.18}_{-0.17}$, and $\sin^2 2\theta_{23} = 1.0^{+0.00}_{-0.02}$.

The uncertainties of the expected number of CC events due to the oscillation parameters $(\Delta m^2_{32}, \sin^2 2\theta_{23})$ are shown in Table 6.8. The effects of these two parameter uncertainties on the expected number of events are uncorrelated.

Table 6.8: Summary of the uncertainties on the CCQE events and the CCothers events due to the oscillation parameters.

interactions	$+\Delta m^2_{23}$		$-\Delta m^2_{23}$		$\sin^2 2\theta_{23}$	
CCQE	+0.077	+5.9%	-0.12	-8.9%	+0.027	+2.0%
CCothers	-0.014	-2.6%	+0.13	+24.6%	+0.14	+27.5%
CC total	+0.064	+3.5%	+0.009	+0.5%	+0.17	+9.2%

The total uncertainty for CC events due to the oscillation parameters is 10%. Since only 4% of the number of de-excitation γ-ray events comes from CC event, the uncertainty due to the oscillation parameters is 0.4%.

6.6 Uncertainty of beam-unrelated events

The uncertainty on the number of beam-unrelated background events is based on the statistical uncertainty of accidental events during 23 hours SK live-time data. Total off-timing $\Delta T_0 \in (-500\ \mu\text{s}, -5\ \mu\text{s})$ of the T2K spill data is about 23 hours.

6.7 Summary of uncertainties

Table 6.9: Summary of the systematic uncertainties on the expected number of NCQE events and background events.

Systematic error	Signal	Background		
interactions	NCQE	NCothers	CC	beam-unrelated
fraction of events	68%	25%	4%	2%
Flux	11%	10%	12%	–
Cross-section	–	18%	24%	–
Primary γ production	10%	3%	6%	–
Secondary γ production	13%	13%	7.6%	–
Detector response	2.2%	2.2%	2.2%	–
Oscillation parameters	–	–	10%	–
Total systematic error	20%	25%	30%	0.8%

Table 6.9 summarizes the systematic uncertainties from each error source. They are estimated based on the variances for the expected numbers of NCQE events and background events. Because the de-excitation γ-ray events induced by true NCQE reactions is 69% of the total number of the selected γ-ray events, the 20% uncertainty on the NCQE events dominates the uncertainty on the NCQE cross-section measurement. Among the error sources considered in estimation for the NCQE events, the uncertainty due to the secondary γ-ray production is largest. A future experiment at RCNP is expected to reduce this uncertainty due to secondary γ-ray production, and the proposal is described in Section H. The uncertainty due to the neutrino flux for the NCQE events is 11% and is constrained by the CERN NA61 experiment. T2K has a plan to include additional NA61 results to give a stricter constraint on the error size in future. The uncertainty due to primary γ-ray production is 10%, and is dominated by the uncertainty on the γ-rays produced from the multi-holes states (9%). The uncertainties of the NCothers events and CC events are 25% and 30% respectively, and the fraction of the beam-related background events (NCothers+CC) is $\sim$30%. Therefore, the uncertainties of the NC other events and CC events are minor in the NCQE cross-section measurement.

The calculation of the NCQE cross-section including each uncertainty (see Equation 7.1) is obtained by shifting an error envelop that will include the uncertainties from each error source. The details of the method are described in Appendix F.

Chapter 7

Result

We use the de-excitation γ-ray event rate induced by NCQE reactions to measure the NCQE cross-section value $\sigma_{\nu,NCQE}$. The flux-averaged cross-section $< \sigma^{obs}_{\nu,NCQE} >$ value is measured by scaling the theoretical flux-averaged cross-section $< \sigma^{theory}_{\nu,NCQE} >$ as follows:

$$< \sigma^{obs}_{\nu,NCQE} >= \frac{N^{obs} - N^{exp}_{bkg}}{N^{exp} - N^{exp}_{bkg}} < \sigma^{theory}_{\nu,NCQE} > \tag{7.1}$$

where the observed number of events is N^{obs}, which includes the NCQE signal and the background events. The expected number of beam-related background events and beam-unrelated background is written as N^{exp}_{bkg}, which is $\sim 30\%$ of total events. N^{exp} is the expected number of total events, and $N^{exp} - N^{exp}_{bkg}$ is equal to $N^{exp}_{\nu,NCQE}$. The expected number of backgrounds N^{exp}_{bkg} is written as

$$N^{exp}_{bkg} = N^{exp}_{beam-unrelated} + N^{exp}_{NCothers} + N^{exp}_{CC} + N^{exp}_{\overline{\nu}} \tag{7.2}$$

$N_{beam-unrelated}$ is the expected number of beam-unrelated events which are from radioactive impurities in the detector wall and the PMTs. $N_{NCothers}$ is the expected number of neutral current background events. N_{CC} is the expected number of charge current background events. $N^{exp}_{\overline{\nu}}$ is the expected number of events which are induced by anti-neutrinos.

In the following sections, we will discuss the details of cross-section calculation from the observed number of events N^{obs}.

7.1 Measurement of ν NCQE cross-section

Theoretical NCQE cross-section

The flux-averaged NCQE cross-section $< \sigma^{theory}_{\nu,NCQE} >$ is calculated as follows

$$< \sigma^{theory}_{\nu,NCQE} >= \frac{\sum_{E_\nu=0GeV}^{10GeV} \sum_i r_i \frac{d\Phi_i(E_\nu)}{dE_\nu} \Delta E_\nu \times \sigma^{theory}_{\nu,NCQE}(E_\nu)}{\sum_{E_\nu=0GeV}^{10GeV} \sum_i r_i \frac{d\Phi_i(E_\nu)}{dE_\nu} \Delta E_\nu} \tag{7.3}$$

where E_ν is the neutrino energy, and we sum up every energy bin from 0 to 10 GeV, and $\sigma^{theory}_{\nu,NCQE}(E_\nu)$ is the theoretical NCQE cross-section from Ref. [115]. The r_i is the P.O.T. fraction for i-th T2K RUN, and $i = 1 \sim 3$. The combination of ν_μ, ν_e and $\overline{\nu}_\mu$ flux is denoted as $\Phi_i(E_\nu)$.

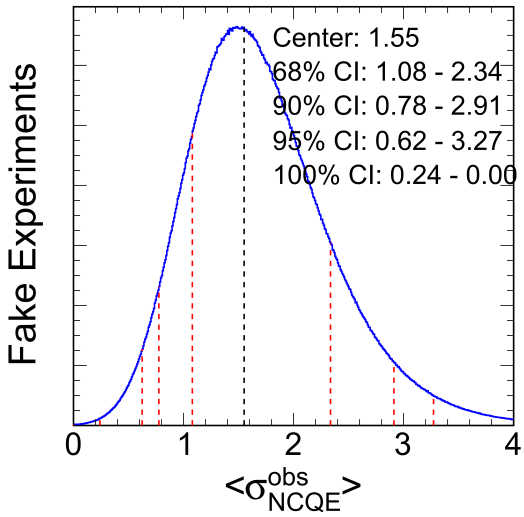

Figure 7.1: The NCQE cross-section distribution for T2K RUN1-3 observation is made using toy experiments. The details of toy experiments are in Appendix F. The vertical black dashed line shows the center of the integral area, and that represents the center value for the cross-section result as $1.55 \times 10^{-38}\mathrm{cm}^2$. The red dashed lines denote the bondaries of α% C.L. region, which is calculated by the α% fraction of integral area from the center value. Here, we calculate the fraction of integral area as $\alpha = 68, 90, 95, 100$. As a result, the 68% confidence interval is $(1.08,2.34)\times10^{-38}\mathrm{cm}^2$, and the 90% confidence interval is $(0.78,2.91)\times10^{-38}\mathrm{cm}^2$.

The median energy of the T2K beam flux is at 0.63GeV, and the 68% region around this center value is within (0.40GeV, 0.95GeV). As a result, $< \sigma^{theory}_{\nu,NCQE} >$ is calculated as $2.01 \times 10^{-38}\mathrm{cm}^2$.

Measured cross-section

The expected number of total events is $N^{exp}_{tot} = 51.0$, and the expected background number is $N^{exp}_{bkg} = 16.2$. The observed number of events is $N^{obs} = 43$. Hence, the NCQE cross-section is calculated as below.

$$< \sigma^{obs}_{\nu,NCQE} >= \frac{43 - 16.2}{51.0 - 16.2} \times 2.01 \times 10^{-38} = 1.55 \times 10^{-38} cm^2 \tag{7.4}$$

Uncertainties

As described in Section 6.7, we assigned the systematic uncertainties for the NCQE signal events and the backgrounds events (NCothers, CC, and beam un-related) separately as shown in Table 6.9. Many toy experiments with systematic and statistical fluctuation are conducted to evaluate the total uncertainty as mentioned in Fig F.1. The measured NCQE cross-section distribution with the uncertainty is shown as Figure 7.1. In the plot, the center value represent the measured cross-section value, and the integrated area below the center value $(A/2)$ is the same with the one above the center value $(A/2)$. A $\pm1\sigma$ confidence level interval of the measurement is the inverval between two boundaries of $\pm\frac{68}{2}$% of the integrated area from the center value $(\pm\frac{68}{2}\%A)$. The statistical uncertainty is calculated from the observed number of events, and the error is $1/\sqrt{43} \sim 15\%$.

Here, the 68% confidence interval on the cross-section is $(1.08, 2.34) \times 10^{-38}\text{cm}^2$, and this region includes systematic uncertainty and statistical uncertainty.

Results

The flux-averaged ν-oxygen NCQE cross-section measurement is $< \sigma^{obs}_{\nu,NCQE} >= 1.55 \times 10^{-38}\text{cm}^2$ with a 68% confidence level interval of $(1.08, 2.34) \times 10^{-38}\text{cm}^2$. Figure 7.2 shows the comparison between the theoretical prediction and this result, and the theoretical NCQE cross-section is consistent with the measured cross-section at 68% C.L. interval.

Here, we separate the uncertainty into the systematic uncertainty and the statistical uncertainty, the measurement results are written as

$$< \sigma^{obs}_{\nu,NCQE} >= 1.55 \pm 0.395(stat.)^{+0.65}_{-0.33}(sys.) \times 10^{-38} cm^2 \tag{7.5}$$

The p-value of a background-only hypothesis (No NCQE) is 4×10^{-8}, and the hypothesis is rejected with a probability of 5.4σ. Thus, the measurement provides an evidence for NCQE signal.

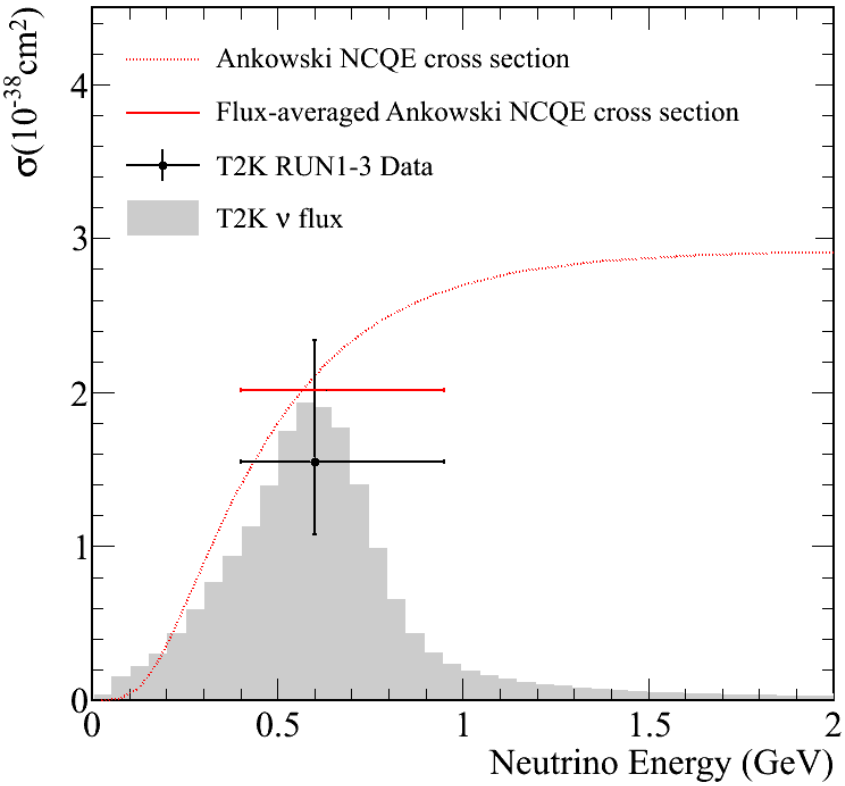

Figure 7.2: The T2K measurement of the flux-averaged NCQE cross-section. The measurement result is denoted as the black point. The vertical black line represents 68% confidence level interval of the measurement. While the red dashed line denotes the theoretical cross-section from Ref. [115], and the flux-averaged theoretical cross-section is shown as horizontal red line. The theoretical cross-section value is within 68% confidence interval of the measurement. The horizontal error bars are representing the 68% region from the flux center at each side of the median energy. The gray histogram shows the non-oscillated T2K neutrino flux at Super-K.

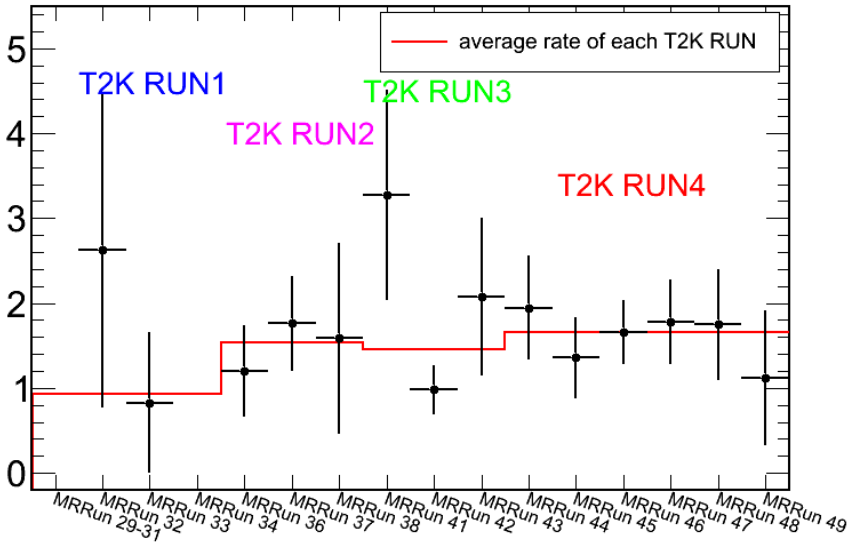

Figure 7.3: Event rate of each MR Run normalized by 10^{19} POT. The red histogram is representing the average event rate of each T2K RUN.

7.2 Updates with T2K RUN4 data

Here, we add the T2K RUN4 data to the samples for measuring the NCQE cross-section. T2K RUN4 started from October 2012 to May 2013, the accumulated POT is 3.56×10^{20}, which is more than that of T2K RUN1-3. The event selection cuts as mentioned previously are used to select 59 γ-ray candidates in T2K RUN4 data. The expected number of beam-related events is calculated to be 60.0, and the expected number of beam-unrelated events is 1.2. The details of T2K RUN4 events are described in Appendix G. The rate of events and the distributions of events for T2K RUN1-4 are described in the following paragraphs.

Event rate for T2K RUN1-4 The event rates for every MR runs (main ring) and every T2K runs (1-4) are shown in Figure 7.3, and a summary of the average rates of each T2K RUN is in Table 7.1. One hundred and two events are found with accumulated POT is 65.70×10^{19}, and the average event rate is 1.55 events per 10^{19} POT. The event rate of T2K RUN1-3 is 1.43 events per 10^{19} POT, and the two event rates are consistent in statistics.

Table 7.1: Summary of the numbers de-excitation γ-ray event candidates in every T2K RUN and the event rates per 10^{19} POT.

T2K Run	RUN1	RUN2	RUN3	RUN4
Number of events	3	17	23	59
Event rate per 10^{19}POT	0.928	1.534	1.457	1.657

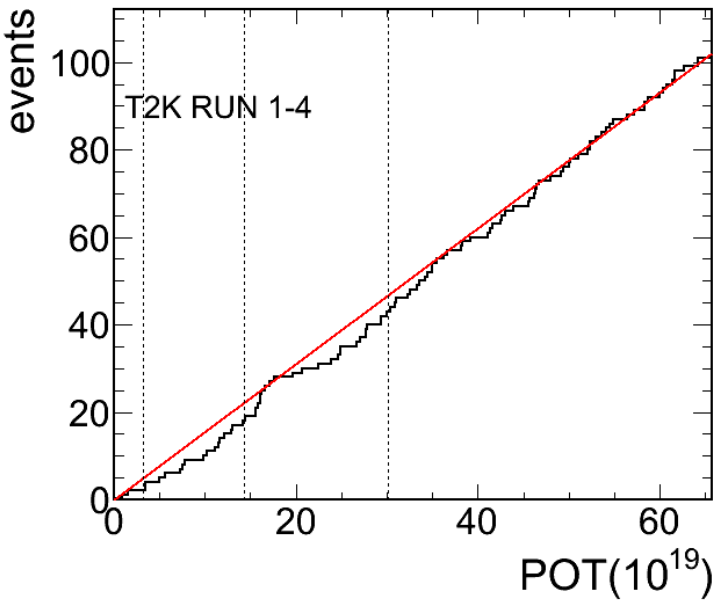

Figure 7.4: he de-excitation γ-ray candidates as a function of the accumulative POT for T2K RUN4. The red line is supposed as the cumulative probability distribution function for the uniform accumulative rate. The vertical dash lines are showing the boundaries of each T2K RUN.

Kolmogov-Smirnov test We use the Kolmogov-Smirnov test to check event rate of T2K RUN1-4 in unit of 10^{19} proton-on-target (POT). Figure 7.4 shows the number of γ-ray candidate events as a function of accumulative POT, and the red line is the cumulative probability distribution function for the uniform accumulative rate. The D value of K-S test is 0.0532, and significance is 0.929. The uniform distribution hypothesis is not rejected at the 92% level. The uniformity of T2K RUN 1-4 event rate is improved from that of T2K RUN1-3 event rate.

Energy and other parameters distributions The reconstruction energy distributions of data events and the expected events for T2K RUN1-4 are shown in Figure 7.5. The distribution of data events is consistent with that of expected events in statistics.

Figure 7.6 shows the Cherenkov angle distributions of data events and expected events for T2K RUN1-4. In the figure, there are discrepancies at 42 degree and near 90 degree between the expected number of candidate events of MC simulation and that of data events.

There is no statistically-significant difference in the distribution of the other parameters between the data and the expectation as shown in Fig. 7.7. All distributions of the T2K RUN 1-4 events are similar with those of the T2K RUN 1-3 events.

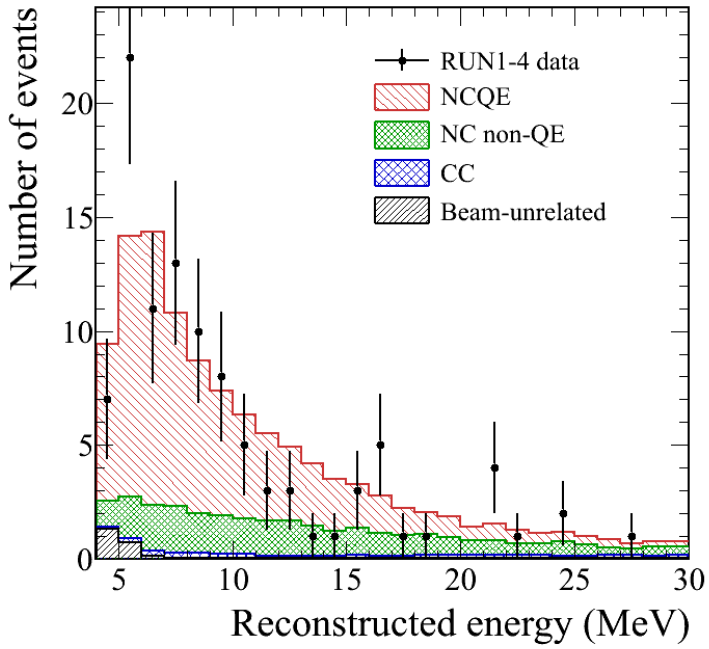

Figure 7.5: Comparison of the reconstructed energy spectrum between the expected events (histogram) and the data (dots) for T2K RUN1-4. The NCQE component is about 68% of total expected number of events.

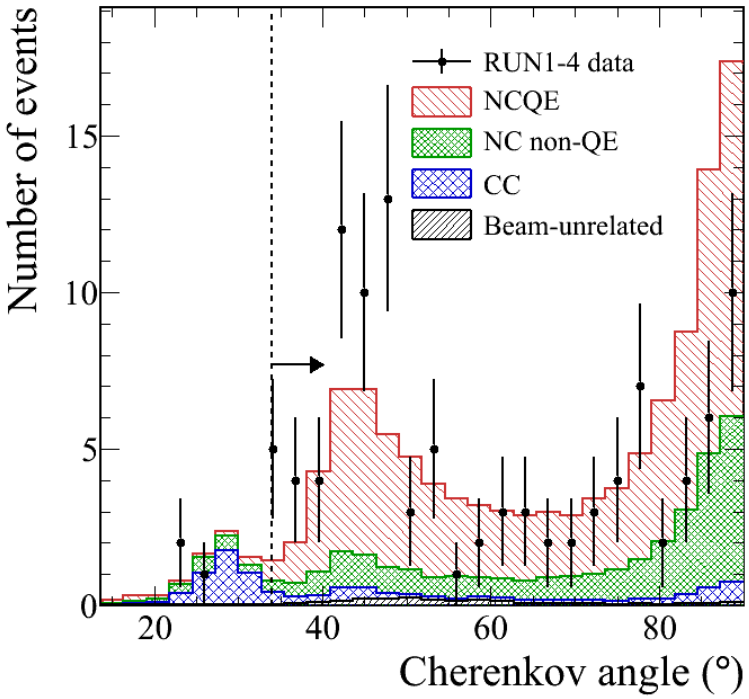

Figure 7.6: Comparison of Cherenkov angle distribution between the expected events and data. The peak near 28^o is composed of CC background events, thus the events with the angle less than 34 degree are removed.

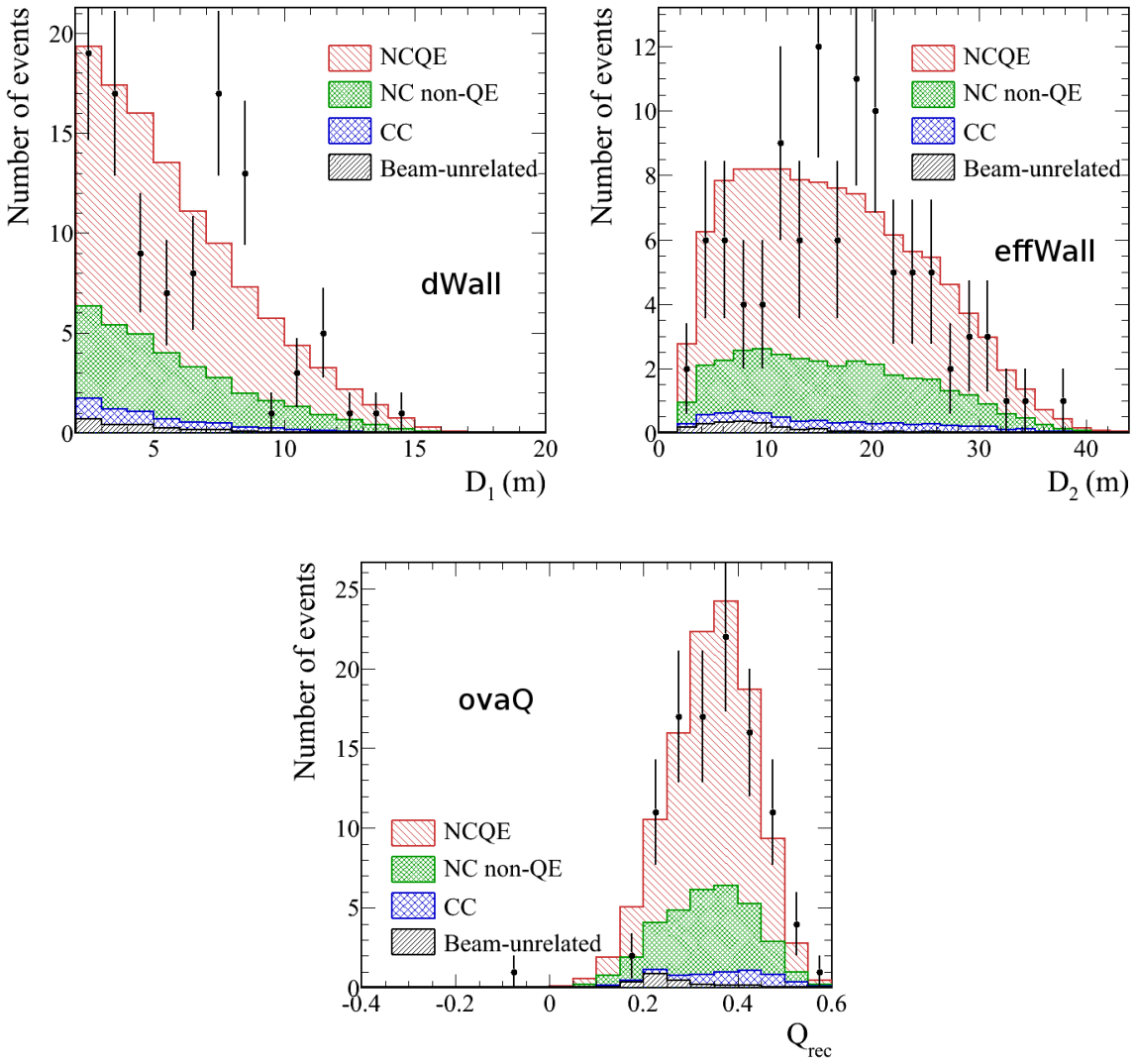

Figure 7.7: Comparison of the dWall, effWall and ovaQ distributions between the expected events (histogram) and the data (dots) of T2K RUN1-4.

Updated result of ν-oxygen NCQE cross section 102(=43+59) events are found as the γ-ray candidate events for T2K RUN1-4 data. While the expected number of events, N_{tot}^{exp}, is 112.2, and the expected number of background events N_{bkg}^{exp} is 34.6. The updated NCQE cross-section is calculated as below

$$< \sigma_{\nu,NCQE}^{obs} >= \frac{102 - 34.6}{112.2 - 34.6} \times 2.01 \times 10^{-38} = 1.75 \times 10^{-38} cm^2 \tag{7.6}$$

As T2K RUN4 has a higher event rate than T2K RUN1-3 as shown in Figure 7.3. The updated cross-section increased by ~13% compared with that of RUN1-3. ($\sigma_{NCQE}^{RUN1-3} = 1.55 \times 10^{-38}\text{cm}^2$). As the updated uncertainty is discribed in Appendix G.3, the 68% confidence level (C.L.) interval is $(1.33, 2.52) \times 10^{-38}\text{cm}^2$, and the 90% C.L. interval region is $(1.04, 3.06) \times 10^{-38}\text{cm}^2$. The comparison between the observed NCQE cross-section and the theoretical one is as shown in Figure 7.8. The updated measurement remains consistent with the theoretical calculation within the 68% confidence level region. The

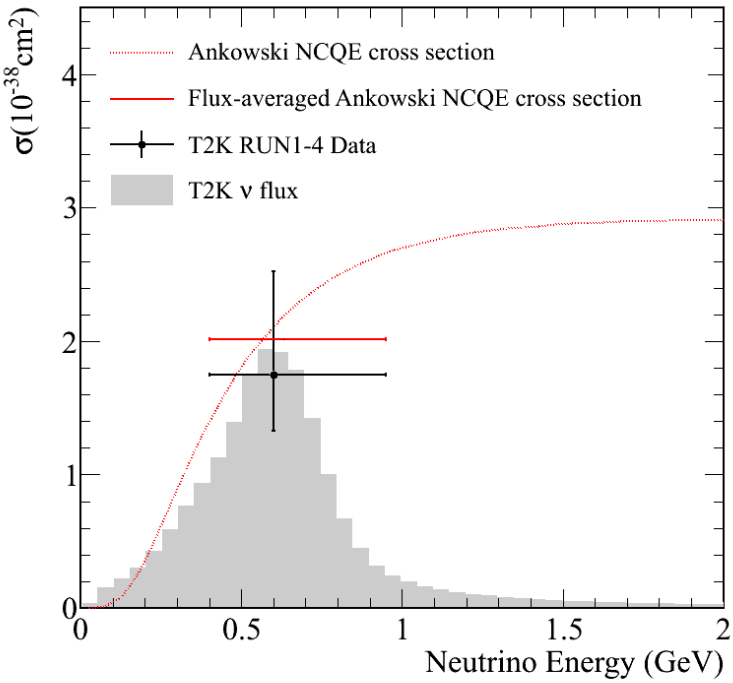

Figure 7.8: The T2K measurement of the flux-averaged NCQE cross-section for T2K RUN1-4 data. The measurement result is denoted as the black point calculated using Equation 7.7. The vertical line represents the 68% confience interval of the measured cross-section. As the event rate for RUN4 is higher, the observed cross-section value increases by about 13%. The theoretical cross-section value is also within the 68% confidence interval of the measurement.

NCQE cross-section with the systematic and statistical errors is written as

$$< \sigma^{obs}_{\nu,NCQE} >= 1.75 \pm 0.27(stat.)^{+0.70}_{-0.36}(sys.) \times 10^{-38} cm^2 \tag{7.7}$$

where the systematic uncertainty dominates the whole uncertainty. With adding the data of T2K RUN4, we reject the background-only hypothesis $\sigma_{NCQE} = 0$ with a $p-$value of 1.42×10^{-20}.

The summary of cross-section results between the previous (RUN1-3) and RUN 1-4 are as shown in Table 7.2. The updated statistical uncertainty decreases by a large amount, while the systematic uncertainty remains the same. The analysis reached the systematic error limit, so the updated accuracy of the cross-section is not improved by a large amount.

Table 7.2: Summary of NCQE cross-section measurement for T2K RUN1-3 and T2K RUN1-4.

T2K RUNs	N^{obs}	N^{exp}_{sig}	N^{exp}_{bg}	$< \sigma^{obs}_{\nu,NCQE} >$	Stat. error	Sys. error
1-3	43	34.8	16.2	1.55×10^{-38}cm^2	$\pm 25.48\%$	$^{+41.93\%}_{-21.29\%}$
1-4	102	77.6	34.6	1.75×10^{-38}cm^2	$\pm 15.42\%$	$^{+40.0\%}_{-20.57\%}$

7.3 Future improvement

As we saw in Equation 7.7, the systematic uncertainty dominates in the total uncertainty for the NCQE cross-section measurement. The uncertainty of the NCQE signal events is 20%, and the uncertainty due to secondary γ-ray production is 13% that dominates the uncertainty of signal events as shown in Table 6.9. But there is no previous experimental data about the observation of the γ-rays induced by neutron-water reactions, the uncertainty due to secondary γ-ray production is estimated using a different simulation. Appendix H describes the experimental proposal at Reach Center for nuclear Physics (RCNP) to measure the γ-rays produced from neutron-water reactions. The measurements of neutron-water experiment are expected to reduce the uncertainty due to secondary γ-ray production. There are some improvements by analysis method as described in Appendix I.

Chapter 8

Impact to other physics

8.1 Sterile neutrino search in T2K experiment

The neutrino oscillation scenario with one sterile neutrino state mixing with three active neutrino states is studied in this chapter. If there exist sterile neutrino states, active-to-sterile oscillation is expected to decrease the flux summed over the three active neutrinos. As sterile neutrinos do not interact with matter via weak current, disappearance of neutral current events is a useful tool to probe the existence of sterile neutrino. The disappearance of de-excitation γ-ray events induced by neutral current reaction in the far detector can be used to search for the sterile neutrino at the T2K experiment.

To explain the LSND anomaly, a scenario with one sterile neutrino ν_s mixing with the three active neutrinos ν_e, ν_μ, ν_τ was introduced. The oscillation probabilities with one sterile neutrino state are described in Appendix A.3.

8.1.1 Oscillation probabilities of four mass eigenstates

For the scenario with one sterile neutrino and three active neutrinos, Figure 8.1 shows possible mass hierarchies, if normal hierarchy is assumed for the active neutrinos ($m_3 > m_2, m_1$). Three following models are introduced: $m_4 \simeq m_1$ model, $m_4 \simeq m_3$ and $m_4 >> m_3$ model. Three CP delta phase angles δ_i and θ_{14} are assumed to be zero, as the long base-line experiments such as T2K have no sensitivity to study those angles.

$m_4 \simeq m_3$ model A scenario has a degenerate between the third and the fourth mass eighestates. The SNO results [142] indicate that there is no discernible mixing between active and sterile neutrinos. The oscillation is too small to be observed in long base-line experiment such as T2K, MINOS [40]. Therefore, we do not study on this model.

$m_4 \simeq m_1$ model Because the degeneracy of $m_4 \simeq m_1$ and $|\Delta m^2_{13}| >> |\Delta m^2_{12}|$, $m_4 \sim m_2$ is assumed. For the oscillation experiment with baseline of $\mathcal{O}(10^2\text{km})$, there is no sensitivity for θ_{14} and θ_{24} with the assumption. We set the mixing angle $\theta_{14} = \theta_{24} = 0°$. Then, the oscillation probabilities are simplified as follows.

$$P_{\nu_\mu \to \nu_\mu} = 1 - 4|U_{\mu 3}|^2(1 - |U_{\mu 3}|^2)\sin^2 \Delta_{31}, \tag{8.1}$$

$$P_{\nu_\mu \to \nu_\alpha} = 4|U_{\mu 3}|^2|U_{\alpha 3}|^2 \sin^2 \Delta_{31}, \tag{8.2}$$

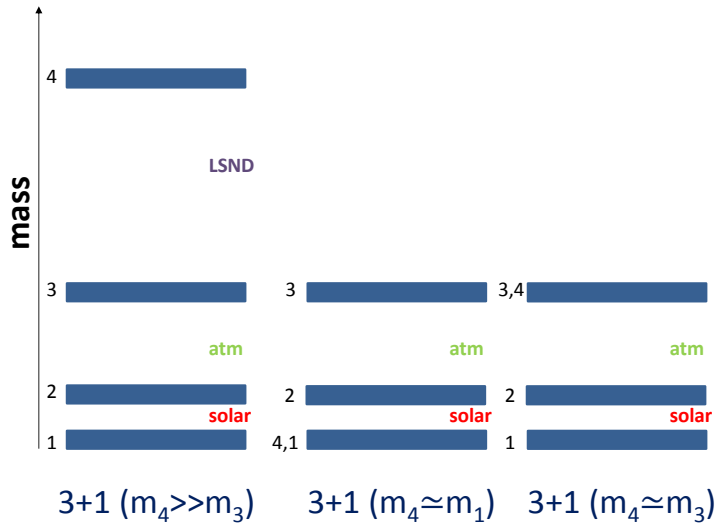

Figure 8.1: The schematic of three possible mass hierarchy for four mass eigenstates. Here, the normal hierarchy is assumed, so the $m_3 > m_2, m_1$. The two right models show that expanded mass state m_4 is degenerate with m_1 and m_3. The left one shows the mass eigenstate m_4 is heavier than the other states, and we assume the mass-squared splitting Δm_{41} is same as suggested by the LSND result of $\mathcal{O}(1\ \mathrm{eV}^2)$.

where $\alpha = e, \tau, s$, $U_{\mu 3} = c_{13}s_{23}$, and $U_{s3} = -c_{13}c_{23}s_{34}$. Equation 8.1 shows the ν_μ disappearance probability which doesn't include θ_{34} term. The probability is the same with one of only three active neutrino mixing.

$m_4 >> m_3$ **model** Here, Δm^2_{43} is assumed to be $\mathcal{O}(1\ \mathrm{eV}^2)$. The oscillation term of $\sin^2\Delta_{4i}$ changes rapidly, so we take the average value to substitute the oscillation terms. The average of $\sin^2\Delta_{41}$ or $\sin^2\Delta_{43}$ is $\frac{1}{2}$, while the average of $\sin 2\Delta_{41}$ or $\sin 2\Delta_{41}$ is zero. On the other hand, the Δm_{31} terms are relevant at far site, as $L/E_\nu = 295.0[\mathrm{km}]/0.63[\mathrm{GeV}] \sim 468$. $\theta_{14} = 0°$ and $\delta_2 = 0°$ are assumed, then the oscillation probabilities become

$$P_{\nu_\mu\to\nu_\mu} = 1 - 4\{|U_{\mu 3}|^2(1-|U_{\mu 3}|^2-|U_{\mu 4}|^2)\sin^2\Delta_{31} + \frac{1}{2}|U_{\mu 4}|^2(1-|U_{\mu 4}|^2)\}, \tag{8.3}$$

$$P_{\nu_\mu\to\nu_\alpha} = 4\mathcal{R}]\{(|U_{\mu 3}|^2|U_{\alpha 3}|^2 + U^*_{\mu 4}U_{\alpha 4}U_{\mu 3}U^*_{\alpha 3})\sin^2\Delta_{31} + \frac{1}{2}|U_{\mu 4}|^2|U_{\alpha 4}|^2\}, \tag{8.4}$$

where the elements of the mixing matrix are written as below

$$\begin{aligned} U_{\mu 3} &= c_{13}s_{23}c_{24}, \\ U_{\mu 4} &= s_{24}, \\ U_{s3} &= -c_{13}s_{23}c_{34}s_{24} - c_{13}c_{23}s_{34}, \\ U_{s4} &= c_{24}c_{34}, \end{aligned} \tag{8.5}$$

For Super-K atmospheric neutrino oscillation, the ν_μ disappearance result gave a strict upper bound on $\theta_{24} = 7.7°$ [35]. Here we set the $\theta_{24} = 0°$, the ν_μ disappearance probability

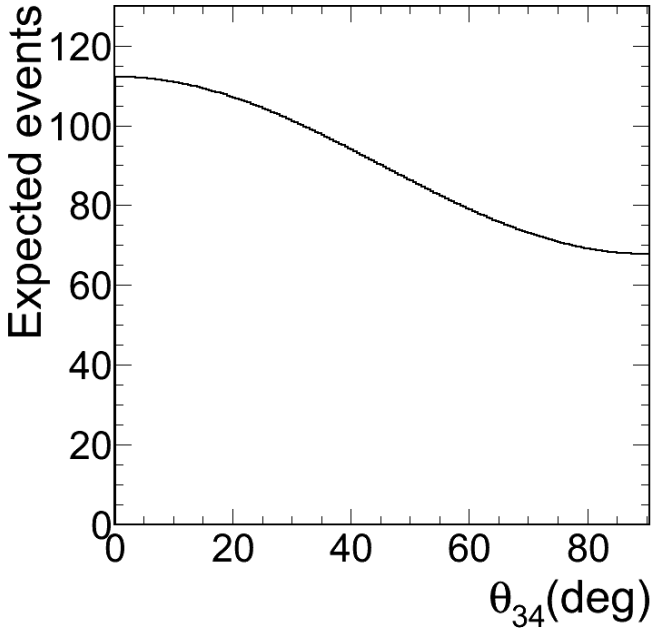

Figure 8.2: The expected number of de-excitation γ-ray events for T2K RUN1-4 as a function of θ_{34}. The accumulative POT is 6.57×10^{20}.

is simplified to be the same with the probability of assuming only three active neutrino mixing. With the assumption, the oscillation probability $P(\nu_\mu \to \nu_s)$ of $m_4 >> m_3$ model is the same with that of $m_4 \simeq m_1$ model.

8.1.2 Sensitivity of θ_{34} using T2K RUN1-4 de-excitation γ-ray events

Here, we consider the sensitivity of θ_{34} using the de-excitation γ-ray events induced by the T2K neutrino beam. As shown in Table 5.8 and Table G.5, there are $> 93\%$ fraction of neutral current events (NCQE+NCothers) in the γ-ray candidate events. Figure 8.2 shows the expected number of events as a function of θ_{34} under the sterile ν models ($m_4 = m_1$, $m_4 >> m_3$). The ν_μ disappearance probability is simplified to be the same with the probability of only three active neutrino mixing, so the measurement of $\sin^2\theta_{23}$ and Δm^2_{32} under one sterile neutrino scenario are the same with the measurement under only three active neutrino scenario. The T2K's best-fit result [26] of $\sin^2\theta_{23} = 0.514$ and $\Delta m^2_{32} = 2.51 \times 10^{-3}$ eV^2/c^4 are used. For θ_{13}, the result of $\sin^2 2\theta_{13} = 0.09$ from the DayaBay is used [28].

To constrain the mixing angle θ_{34}, we compare the true (observed) number of events (N_{obs}) with some assigned values of θ_{14} to the expected number of events N_{exp} calculated based on the oscillation probabilities of Equation 8.3 and Equation 8.4. Here, the χ^2 is used to predict the sensitivities to the mixing angle θ_{34}:

$$\chi^2(\theta_{34}) \equiv 2\{N_{exp} - N_{obs} + N_{obs} ln(\frac{N_{obs}}{N_{exp}})\} + \sum_i (\frac{\epsilon_i}{\sigma_{sys,i}})^2, \tag{8.6}$$

$$N_{exp} = \sum_i (1 + \epsilon_i) N_{exp,i} \tag{8.7}$$

Table 8.1: The summary of systematic uncertainties based on the expected number of the NCQE events and the background events. The uncertainties of the NCothers events and the CC events due to the flux and the cross-section are assigned with the correlation matrix including the ND280 data.

interactions	NCQE	NCothers	CC	beam-unrelated
fraction of events	68%	25%	4%	2%
Flux	11%	18%	10%	–
Cross-section	15%			–
Primary γ production	10%	3%	6%	–
Secondary γ production	13%	13%	7.6%	–
Detector response	2.2%	2.2%	2.2%	–
Oscillation parameters	–	–	10%	–
Total systematic error	25%	23%	17.2%	0.8%

where $N_{exp,i}$ denotes the expected number of i-th reaction events, where the i-th reaction is NCQE, NCothers, CC, and beam-unrelated. The systematics nuisance parameter ϵ_i is a shift from the nominal value for the i-th reaction events. The $\sigma_{sys,i}$ is the systematic uncertainty of the i-th reaction. We use the ND280 fitting results to give a constrained errors for NCothers and CC reactions, whose correlation matrix is shown in right plot of Figure 6.1. The systematic uncertainties of the de-excitation γ-ray events are summarized in Table 8.1. Because the ND280 detectors measure the "flux×cross-section", the uncertainties due to the neutrino flux and the cross-section are entangled in the table. For the NCQE events, the uncertainty due to the flux is the same as Table 6.9, and the uncertainty due to the cross-section is assumed to be 15% according to the recent theoretic calculation[143].

To minimize the sensitivity function $\chi^2(\theta_{34})$ for every θ_{34}, the ϵ_i is derived by solving the equality $\partial\chi^{2(\theta_{34})}/\partial\epsilon_i = 0$,

$$\epsilon_i = \sigma^2_{sys,i} N_{exp,i}\left(\frac{N_{obs}}{\sum_i N_{exp,i} + \sum_i \epsilon_i N_{exp,i}} - 1\right) \tag{8.8}$$

and

$$\begin{aligned}\sum_i \epsilon_i N_{exp,i} = {} & \frac{-1}{2}\left(\sum_i N_{exp,i} + \sum_i \sigma^2_{sys,i} N^2_{exp}\right) \\ + {} & \frac{1}{2}\sqrt{\left(\sum_i N_{exp,i} + \sum_i \sigma^2_{sys,i} N_{exp,i}\right)^2 - 4\left(\sum_i N_{exp,i} \sum_i \sigma^2_{sys,i} N_{exp,i} - N_{obs} \sum_i \sigma^2_{sys,i} N_{exp,i}\right)},\end{aligned} \tag{8.9}$$

Figure 8.3 shows the sensitivity of θ_{34}, the true value of θ^{true}_{34} is assumed to be 0 degree and 20 degree. The sensitivity result of $\theta^{true}_{34} = 0^\circ$ (20°) is drawn as black line (dashed line) in the figure, and the best fit value is at 0° (20°) and upper limit is 53.5 (59) degree at 90% confidence level (C.L.).

Future sensitivity

As mentioned previously, the T2K experiment plans to accumulate data equivalent to 7.8×10^{21} POT, and the ratio of neutrino beam to anti-neutrino beam will be about

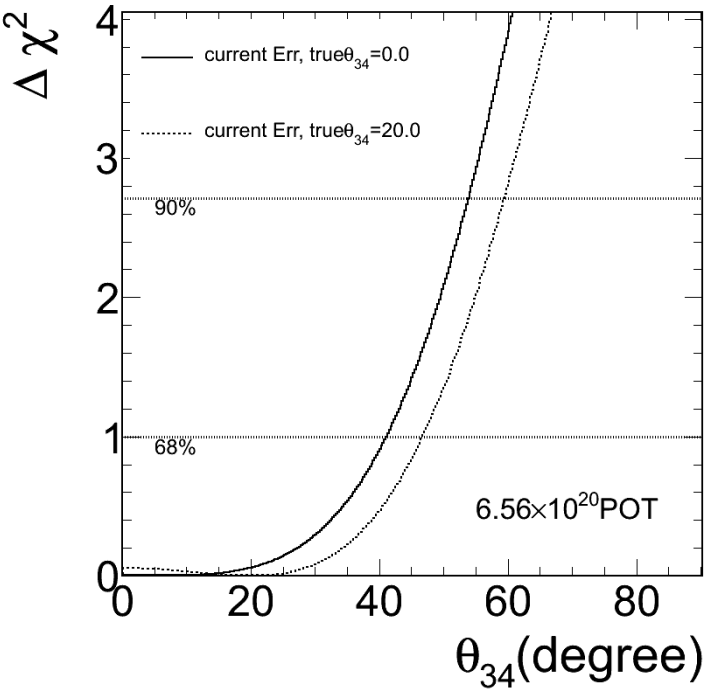

Figure 8.3: The sensitivity of θ_{34} for the T2K RUN1-4 period. The true value of θ_{34}^{true} is set to be 0 degree and 20 degree. The expected number of events is calculated with the statistics of 6.57×10^{20} POT. The black line (dashed line) shows the result with θ_{34}^{true} set to be 0 (20) degree. The systematic error is shown in Table 8.1.

1 : 1. Because the analysis of the de-excitation γ-ray induced by anti-neutrino does not finish yet, this thesis uses data of neutrino beam to search for sterile neutrinos, and the accumulative POT is about half of total accumulative POT in future.

Now, the systematic uncertainty for the sterile search is 24%. There are several ideas to reduce the systematic error in future. As mentioned in Section H, the neutron-water experiment at RCNP is expected to reduce the uncertainty due to secondary γ-ray production. The ND280 has a ability to measure the proton induced by the NCQE reactions, so it is possible to reduce the uncertainties due to flux and cross-section. It is possible to lower the systematic error to $\sim$ 15% with the results of experiment at RCNP and the ND280 results. Furthermore, there is a proposal to build a water Cherenkov detector in the near site. With the water detector, the systematic uncertainty may be reduced to a few percent in future.

Figure 8.4 shows the sensitivities of θ_{34} with the different error sizes of $25\%, 15\%$, and 5%, which are corresponding to the possible error sizes in future. In the figure, the true angle θ_{34}^{true} =0.0, 20.0 degree is assigned. If the true θ_{34}^{true} is 0.0 degree, the 90% C.L. limits on the θ_{34} for error sizes of $25\%, 15\%$, and 5% are $51°, 40°$,and $28°$ respectively. The rejection regions at 90% C.L. are highly dependent on the error sizes. If the true mixing angle θ_{34} is 20.0 degree, the the 90% C.L. limits on the θ_{34} for error sizes of $25\%, 15\%$, and 5% become $56°, 46°$,and $34.5°$ respectively. The rejection regions of θ_{34} at 90% C.L. are highly dependent on the error sizes.

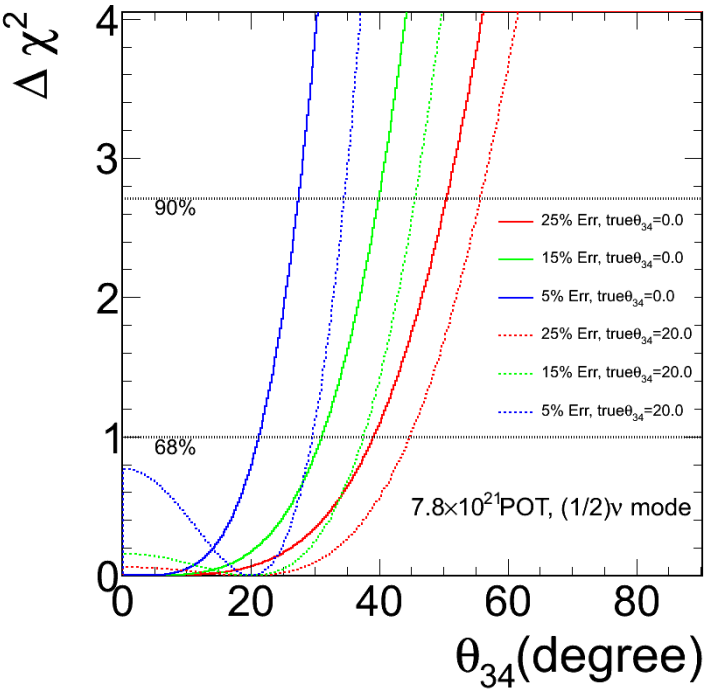

Figure 8.4: The sensitivities of θ_{34} with different error sizes for the T2K future target. The true value of θ_{34} is set to be 0 and 20.0 degree. The expected number of events is calculated with the T2K goal statistics of 7.8×10^{21} POT, and only half of the data are used. The red line, green line and blue line represent the results with error sizes of $25\%, 15\%$, and 5% respectively, and the true mixing angle θ_{34}^{true} is set to be zero degree. The dash lines of red, green, and blue are representing the results with error sizes of $25\%, 15\%$, and 5%, if the true mixing angle θ_{34}^{true} is set to be 20.0 degree.

8.1.3 Discussion

Comparison to the results of MINOS

As mentioned previously, the MINOS experiment gave the strictest results of the mixing angle θ_{34}[40, 41]. For $m_4 \simeq m_1$ model, the θ_{34} limit at 90% C.L. is 37° (here, $\theta_{13} = 11.5°$). For $m_4 >> m_1$ model, the θ_{34} limit at 90% C.L. is 37°. Disappearance of NC events is not found in the observation, so the best fit is $\theta_{34} = 0.0$. Compare to the T2K future sensitivities, the results with error size of 15% have a comparable limit (40^o) with the limit of MINOS.

If the error size is reduced to a few percents in future, the result of θ_{34} is expected to give a stricter limit than the MINOS result.

8.2 Impact to supernova relic neutrino search at Super-K

The supernova relic neutrino (SRN) search at Super-Kamiokande has been conducted via the inverse beta decay reaction ($\overline{\nu}_e + p \rightarrow n + e^+$) [56]. To reduce the background event rate, there is a plan for future Super-K to add gadolinium compound to detect the

produced neutron by observing the 8 MeV γ-ray in neutron-Gadolinium capture reaction. But, the NCQE reaction produces neutrons in water, so the de-excitation γ-rays induced by the NCQE interaction are remaining background events in the SRN search. Here, we discuss about the impact of uncertainty size of de-excitation γ-ray for the SRN search.

8.2.1 Event spectrum under Gd-enhance neutron tagging

As mentioned in Section 1.4, the neutron tagging method can remove the nuclear spallation events and the atmospheric neutrino reaction events. But an efficiency of neutron detection is only $\sim 17\%$ with the delayed 2.2 MeV γ-ray[57].

To improve the efficiency of neutron detection, the SK-Gd is proposed to add soluble gadolinium compound (Gd_2SO_4) into Super-K water. A neutron is captured on gadolinium (Gd) by 90% efficiency[144]. The neutron capture yields a 7.9 MeV delayed γ-ray by 80.5% probability or a 8.5 MeV delayed γ-ray by probability of 19.3%. The detection efficiency of 8 MeV γ-ray signal is $\sim 74\%$ under the following selections:

1. The reconstructed vertex of γ-ray event is located within 200 cm from the prompt event.

2. The reconstructed energy of γ-ray event is larger than 3 MeV.

3. The time of γ-ray event is within 60 μs after the prompt event.

After the selections, the coincidence probability of accidental background events is $\sim 2\times10^{-4}$. As a result, the efficiency of neutron detection is expected to about $0.90\times0.74 = 67\%$, which is much larger than the efficiency by observing the 2.2 MeV γ-ray signal.

It is possible to lower the energy threshold to 12 MeV or even to 10 MeV with low background rate of spallation events.[1] Figure 8.5 shows the reconstructed energy distributions of the SRN events and the other background events using Gd-enhanced neutron tagging method. Here, the LMA model[50] is used to predict SRN flux for observation of ten years, and we use the atmospheric ν flux to predict the background events for the same observation period. The de-excitation γ-ray events are induced by neutrino neutral current interactions, and most of the NC reactions are NCQE and NC1π reactions. The simulation is used to estimate the neutron multiplicity, and the efficiency of selection is applied to estimate a detected neutron multiplicity. Only one detected neutron capture on Gd signal is 37% of the area of detected neutron multiplicity [120]. We suppose that 37% fraction of NC events remain after the selection. The energy distribution of NC events is shown as the blue dash-line in Figure 8.5.

8.2.2 Sensitivity of SRN

χ^2 function As mentioned in Sec. 1.4, LMA model predicts the flux of SRN. Here, we use a sensitivity function to estimate a discovery potential of SRN under a prediction of SRN flux by LMA model. The "discovery" of SRN represents that we can exclude the "no SRN signal" hypothesis $N_{sig} = 0$ by the confidence level of 3σ. The uncertainty

[1] With the selection of neutron tagging, the remaining background events are induced by the reactor neutrinos and the spallation of ^{9}Li nucleus. The reconstructed energy of reactor neutrinos and ^{9}Li decay events are distributed below 10 MeV mostly.

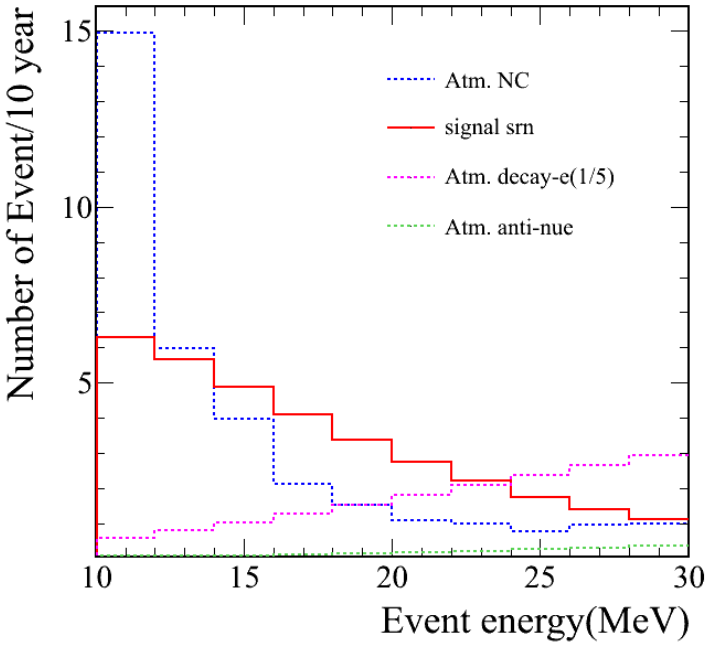

Figure 8.5: The spectrum of supernova relic neutrino events and background events in SK-Gd proposal. The red line shows the spectrum of SRN signal for ten years observation, and it is estimated by LMA model[50]. Other dash-lines are showing the background spectrum from atmospheric neutrino. The blue dash-line is the de-excitation γ-ray induced by NCQE and NC1π reactions. The rate of decay electron backgrounds after CC reactions are expected to be reduced to 1/5 under the Gd-enhanced neutron tagging. The pink dash-line is showing the reduced decay-e background events. The green dash-line is the remained anti-nue events.

of number of NC events has influence on the sensitivity of SRN search. Therefore, the sensitivity function χ^2 is defined as

$$\chi^2(N_{sig}^{exp}) \equiv \frac{(N_{obs} - N_{bkg}^{exp} - N_{sig}^{exp})^2}{\sigma_{stat}^2 + \sigma_{NC,sys}^2} \tag{8.10}$$

where the testing number N_{sig}^{exp} is the expected number of SRN signal events with the reconstructed energy at region of (10 MeV,30 MeV). N_{bkg}^{exp} is the expected number of background events with the reconstructed energy at region of (10 MeV,30 MeV). N_{bkg}^{exp} includes the number of decay electron events $N_{decay-e}$, the number of anti-nue events $N_{\overline{\nu}_e}$, and the number of de-excitation γ-ray events induced by NC interactions N_{NC} (or called NC events) $N_{bkg}^{exp} = N_{decay-e} + N_{\overline{\nu}_e} + N_{NC}$. The observed number (true) of events is assigned as $N_{obs} = N_{sig}^{true} + N_{bkg}^{exp}$, where N_{sig}^{true} is the number of SRN signal predicted by LMA model [50]. The true number of the signal events and the expected numbers of background events are summarized in Table 8.2. The statistical error is the square root of the observed number of event $\sigma_{stat} \equiv \sqrt{N_{obs}}$. For background, we consider only the uncertainty of the number of NC events $\sigma_{NC,sys}$, and the uncertainty is written as

$$\sigma_{NC,sys} \equiv N_{NC} \cdot \delta\varepsilon_{NC,sys}, \tag{8.11}$$

where $\delta\varepsilon_{NC,sys}$ is the uncertainty of de-excitation γ-ray events induced by NC interactions.

Table 8.2: Summary of the number of the SRN events predicted by LMA model [50] and the expected number of background events. The numbers of events having the reconstructed energy E_{rec} within energy region of (10 MeV,30 MeV) and (12 MeV,30 MeV) are listed.

E_{rec} region	10-30MeV	12-30MeV
N_{sig}^{true}	33.55	27.25
N_{NC}	33.34	18.38
$N_{\overline{\nu}_e}$	1.65	1.62
$N_{decay-e}$	17.06	16.46
N_{bkg}^{exp}	52.05	36.47

Uncertainty of NC events As mentioned in Section 1.4, the events with the Cherenkov angle $38^\circ \leq \theta_{res} \leq 50^\circ$ are selected in the SRN search. As shown in Figure 5.19, there is a discrepancy between the Cherenkov angle distributions of the observed data events and the expected events. As mentioned in Subsection 5.3.4, the discrepancy is due to the secondary γ-ray multiplicity. The discontinuity at the distribution of simulated γ-rays as shown in Figure 4.13 is used to estimated the uncertainty due to the multiplicity of secondary γ-rays to be 50% [120].

Besides the uncertainty due to the secondary γ multiplicity, there are other error source of NC events induced by atmospheric neutrinos such as atmospheric neutrino flux, primary γ-ray production, detector response, etc. If the energy of atmospheric neutrino is $(10^{-1}, 10^2)$ GeV, the systematic uncertainty due to atmospheric flux is $8\% \sim 20\%$[148]. Therefore, $\delta\varepsilon_{NC,sys}$ is $\sim 60\%$ which is obtained including the uncertainty due to secondary γ-ray multiplicity and the maximum uncertainty of atmospheric neutrino flux, and other uncertainties. In this thesis, we test $\delta\varepsilon_{NC,sys} = 0.6$ to have a study on the sensitivity of SRN search.

In future, it is possible to reduce the $\delta\varepsilon_{NC,sys}$ by the neutron-water experiment at RCNP and the de-excitation γ-rays observation at the T2K experiment. We estimate the sensitivities of SRN search with $\delta\varepsilon_{NC,sys}$ range of 10%∼60% in the next paragraph.

Sensitivity of the SRN search Left plot in Figure 8.6 shows the sensitivities for SRN search with different error sizes of NC background events, and the energy threshold is 10 MeV. The plot shows the sensitivities with three kinds error sizes of $\delta\varepsilon_{NC,sys}$: 10%, 30%, and 60%. Only the distribution with error size of 10% rejects no SRN hypothesis at 3σ confidence level. The right plot in the Figure 8.6 shows the sensitivities with the energy threshold of 12 MeV. The sensitivities are similar with those with threshold 10 MeV.

Now, the SK-Gd proposal is approved as the Super-K project. It is important for the SRN search to reduce the error size of NC events using the external experiment data. In near future, the reduced uncertainty of NC events leads the SK-Gd proposal having high potential to search for the SRN signal.

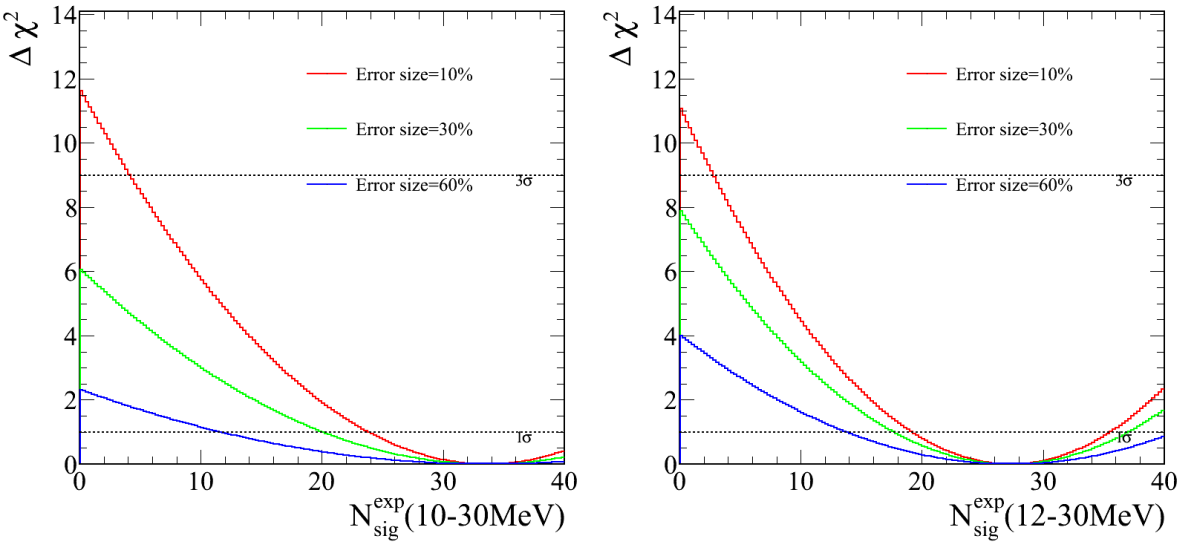

Figure 8.6: The sensitivities of SRN under the SK-Gd proposal with different error size of NC events. The left plot shows sensitivities with the energy threshold of 10 MeV, and the right plot shows the sensitivities with the energy threshold of 12 MeV.

Chapter 9

Conclusion

The study of the de-excitation γ-ray events induced by the neutral current quasi-elastic (NCQE) reactions has the two motivations: First, the de-excitation γ-ray events mostly induced by NCQE reactions from atmospheric neutrinos are one of the main background events for the supernova relic neutrino search. Second, the $> 93\%$ fraction of the de-excitation γ-ray events are induced by neutral current reactions, including NCQE reactions. It is possible to use the events to search for the active-to-sterile neutrino oscillation.

There was an observation of the NCQE events at the near detector of the K2K experiment, but they didn't give a measurement of the ν-water NCQE cross-section. The average energy of T2K neutrinos is 630 MeV, and the NCQE cross-section dominates in all NC reaction cross-sections. It is possible to give a measurement at Super-K of the NCQE cross-section with the T2K neutrino beam.

This thesis reports the first neutrino-oxygen NCQE cross-section measurement by observing the de-excitation γ-rays induced by the T2K neutrino beam. To measure the cross-section, we scale up the theoretical cross-section by a factor obtained from the comparison between the expected number of events and the observed number of candidate events.

The expected number of de-excitation γ-ray events is estimated by the MC simulations, and the procedures of the simulation are as follows: a neutrino beam simulation, a neutrino interaction simulation, and a detector simulation. In the analysis, we update the NCQE cross-section model and the spectroscopic factors and the γ-rays emission branching ratios, then the expected number of candidate events are 51.0. Among the candidate events, 68.2% fraction of events are expected as the NCQE events, and the main background events are from NC1π resonance interaction.

In observation, the de-excitation γ-ray events are selected from the T2K RUN1-3 spill data. To remove the background events, we use the following information of the events: energy, timing, vertex, direction, goodness of reconstruction, Cherenkov angle, and pre-activity. Forty-three candidate events are found in T2K RUN1-3 data after selections. The comparison between the observed events and the expected events shows that there are no statistically-significant differences except the Cherenkov angle distribution.

The measurement of flux-averaged ν-oxygen NCQE cross-section $\sigma_{\nu,NCQE}$ during the T2K RUN1-3 period is $< \sigma_{\nu,NCQE}^{obs,T2KRUN1-3} >= 1.55 \times 10^{-38}\mathrm{cm}^2$ with a 68% confidence level interval of $(1.08, 2.34) \times 10^{-38}\mathrm{cm}^2$. The theoretical NCQE cross-section $< \sigma_{\nu,NCQE}^{theory} >= 2.01 \times 10^{-38}\mathrm{cm}^2$ is consistent to the measurement within 68% confidence level. The results

are written with separated systematic and statistical uncertainty as

$$< \sigma_{\nu,NCQE}^{obs,T2KRUN1-3} >= 1.55 \pm 0.395(stat.)^{+0.65}_{-0.33}(sys.) \times 10^{-38} cm^2 \quad (9.1)$$

This is the first measurement of ν-oxygen NCQE cross-section. Then, we add the T2K RUN4 data to update the cross-section measurement. The ν-oxygen NCQE cross-section is updated as $< \sigma_{\nu,NCQE}^{T2KRUN1-4} >= 1.75 \times 10^{-38}\mathrm{cm}^2$ with the 68% confidence interval is $(1.33,\ 2.52)\times 10^{-38}\mathrm{cm}^2$. The theoretical cross-section is consistent with the updated measurement at the 68% confidence level. The updated NCQE cross-section is written as

$$< \sigma_{\nu,NCQE}^{obs,T2KRUN1-4} >= 1.75 \pm 0.27(stat.)^{+0.70}_{-0.36}(sys.) \times 10^{-38} cm^2 \quad (9.2)$$

This thesis reported the first measurement of ν-oxygen NCQE cross-section by observing the de-excitation γ-ray, and the results shed light on the study of the active-sterile neutrino oscillation in the T2K experiment and the atmospheric background events for SRN search in Super-K experiment.

According to the measurement of de-excitation γ-ray during the T2K RUN1-4 period, the effects on the sterile neutrino search and the supernova relic neutrino search are discussed. For the sterile neutrino search, we have a potential to measure the extended mixing angle θ_{34} with the simplified assumptions such as $\theta_{14} = \theta_{24} = 0°$. If the true value of θ_{34}^{true} is 0° (20°), the upper limit is 53.5° (59°) at 90% confidence level for the T2K RUN1-4 period. The rejection regions at 90% confidence level are highly dependent on the error sizes. To get the same corresponding limit with the limit of MINOS, the error size should be reduced within 15% for the T2K target of 7.8×10^{21} POT.

In the supernova relic neutrino (SRN) search at Super-K, the de-excitation γ-ray induced by atmospheric neutrino is a source of background. The sensitivity for the SRN search is affected by the following error source of de-excitation γ-ray: the uncertainties of the expected number of neutral current reaction events, the discrepancy at Cherenkov angle distribution between the expectation and the observation. If the error size due to neutral current events is larger than 10%, the SRN discovery does not reach 3σ confidence level with 10 years observation.

We suggest that the poor information about multiplicity of secondary γ-rays leading the discrepancy at angle distribution between data and MC simulations. An experimental proposal in RCNP plans to measure the γ-rays induced by neutrons, and the results are expected to be helpful to reduce the current uncertainty.

Appendix A

Neutrino Mass and Neutrino Oscillation Theory

This chapter describes the theory of neutrino mass, the theory of neutrino oscillation, and the neutrino oscillation probabilities with one sterile neutrino state.

A.1 neutrino mass

A.1.1 Dirac mass

Let us consider the free Dirac particles that have spin of half. The Langrangian is written as below:

$$\mathcal{L} = \overline{\psi}[i\gamma_\mu \frac{\partial}{\partial x_\mu} - m_D]\psi \tag{A.1}$$

The fermion spinor ψ is projected into left-handed part and right-handed part by chiral projections as $\psi = (P_L + P_R)\psi = \frac{1}{2}(1-\gamma_5)\psi + \frac{1}{2}(1+\gamma_5)\psi = \psi_L + \psi_R$, where the two project operators are $P_L = \frac{1}{2}(1-\gamma_5)$ and $P_R = \frac{1}{2}(1+\gamma_5)$. For two arbitrary spinors ψ and ϕ, their relations are like below:

$$\overline{\psi_L}\phi_L = \overline{\psi}P_R P_L \phi = 0, \quad \overline{\psi_R}\phi_R = 0 \tag{A.2}$$

so the product of two spinors is written as

$$\overline{\psi}\phi = (\overline{\psi}_L + \overline{\psi}_R)(\phi_L + \phi_R) = \overline{\psi}_L\phi_R + \overline{\psi}_R\phi L \tag{A.3}$$

The Dirac mass term in Langrangian is written in chiral components as below[1]

$$\mathcal{L} = -m_D(\overline{\psi}_L\phi_R + \overline{\psi}_R\phi_L) + h.c. \tag{A.4}$$

If the ν_R exists in addition to ν_L, the Dirac mass term for 3 flavor neutrinos is described as below

$$\mathcal{L} = -\overline{\psi_R^\alpha} m_{D,\alpha\beta}\psi_L^\beta + h.c. \tag{A.5}$$

where the $m_{\alpha\beta}$ is a mass matrix. We consider the neutrinos have three flavor eigenstates of weak interaction as $\nu^\alpha = (\nu_e, \nu_\mu, \nu_\tau)$. Then, the mass term of Langrangian is diagonalized by a unit transformation matrix as below

$$\nu_L^\beta = U_{\beta,j}\nu_L^{'j} \tag{A.6}$$

[1] *h.c.* signifies Hermitian conjugate

$$\nu_R^{\alpha} = V_{\alpha,i}\nu_R^{'i} \tag{A.7}$$

where the unitary matrix U is the Pontecorvo–Maki–Nakagawa–Sakata (PMNS) matrix[11], which is referred to as the neutrino mixing matrix. The details of the matrix are described in the next section. We substitute the matrix into the Langrangian as follows

$$\begin{aligned}\mathcal{L} &= -\overline{\nu_R^{'i}}V_{i,\alpha}^{\dagger}m_{D,\alpha\beta}U_{\beta,j}\nu_L^{'j} + h.c. \\ &= -\overline{\nu_R^{'i}}m_{D,i}\nu_L^{'i} + h.c.\end{aligned} \tag{A.8}$$

where

$$V_{\alpha,i}^{\dagger}mU_{\beta,j} = m_i \tag{A.9}$$

where m_i is a diagonalized mass matrix here, and the $i = 1 \sim 3$ that means the 3 mass eigenstates. But, only left-handed Dirac neutrinos are found, the neutrino is massless in the Standard Model.

A.1.2 Majorana mass

The spinor ψ and its charge conjugation spinor $\psi_c(\equiv C\gamma^0\psi^*)$ compose the Majorana equation given by

$$i\not{\partial}\psi = m\psi_c \tag{A.10}$$

The two side of the equation have ψ and ψ_c respectively, so the spinor is electrically neutral field. We write the Langrangian mass term as below

$$\mathcal{L}_{mass} = -\frac{1}{2}\overline{\nu}_L^{\alpha c}m_{M,\alpha\beta}\nu_L^{\beta} + h.c. \tag{A.11}$$

In a similar way with Dirac mass, we diagonalize the mass term by substituting Equation A.6

$$\begin{aligned}\mathcal{L}_{mass} &= -\frac{1}{2}\overline{\nu_L^{'ic}}U^{i,\alpha}m_{M,\alpha\beta}U^{\beta,j}\nu_L^{'j} + h.c. \\ &= -\frac{1}{2}\overline{\nu_L^{'ic}}m_{M,i}\nu_L^{'i} + h.c.\end{aligned} \tag{A.12}$$

Next, we consider the invariance of the mass term under a global transformation. A lepton under the global transformation ($e^{i\alpha}$ is as below:

$$\psi \to e^{i\alpha}\psi \qquad \overline{\psi} \to e^{-i\alpha}\overline{\psi} \tag{A.13}$$

The charge conjugate of the lepton spinor under the global transfromation is written as

$$\psi^c \to (e^{i\alpha}\psi)^c = \eta_c C e^{i\overline{\alpha}}\psi^T = e^{-i\alpha}\psi^c \qquad \overline{\psi^c} \to e^{i\alpha}\overline{\psi^c} \tag{A.14}$$

As a result, the mass term of Equation A.12 is not invariant under the global transformation, and this connects to break a lepton number conservation by $\overline{\psi_L^c}\psi_L$.

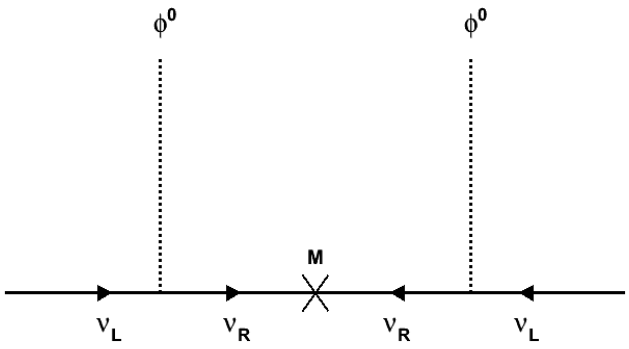

Figure A.1: Diagram of seesaw mechanism. The effective mass appears after the left-handed neutrinos interacting with Higgs field.

A.1.3 Seesaw mechanism

The Higgs field ϕ_0 exists in Yukawa coupling, so the Langrangian of lepton coupling is written as the following equation.

$$\mathcal{L} = f_\nu \overline{\nu}_R \phi l_L. \tag{A.15}$$

Then, the seesaw mechanism introduces the Majorana mass term which is composed from the right-handed neutrinos. Now, the Langrangian is as below.

$$\mathcal{L} = f_\nu \overline{\nu_R} \nu_L \langle \phi^0 \rangle + \frac{1}{2} M \overline{\nu_R^c} \nu_R + h.c. \tag{A.16}$$

The Langrangian is rewritten by diagonalizing the mass matrix,

$$\mathcal{L} = \frac{1}{2} (\overline{\nu_L^c}, \overline{\nu_R}) \begin{pmatrix} 0 & m \\ m & M \end{pmatrix} \begin{pmatrix} \nu_L \\ \nu_R^c \end{pmatrix} \tag{A.17}$$

where the mass matrix is $\begin{pmatrix} 0 & m \\ m & M \end{pmatrix}$, and $f_\nu \langle \phi^0 \rangle = m$. In Equation A.16, the effective mass M is much larger than the Higgs field.

The effective Langrangian is calculated from the diagram as shown in Figure A.1, and the seesaw mechanism gives the left handed neutrino a Majorana mass under Higgs field [15]. The effective Langrangian is written as below:

$$\mathcal{L} = \frac{f_\nu^2}{2M} \phi^0 \phi^0 \overline{\nu_L^c} \nu_L \tag{A.18}$$

The Dirac mass $m = f_\nu \langle \phi^0 \rangle$ compares with the mass matrix in Equation A.17. Then, we know

$$m_{\nu_L} \sim \frac{m^2}{M} \tag{A.19}$$

We know that the left-handed neutrino mass is $\frac{m^2}{M}$ which is very small comparing to other fermion mass in standard model. The right-handed neutrino mass M appears in higher unification theories.

A.2 Theory of neutrino oscillations

The idea of neutrino oscillation is proposed by B. Pontecorvo. First, R. Davis used the reactor anti-neutrino beam to search the following reaction.

$$\overline{\nu_e} + {}^{37}Cl \rightarrow e^- + {}^{37}Ar \tag{A.20}$$

This reaction is only allowed if the lepton number is not conserved. B. Pontecorvo predicted the reaction occurs under the hypothesis of $\overline{\nu} \longleftrightarrow \nu$ mixing [12], which is similar with K^0–$\overline{K^0}$ mixing. Beside that, Pontecorvo predicted that the existence of the following mode in muon decays.

$$\mu \rightarrow e + \gamma \tag{A.21}$$

From Ref. [13], the decay is allowed by the breaking lepton number conservation, and the flavor changing as the following transition: $\nu_\mu \longleftrightarrow \nu_e$. But, the previous two reactions are not found in experiments. In the same paper[13], Pontecorvo pointed out that we have chances to observe the neutrino oscillations from reactor or accelerator sources.

At present, we know that neutrino flavor changing exists. This section describes the neutrino oscillation probabilities.

neutrino mixing

The neutrino mixing is firstly proposed in Nagoya model by Z. Maki, M. Nakagawa, and S. Sakata in 1962 [11]. The two neutrino states in weak interaction is called as two "weak" neutrino states: ν_e, ν_μ. The authors introduced the two "true" neutrino states (ν_1, ν_2) that are expressed by linear combination of the "weak" neutrinos as below.

$$\begin{aligned} \nu_1 &= \nu_e \cos\delta + \nu_\mu \sin\delta \\ \nu_2 &= -\nu_e \sin\delta + \nu_\mu \cos\delta \end{aligned} \tag{A.22}$$

where the mixing angle δ is real number. The unitary mixing matrix $U = \begin{pmatrix} \cos\delta & \sin\delta \\ -\sin\delta & \cos\delta \end{pmatrix}$ connect the weak states and the true states together.

As mentioned previously, there are three generations ($N = 3$) for lepton and quarks in the Standard Model. The three "flavor" neutrino eigenstates $\nu^l = (\nu_e, \nu_\mu, \nu_\tau)$ are written as the linear combination of three "mass" neutrino eigenstates $\nu^i = (\nu_1, \nu_2, \nu_3)$.

$$\nu_L^l = U_{l,i}\nu_L'^i \tag{A.23}$$

where the unitary matrix $U_{l,i}$ is referred to as the Pontecorvo-Maki-Nakagawa-Sakata (PMNS) matrix, which describes the neutrino mixing. In the similar way with the Cabbibo-Kobayashi-Masukawa (CKM) matrix, the parameterization of the PMNS matrix is obtained as the following explanations. The degree of freedom for a N×N unitary matrix U is $2\mathrm{N}^2 - 2 \times \frac{N(N-1)}{2} - N = \mathrm{N}^2$, because of the constrain of $U^\dagger U = 1$. Then, the eigenstate bases are redefined by multiplying a phase, and the physics results do not change. Except an overall common phase, 2N−1 parameters are absorbed into the mass eigenstates and the flavor eigenstates. Thus, the total number of independent parameters is $\mathrm{N}^2 - (2\mathrm{N}-1) = (\mathrm{N}-1)^2$. Of these parameters, N(N−1)/2 variables are the mixing angles θ_{ij}. Other (N−1)(N−2)/2 variables are the complex phases δ_i, such as CP violation phases.

For three Dirac neutrinos, the PMNS matrix has 3 mixing angles and one CP violation phase. The mixing matrix is a product of three rotation matrices, and each of the rotation matrix has an mixing angles between two mass states:

$$U = \begin{pmatrix} 1 & 0 & 0 \\ 0 & c_{23} & s_{23} \\ 0 & -s_{23} & c_{23} \end{pmatrix} \begin{pmatrix} c_{13} & 0 & s_{13}e^{-i\delta} \\ 0 & 1 & 0 \\ -s_{13}e^{i\delta} & 0 & c_{13} \end{pmatrix} \begin{pmatrix} c_{12} & s_{12} & 0 \\ -s_{12} & c_{12} & 0 \\ 0 & 0 & 1 \end{pmatrix}$$

The product of the three matrices is written as

$$U = \begin{pmatrix} c_{12}c_{13} & s_{12}c_{13} & s_{13}e^{-i\delta} \\ -s_{12}c_{23} - c_{12}s_{23}s_{13}e^{i\delta} & c_{12}c_{23} - s_{12}s_{23}s_{13}e^{i\delta} & s_{23}c_{13} \\ s_{12}s_{23} - c_{12}c_{23}s_{13}e^{i\delta} & -c_{12}s_{23} - s_{12}c_{23}s_{13}e^{i\delta} & c_{23}c_{13} \end{pmatrix} \tag{A.24}$$

where $s_{ij} = \sin\theta_{ij}$ and $c_{ij} = \cos\theta_{ij}$. θ_{ij} is a mixing angle, δ is the CP violating phase for Dirac neutrino.

If the neutrino is a Majorana particle, that means that neutrino and anti-neutrino are the same in the mass basis. The $\nu_i^c = \nu_i$ condition constrain the mass eigenstate phase. Only N= 3 parameters are absorbed into the flavor eigenstates, and N(N−1)/2 = 3 complex phases remain in the mixing matrix. In addition to δ phase, we include two more CP-violating phases: α_1 and α_2. The PMNS matrix for the three Majorana neutrino mixing is written as below:

$$U^M = \begin{pmatrix} c_{12}c_{13} & s_{12}c_{13} & s_{13}e^{-i\delta} \\ -s_{12}c_{23} - c_{12}s_{23}s_{13}e^{i\delta} & c_{12}c_{23} - s_{12}s_{23}s_{13}e^{i\delta} & s_{23}c_{13} \\ s_{12}s_{23} - c_{12}c_{23}s_{13}e^{i\delta} & -c_{12}s_{23} - s_{12}c_{23}s_{13}e^{i\delta} & c_{23}c_{13} \end{pmatrix} \begin{pmatrix} e^{i\alpha_1/2} & 0 & 0 \\ 0 & e^{i\alpha_2/2} & 0 \\ 0 & 0 & 1 \end{pmatrix}$$

A.2.1 neutrino Oscillation in Vacuum

The neutrino flavor eigenstates are connected to the neutrino mass eigenstates by PMNS matrix as shown in Equation A.6. The mass eigenstates $|\nu_i\rangle$ are stationary states at the beginning. After a time interval, the mass states under time evaluations are given by

$$|\nu_i(\vec{x}, t)\rangle = e^{-iE_i t}|\nu_i(\vec{x}, t = 0)\rangle \tag{A.25}$$

The flavor neutrino states $|\nu_\alpha(\vec{x}, t)\rangle$ are the linear combination of the mass states.

$$|\nu_\alpha(\vec{x}, t)\rangle = \sum_i U_{\alpha,i}e^{-iE_i t}|\nu_i(\vec{x}, t = 0)\rangle = \sum_{i,\beta} U_{\alpha,i}U^*_{\beta,i}e^{-iE_i t}|\nu_\beta(\vec{x}, t = 0)\rangle \tag{A.26}$$

where the $|\nu_\beta(\vec{x}, t = 0)\rangle$ is the flavor state wave function at $t = 0$. The energy of i-th mass eigenstate E_i is expanded by relativistic approximation as $E_i = \sqrt{m_i^2 + p^2} \simeq p + m_i^2/2p \simeq p + m_i^2/2E_i$. Here, we suppose that $p >> m_i$, so $E \sim p$. The probability of flavor transition amplitude $\mathrm{A}(\alpha \to \beta)(t)$ at the certain time t is given by

$$A(\alpha \to \beta)(t) = \langle\nu_\beta|\nu_\alpha(\vec{x}, t)\rangle = e^{-ipt}\sum_{i,\beta} U^*_{\beta,i}U_{\alpha,i}e^{-im_i^2 t/2E} \tag{A.27}$$

Instead of time t, the distant L from the source to the detector is often used for probing the oscillation in neutrino oscillation. Now, the oscillation probability is derived as a function of distance $P(L) = |\mathrm{A}(\alpha \to \beta)|^2$ as follows:

$$\begin{aligned} P(\nu_\alpha \to \nu_\beta)(L) &= |A^2(\alpha \to \beta)|^2 \\ &= \sum_i \sum_j U_{\alpha i}U^*_{\alpha j}U^*_{\beta i}U_{\beta j}exp(-i\frac{(m_i^2 - m_j^2)L}{2E}) \\ &= \sum_{i,j} |U_{\alpha i}U^*_{\beta i}|^2 + 2Re\sum_{j>i} U_{\alpha i}U^*_{\alpha j}U^*_{\beta i}U_{\beta j}exp(-i\frac{(\Delta m_{ij}^2)L}{2E}) \end{aligned} \tag{A.28}$$

where the mass-squared splitting is $\Delta m^2_{ij} = m^2_i - m^2_j$. The neutrino flavor transition (oscillation) occurs, if at least two neutrino mass are not degenerate ($m_i \neq m_j$).

Two generation oscillation In neutrino oscillation experiments, the two flavor transition probability is measured by the following specific condition: The effect of one mixing angle is much more relevant than the effect from the other two angles, and the effect of one mass-squared splitting is much larger than the effect of the other one. To simplify the calculation, the three-flavor mixing is approximated as only the two-flavor mixing. The approximation of mixing matrix is represented as

$$U = \begin{pmatrix} \cos\theta & \sin\theta \\ -\sin\theta & \cos\theta \end{pmatrix}$$

The two mass eigenstates is $|\nu_i\rangle = \binom{\nu_1}{\nu_2}$. The oscillation probabilities are calculated as

$$\begin{array}{rcl} P(\nu_\alpha \to \nu_\alpha) & = & 1 - \sin^2 2\theta \sin^2(\frac{\Delta m^2 L}{4E}) \\ P(\nu_\alpha \to \nu_\beta) & = & \sin^2 2\theta \sin^2(\frac{\Delta m^2 L}{4E}) \end{array} \tag{A.29}$$

Here, the two neutrino scenario does not include the complex phase, and the CP is invariant in the oscillation. The probability of $\nu_\alpha \to \nu_\beta$ of Equation A.29 is the same with the probability of $\nu_\beta \to \nu_\alpha$, $\overline{\nu}_\alpha \to \overline{\nu}_\beta$, $\overline{\nu}_\beta \to \overline{\nu}_\alpha$.

Three generation oscillation The PMNS matrix of Dirac neutrino is used here, and the oscillation probability of $\nu_\alpha \to \nu_\beta$ is given by

$$\begin{aligned} P(\nu_\alpha \to \nu_\beta) = \delta_{\alpha\beta} &- 4\sum_{i>j}^{3} Re(U_{\alpha i}U^*_{\beta i}U^*_{\alpha j}U_{\beta j}) \sin^2(\frac{\Delta m^2_{ij} L}{4E}) \\ + \quad 4&\sum_{i>j}^{3} Im(U_{\alpha i}U^*_{\beta i}U^*_{\alpha j}U_{\beta j}) \sin(\frac{\Delta m^2_{ij} L}{4E}) \cos(\frac{\Delta m^2_{ij} L}{4E}) \end{aligned} \tag{A.30}$$

For the $\nu_\mu \to \nu_\mu$ oscillation, the probability under the limit $|\Delta m^2_{32}| >> |\Delta m^2_{21}|$ is

$$P(\nu_\mu \to \nu_\mu) \simeq 1 - 4c^2_{13}s^2_{23}(1 - c^2_{13}s^2_{23}) \sin^2(\frac{\Delta m^2_{32} L}{4E_\nu}) \tag{A.31}$$

The leading term of $\nu_\mu \to \nu_e$ oscillation probability is given by:

$$P(\nu_\mu \to \nu_e) \simeq 4c^2_{13}s^2_{13}s^2_{23} \sin^2(\Delta_{31}) \tag{A.32}$$

where the phase factor is given by

$$\Delta_{ij} = \frac{\Delta m^2_{ij} L}{4E_\nu} = 1.27 \frac{\Delta m^2_{ij}[eV^2] L[km]}{E_\nu[GeV]} \tag{A.33}$$

A.2.2 Neutrino Oscillation in Matter

The missing solar neutrino problem as mentioned in Section 1.3.2 is solved by the neutrino oscillations as the following descriptions: The ν_e disappearance occurs inside the Sun and in the vacuum space. The disappearance results of solar neutrino are compared

to the disappearance results of reactor neutrino oscillation, and there is expected to the extra mixing effect for traveling in dense matter of the Sun (the MSW effect or matter effect). The modified oscillation model in matter is proposed by Stanislav Mikheyev, Alexei Smirnov, and Lincoln Wolfenstein [16, 17].

The physical scenario of the MSW effect is as follows: If ν travel travel in matter, all three flavors of neutrinos interact with electrons of matter via neutral weak current, and only ν_es interact with electrons in matter via both charge weak current and neutral weak current. The NC interactions only induce a phase term over all flavors, so the NC effect does not change the oscillation results. While the CC interactions have contributions to ν_es, and the effective Hamiltonian due to the MSW effect is given by

$$H_{MSW} = \frac{G_F}{\sqrt{2}}[\overline{e}\gamma^\mu(1-\gamma_5)\nu_e][\overline{\nu_e}\gamma_\mu(1-\gamma_5)e]. \tag{A.34}$$

After a Fierz transformation, the Hamiltonian becomes

$$H_{MSW} = \frac{G_F}{\sqrt{2}}[\overline{\nu_e}\gamma^\mu(1-\gamma_5)\nu_e][\overline{e}\gamma_\mu(1-\gamma_5)e]. \tag{A.35}$$

The second term of the Hamiltonian represent the four-current density of the electrons. As there is no permanent current density in the Sun, the spatial components of current must be zero. The four-current density of the electrons is as follows

$$\begin{aligned} \langle e|\overline{e}\gamma^i(1-\gamma_5)e|e\rangle &= 0 \\ \langle e|\overline{e}\gamma^0(1-\gamma_5)e|e\rangle &= N_e \end{aligned}$$

where the N_e is the electron number density in matter. For the left-handed neutrinos, $(1-\gamma_5)$ is replaced by 2. Now, the effective Hamiltonian is written as

$$H_{MSW} = \sqrt{2}G_F N_e \overline{\nu_e}\gamma_0\nu_e = V_{eff}\overline{\nu_e}\gamma_0\nu_e \tag{A.36}$$

ν_e receives a potential $V_{eff} = \sqrt{2}G_F N_e$ in matter, while $\overline{\nu}_e$ receives a potential of $-\sqrt{2}G_F N_e$. Let us consider a two-flavor oscillation, the Schrodinger equation of neutrino is given by

$$i\frac{d}{dt}|\nu^\alpha\rangle_t = (\frac{m^\dagger m}{2E} + V_{eff})|\nu^\alpha\rangle \tag{A.37}$$

where the m is the mass matrix, and the mass term is written as $m^\dagger m = U m^2_{diag} U^\dagger$. Here, the two mass square m_1^2, m_2^2 are replaced with mass-squares splitting Δm^2. Then, $\sqrt{2}G_F N_e$ substitutes V_{eff} for only electron neutrinos, the equation becomes

$$i\frac{d}{dt}\begin{pmatrix}\nu_e\\ \nu_\mu\end{pmatrix} = \begin{pmatrix} -\frac{\Delta m^2}{4E}\cos 2\theta + \sqrt{2}G_F N_e & \frac{\Delta m^2}{4E}\sin 2\theta \\ \frac{\Delta m^2}{4E}\sin 2\theta & \frac{\Delta m^2}{4E}\cos 2\theta \end{pmatrix}\begin{pmatrix}\nu_e\\ \nu_\mu\end{pmatrix} \tag{A.38}$$

We diagonalize the above Hamiltonian as follows

$$\begin{pmatrix}\nu_e\\ \nu_\mu\end{pmatrix} = U\begin{pmatrix}\tilde{\nu_1}\\ \tilde{\nu_2}\end{pmatrix} = \begin{pmatrix}\cos\tilde{\theta} & \sin\tilde{\theta}\\ -\sin\tilde{\theta} & \cos\tilde{\theta}\end{pmatrix}\begin{pmatrix}\tilde{\nu_1}\\ \tilde{\nu_2}\end{pmatrix} \tag{A.39}$$

where the $\tilde{\theta}$ is given by

$$\cos 2\tilde{\theta} = \frac{-A/\Delta m^2 + \cos 2\theta}{\sqrt{(A/\Delta m^2 - \cos 2\theta)^2 + \sin^2 2\theta}} \tag{A.40}$$

$$\sin 2\tilde{\theta} = \frac{\sin 2\theta}{\sqrt{(A/\Delta m^2 - \cos 2\theta)^2 + \sin^2 2\theta}} \tag{A.41}$$

and A is given by

$$A(x) = 2\sqrt{2}G_F E N_e \approx 7.56 \times 10^{-5} eV^2 (\frac{\rho(x)}{g/cm^3})(\frac{E}{GeV}), \tag{A.42}$$

where G_F is the Fermi coupling constant, E is the neutrino energy, and N_e is the electron number density in the matter. N_e is proportional to the matter density $\rho(x)$ inside the Sun. Here, the modified mass eigenvalues $\tilde{m}^2_{1,2}$ become

$$\tilde{m}^2_{1,2} = \frac{A}{2} \mp \frac{1}{2}\sqrt{(A - \Delta m^2 \cos 2\theta) + (\Delta m^2)^2 \sin^2 2\theta}. \tag{A.43}$$

As a result, we use the same equation of oscillation probability with modified parameters. The $\nu_e \to \nu_e$ probability averaged by time becomes as follows.

$$P_{\nu_e \to \nu_e} = \sin^2\theta \sin^2\tilde{\theta} + \cos^2\theta \cos^2\tilde{\theta} \tag{A.44}$$

If the neutrino mixing reaches maximum, the modified angle is $\tilde{\theta} = \frac{\pi}{4}$. The maximum mixing is referred to as "resonance", and the resonance occurs at $A = \Delta m^2 \cos 2\theta$, where the electron density $N_{e,crit}$ is

$$N_{e,crit} \equiv \frac{1}{2\sqrt{2}G_F}\frac{\Delta m^2 \cos 2\theta}{E} \tag{A.45}$$

where $N_{e,crit}$ is called as "critical" electron density. We suppose that the density of Sun is decreasing exponentially from the Sun's core. If the electron neutrinos travel somewhere with mass density that is the same with the critical density, the electron flavor changes to muon flavor maximumly at there. After the resonance occurring, the flavor transition is relatively small until the arrival to Earth.

For long-baseline accelerator neutrino experiments, the mass effect also appears as a minor term of oscillation probability $P(\nu_\mu \to \nu_e)$, which is written as below

$$P(\nu_\mu \to \nu_e) \approx (1 \pm 2\frac{A(x)}{\Delta m^2_{32}}) P_{vac}(\nu_\mu \to \nu_e) \tag{A.46}$$

where $P_{vac}(\nu_\mu \to \nu_e)$ is the oscillation probability in vacuum. In the extra term of $\pm 2\frac{A(x)}{\Delta m^2_{32}}$, the plus sign refers to neutrino, and minus refers to anti-neutrino. If the sign of Δm^2_{32} is plus, the mass effect enhances (suppresses) the oscillation probability for neutrino (anti-neutrino). This is vice versa for the minus sign of Δm^2_{32}. We call the plus (minus) sign of Δm^2_{32} is normal (inverted) hierarchy of neutrino mass. The mass effect gives us a chance to determine the mass hierarchy and the baseline mass density by accelerator neutrino experiments.

A.2.3 CP violation

If we apply a $\mathcal{CP}$ operator to a particle with velocity $\mathbf{v}$, the corresponding antiparticle with velocity $-\mathbf{v}$ is obtained. The CP symmetry refers command physical laws for particles and anti-particles. Hence, searching for a CP violation is a key to solve intrinsic

difference for matter and anti-matter. The CP violation appears in the oscillation probabilities difference between neutrino and anti-neutrino. Here, the CP violation in the neutrino oscillations is described.

Let us recall the neutrino oscillation probability as below:

$$P(\nu_\alpha \to \nu_\beta; U)(L) = \sum_i \sum_j U_{\alpha i} U^*_{\alpha j} U^*_{\beta i} U_{\beta j} exp(-i\frac{(m_i^2 - m_j^2)L}{2E})$$

If we exchange the two flavors, the oscillation probability of $P(\nu_\beta \to \nu_\alpha)$ is given by

$$P(\nu_\beta \to \nu_\alpha; U)(L) = \sum_i \sum_j U_{\beta i} U^*_{\beta j} U^*_{\alpha i} U_{\alpha j} exp(-i\frac{(m_i^2 - m_j^2)L}{2E}) = P(\nu_\alpha \to \nu_\beta; U^*)(L) \tag{A.47}$$

By the way, the CPT invariant suggests as the following equation.

$$P(\nu_\beta \to \nu_\alpha; U) = P(\overline{\nu}_\alpha \to \overline{\nu}_\beta; U) \tag{A.48}$$

We compare Equation A.47 and Equation A.48 to obtain the following equation.

$$P(\overline{\nu}_\alpha \to \overline{\nu}_\beta; U) = P(\nu_\alpha \to \nu_\beta; U^*) \tag{A.49}$$

The anti-neutrino oscillation probability is obtained by replacing unitary matrix U with its complex conjugate matrix U^* in neutrino oscillation probability. For Dirac neutrinos, the complex conjugate matrix U^* of the PMNS matrix replaces its complex phase δ with $-\delta$. Therefore, we replace the CP phase δ in the neutrino oscillation probability with $-\delta$ to get anti-neutrino oscillation probability. In practice, the CP violation is observed from the difference between $P(\nu_\mu \to \nu_e)$ and $P(\overline{\nu}_\mu \to \overline{\nu}_e)$. The neutrino oscillation probability of $\nu_\mu \to \nu_e$ is written as

$$\begin{aligned}
P(\nu_\mu \to \nu_e) = & \; 4c_{13}^2 s_{13}^2 s_{23}^2 \sin^2\Delta_{31} \\
+ & \; 8c_{13}^2 s_{12} s_{13} s_{23}(c_{12}c_{23}\cos\delta - s_{12}s_{13}s_{23})\cos\Delta_{32}\sin\Delta_{31}\sin\Delta_{21} \\
- & \; 8c_{13}^2 c_{12}c_{23}s_{12}s_{13}s_{23}\sin\delta\sin\Delta_{32}\sin\Delta_{31}\sin\Delta_{21} \\
+ & \; 4s_{12}^2 c_{13}^2(c_{12}^2 c_{23}^2 + s_{12}^2 s_{23}^2 s_{13}^2 - 2c_{12}c_{23}s_{12}s_{23}s_{13}\cos\delta)\sin^2\Delta_{21} \\
+ & \; 8c_{13}^2 s_{13}^2 s_{23}^2(1-2s_{13}^2)(\frac{a}{\Delta m_{31}^2}\sin^2\Delta_{31} - \frac{a\cdot L}{4E_\nu}\cos\Delta_{32}\sin\Delta_{31})
\end{aligned} \tag{A.50}$$

where the last term in the equation is due to the matter effect for long base-line, and the coefficient a is a[eV]$= 7.56 \times 10^{-5}\rho$[g/cm^3]$E_\nu$[GeV]. The corresponding probability of anti-neutrino oscillation is obtained by $\delta \to -\delta$ and $a \to -a$. Now, the magnitude of the difference of neutrino-antineutrino oscillation probability in vacuum is given by

$$\Delta P = P(\nu_\mu \to \nu_e) - P(\overline{\nu}_\mu \to \overline{\nu}_e) = -16\sin\delta \cdot c_{13}^2 c_{12}c_{23}s_{12}s_{13}s_{23}\sin\Delta_{32}\sin\Delta_{31}\sin\Delta_{21} \tag{A.51}$$

The difference between the two probabilities depends on the CP phase δ. For example, if the delta angle is $\delta = \pm\pi/2$, the CP violance of neutrino oscillation is at maximum. The oscillation probabilities of $\nu_\mu \to \nu_e$ and $\overline{\nu}_\mu \to \overline{\nu}_e$ at the T2K experiment are shown in Figure A.2. The T2K experiment has high potential to measurement the probability difference ΔP leading to prove CP violation in lepton sector in future.

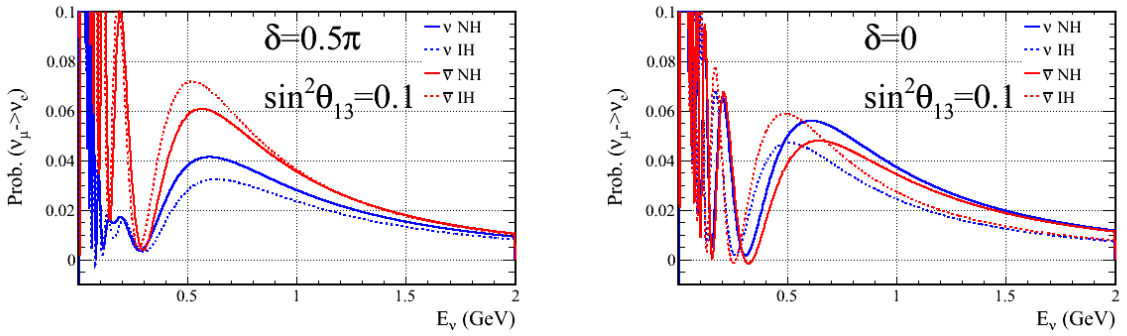

Figure A.2: The oscillation probabilities of $P(\nu_\mu \to \nu_e)$ and $P(\overline{\nu}_\mu \to \overline{\nu}_e)$ at the T2K experiment are shown, and the base-line length is 295km. If the delta angle is $\delta = \pi/2$ as shown in the left plot, the difference of two probabilities is large at $E_\nu = 600$ MeV. If the delta angle δ is zero, there is no obvious difference of the two neutrino oscillation probabilities at $E_\nu = 600$ MeV as shown in the right plot.

A.3 Oscillation probabilities with one sterile neutrino state

As mentioned in Section 1.3.3, there are "3+2" model and "3+1" model to explain the LSND anomalies. For long-baseline neutrino experiments, there is a chance to find active-sterile neutrino oscillation by searching the disappearance of neutron current events in far detector. Here, the scenario with one sterile neutrino ν_s and three active neutrinos ν_e, ν_μ, ν_τ is studied. Therefore, one more mass state ν_4 is introduced the expanded 4×4 unitary mixing matrix given by

$$\begin{aligned} U &= R_{34}(\theta_{34})R_{24}(\theta_{24},\delta_2)R_{14}(\theta_{14})R_{23}(\theta_{23})R_{13}(\theta_{13},\delta_1)R_{12}(\theta_{12},\delta_3) \\ &\simeq R_{34}(\theta_{34})R_{24}(\theta_{24},\delta_2)R_{14}(\theta_{14})R_{23}(\theta_{23})R_{13}(\theta_{13},\delta_1) \end{aligned} \tag{A.52}$$

where R_{ij} means an element of mixing matrix. Because of $L/E_\nu = 295.0[\text{km}]/0.63[\text{GeV}] \sim 468$, the oscillation is more sensitive to Δm_{32} than Δm_{21}. The two mass states m_1, m_2 are assumed to be degenerate in the analysis, the mixing matrix is represented as the approximation in the second line of Equation A.52.

Then, the mixing matrix is written as

$$U = \begin{pmatrix} U_{e1} & U_{e2} & c_{14}s_{13}e^{-i\delta_1} & s_{14} \\ U_{\mu 1} & U_{\mu 2} & -s_{14}s_{13}s_{24}e^{-i(\delta_1+\delta_2)} + c_{13}s_{23}c_{24} & c_{14}s_{24}e^{-i\delta_2} \\ U_{\tau 1} & U_{\tau 2} & -s_{14}c_{24}s_{34}s_{13}e^{-i\delta_1} - c_{13}s_{23}s_{34}s_{24}e^{i\delta_2} + c_{13}c_{23}c_{34} & c_{14}c_{24}s_{34} \\ U_{s1} & U_{s2} & -s_{14}c_{24}c_{34}s_{13}e^{-i\delta_1} - c_{13}s_{23}c_{34}s_{24}e^{i\delta_2} - c_{13}c_{23}s_{34} & c_{14}c_{24}c_{34} \end{pmatrix} \tag{A.53}$$

where s_{ij} is $\sin\theta_{ij}$, c_{ij} is $\cos\theta_{ij}$, and δ_i is the CP phase of mixing matrix for Dirac neutrinos. As discussed in Section 1.3.1, the oscillation probability of ν_μ disappearance is given by

$$\begin{aligned} P(\nu_\mu \to \nu_\mu)(L) = 1 - 4\{&|U_{\mu 3}|^2(1 - |U_{\mu 3}|^2 - |U_{\mu 4}|^2)\sin^2\Delta_{31} \\ &+|U_{\mu 4}|^2|U_{\mu 3}|^2\sin^2\Delta_{43} + |U_{\mu 4}|^2(1 - |U_{\mu 3}|^2 - |U_{\mu 4}|^2)\sin^2\Delta_{41}\}, \end{aligned} \tag{A.54}$$

and the other oscillation probabilities are written as

$$\begin{aligned} P(\nu_\mu \to \nu_\alpha)(L) = 4Re\{&|U_{\mu 3}|^2|U_{\alpha 3}|^2 \sin^2 \Delta_{31} + |U_{\mu 4}|^2|U_{\alpha 4}|^2 \sin^2 \Delta_{41} \\ &+U^*_{\mu 4}U_{\alpha 4}U_{\mu 3}U^*_{\alpha 3}(\sin^2 \Delta_{31} - \sin^2 \Delta_{43} + \sin^2 \Delta_{41})\} \\ &+2Im\{U^*_{\mu 4}U_{\alpha 4}U_{\mu 3}U^*_{\alpha 3}(\sin 2\Delta_{31} - \sin 2\Delta_{41} + \sin 2\Delta_{43})\}, \end{aligned} \tag{A.55}$$

where ν_α is ν_e, ν_τ or sterile neutrino ν_s, and ν_s does not interact with nucleus via weak interactions. As the effective potential for three active neutrino are the same, so the mass effect is neglected in the sterile search analysis.

Appendix B

Event reconstruction

B.1 Cherenkov radiation in Super-K

The Super-Kamikande detector observes Cherenkov light emitted in water. If a charge particle travels through a material at a speed βc faster than the speed of light c/n through the material ($\beta c \geq c/n$), and the charger particle emits Cherenkov lights. The Cherenkov light is emitted in a cone pattern, and the cone angle obeys the Cherenkov angle formula as below:

$$\cos\theta_c = \frac{ct/n}{\beta ct} = \frac{1}{n\beta}, \quad \beta > \frac{1}{n} \tag{B.1}$$

where the refractive index of water is $n = 1.33$. On other hand, a minimal velocity for a charge particle to emit Cherenkov in water is 0.75c as follows

$$\beta = \frac{1}{n} = \frac{1}{1.33} = 0.75 \tag{B.2}$$

For the analysis, the electrons with 10 MeV emit Cherenkov light with a Cherenkov angle of $\sim 42^o$ as below

$$\beta = \sqrt{1 - \frac{m_e^2}{E_e^2}} = \sqrt{1 - \frac{0.511^2}{10^2}} = 0.9987 \quad (\text{if } \mathsf{E_e} = 10\mathsf{MeV})$$

$$\cos\theta_c = \frac{1}{n\beta} = \frac{1}{1.33 \times 0.9987} \sim 0.75 \quad \theta_c \sim 42 \ \mathsf{degree} \tag{B.3}$$

The number of photons emitted per unit wavelength $d\lambda$ per unit distance dx is given by

$$\frac{d^2N_\gamma}{dxd\lambda} = \frac{2\pi\alpha z^2}{\lambda^2}(1 - \frac{1}{n^2\beta^2}) = \frac{2\pi\alpha z^2}{\lambda^2}\sin^2\theta_c \tag{B.4}$$

where α is the fine structure constant, and the transverse particle have a charge of ze. If a relativistic electron is traveling through the Super-K water, the number of emitted Cherenkov photons is estimated as $300 \sim 400$ per cm.

The de-excitation γ-rays have energy of $\mathcal{O}$(MeV), and the γ-rays scatter with electrons in water easily. Super-K observes the Cherenkov photons produced by the Compton scattered electrons. The selection for the reconstructed energy of γ-rays are the energy region of $4 \sim 30$ MeV, and the number of emitted Cherenkov photon is a distribution of

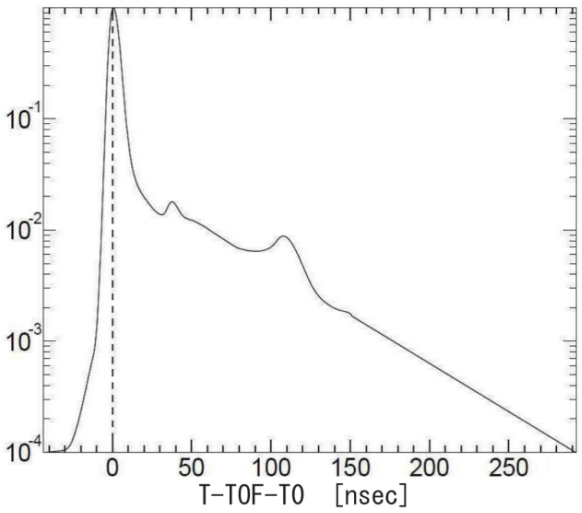

Figure B.1: Probability density function which is obtained from LINAC calibration [120]. The maximum peak is at 0 ns. The peaks at 40 ns and 110 ns are caused by after pulse of PMTs.

region $600 \sim 6000$, and the number of hit PMTs is a distribution of $25 \sim 200$ hit PMTs. In an event, most signal of hit PMTs are only one photo-electron. Thereby, it is not easy to obtain the event information by the numbers of photoelectrons of the hit PMTs. The timing and the position of all hit PMTs are used for reconstructing the information of events. The event reconstruction is described in the following sections.

B.2 Low energy event reconstruction

BONSAI (branch optimization navigating successive annealing iterations) fit is used as a reconstruction tool, which is suitable for Super-K events with the energy lower than 100MeV [85]. This section describes how the BONSAI fit reconstructs vertex information, and other tools to reconstruct direction, energy information. The details of the reconstruction are mentioned in Ref. [86]. Firstly, we use the BONSAI fit to search the vertex inside the Super-K tank. Then, the vertex information is used to reconstruct other event information.

B.2.1 Vertex Reconstruction

The vertex of an event refers to the position where the track of a charge particle started out, so the vertex is not far from the position of the neutrino interaction.

To search the vertex of the event, the BONSAI fitter performs a maximum likelihood fit to the timing residuals of all hit PMTs. The residual timing t_{res} of *i-th* hit PMT is defined by

$$t_{res,i}(\vec{x}) = t_i - t_{tof,i} = t_i - \frac{|\vec{h_i} - \vec{x}|}{c'}, \tag{B.5}$$

where the t_i is the time of *i-th* hit PMT, and $t_{tof,i}$ is the time of flight (TOF) which means Cherenkov light incident from the hypothesis vertex into the *i-th* hit PMT. h_i is position of *i-th* hit PMT, and $\vec{x}$ is the position of hypothesis vertex. If the real vertex is substituted into $\vec{x}$, $t_{res,i}$ of all hit PMTs have a common value. We build a likelihood

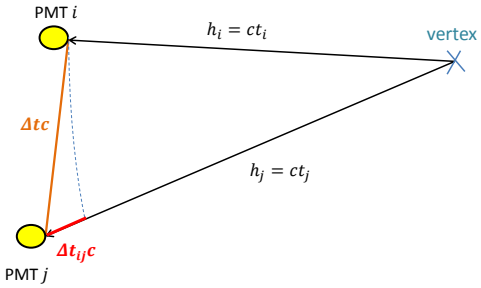

Figure B.2: The inequality for a possible vertex and two hit PMTs is written as $\Delta t_{ij} < \Delta x/c = |\vec{h_i} - \vec{h_j}|/c$.

function that has maximum value with the same residual timing $t_{res,i}$. The likelihood function is given by:

$$\mathcal{L}(\vec{x}, t_0) = \sum_{i=1}^{N_{hit}} log(P(t_i - t_{tof} - t_0)) \tag{B.6}$$

where t_0 is time offset of the iteration result, and t_0 represents a common value of $t_{res,i}$. To deal with the real detector response of events, we use the LINAC calibration data to construct a probability density function $P(t_{res,i} - t_0)$ as shown in Fig. B.1. The function $P(t_{res,i} - t_0)$ has a highest peak at $t_{res,i} - t_0 = 0$, that is consistent with the feature of timing distribution of the hit PMTs.

To calculate the likelihood value, we select a set of hit PMTs, and the difference of the arrival timings Δt_{ij} have to satisfy the triangle inequality as below

$$\Delta t_{ij} < \Delta x/c = |\vec{h_i} - \vec{h_j}|/c \tag{B.7}$$

Figure B.2 shows that the triangle consists of a vertex and two hit PMTs, so the hit PMTs corresponding to the vertex by the above inequality. We choose the set of hit PMTs with the largest number of selected hit PMTs. To remove the effect of dark noise, we remove the hit PMTs which are located more than 12.5 meter or 35 ns apart from any other hit PMTs.

Because the tracks of Compton scattered electrons are only several centimeters, we view the tracks to be a point at the vertex. Since the photons are produced at the vertex and travel on a light cone in Minkowski space, we write down the four equations to solve a vertex. In the set of hit PMTs, any four hit PMTs construct a vertex $\nu_\alpha = (\nu_x, \nu_y, \nu_z, ct)$ that satisfy the below equation.

$$\sum_\alpha (x_{i\alpha} - \nu_{i\alpha})(x^{i\alpha} - \nu^{i\alpha}) = 0 \quad (\mathsf{i} = 1 \sim 4\,\mathsf{hit\,PMT}) \tag{B.8}$$

where the coordinates of the four hit PMTs are $x_{i\alpha} = (x_{ix}, x_{iy}, x_{iz}, ct_i)$. We use the likelihood function of Equation B.6 to get likelihood values of all possible vertices. At the beginning, we pick up the vertex with maximum likelihood value as the beginning vertex. Next, we calculate the 12 likelihood values using 12 vertices around the beginning vertex. These vertices are 7.8 meter distant with each other, then we select the vertex maximum likelihood from the 12 vertex and the beginning vertex. We iterate the similar

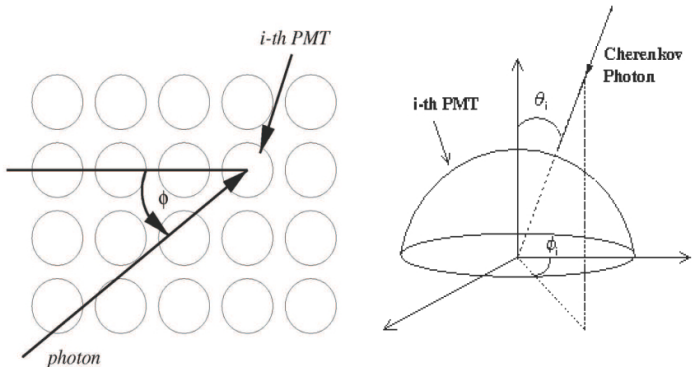

Figure B.3: Definition of the incident angle (θ_i, ϕ_i) of the i-th hit PMT [121].

searches to find the fine position by contract the search grid of 0.36 times than previous length every time. Until the the length of search grid is less than 1cm, we stop the vertex search. The vertex solution is found as $\sim$ 77 cm for 6 MeV electrons by calibrations.

B.2.2 Direction Reconstruction

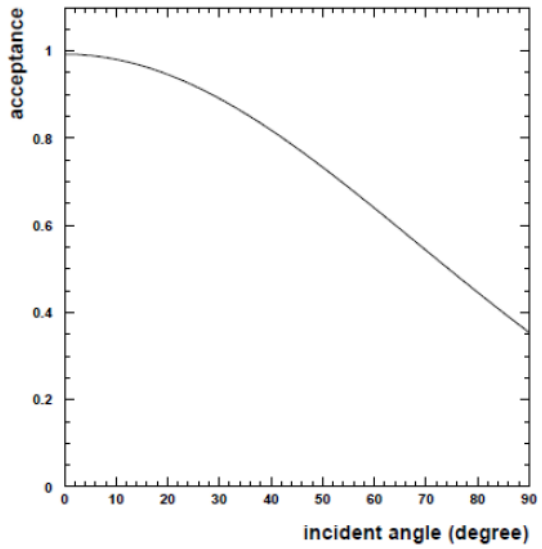

Figure B.4: The incident angle distribution of PMT acceptance $a(\theta_i)$ [121].

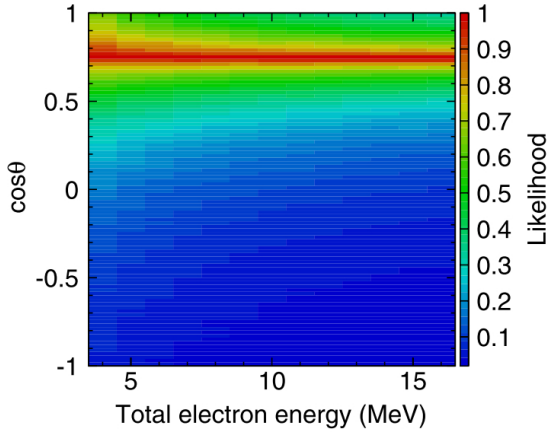

Figure B.5: The likelihood function for reconstruction of direction is a function of a reconstructed energy and a opening angle. The opening angle of the i-th PMT is angle between the reconstructed direction and the direction from vertex to each hit PMT [121].

After determining the vertex position, the vertex information is used to do a maximum likelihood fit with Cherenkov ring pattern to find the direction of scattered electron. First, the hit PMTs are rearranged by residual timing $t_{res,i}(\vec{x})$ order. Second, we find a maximum number of hit PMTs within 20 ns N_{20}, and the hit PMTs of N_{20} are expected to compose a ring pattern. Third, a likelihood function is used to find most possible direction that construct the Cherenkov light cone. The likelihood function is written as

below:

$$\mathcal{L}(\vec{d}) = \sum_{i=1}^{N_{20}} log(P_i(\cos\theta_{dir,i}, E_{rec}) \times \frac{\cos\theta_i}{a(\theta_i)}) \tag{B.9}$$

where $\vec{d}$ is a hypothesis direction, and θ_{dir} is the angle between $\vec{d}$ and the direction from the vertex to the *i-th* hit PMT. The incident angle θ_i of a photon onto a PMT is as shown in Fig.B.3. The acceptance of PMT a is a function of an incident angle θ_i, as shown in Figure B.4. Therefore, we have to consider a correction in the likelihood function, and the correction term is written as $\cos\theta_i/a(\theta_i)$.

$P_i(\cos\theta_{dir,i}, E)$ is probability density function of θ_{dir} and the reconstructed energy E_{rec}. Figure B.5 shows the 2-dimension distribution of the p.d.f. function $P_i(\cos\theta_{dir}, E_{rec})$, and the peaks locate at the energy to the corresponding $\cos\theta_{dir}$. The direction reconstruction is depend on a reconstructed energy value, so we iterate the direction reconstruction and the energy reconstruction to get the final values.

B.2.3 Energy Reconstruction

To reconstruct the energy value of the event, we find the maximum number of hit PMTs within 50 ns window N_{50}. The selected hit PMTs of N_{50} are used for the energy reconstruction. Several corrections and subtract dark noise are done to estimate the number of real effective hit PMTs, we call the number as N_{eff}. N_{eff} of an event is calculated by

$$N_{eff} = \sum_{i=1}^{N_{50}} \{X_i + \epsilon_{tail} - \epsilon_{dark}) \times \frac{N_{all}}{N_{alive}} \frac{1}{S(\theta_i, \phi_i)} \times exp(\frac{r_i}{\lambda(t)}) \times G_i(t)\} \tag{B.10}$$

The explanations for correction factors and dark noises term in Equation B.10 are as follows:

X_i: The factor estimates the number of multiple photoelectrons in the i-th hit PMT. If the hit PMT is close to the vertex, the Cherenkov cone does not expand widely. The observed number of photoelectrons is expected to be more than one. X_i is defined as

$$X_i = \begin{cases} \frac{log\frac{1}{1-x_i}}{x_i}, & x_i < 1 \\ 3.0, & x_i = 1 \end{cases} \tag{B.11}$$

$$x_i = \frac{N_{neigh,hit,i}}{N_{neigh,i}} \tag{B.12}$$

where $N_{neigh,i}$ is number of live PMT in 3×3 PMT surrounding the i-th hit PMT, and that means the neighboring 8 PMTs minus the number of bad PMTs. $N_{neigh,hit,i}$ is a number of hit PMTs among the 8 neighboring PMTs excluding the bad PMTs. The $log(1-x_i)^{-1}$ term expresses the average number of photoelectron per PMT in the area obtained from the Poisson statics.

ϵ_{tail}: Late (tail) hit correction factor. Some Cherenkov photons are scattered in water or reflected by surface of inner wall, thus they are too late to be included within 50 ns window. Here, the number of hits PMT within 100 ns window N_{100} is used to estimate

the effect of the late hit PMTs. The hit PMTs due to dark noise are subtracted to get ϵ_{tail} as below:

$$\epsilon_{tail} = \frac{N_{100} - N_{50} - N_{alive} \times R_{dark} \times 50ns}{N_{50}} \tag{B.13}$$

where N_{alive} is the number of all functional PMTs, that means the number of all PMT minus the number of bad PMT. R_{dark} is the dark noise rate.

ϵ_{dark}: The factor of the accidental dark noise of PMTs. The dark noise rate during the SK IV period is about 4.5KHz.

$$\epsilon_{dark} = \frac{N_{alive} \times R_{dark} \times 50ns}{N_{50}} \tag{B.14}$$

$\frac{N_{all}}{N_{alive}}$: Correction factor for the number of dead PMT. The number of total PMT N_{all} is 11,129 during the SK IV period.

$\frac{1}{S(\theta_i,\phi_i)}$: PMT photo-cathode coverage correction. $S(\theta_i, \phi_i)$ is an effective photo-cathode area as viewing from the angles (θ_i, ϕ_i), and the definition of angle (θ_i, ϕ_i) is shown in Figure B.3. The function $S(\theta_i, \phi_i)$ is determined by MC simulation with the fiber-reinforced plastic PMT covers. The LINAC calibration and DT calibration are used to check the effect of photo-cathode coverage correction on N_{eff}.

$exp(\frac{r_i}{\lambda(t)})$: Correction factor for water transparency. r_i is the distance from the vertex to the i-th PMT. $\lambda(t)$ is the water transparency factor which is varying with the SK RUN period.

$G_i(t)$: This factor adjusts relative quantum efficiency for all PMTs. The calibration for Q.E. of all PMTs is described in Ref. [82].

N_{eff} is determinated by the Equation B.10, and we use N_{eff} to determine the reconstructed energy of the event E_{rec}. The reconstruction energy $E_{rec}(N_{eff})$ is obtained by MC simulation events which are using a mono-energetic electron source. In low energy region ($E_{rec} < 25$ MeV), $E_{rec}(N_{eff})$ is a fourth order function of N_{eff} given by

$$E_{rec} = 0.82 + 0.13 \times N_{eff} - 1.11 \times 10\ -4N_{eff}^2 + 1.25 \times 10^{-6} N_{eff}^3 - 3.42 \times 10^{-9} N_{eff}^4 \tag{B.15}$$

If the reconstructed energy exceeds 25 MeV, the fitting function is first order of N_{eff}:

$$E_{rec} = 25.0 + 0.138 \times (N_{eff} - 189.8) \tag{B.16}$$

B.3 Cherenkov Angle Reconstruction

For loe energy events ($E_{rec} \leq 100MeV$) of Super-K, there are three particle sources: electron, muon, and multi-gamma. Figure B.6 shows the event displayers of each source. In the figure, there is no clear ring pattern in multi-gamma event. The number of photo-electrons for the low energy events of Super-K is only $25 \sim 200$ p.e., so Cherenkov ring pattern is not fitted very well. To reconstruct the Cherenkov angle value of an low energy event, we fill the 1-D histogram with the all possible opening angles that are constructed by any three hit PMTs. The 1-D histogram is referred to as "3 hit pmt angle histogram". The reconstruction procedures for Cherenkov angle are as follows:

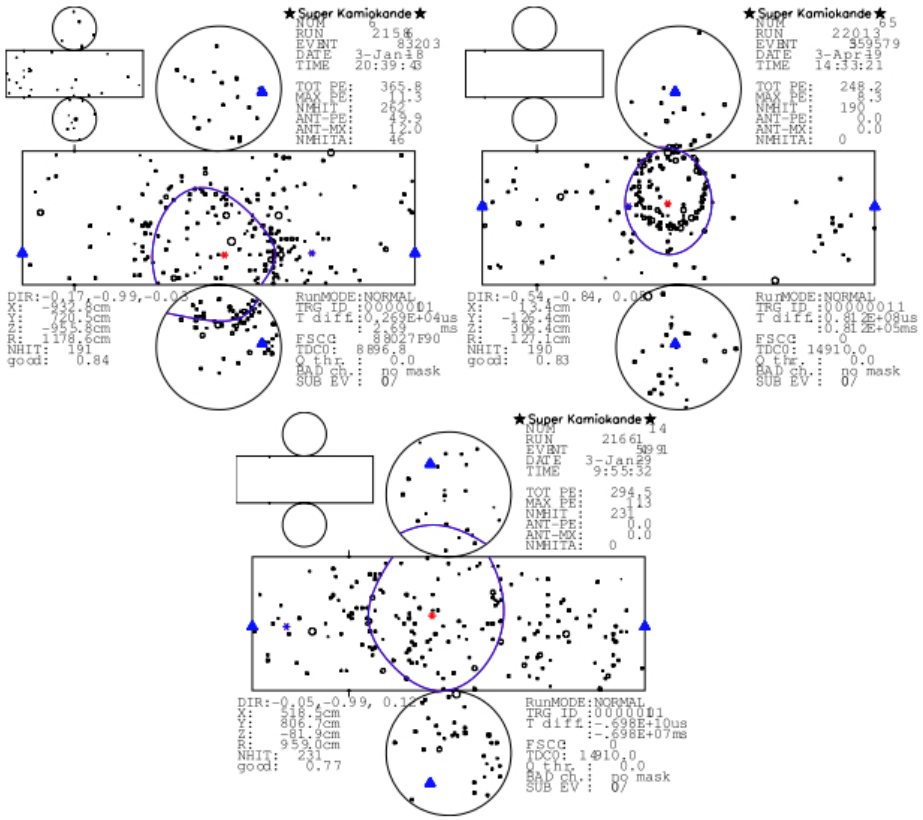

Figure B.6: The event displayers of the typical particle sources are shown in here. The upper two plots show an electron (left) event and a muon event (right), a Cherenkov ring is seen clearly in the electron event and the muon event. An multi-gamma event is shown in the below plot, and the Cherenkov ring is not seen in the multi-gamma rays event [120].

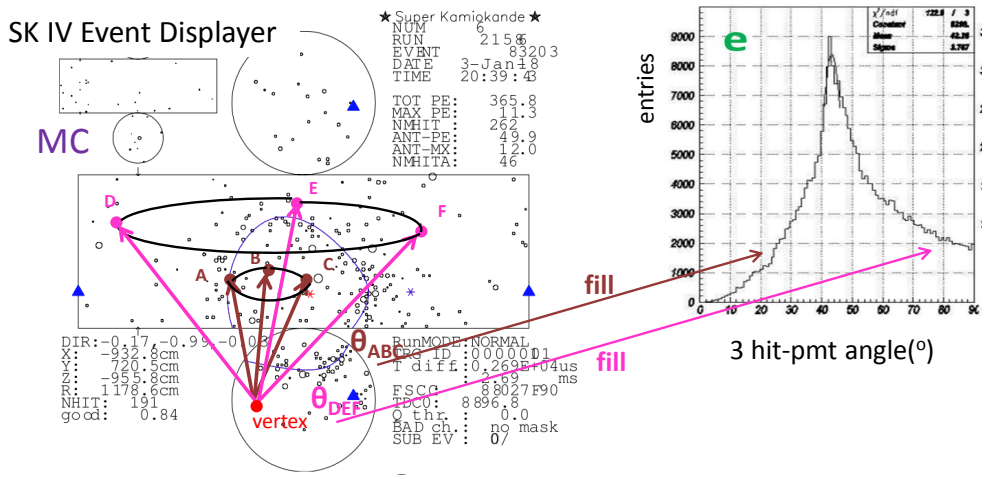

Figure B.7: The reconstructed vertex and arbitrary 3 hit PMTs compose a circular cone. We calculate the opening angle of the circular cone, then fill the angle value into the "3 hit pmt angle histogram" in the right plot of the figure.

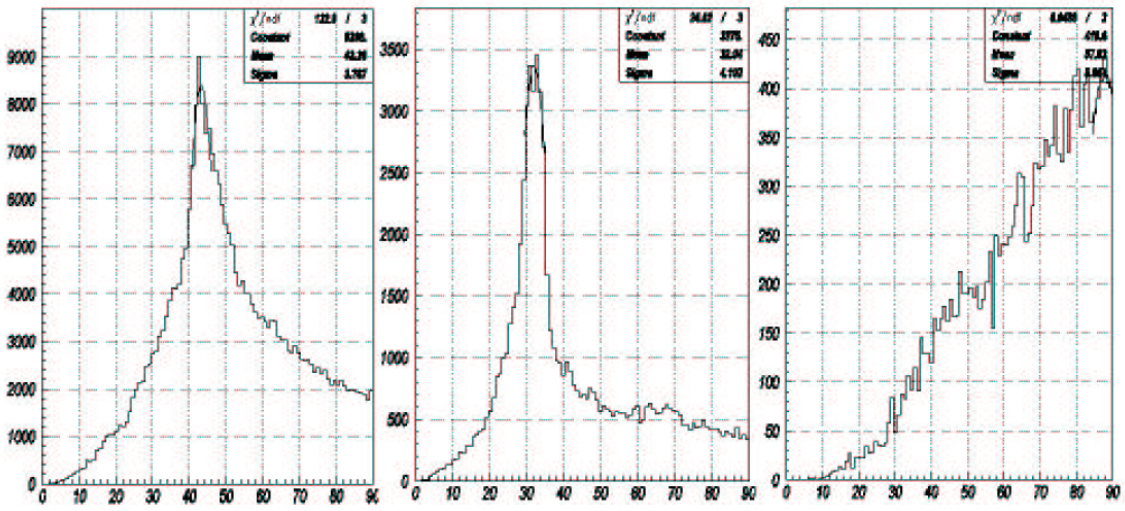

Figure B.8: The histograms are shown from left to right corresponding to an electron event, a muon event, and a multi-gamma event [120].

1. We sort all the hit PMTs by their residual time $t_{res,i} = t_i - t_{tof,i}$. We search the maximum number of hit PMT within 15 ns window N_{15}. The hit PMTs of N_{15} are prepared to calculate the opening angles of all combinations.

2. The reconstructed vertex is used as the apex, and we connect the apex with arbitrary three hit PMTs (for example: A, B, C in Fig. B.7) in N_{15} to compose a circular cone. Then, the opening angle θ_{ABC} of the cone is calculated.

3. Fill the θ_{ABC} value in the 1-D histogram. As the filled values are the opening angle of the cone consisting of the vertex and the 3 hit PMTs. we called the histogram as "3 hit pmt angle histogram". The histogram has 100 bins from 0^o to 90^o.

4. Repeat the step 2, 3 with another combination of arbitrary 3 hit PMTs until finishing the calculation of all combinations of 3 hit PMTs.

5. Find highest peak in the histogram: We sum up the height (entries) of 7 neighboring bins as the height value at angle θ_i which is the angle value of middle bin (4th bin). The largest value of height value is selected.

6. The $\theta_{i,heighest}$ with the largest value of height value is assigned to be the Cherenkov angle of the event.

Fig.B.8 shows the three typical histograms. Muon signal pass the energy selection mentioned previously, if the momentum of the muon is $p \leq 250$ MeV/c. The Cherenkov angle of the muon is expected to be less than 34 degree, which is calculated in below.

$$E_\mu = \sqrt{p_\mu^2 + m_\mu^2} = \sqrt{250.0^2 + 105.6^2} \simeq 271\mathsf{MeV} \tag{B.17}$$

$$\beta_\mu = \sqrt{1 - \frac{m_\mu^2}{E_\mu^2}} = \sqrt{1 - \frac{105.6^2}{271^2}} = 0.92 \tag{B.18}$$

$$\cos\theta_{\mu,max} = \frac{1}{1.33 \times 0.92} = 0.82, \quad \theta_{\mu,max} \simeq 34\ \mathsf{degree} \tag{B.19}$$

The Cherenkov angles of the events with single γ-ray are reconstructed near ~ 42 degree. While the Cherenkov angles of the events with multi-gamma rays are reconstructed near ~ 90 degree, since the hit PMTs are widely distributed as shown in the bottom plot of Figure B.6.

Appendix C

Super-K calibration

For the event analysis, it is essential to have precise calibration about the event energy scale, energy resolution, vertex position, angular resolution, and other detector efficiencies. This chapter describes the three calibration methods for Super-K.

C.1 LINAC calibration

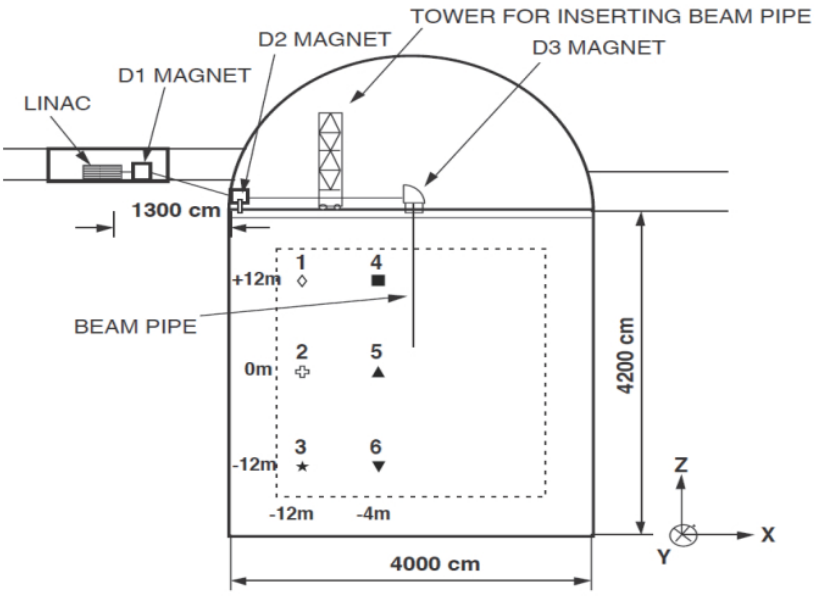

Figure C.1: LINAC and the test positions at the SK detector [81]. The fiducial volume for low energy neutrino measurement is indicated by the dash lines. The six markers are the positions where the mono-energy electrons are injected from LINAC.

The LINAC system [81] is an electron accelerator that accelerates electrons to the momentum range of (4.4,18.0) MeV/c, and the momentum range matches the momentum of recoil electrons from solar neutrinos. Figure C.1 shows LINAC and the six calibration positions where the electron beam is emitted into the Super-K fiducial volume.

The details of the LINAC system are shown in Figure C.2. A special electron gun adjusts its output current to enter an accelerating tube. Inside the tube, we use microwave

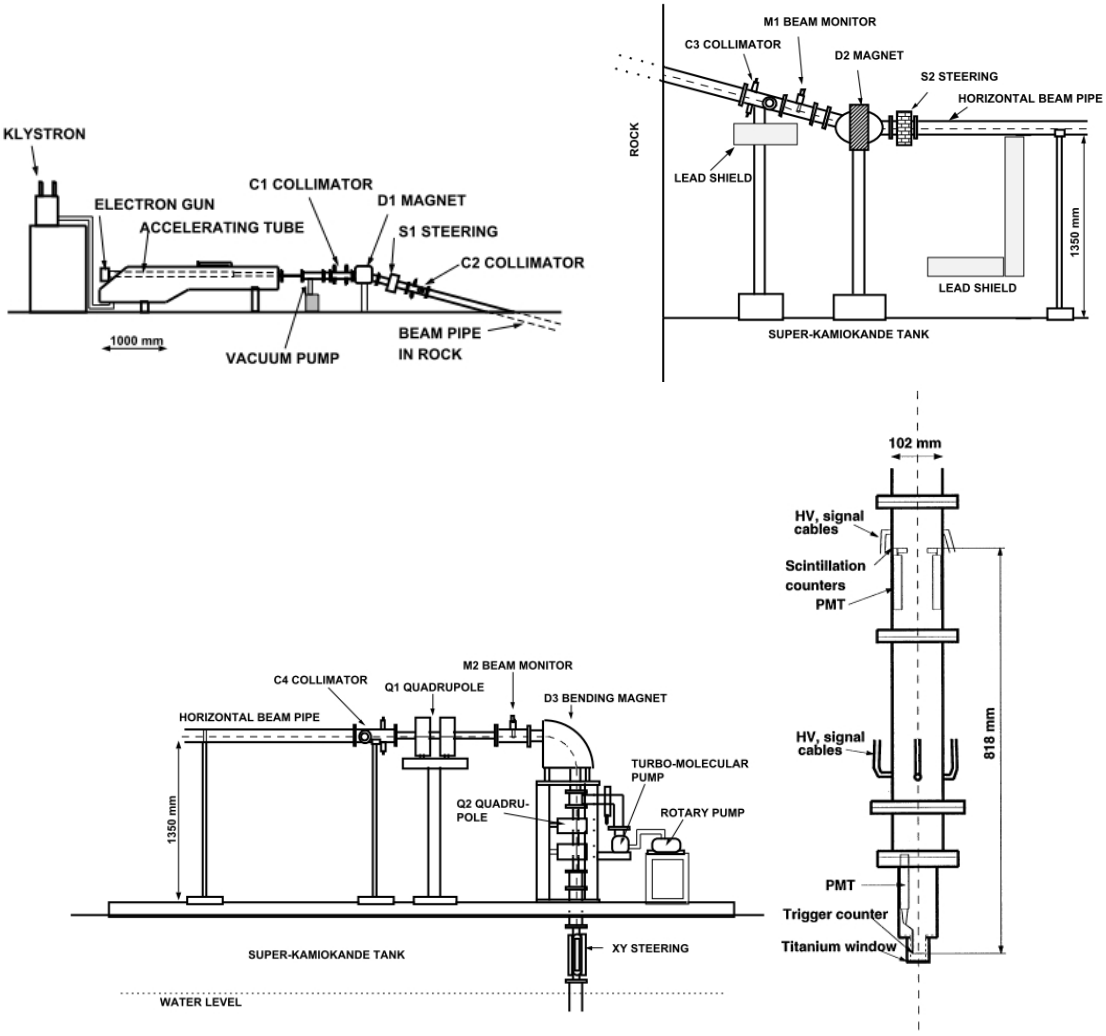

Figure C.2: The details of LINAC beam-line [81]. The upper left figure is the first section of the LINAC beam-line, the bending magnet (D1) and the collimators near D1 (C1, C2, C3) select the mono-energy electrons. The upper right figure is the second section of the LINAC beam-line, and the beam-line return to horizontal direction. The bottom left figure is the third section of the LINAC beam-line, the D3 magnet bends the LINAC beam-line by 90 degree to access into the six FV calibration positions. The bottom right figure is the endcap of LINAC, and the trigger counter above the titanium count the beam pulses.

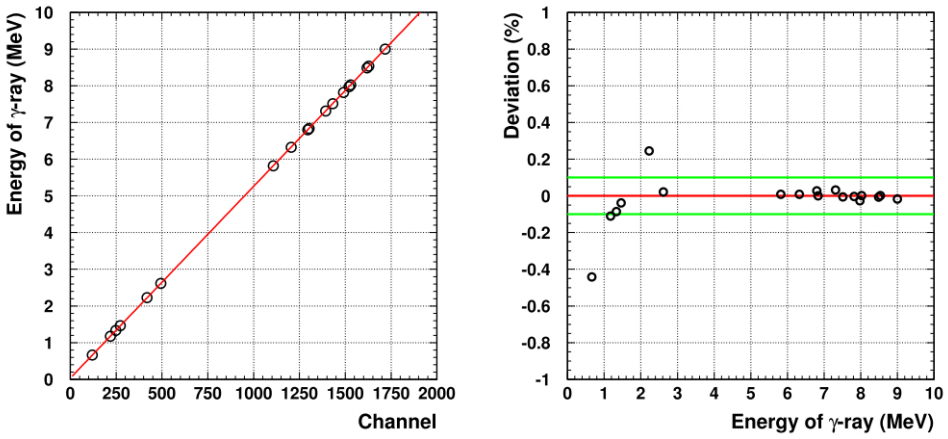

Figure C.3: The left figure shows the γ-ray calibration result for germanium detector. The horizontal axis is the output from the Ge detector output, and the vertical axis is the energy of calibration γ-ray source in unit of MeV. The right figure shows the deviation ratio (%) of the calibration testing points from the fitted line. Above 4 MeV for solar neutrino energy region, the differences are within 1%. [120]

pulses to accelerate the electron beam. The average momentum of electron beam is changed by adjusting the input power and frequency of the microwave pulses. Next, mono-energetic electrons are selected by the bending magnet (D1) and the collimators (C1, C2, and C3). The momentum spread of electron beam is reduced to 0.5% at FWHM, and the beam intensity is reduced to few electrons per microwave pulse. Then the electron beam-line is bent by 90 degree to access inner detector calibration positions.

The absolute beam energy is measured by a germanium detector. If the germanium detector measurement is practiced, the section of vertical beam pipe is assembled horizontally. The germanium detector is placed right after the titanium window of the pipe. The linearity of the germanium detector response is tested by γ-ray source with E_γ in the energy region (0.662, 9.0) MeV. The γ-ray calibration for the germanium detector results are as shown in Figure C.3. The deviations of calibration results from the fitted line are within 0.1% for $E_\gamma > 4.0$ MeV, that is the lower threshold for analysis during the SK IV period. The deviations have contribute a 0.21% to the systematic uncertainty due to energy scale.

As shown in Figure C.1, the mono-energetic electron beam is injected downward at the six positions. The positions are the combination of X=-12 or -4m and Z=-12, or 0, or +12m, where X, Z are the Super-K coordinates. N_{eff} distribution of the calibration result is a normal distribution, and the mean values of N_{eff} are used for energy reconstruction as mentioned in Appendix B.2.

To get the uncertainty due to energy scale, we compare the mean of N_{eff} of the LINAC calibration and the MC simulation using electron beam with energy of 7.0 MeV and 13.7 MeV as shown in Figure C.4. The differences are within 1.5%. As a result, the accuracy of energy scale is 1% from the comparison.

LINAC is also used to obtain the uncertainty due to energy resolution. Figure C.5 shows the differences of the energy resolution between the LINAC calibration and the MC simulation, and the differences are within $\pm$3%.

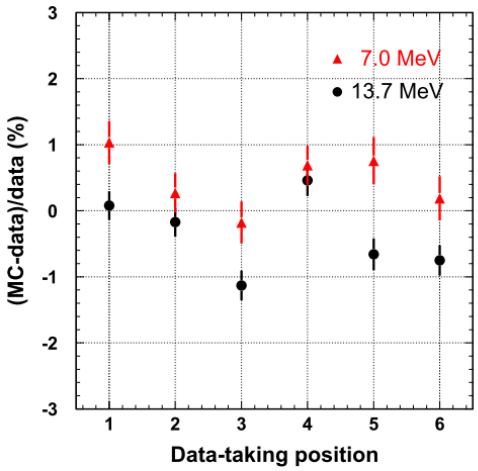

Figure C.4: The mean values of N_{eff} from the LINAC calibration and the MC simulation [121]. The calibration is made at the six injecting positions, where are shown in Figure C.1.

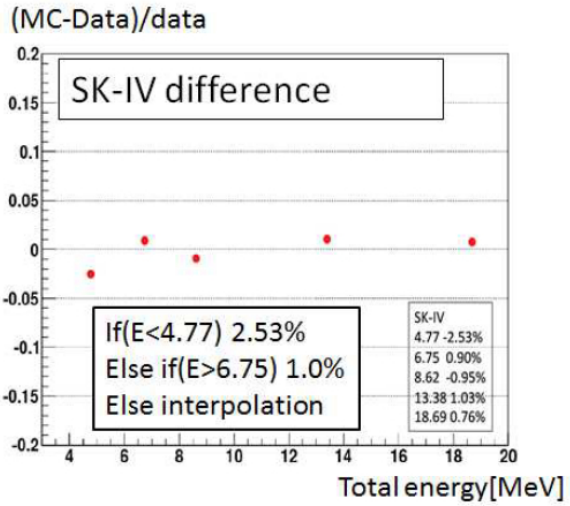

Figure C.5: The differences of energy resolution between the LINAC calibration and the MC simulation are within 3% [121].

C.2 DT calibration

The deuterium-tritium neutron generator (DT generator) is a device, and DT generate deuterium-tritium reactions to produce neutrons in the water [80]. The reaction is as follows

$$^{3}\mathrm{H} + {}^{2}\mathrm{H} \rightarrow {}^{4}\mathrm{He} + \mathrm{n} \tag{C.1}$$

Deuterium-tritium reactions produce isotropically distributed neutrons with an energy of 14.2 MeV. The DT generator device is encased in a stainless housing which is 150cm height and 16.5 cm in diameter as shown in Figure C.6. As the DT generator is easy to handle, the DT generator provides more calibration positions than LINAC.

Inside the accelerator head, the deuterium and tritium ions are created by a Penning ion source, and the ions form a plasma. The ion plasma is accelerated toward the target by the high voltage pulse of 80-180 kV, which is supplied by the pulse-forming electronics. The target is made by metal hydride which contains equal parts of deuterium and tritium, deuterium-tritium reactions occur on the target. 14.2 MeV neutrons are produced at the reactions.

The neutron with energy larger than 11 MeV interacts with ^{16}O nucleus to form ^{16}N in water. The beta decay of ^{16}N have 66% probability to produce a 4.3 MeV electron and a 6.13 MeV γ-ray, and 28% probability to produce a 10.4 MeV electron [84]. The decay electrons and the de-excited γ-rays are isotropically emitted, so the DT generator provides uniformity calibrations.

To estimate the accuracy of energy scale, the results of DT calibrations are compared to the MC simulations Figure C.7 shows that the reconstructed energy differences between the DT calibration and the MC simulation for different positions are within 1%. Figure C.8 shows that reconstructed energy differences between the DT calibration and the MC simulation for the different direction are within 0.4%. Therefore, the uncertainty of energy scale is within 1% which is consistent with the LINAC results.

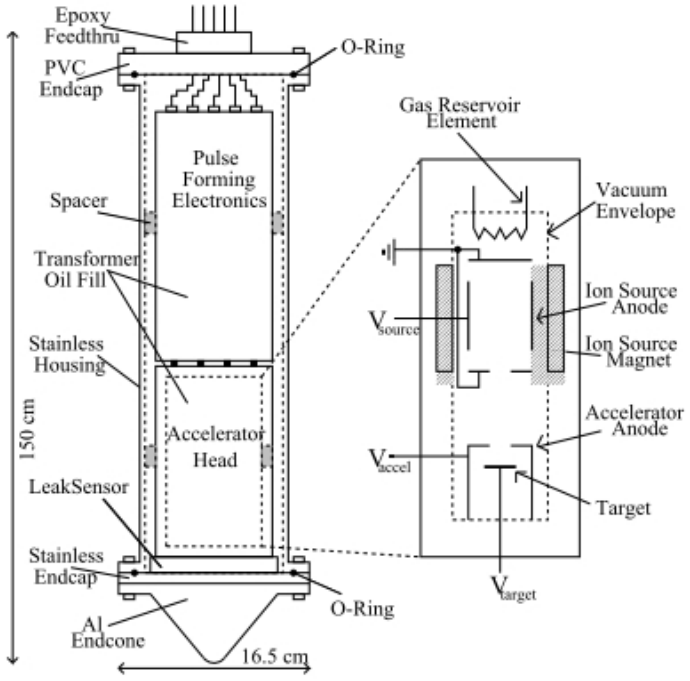

Figure C.6: The schematic of DT generator [80]. It consists a pulse-forming electronics and accelerator head. Right figure is the detail of the accelerator.

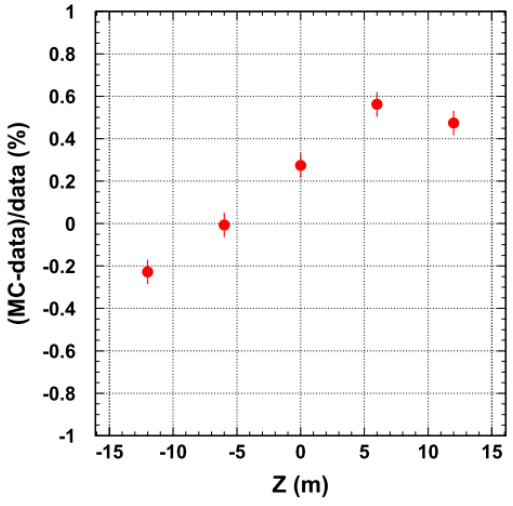

Figure C.7: The energy differences (%) between the DT calibration and the MC simulation at several positions [120]. Each data point is the position weighted average over data-taking positions in FV: (X(m),Y(m))= (-12,7), (-4,-0.7), (0.35,-12), (-0.35,12), (0.35,-7), (11,-0.7). The error bars represent the statistical errors.

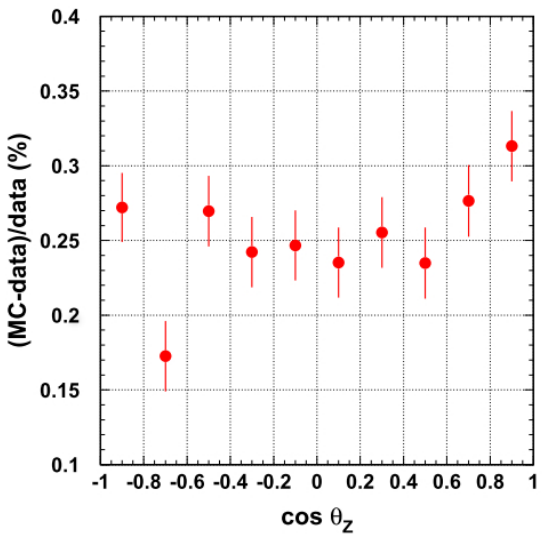

Figure C.8: The energy differences (%) between the DT calibration and the MC simulation with different directions [120]. Each point is the position weighted average over data-taking positions inside FV. The error bars represent the statistical errors.

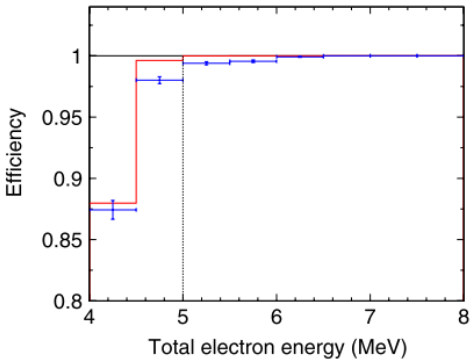

Figure C.9: The trigger efficiency (SLE) is a function of the reconstructed energy from Ref. [86]. The red histogram is the MC simulation result. The DT calibration results are represented as the markers.

Table C.1: The abundance of Ni isotopic in the ball and the energy of produced γ-ray.

Reaction	isotope abundance (%)	sum of all γ energy (MeV)
^{58}Ni(n,γ)^{59}Ni	67.9	9.0
^{60}Ni(n,γ)^{61}Ni	26.23	7.8
^{62}Ni(n,γ)^{63}Ni	3.66	6.8
^{64}Ni(n,γ)^{65}Ni	1.08	6.1

The DT calibration is used to estimate the trigger efficiency. As mentioned previously, the trigger levels are summarized in Table 2.3. Figure C.9 shows the efficiency of the SLE trigger level [86]. At reconstructed energy region of 4.5∼5.0 MeV, the difference between MC simulation and calibration data is $\sim 2\%$.

C.3 Nickel calibration

The "nickel source" provides an isotropically γ-rays source for calibration at single-photoelectron level [78, 82]. The γ-rays production is as follows: The spontaneous fission of ^{252}Cf is used to produce thermal neutrons, and 3.76 neutrons per fission are produced averagely. The thermal neutrons are captured by nickel, and the ^{n}Ni(n,γ)$^{n+1}$Ni reaction emits a 9 MeV γ-ray. We put a Cf source in the middle of "nickel ball", which consists of 6.5 kg of NiO and 3.5 kg of polyethylene as shown in Figure C.10. Table C.1 summarizes the abundance of Ni isotopic in the ball and the energy of produced γ-ray.

The nickel source is easy to handle, and it has high stability for producing γ-rays which are emitted isotropically. The nickel calibration is used to perform the single photoelectron calibration for PMTs, and other calibrations such as water conditions, trigger efficiency, and quality of reconstructed vertex position.

Here, the quality check of the reconstructed vertex position is described. Figure C.11 shows the vertex shift results using the Nickel calibration. The arrows in the figure indicate the shift length and the shift direction, and the most shifts are magnitude of $O(1)$ cm inside the fiducial volume (FV). At the bottom corner of FV, the reconstructed vertices are shifted about ~ 7 cm from the positions of the Nickel ball.

Figure C.10: The nickel ball is a γ-ray source [82]. The ball is made of 6.5 kg of NiO and 3.5 kg of polyethylene. The Cf source is inserted into the center of the ball and hold there by a brass rod.

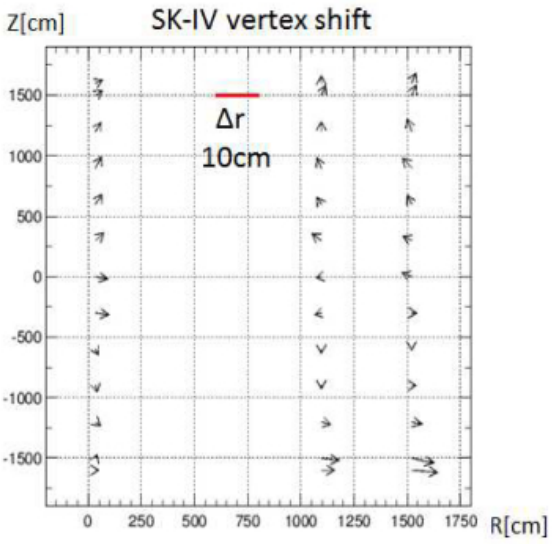

Figure C.11: Vertex shift of the Nickel calibration [121]. The origin of arrow shows the positions of the Nickel ball, and the directions of the arrows indicate the shift directions. The length of the arrows indicate the magnitudes of the vertex shift. All arrows are scaled by a factor of 20 to make them easier to see. The red line shows the real 10 cm length by 20 times.

Appendix D

Goodness of the reconstruction

There are some background events with the mis-reconstructed vertices by the fitter as mentioned in Appendix B.2. The following fitting results are used to remove those background events: A vertex goodness parameter G_V. A direction goodness parameter G_A.

We define the goodness of the event fit result as ovaQ$\equiv G_V^2 - G_A^2$ (one dimensional variable of vertex and angular reconstruction qualities). For a well-reconstructed event, G_V is large and G_A is small. Here, the details of the ovaQ parameter is described.

The vertex goodness G_V is defined using the timing information of hit PMTs as below

$$G_V = \frac{\sum_i^{allhitpmt} w_i e^{-\frac{1}{2}(\frac{\Delta t_i}{\sigma})^2}}{\sum_i^{allhitpmt} w_i} \tag{D.1}$$

where the constant σ is 5ns to test the time goodness. To reduce the accidental noise, the weighting factor w_i of the i-th hit PMT is given by

$$w_i = e^{-\frac{1}{2}(\frac{\Delta t_i}{w})^2}, \quad w = 60\,(\mathsf{ns}) \tag{D.2}$$

where i means the i-th hit PMT. The timing difference of the i-th hit PMT is $\Delta t_i = t_{res,i}(\vec{x}) - t_0$, where the definitions of $t_{res,i}(\vec{x})$ and t_0 are same with Equation B.5. If the values of Δt_i have a narrow distribution at zero, the value of G_V is larger. That means the vertex is reconstructed precisely with a sharp timing distribution.

The hit PMT pattern of well-reconstructed event is expected to be distributed uniformly on the Cherenkov ring. The direction (angular) goodness G_A is a testing of the uniformity of the spatial distribution of hit PMTs over azimuthal angle. A azimuthal angle between the reconstructed direction and vector from the vertex to the i-th PMT is shown in Figure 5.3. The two right plots of Figure D.1 show two examples of azimuthal angle distribution of the hit PMTs. The upper plot shows the angle distribution for a good event, while the bottom plots show the distribution for bad one. We use the Kolmogorov-Smirnov (KS) test to define G_A as the below formula.

$$G_A = \frac{max\Big\{\angle_{uni}(i) - \angle_{data}(i)\Big\} - min\Big\{\angle_{uni}(i) - \angle_{data}(i)\Big\}}{2\pi} \tag{D.3}$$

where the uniform angle of azimuthal angle of the i-th virtual hit PMT is defined as follows

$$\angle_{uni}(i) = \frac{2\pi}{N_{50}} \times i \tag{D.4}$$

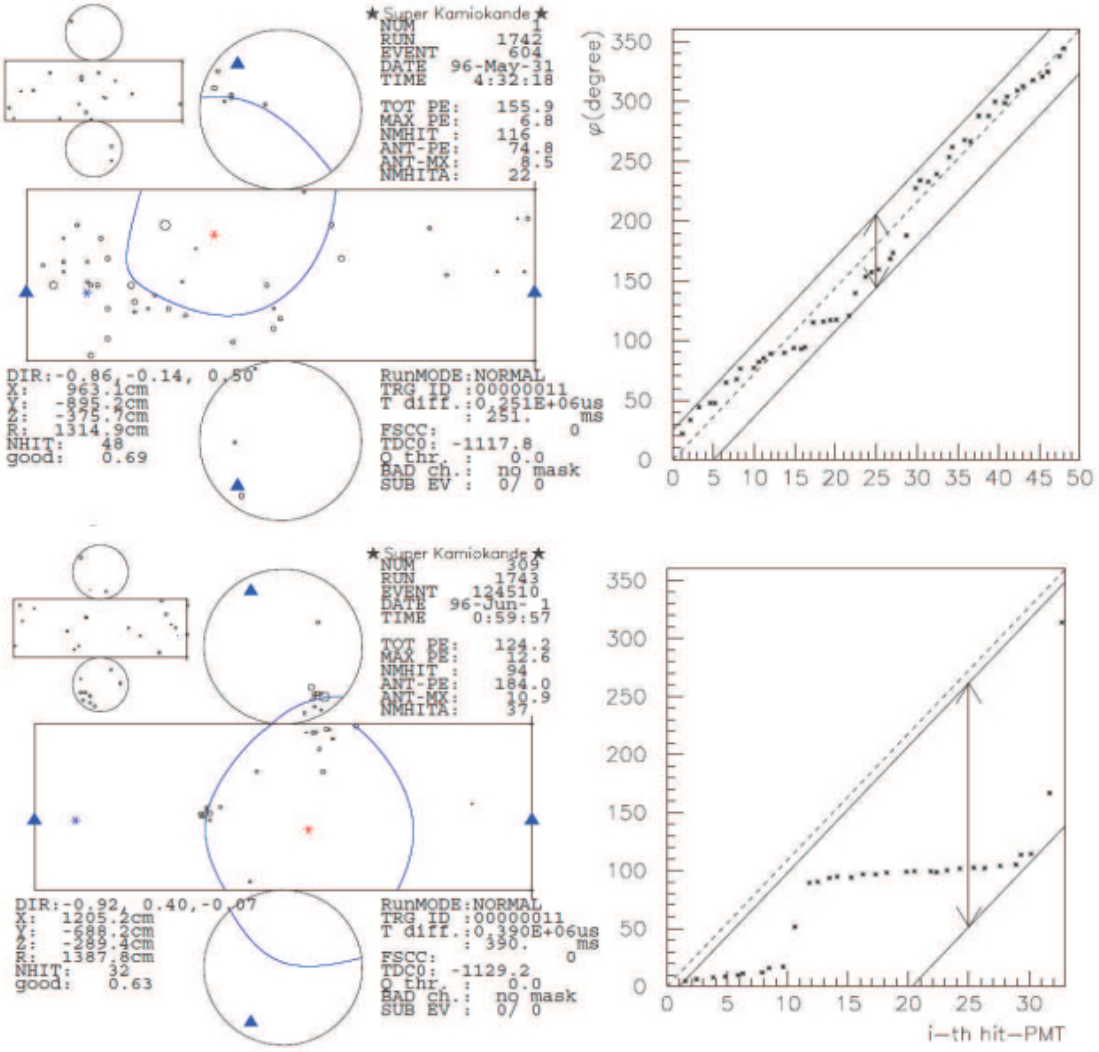

Figure D.1: The top (bottom) shows an example of a good event (bad event) whose direction reconstruction goodness (G_A) is small (large). The two right plots show that azimuthal angle distribution of the i-th hit PMT. In the two plots, the dash line shows the uniform distribution line, and the two solid lines represent parallel lines that the max and min of difference between the i-th hit PMT angle and uniform angle [120].

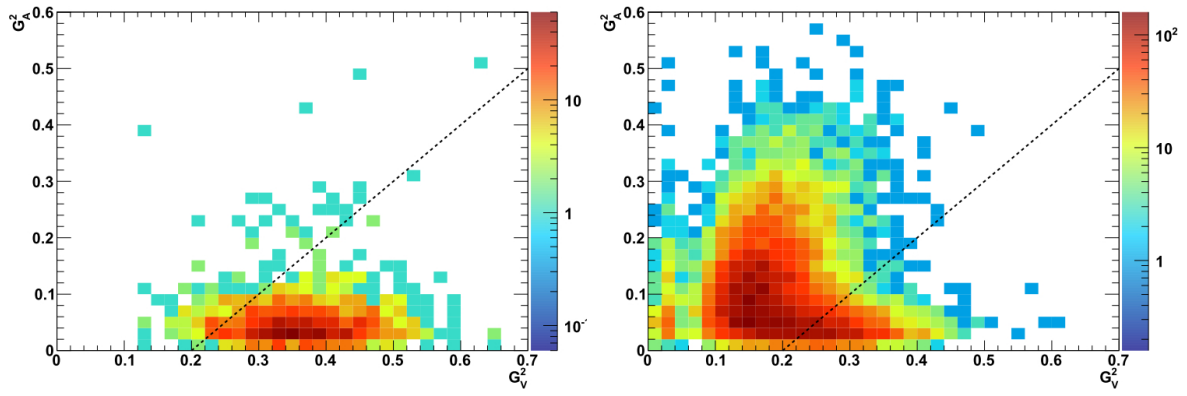

Figure D.2: Distributions of G_V^2 and G_A^2 of γ-ray events with reconstructed energy region of 4.5 MeV-5.0 MeV. The left plot is the distribution of the T2K beam ν_μ simulated events, and the right plot is distribution of the off-timing data events which are used to esitmate the beam unrelated events. The dash lines are the cut threshold ovaQ$\equiv G_V^2 - G_A^2 = 0.2$, and most of neutrino beam events has ovaQ value larger than 0.2, while most of beam unrelativeevents have smaller values than 0.2.

We use the number of the hit PMTs within 50 ns timing window (N_{50}) to calculate the direction (angular) goodness. The $\angle_{data}(i)$ is the azimuthal angle of i-th real hit PMTs. As we saw in Figure D.1, it is apparent that $max\{\angle_{uni}(i) - \angle_{data}(i)\} - min\{\angle_{uni}(i) - \angle_{data}(i)\}$ is large in non-uniform angle distribution. If G_A value is getting closer to zero, which indicates that the hit pattern is distributed very uniformly.

As a result, we define the goodness of the event fit result as ovaQ$\equiv G_V^2 - G_A^2$ (one dimensional variable of vertex and angular reconstruction qualities). G_V should be large and G_A should be small for a well-reconstructed event. Figure D.2 shows the G_V^2-G_A^2 distributions of the T2K ν beam simulation events (left) and beam-unrelated events (right). The dash lines in the plots are ovaQ$\equiv G_V^2 - G_A^2 = 0.2$ which separate T2K beam-related events with beam-unrelated events efficiently. The optimization of ovaQ threshold is described in the following chapter.

Appendix E

Optimization of cut threshold

This chapter describes the optimization for the threshold of dWall, threshold of effWall, and threshold of ovaQ to obtain the maximum signal-to-noise (S/N) ratio. The S/N ratio depends on radioactive impurities of ID wall, water transparency and other parameters at Super-K and the T2K ν beam power. The background event rates highly depend on their energies as shown in Figure E.1. The S/N ratios are different at different energy range, so we optimize the thresholds in every energy bin width of 0.5 MeV to achieve the good S/N ratio for every T2K RUN period respectively.

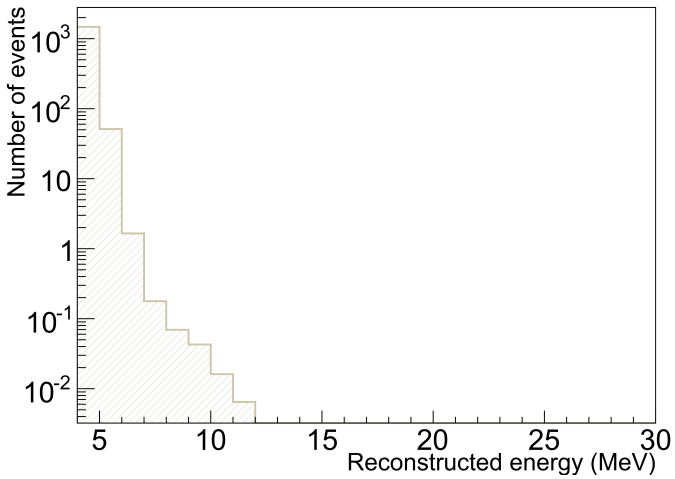

Figure E.1: The "off-timing" events are used to estimate the expected number of beam-unrelated background events. The background event rate is high in low energy region.

To obtain a larger S/N ratio, we search the maximum value of the figure-of-merit (FOM) by testing different thresholds of (dWall, effWall, ovaQ). The definition of FOM is given by

$$FOM \equiv \frac{N_{signal}}{\sqrt{N_{signal} + N_{background}}} \tag{E.1}$$

where N_{signal} and $N_{background}$ are the numbers of the expected event of beam signal and background with the thresholds of (dWall, effWall, ovaQ). N_{signal} is estimated as the total number of the beam-related events (NCQE events and other ν reaction events). The left plot in Figure E.2 shows the effWall-ovaQ threshold distribution of N_{signal} with 4.0 MeV$\leq E_{rec}$ <4.5 MeV. $N_{background}$ is estimated from the "off-timing" events with

the timing ΔT_0 ∈(-500 μs, -5 μs). As mentioned previously, the live-time for our timing window is $N_{bunch} \times 200$ ns for each spill, and N_{bunch} is the numer of bunch in single spill. By scaling the number of off-timing events, we estimate the number of the beam-unrelated event occurring within our live-time. The scaling value is as below

$$w_{background} = \frac{0.1\,\mu s \times 2 \times N_{bunch}}{-5\,\mu s - (-500\,\mu s)} \tag{E.2}$$

N_{bunch} is six in RUN 1 and eight in other RUNs. The right plot of Figure E.2 shows the effWall-ovaQ distribution of $N_{background}$ with 4.0 MeV≤ E_{rec} <4.5 MeV. As a result, the FOM values for thresholds of (dWall, effWall, ovaQ) are calculated as shown in Figure E.3, the thresholds that result in maximum value of FOM is chosen as the optimized thresholds for the energy region.

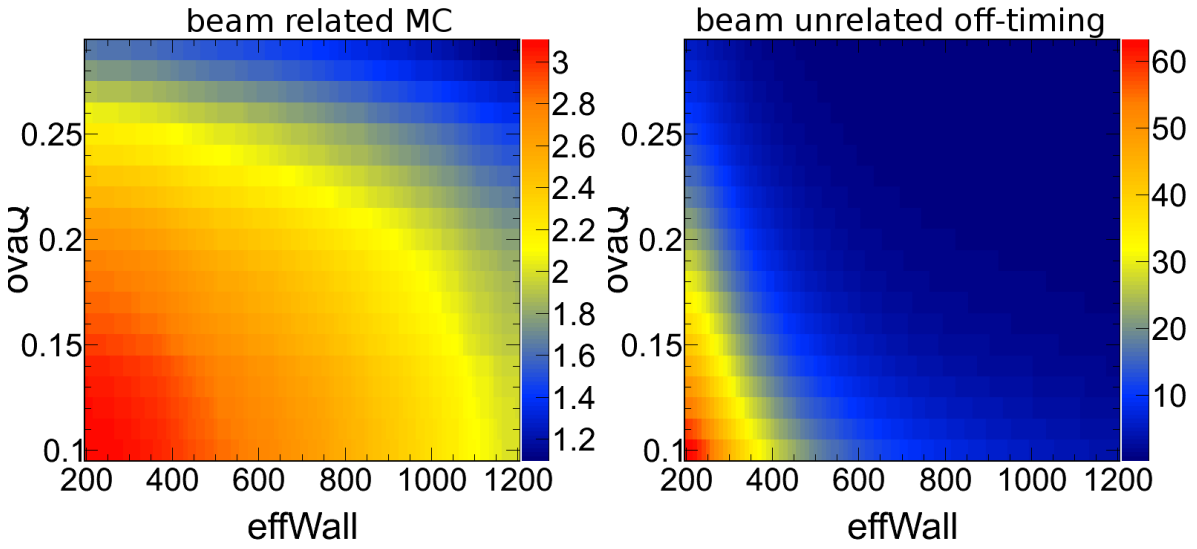

Figure E.2: The left plot shows that the expected number of beam related MC events for a example is drawn as effWall-ovaQ distribution. The right plot shows that the expected number of beam-unrelated events for a example is drawn as effWall-ovaQ distribution. The dWall is set to be 200 cm here. N_{signal} and $N_{background}$ are the expected number of signal events and background events with the reconstructed energy in the region of 4.0 MeV≤ E_{rec} <4.5 MeV.

Since the background event rate with $E_{rec} \geq 6.5$ MeV is low, the search for optimized thresholds is only done for the following five energy regions: $(4.0, 4.5)$ MeV, $(4.5, 5.0)$ MeV, $(5.0, 5.5)$ MeV, $(5.5, 6.0)$ MeV, and $(6.0, 6.5)$ MeV. To cover all energy region, we fit the optimized points with a linear function which is used to decide the threshold for cuts. Figure 5.4 shows the optimization results (point) and fitted lines for the thresholds. The fitted lines are used as the cut threshold for every energy region. The parameters of the threshold linear functions are summarized in Table E.1.

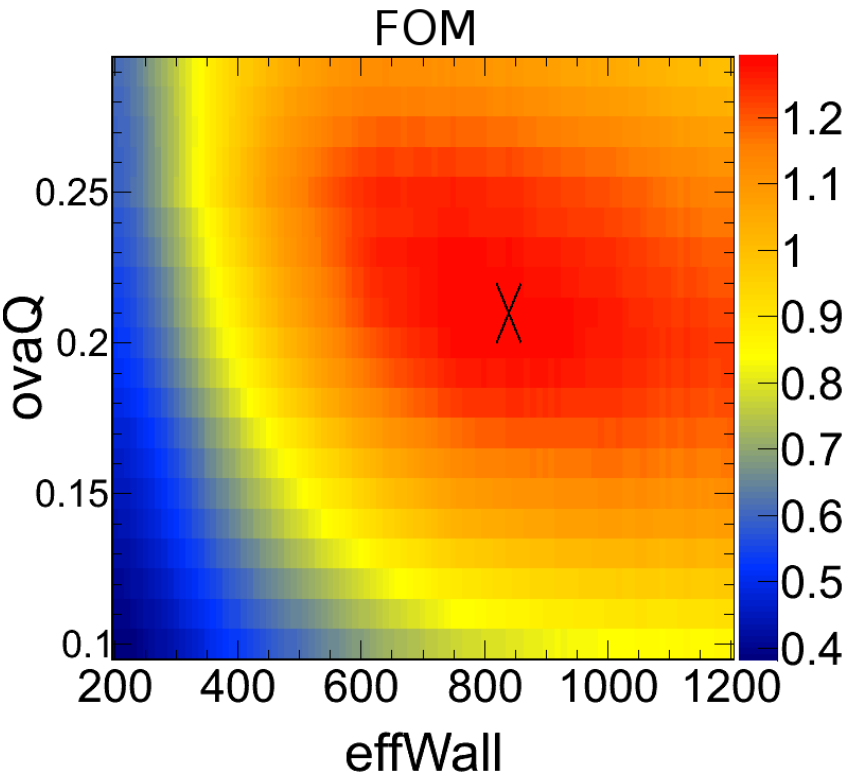

Figure E.3: The FOM value of a example is drawn as a effWall-ovaQ distribution. The dWall parameter is set to be 200cm here. N_{signal} and $N_{background}$ are the expected number of signal events and background events with the reconstructed energy in the region of 4.0 MeV$\leq E_{rec}$ <4.5 MeV. The black X denotes the maximum FOM value in the figure.

Table E.1: Summary of cut criteria function for T2K RUN1-3. To apply the cut criteria to all the energy region, we fit the optimization points with linear function as $t = p_0 + p_1 \times e$. Where the t means threshold value of a parameter, and e is the reconstructed energy of de-excitation γ-ray event.

T2K RUN	cut criteria	dWall $\geq$ 200	effWall $\geq$ 200	ovaQ
RUN1	p_0	705.	2699.5	0.4580
	p_1	-100.	-406	-0.048
RUN2	p_0	960.	2480	0.4445
	p_1	-160.	-388	-0.050
RUN3b,3c	p_0	960.	2565	0.487
	p_1	-160.	-420	-0.060

Appendix F

Error shift

The calculation of NCQE cross-section including each uncertainty (see Equation 7.1) is obtained by shifting an error envelop that will include the uncertainties from each error source as shown in Figure F.1. To include the uncertainties of each error source, the "toy MC simulation" method (or called Fake experiment) is used to generate random numbers based on a Gaussian distribution.

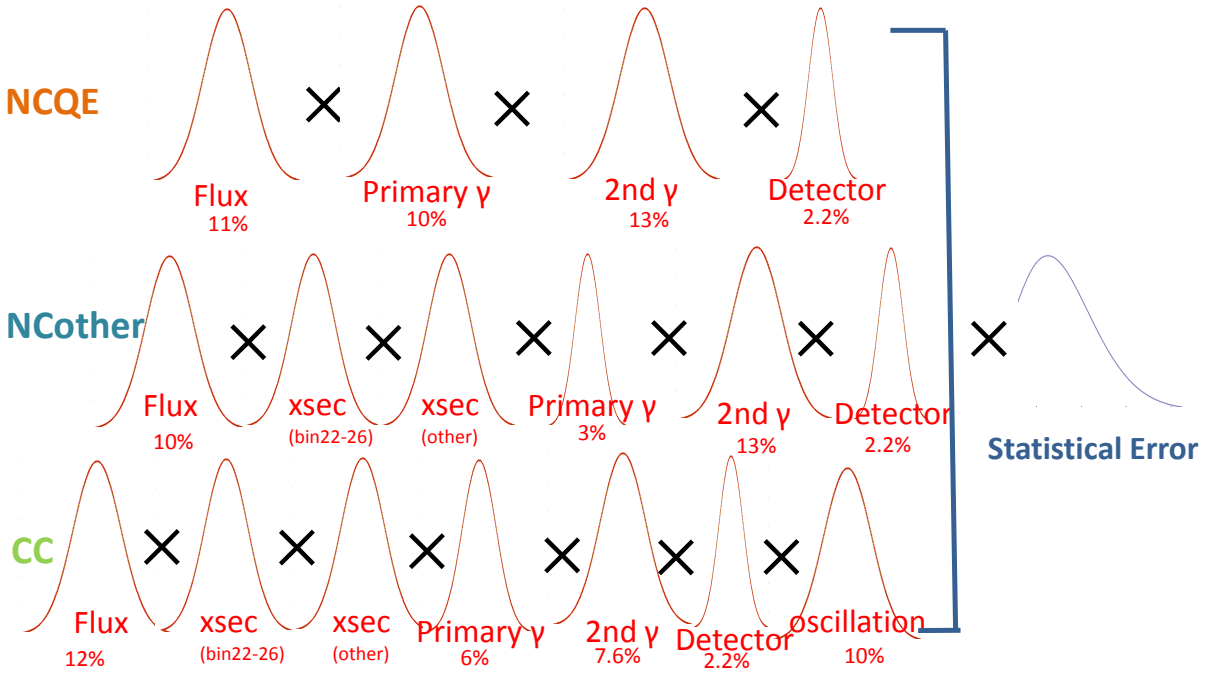

Figure F.1: The cross-section calculation including the uncertainties is made using a toy MC experiment method. We generate 500 random numbers based on the flux and cross-section error. After the integral of simulated events, we multiply the error envelop for each reactions with a series of random numbers that are based on a series of Gaussian distributions, and the deviation of the Gaussian distribution is the error from a specific error source. The $500 \times 50,000$ sets of the expected number of events are used to calculate NCQE cross-section.

First, an error envelop is generated for every MC simulated events, and the error envelop is made of the 500 random numbers based on the flux and cross-section errors.

The center value of error envelop is the correction value of the flux and the cross-section.

Second, the expected number of the NCQE events and the other background events are calculated respectively by integrating all the produced MC simulation events with weighting values, which are dependent on the cut criteria, the accumulated POT, the ν reaction, etc. Now, the center values of error envelops represent the nominal values of the expected number of the reaction events.

Third, for including the uncertainties of other error sources (e.g. primary γ-ray, secondary γ-ray, detector response, oscillation parameters), the NCQE cross-section are calculated for $500 \times 50,000$ times. In each calculation, we generate a set of random numbers based on a series of Gaussian distributions whose the standard deviation is the uncertainty of the specific error source.[1] Then, the error envelop elements for each reaction events are multiplied by the corresponding random numbers, the error shifting is as shown in Figure F.1.

Finally, the $500 \times 50,000$ sets of the expected number of events are used to calculate NCQE cross-section, and the calculated cross-section values distribution are shown in Fig. 7.1. The center value is the NCQE cross-section nominal value, and the values of $\pm 68\%$ of the higher (lower) region from center is the 68% confidence level region boundaries.

[1] We generate a random number based on Poisson distribution for including the statistical uncertainty.

Appendix G

Event selection and results for the T2K RUN4

This chapter describes the analysis for the T2K RUN4 data. The event selections is as mentioned in Section 5.1, but the optimized thresholds are using the T2K RUN4 data. As a result, we got the results that are consistent with RUN1-3.

The uncertainty of NCQE cross-section using T2K RUN1-4 data is described at the end of this chapter.

G.1 Event reduction

G.1.1 Data set and good spill selection

Data set The T2K RUN4 period is from Oct. 2012 to May 2013, and the accumulative proton on target is 3.56×10^{20}.

Table G.1: Summaries of T2K Run4 data set. The total accumulative POT is 35.6×10^{19}.

T2K Run	MR Run	SK Run	POT($\times 10^{19}$)	Period: Start-End
	44	70524-70619	5.14	19, Oct.–12, Nov., 2012
	45	70670-70721	5.90	21, Nov.–12, Dec., 2012
RUN4	46	70829-70882	11.47	18, Jan.–22, Feb., 2013
	47	70901-71042	7.31	25, Feb.–01, Apr., 2013
	48	71042-71067	4.01	01, Apr.–12, Apr., 2013
	49	71239-71245	1.78	01, May.–08, May., 2013
Total			35.6	

Good spill selection The "beam good spill" selection and "SK data quality" selection are the same with T2K RUN1-3, and we include a GPS error selection after T2K RUN4. If the $|GPS1 - GPS2 - \text{offset}| > 100$ ns, the spill is marked as a bad spill. Table G.2 shows the summary of good spills of T2K RUN4. The inefficiency of the "SK quality" is below 0.6%.

Table G.2: Summary of good spill for T2K Run4 data set. The Total POT is 35.60×10^{19}.

T2K Run	RUN4	Inefficiency
# of good spill($\times 10^6$)	3.306	0.59%
Bunch # in per spill	8	

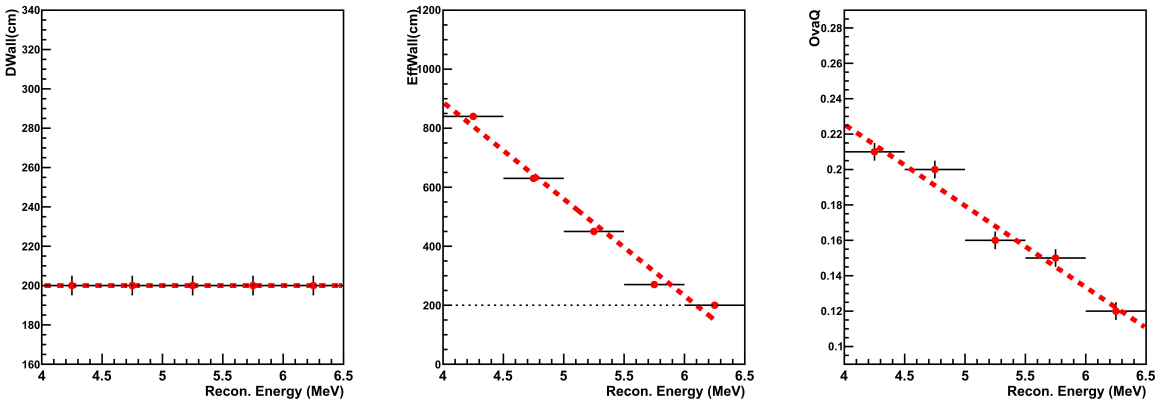

Figure G.1: Cut thresholds of dWall, effWall and ovaQ for T2K RUN4. The red points represent the optimization cut results for each energy bin. The red dash lines are the fitting lines using red optimization points, and the fitting lines and their extrapolation are used for the thresholds of (dWall, effWall, ovaQ). The dWall or effWall for event with vertex inside FV are not shorter than 200cm, as the black dash lines show the lines of 200 cm.

G.1.2 Optimization of cut threshold

The optimization results for the threshold of dWall, the threshold of effWall, and the threshold of ovaQ are described here. Figure G.1 shows the optimization results (points) and the fitted lines. The fitted lines are used as the thresholds for every energy region. We summarize the parameters of the fitted lines in Table G.3.

G.1.3 Efficiency of expected events

We apply the selection processes to estimate the expected numbers of beam-related events and beam-unrelated events. As a result, Figure G.2 shows the energy distributions

Table G.3: Summaries of cut criteria function for T2K RUN4. To apply the cut criteria to all the energy region, we fit the optimization points with linear function as $t = p_0 + p_1 \times e$. Where the t means threshold value of a parameter, and e is the reconstructed energy of de-excitation γ-ray event.

T2K RUN	cut criteria	dWall $\geq$ 200	effWall $\geq$ 200	ovaQ
RUN4	p_0	200.	2200	0.4095
	p_1	0.	-328.0	-0.046

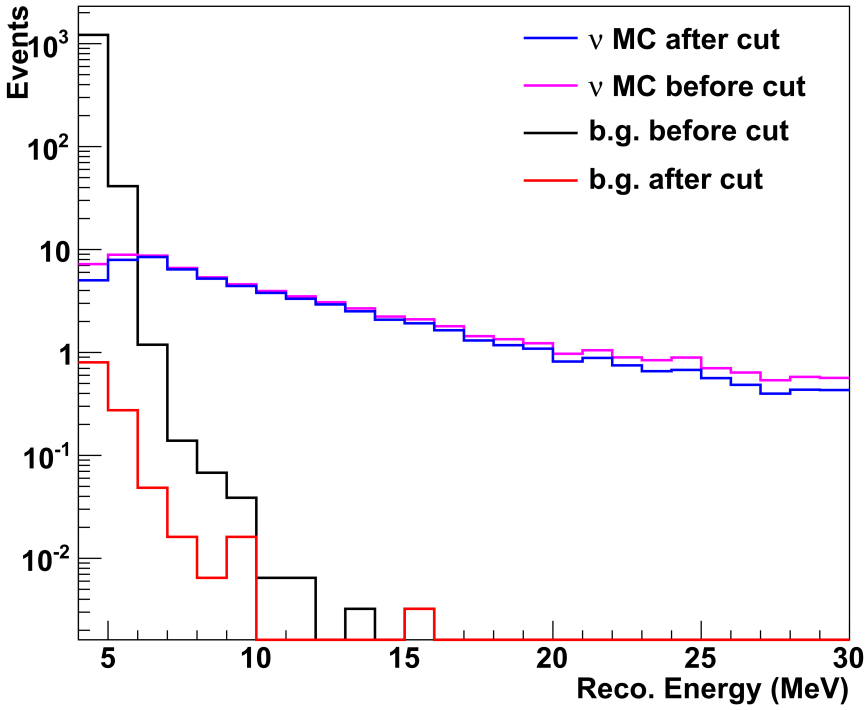

Figure G.2: A energy distribution of expected events for T2K beam MC and off-timing data for T2K RUN4. The plot shows that the dWall, effWall and ovaQ cuts remove the background events effectively to less than 0.1%. After selections, the beam-unrelated events are expected to be only 1.2 events for T2K RUN4.

of expected events in range of (4 MeV, 30 MeV) before and after the selections. After the selections, the number of off-timing events is reduced to only 1.2 events, and the efficiency is below 0.1%. While the number of beam-related events of T2K RUN4 is 60.0 after the cuts, and the efficiency is about 90%.

G.1.4 Summation of selection

Observed number of selected events We apply the selection process to select de-excitation γ-ray candidates from T2K RUN4 spill data. Table G.4 shows the summaries of events of T2K spill data in every selection process. The vertex distributions of events in each selection process are shown in Figure G.3. After the selections, 59 data events are selected as the γ-ray candidates.

Comparison between expected events and observed events Table G.4 shows the comparison between the numbers of events of T2K spill data and the numbers of expected event at each selection process. Before the selections, the most data samples are from the beam-unrelated backgrounds. After the selections, the beam-unrelated background are expected only $\sim 2\%$ fraction of total samples.

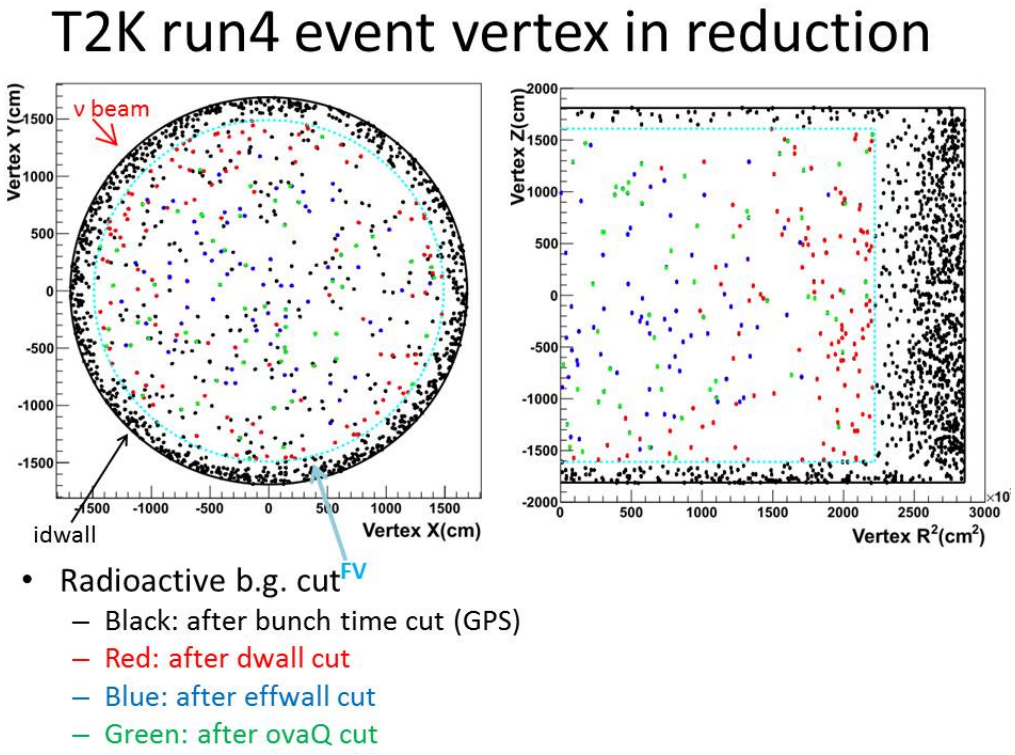

Figure G.3: Vertex distribution of selected γ-ray events at each selection process for T2K RUN4 data.

Table G.4: The numbers of selected events at each selection procedure for T2K Run4. The expected numbers of events include beam-related MC simulation and off-timing (beam-unrelated). The expected numbers of selected event is consistent with the numbers of observed data events N_{obs} in each procedure.

T2K RUN4	N_{obs}	N_{exp}		
Reduction cuts	On-timimg data	beam-related MC	off-timing	summation
energy & timing	1313	66.94	1301.62	1368.56
dWall	250	66.94	179.23	246.17
effWall	130	65.47	61.73	127.2
ovaQ	61	64.06	1.26	65.32
angle & pre-activity	59	60.02	1.20	61.22
cut effiency	–	89.6%	0.09%	

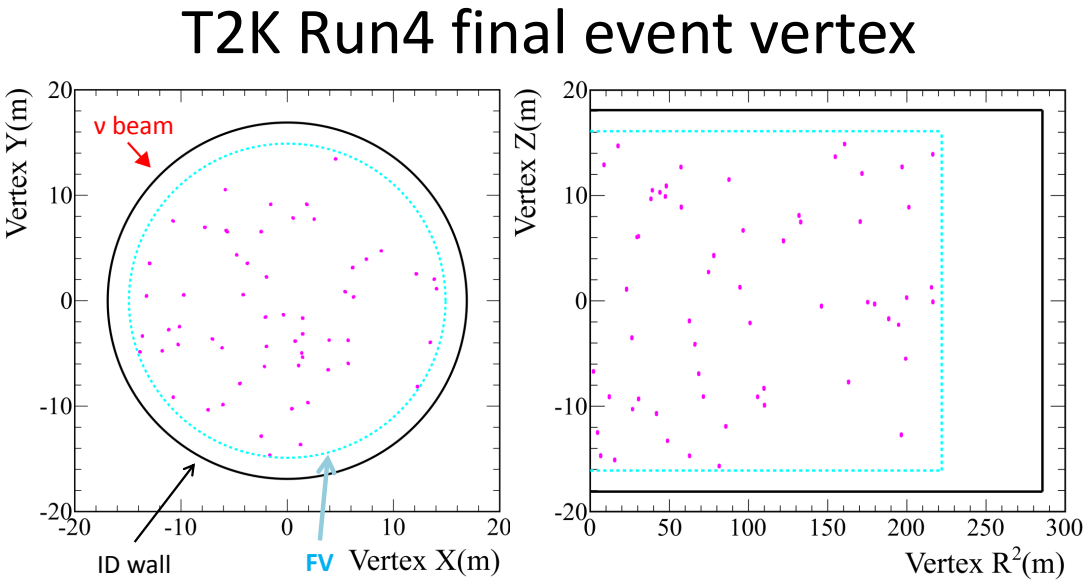

Figure G.4: Vertex distribution of de-excitation γ-ray candidate events inside Super-K ID tank for T2K RUN4 data. The black lines are Super-K ID wall, and the blue dash lines are boundary of FV that is 2m distance inside Super-K ID wall. X, Y, Z are the three orthogonal axises, and Z is vertical axis. R^2 is distance from circle center, and that is equal to $X^2 + Y^2$.

G.2 Selection results

As shown in Table G.4, 59 events are selected as final de-excitation γ-ray candidates for T2K RUN4, while the expected number of events is calculated as 61.2. Here, the comparisons between the data events and the expected events are described.

G.2.1 Vertex distribution

The vertex 2-D distributions of final event candidates inside the Super-K ID tank are shown in Figure G.4. The vertex distribution is uniform inside fiducial volume.

G.2.2 Timing distribution

Figure G.5 shows the ΔT_0 timing distribution of data events, and there is the clear structure of eight bunch. We expect that there are 3.6 events that outside the eight bunch window, and two events are found outside the timing windows. The number of events outside the eight bunch window is consistent with the expectations.

We check the residual time of event, that is relative time to the nearest bunch center. Figure G.6 shows that the selected events are distributed closely to the bunch centers, and the R.M.S. of the on-timing events is also about 25 ns.

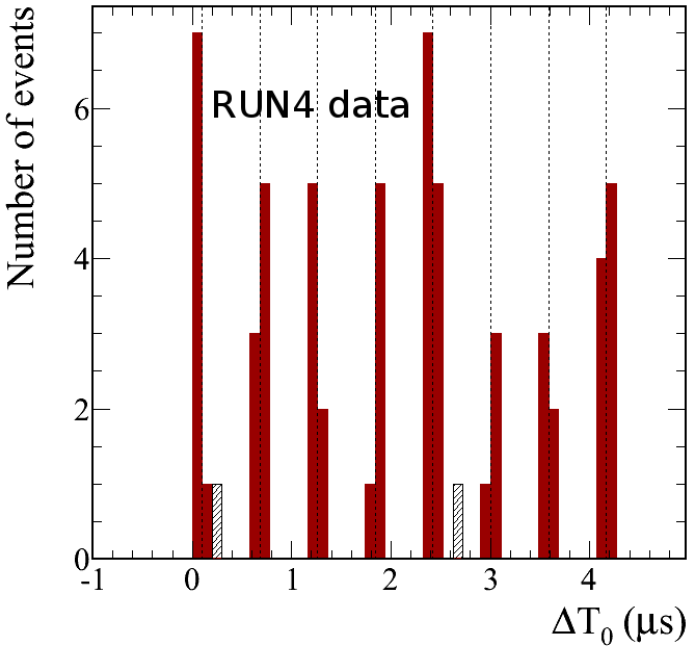

Figure G.5: The ΔT_0 distribution of candidate data events of T2K Run4. The bunch centers are denoted as eight vertical dashed lines. The on-timing and off-timing events are shown in solid and hashed, respectively.

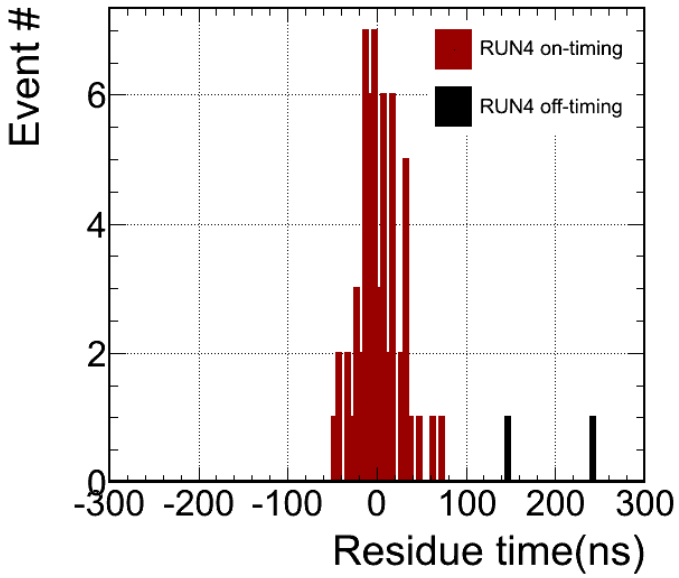

Figure G.6: The residual timing distribution of events. The residual timings are relative to each nearest bunch center. T2K RUN4 candidate events are shown as the red histogram that distributed within ±100 ns. The RMS of all on-timing events are ∼25 ns. Two events with black solid are off-timing events.

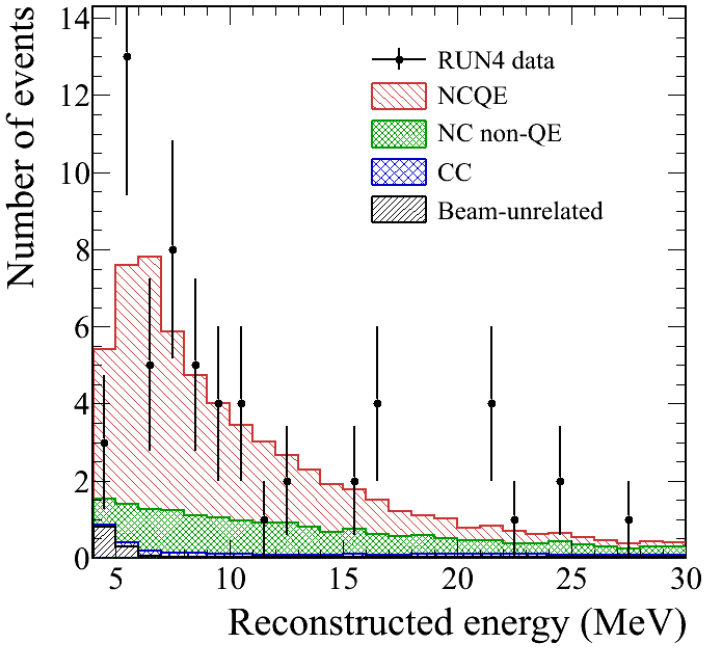

Figure G.7: Comparison of the reconstructed energy spectrum between the expected numbers (histogram) and the data samples(dots) for T2K RUN4. The NCQE component is about 70% of total expected number of events.

G.2.3 Energy and other parameters distributions

After all the selections, the expected numbers of each neutrino reactions are summarized in Table G.5. The NCQE signal is expected $\sim 69\%$ fraction of the total candidate events, while beam-unrelated background is only about 2%. The observed number of candidate events is 59 which is less than expected number of candidate events of 61.2. The comparison between data events and expected events are discussed as follows.

Table G.5: Summary of the expected numbers of events of T2K RUN4. The NCQE signal is $\sim 69\%$ of the final event candidates.

T2K Run	RUN4	Fraction
NCQE	41.9	68.6%
NCothers	15.6	25.5%
CC	2.47	4.0%
Beam un-related	1.2	2.0%
Total	61.2	–

Energy distribution

The reconstruction energy distributions of data events and the expected events for T2K Run4 are shown in Figure G.7. The distribution of data events is consistent with that of expected events in statistics.

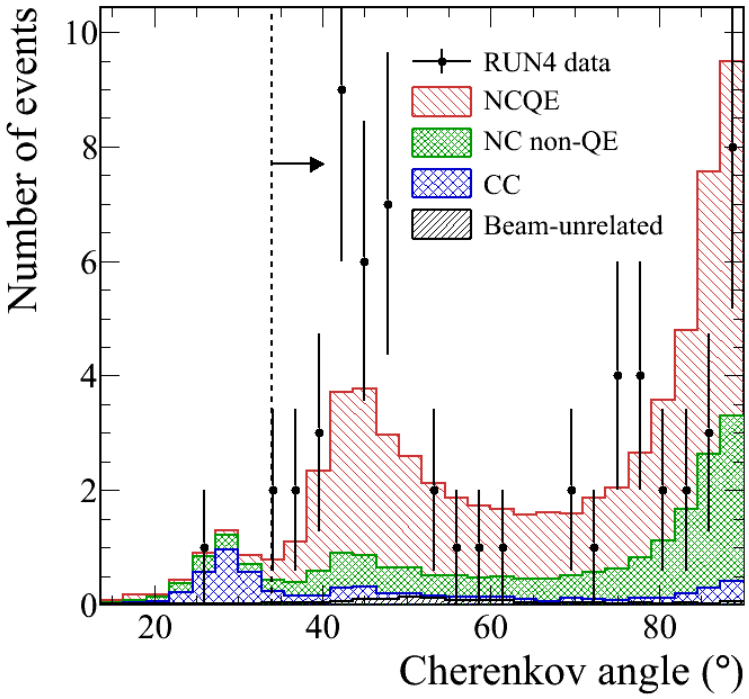

Figure G.8: Comparison of Cherenkov angle distribution between the expected events and data events. The peak near 28^o is composed of CC background events, thus the events with the angle less than 34 degree are removed.

Cherenkov angle distribution

The Cherenkov angle distributions of data events and expected events are shown in Figure G.8. From the figure, the expected number of candidate events of MC simulation is larger than that of data events near 90 degree, while the expected number of candidate events are smaller than that of data events near 42 degree.

dWall, effWall and ovaQ distributions

There is no statistically-significant difference in the distribution of the other parameters between the candidate events of the data events and those of the expected events as shown in Fig. G.9.

G.2.4 Summary of candidate events

This section describes the 59 observed events as follows: The vertex distribution of 59 events is uniformly inside FV. Because the event rate of T2K RUN4 is higher than T2K RUN1-3, so the event rate of T2K RUN1-4 is 1.55 event per 10^{19} POT. The event rate is proportional to the T2K POT linearly with 92.9% significance.

Then, we compare the observed events with the expected events, and we know that there are no statistically-significant difference between the candidate events of the real data events and those of the expected events in most parameter distributions, except the Cherenkov angle distribution. The results of T2K RUN4 is consistent with the results of T2K RUN1-3.

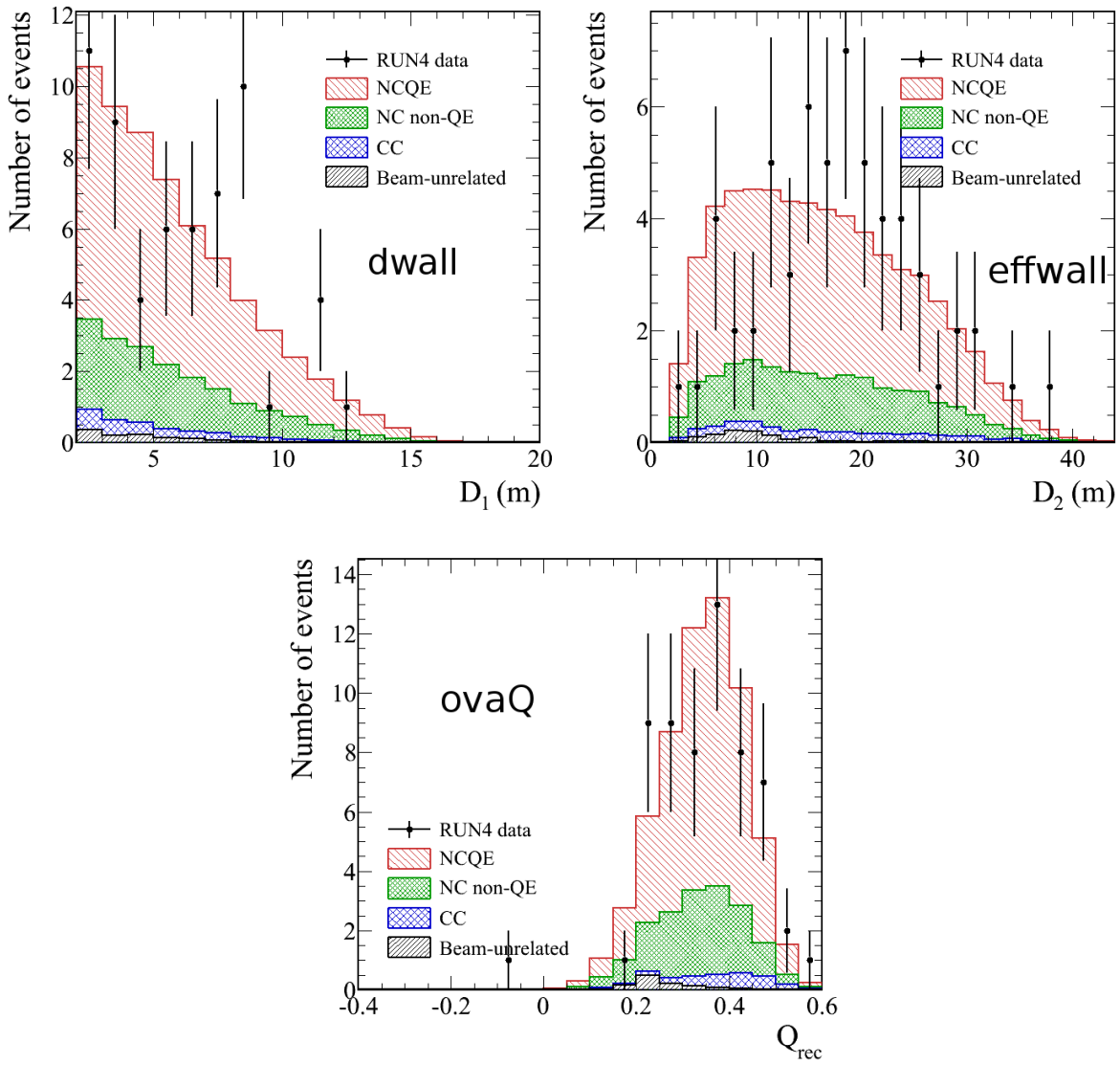

Figure G.9: Dwall (upper left), effWall (upper right) and ovaq (bottom) distribution of T2K RUN4.

G.3 Uncertainty of NCQE cross-section measurement using T2K RUN1-4 data

We assigned the systematic uncertainties of NCQE signal and each backgrounds (NCothers, CC, and beam un-related) separately as shown in Table 6.9. Many toy experiments are made to shift the errors to evaluate the total uncertainties as shown in Fig F.1.

The observed NCQE cross-section distribution by the many toy experiments is shown as Fig. G.10. In the plot, the 68% of the above (below) area from the central value shows the 1σ confidence level interval. The statistical uncertainty is calculated from observed number of candidate events as $1/\sqrt{102} = 9.9\%$. Here, the 68% confidence interval on the observed cross-section is $(1.33, 2.52) \times 10^{-38}\mathrm{cm}^2$.

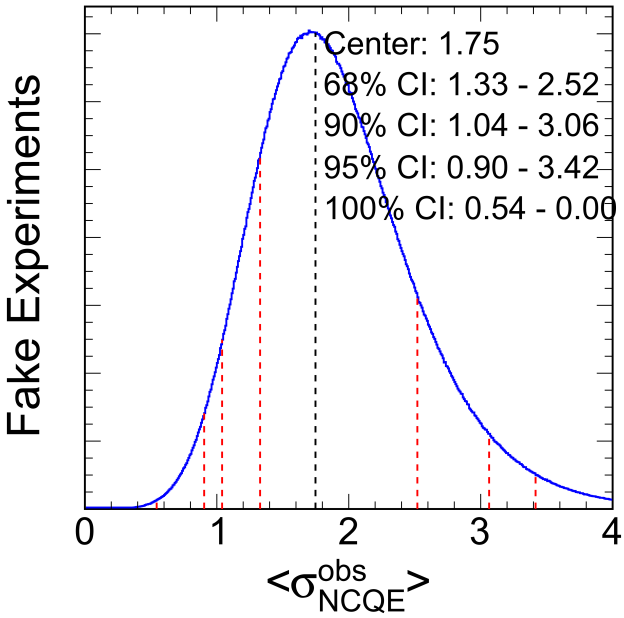

Figure G.10: The updated NCQE cross-section distribution with T2K RUN1-4 observation is made using many toy experiments. The vertical black line shows the center of the integral area, that represent the center value of cross-section results by $1.75 \times 10^{-38}\mathrm{cm}^2$. The red dash lines denote the boundaries of α% C.L. region, which is calculated by the α% fraction of integral area from the center value. Here, we calculate the fraction of integral area as $\alpha = 68, 90, 95, 100$. The 68% confidence interval is (1.33, 2.52)$\times 10^{-38}\mathrm{cm}^2$, and the 90% confidence interval is (1.04,3.06)$\times 10^{-38}\mathrm{cm}^2$.

Appendix H

Improvement by neutron-water experiment

As described previously, the systematic uncertainty due to secondary γ-ray production dominates the systematic error of the NCQE events. Most secondary γ-rays are produced from neutron-water reactions. To reduce the uncertainty due to the secondary γ-ray production, there is a proposal to use a neutron beam irradiating water at RCNP.

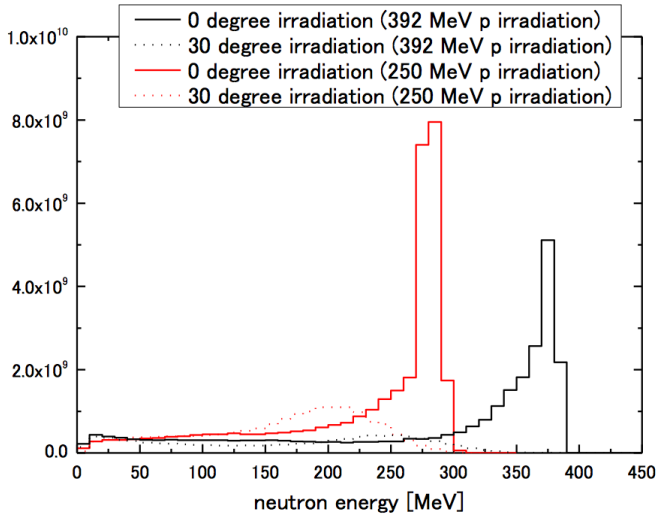

Figure H.1: The energy distribution of the neutrino beam at RCNP. The lines represent the energy spectrum of the neutron beam with the character of the semi-monochromatic energy at zero degrees to the incident proton beam after the Li target. The dashed lines show the energy spectrum of neutrons at 30 degrees with the incident proton beam after the Li target.

Measurement of γ-rays induced by neutron-water reactions at RCNP The experiment aims to have a measurement of multiplicity and energy of γ-rays emitted by neutron-water reactions. The RCNP N0 course uses a proton beam impinging on a Lithium target to produce a semi-monochromatic energy neutron beam. Figure H.1 shows the energy spectrum of the neutron beam. The energy of the incident proton beam is adjustable, such that the energy of neutron beam can be tuned to the energy demanded.

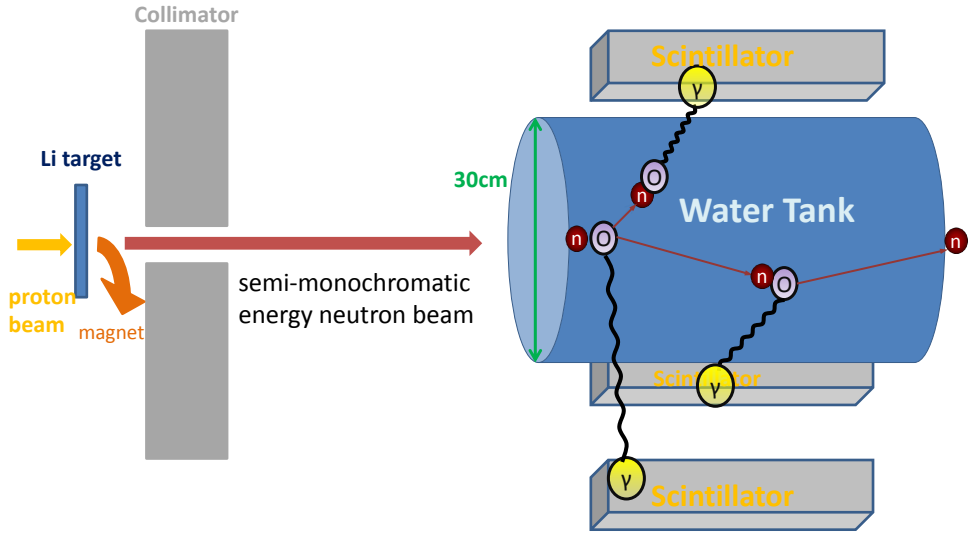

Figure H.2: Schematic of the experiment at RCNP N0 course. The neutron beam with semi-monochromatic energy irradiates the water target, and the scintillators around the tank observe the γ-rays produced by neutron-water reactions.

Figure H.2 shows the schematic of the proposed experiment. The transparent tank filled with water is placed at 17∼38 meters downstream of the Li target, and the neutron beam irradiates the water target. There are several scintillators around the water tank to observe the γ-rays emitted from neutron-water reactions. To separate the scattering neutrons from the γ-rays, the experiment plans to use several kinds of scintillators such as NaI, CsI, BGO, etc.

In the proposal, the experiment uses the neutron beam with maximum energy of 80 MeV as well as 392 MeV to observe the γ-rays production from neutron-water reactions. The precision measurements with the two neutron energies are expected to provide a constraint on the uncertainty due to the secondary γ-ray production in the near future.

.

Appendix I

Furthur improvements

As mentioned in Section 5.3.4, a discrepancy at Cherenkov angle distributions between data and simulation exists. The discrepancy is suggested due to the γ-ray multipliticity induced by the neutron-water reactions. There is no previous study of γ-ray production at neutron-water reactions.. This chapter introduces several improvements to get more information about the secondary γ-rays, which are produced by neutron-water reactions mostly.

Besides, the binning number of 3 hit pmt angle histogram is described at the end of this chapter.

I.1 Neutron Tagging

As shown in Figure 4.14, the number of γ-rays induced by the neutrons has a gap at one. The simulation by GEANT3 does not predict the number of secondary γ-rays from neutron-water interactions well.

As the number of secondary γ-ray induced by neutrons has large uncertainty, the number of produced neutrons is a hint to know the γ-ray multiplicity. Here, a "neutron tagging" method is introduced to study the number of neutrons induced by NCQE reactions. The physical principle of "neutron tagging" is mentioned as follows: A thermal neutron is captured by a hydrogen nucleus, and produce a γ-ray with 2.2 MeV energy as below.

$$n + p \rightarrow d + \gamma\,(2.2\,\mathrm{MeV}), \tag{I.1}$$

The 2.2 MeV γ-rays are observed after the de-excitation γ-ray signal, as the produced thermal neutrons are captured by hydrogen nucleus. The "neutron tagging" refers the signal of 2.2 MeV γ-ray produced by neutrons.

I.1.1 2.2 MeV γ-ray by neutron capture reaction

The neutron tagging method at Super-K was first studied by H. Watanabe and H. Zhang, and the method intends to reduce background in supernova relic neutrino search [145]. Beside the SRN search, in the atmospheric neutrinos analysis the neutron tagging method is applied to mark anti-neutrino CCQE events [147]. This thesis applies the neutron tagging method to study the neutron multiplicity induced by the NCQE reactions.

The free neutrons produced by ν-oxygen NCQE interaction are thermalized to room temperature (0.025 eV) quickly ($\sim 10\,\mu$s). After the thermalization, the neutrons could

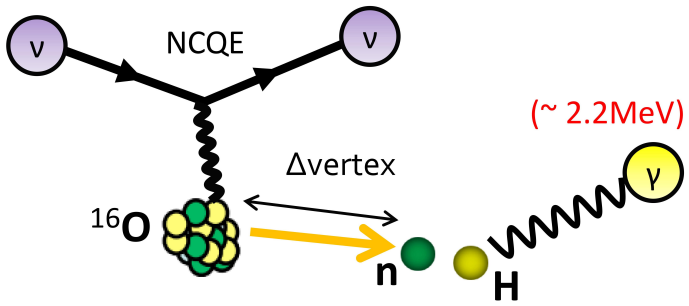

Figure I.1: Schematic of 2.2 MeV γ-ray from the neutron capture reaction. The thermal neutron is produced by the ν-oxygen NCQE reaction.

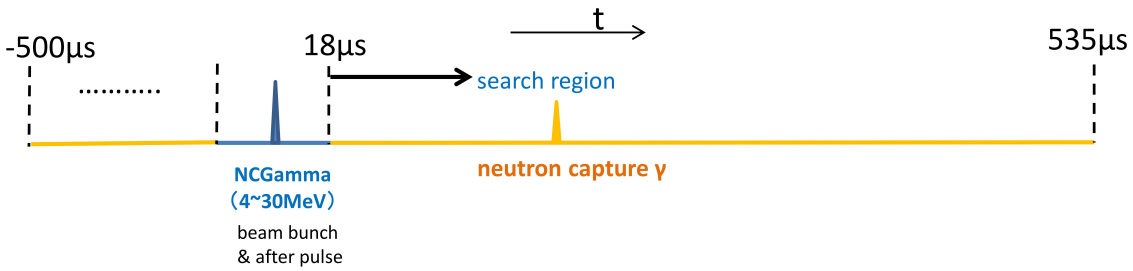

Figure I.2: The 2.2 MeV γ-rays is observed after the de-excitation γ-ray signal. All information of the hit PMTs within $\pm 500\,\mu$s near the neutrino arrival time are saved in T2K spill data. The neutron capture signal are searched at the timing region of (18μs, 535μs) after the de-excitation γ-ray.

be captured by the hydrogen nucleus, and the neutron capture reaction emits a γ-ray with energy of 2.2 MeV as shown in Figure I.1. The cross-section of the neutron capture is 332.6 ± 0.7 mb, and the lifetime of neutron capture is measured as 204.8μs from Ref. [146]. Hence, the γ-rays from the neutron captures are expected to be found until hundreds of μsec after the NCQE interaction, and the timing distribution of the neutron captures is a decay structure with decay time constant of $\sim 204\,\mu$s.

The T2K trigger save the information of all hit PMTs within $\pm 500\,\mu$sec in the spill data. After the de-excitation γ-ray signal, we search the neutron capture signals as shown in Figure I.2. As the average energy of atmospheric neutrinos is similar with the average energy of the T2K beam neutrinos, we use the analysis method of atmospheric neutrino from Ref [147]. Here, the neutron tagging results for the T2K RUN1-4 102 γ-ray candidate events are reported.

I.1.2 Estimation of signal and background

After the simulation of de-excitation γ-ray signal, we extend the simulation to $\Delta T_0 = 535\,\mu$s which is same with the record length of the T2K spill data. The extended simulation is used to estimate the neutron capture reactions. The backgrounds are expected from the radioactive impurities, and the dark noises of PMTs. Instead of MC simulation, the T2K dummy trigger data is used to estimate the background in the searching timing region of (18 μs, 535 μs). The T2K dummy trigger data are taken with the same period of the T2K spill data, and the T2K dummy trigger data are viewed as random trigger

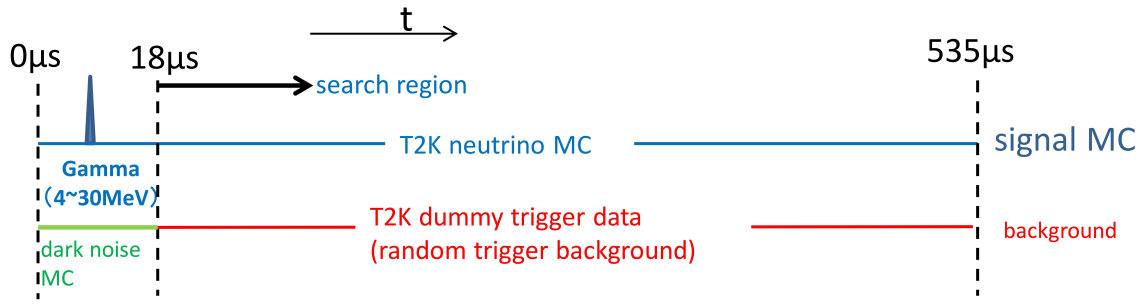

Figure I.3: The simulation for neutron capture signal and background after the de-excitation γ-ray signal. The MC simulation of neutron capture signal is made until 535μs, and the expected background of the search timing region is made by the T2K dummy trigger data.

data without T2K beam neutrinos. Figure I.3 shows the estimation of neutron capture using MC simulation and the T2K dummy trigger data.

I.1.3 Event selection

The 2.2 MeV γ-ray signal after the NCQE neutrino interaction has some features such as follows: The reconstructed energy is $\sim$ 2.2 MeV. The timings of hit PMTs distribute narrowly. The reconstructed vertex of neutron capture signal is expected near the vertex of de-excitation γ-ray signal.

On the other hand, the background result from several sources such as radioactive impurities of ID wall, radon contamination in water, PMT dark noises. Some background events with hit PMTs which are distributed widely in timing, and some background events with vertex near SK ID wall.

To select the neutron capture signal from T2K data, the characteristics of signal and the background are used. The neutron tagging signals appear at timing region of $\Delta T_0 = (+5, +535)\,\mu$sec, but there are the after-pulse of the PMTs appear at the timing region of ΔT_0=+12$\sim$+18 μs. Therefore, we search the 2.2 MeV γ-rays signal at the timing region of $\Delta T_0 = (+18, +535)\,\mu$sec. Next, most neutron capture events with the reconstructed vertices are supposed to be within 200cm from the vertices of the de-excitation γ-ray. The events with $\Delta v \leq 200$ cm are selected.

The 2.2 MeV γ-ray from neutron capture are selected by the two following steps: First, we sort all the hit PMTs by their residual time $t_{i,res} = t_i - t_{i,tof}$, where the $t_{i,tof}$ is time of flight from the reconstructed vertex of de-excitation γ-ray to the i-th PMT. By sliding a 10 ns window in the timing region of $\Delta T_0 = (+18, +535)\mu$sec, the number of hit PMTs within 10 ns N_{10} is used to search signal peaks. Next, we prepare a set of 16 variables for each event, and the set of variables is fed into a neural network calculation to obtain the output value. The second selection of the event candidates is based on the output values of neural network.

Initial candidates selection We search signal peaks with the number of hit PMT within 10ns window larger than 7 as below

$$N_{10} \geq 7 \tag{I.2}$$

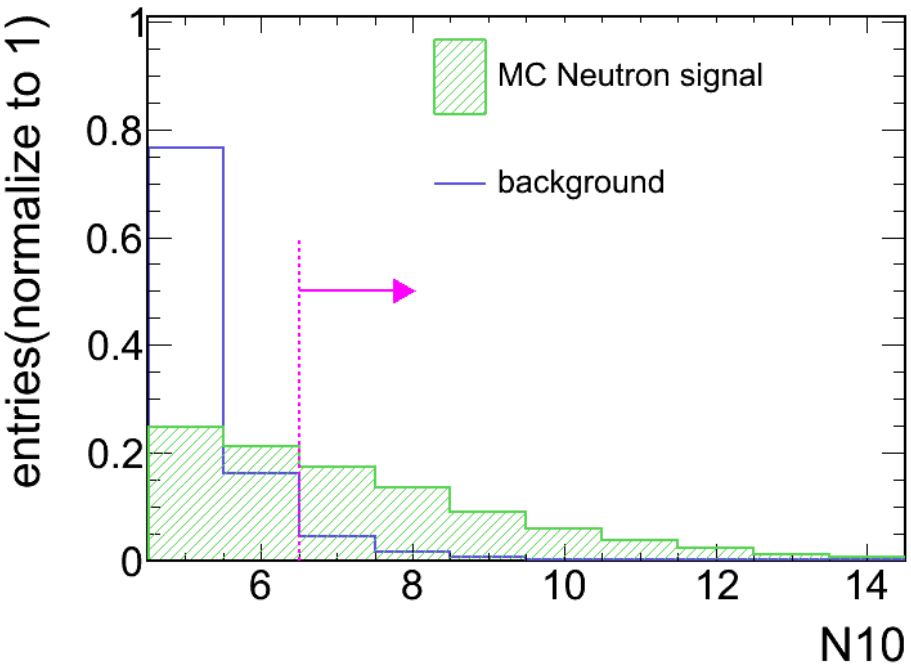

Figure I.4: The N_{10} distribution of the simulated signal and the expected background events. The vertical dash line shows the selection of $N_{10} \geq 7$. The initial selection remove the background events with low energy.

The first timing t_i of hit PMT in N_{10} is assigned to be the timing T_0 of the event. Then, we jump to t_0+20 ns to search a next peak. That avoids a double counting of the same signal peak. The event includes the hit PMTs within the timing region of $(t_0, t_0$+20) ns. The high energy events are removed as below.

$$N_{10} \leq 50 \tag{I.3}$$

To remove the cosmic ray muon events, the activity neighboring 200 ns are checked as the following selection.

$$N_{200} \leq 200 \tag{I.4}$$

where N_{200} is the number of hit PMTs within 200ns surrounding the γ candidate at t_0. N_{10} distributions of the simulated signal and the expected background is shown in Figure I.4. The background events with low energy are removed.

490 γ-ray of neutron capture events after the 102 de-excitation γ-rays data events are left after the initial selection.

Second selection by neural network It is hard to select the neutron capture signal using single parameter, so "Neural network" method is used to separate the signal and the backgrounds. Neural network is a machine learning tool, which computes the classification task in analysis.

We perform the neural network to be fed with 16 variables and evaluate the output value for identification of a 2.2 MeV γ-ray signal. A set of 16 variables is used as the input of neural network calculation, and the detail of the 16 variables are in Ref. [147]. The 16 variables are listed as the following:

- N_{10}: Number of hit PMTs within 10ns
- N_c: Number of clustered hit PMTs in N_{10}
- N_{low}: Number of hits on low probability PMTs within N_{10}
- N_{300}: Number of hit PMTs within 300ns
- ϕ_{rms}: Hit vector RMS
- θ_{mean}: Mean opening angle
- t_{rms}: Root of mean square (RMS) for hit PMT timing
- min$t_{rms,3hit}$: Minimum RMS of 3 hits timing
- min$t_{rms,6hit}$: Minimum RMS of 6 hits timing
- E_{Bonsai}: Reconstructed energy using BONSAI fit
- dwall$_{Bonsai}$: Reconstructed dwall using BONSAI fit
- NF_{wall}: Reconstructed dwall using Neut fit
- ΔN_{10}: Difference of N_{10} between using vertex of Neut fit to sort hit PMTs timing and using primary vertex
- Δt_{rms}: Difference of t_{rms} between using vertex of Neut fit to sort hit PMTs timing and using primary vertex
- $\Delta v(NF-BS)$: Distance difference of two vertices between using Neut fit and using BONSAI fit
- $\Delta v(NF-AP)$: Distance difference of primary vertex and vertex using Neut fit

Figure I.5 shows the results of neural network. In the figure, the simulated signal events are separated with the expected backgrounds successfully with the output of the neural network. We choose the data events with output larger than 0.832 as the neutron capture candidate events.

I.1.4 Results

After the 2.2 MeV γ-ray selections, the expected efficiency of 2.2 MeV γ-ray selection is defined as

$$\frac{N_{sig}^{exp}}{N_{all\,capture}^{exp}} = 15.5\%, \tag{I.5}$$

where $N_{all\,capture}^{exp}$ is the expected number of all neutron captures, and N_{sig}^{exp} is the expected number of signal events that selected as the 2.2 MeV γ-ray candidates.

The expected background per observed event is defined as

$$\frac{N_{bkg}^{exp}}{N^{exp}} = \frac{N_{bkg}^{exp}}{N_{sig}^{exp} + N_{bkg}^{exp}} = 4.7\%, \tag{I.6}$$

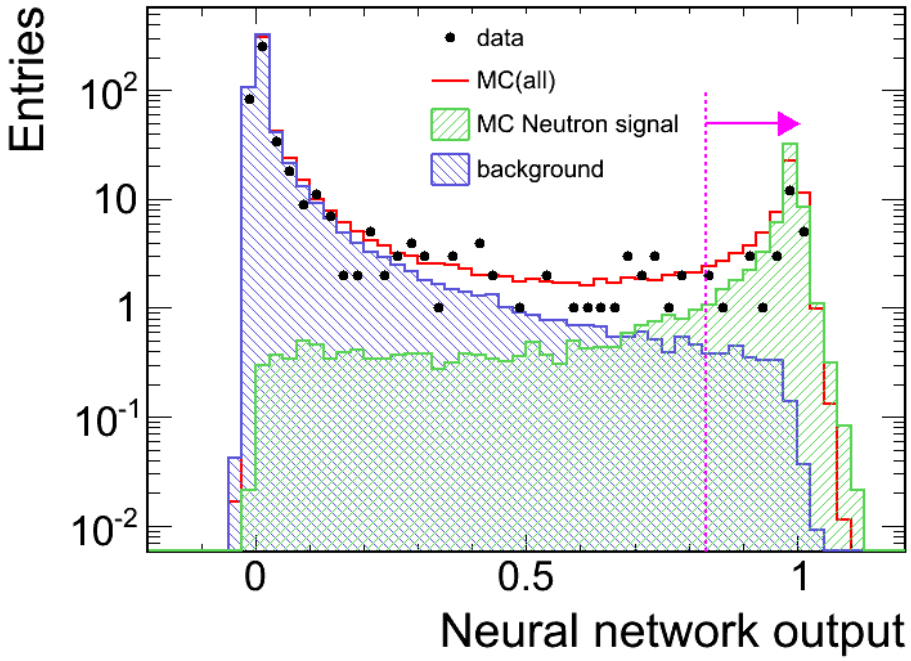

Figure I.5: The neural network output distributions. The green histogram shows the output distribution of simulated neutron capture, and blue histogram shows the output distribution of the expected background events. The output distribution of data is the black dots. The distribution of data is consistent with the expectation which is made by the signal simulation and the T2K dummy trigger data. We select the events with output value larger than 0.832 as the neutron capture candidate events.

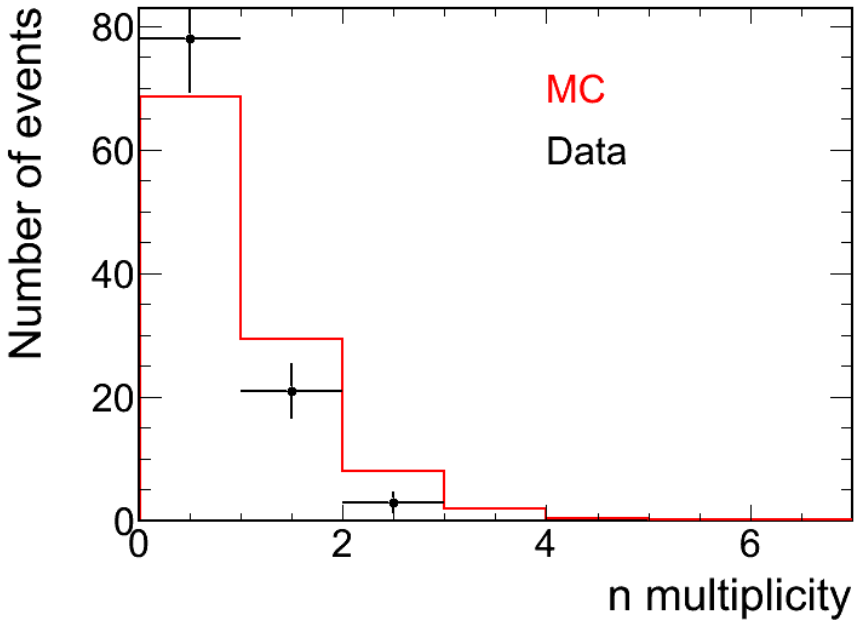

Figure I.6: The multiplicity of neutron (tagging) of the 102 de-excitation γ-ray events. The number of candidate events is 27.

where N^{exp} is the expected number of events including the expected number of signal events N^{exp}_{sig} and the expected number of background events N^{exp}_{bkg}. An estimation of N^{exp}_{bkg} is derived from the T2K dummy trigger data.

For the 102 de-excitation γ-rays events, only 27 neutron capture of data candidates N^{obs} are found, while the expected number of neutron capture events from the simulation and T2K dummy trigger data $N^{exp} = N^{exp}_{sig} + N^{exp}_{bkg}$ is 53.53. The number of data events is less than the expectation obviously, and the discrepancy between the simulation and data gives a hint to the discrepancy of Cherenkov angle distribution between the simulation and data. The neutron multiplicity of the 102 de-excitation γ-ray events is shown in Figure I.6. The Kolmogov-Smirnov test is made to compare the data result and the expectation, and the K-S probability is 0.534.

The Δt_0 timing distribution is checked as shown in Figure I.7. Since the observed number of events N^{obs} is only 27, there is no clear decay structure in statistics. Thus, we are not certain to claim that the 27 events are identified as 2.2 MeV γ-ray signal induced by neutron captures.

I.1.5 Summary

This section gave the first study of neutron multiplicity by observing the 2.2 MeV γ-rays after the de-excitation γ-rays. The initial selection and the selection of neural network output are made to select the neutron capture events. As the result, the expected number of events is larger than the observed number of data events obviously. This discrepancy gives a hint to the γ-ray multiplicity of simulation and data.

But the observed number of 2.2 MeV γ-ray candidate events is not enough in statistics, we are not sure that the observed candidate events are the neutron tagging events. For near future, more neutron capture events after de-excitation γ-ray samples are expected,

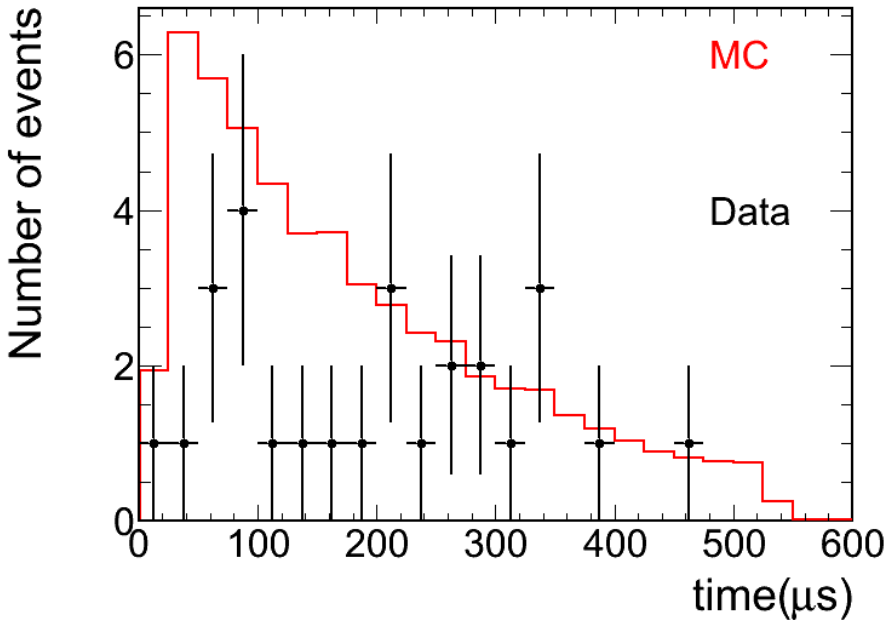

Figure I.7: The neutron tagging time (ΔT_0) distribution. Because the number of observed events is only 27, and a clear decay structure is not seen in the figure.

and more events provide in statistics to make sure the neutron capture signals.

There are other candidate simulator for the simulation of secondary γ-ray production such as GEANT4, FLUKA, and PHITS. As the first study of neutron tagging is done, the method is expected to provide an indicator to pick up a suitable simulator for seocndary γ-ray production in future.

I.2 Event Categorization

I.2.1 Patterns of angle histogram

To study the solution for the discrepancy at the Cherenkov distributions between the data events and the expected events, we attempt to acquire more information about multi-γ events from patterns of the 3 hit pmt angle histograms. Therefore, we survey every 3 hit pmt angle histograms of the simulated events with a large Cherenkov angle ($\geq 75^o$). The 3 hit pmt angle histograms are categorized into the three following patterns: linear, highland, two-peak (or multi-peak).

Figure I.8 shows a angle histogram with the linear pattern, and the linear pattern is straight line that starts near 0 degree and extends to the maximum peak at 90 degree. The events of typical multi-γ rays are considered to have 3 hit pmt angle histogram that is linear pattern as shown in the right plot of Figure B.8.

Figure I.9 shows a angle histogram with the highland pattern. The highland pattern is a function that inclines from ± 10 degree to turning point at the range of $(40^o, 60^o)$ and extends horizontally to 90 degree flatly.

Figure I.10 shows a angle histogram with the "two-peak" pattern. If the angle of highest peak of the histogram is large, but there are obvious minor peaks locating smaller than 34 degree. The angle of the minor peak is smaller than 34 degree, because Cherenkov

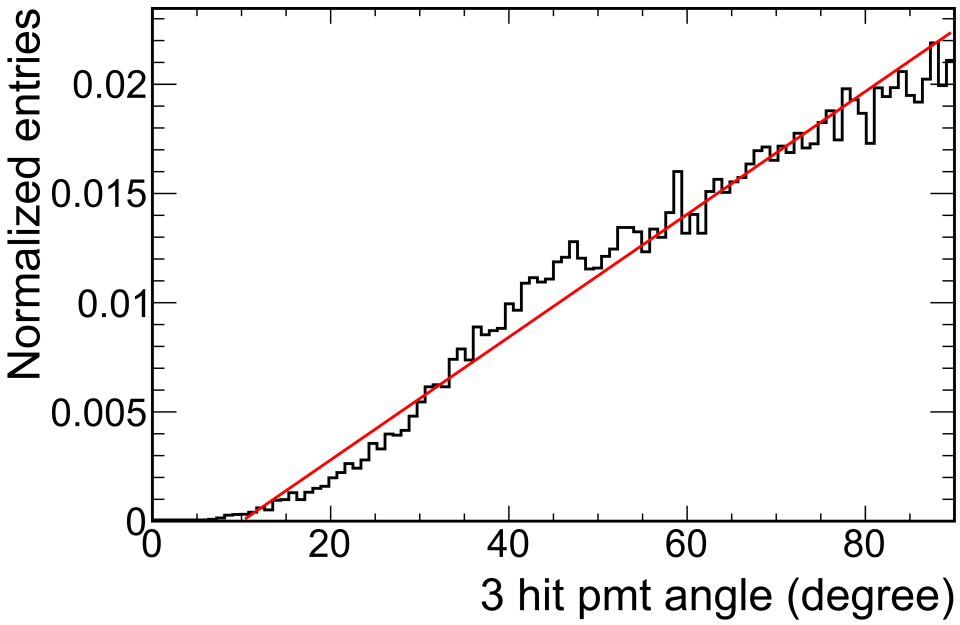

Figure I.8: The linear like pattern has the highest peak at about 90 degree. The black histogram shows the event with large Cherenkov angle. The red line is the fitting result using a linear function.

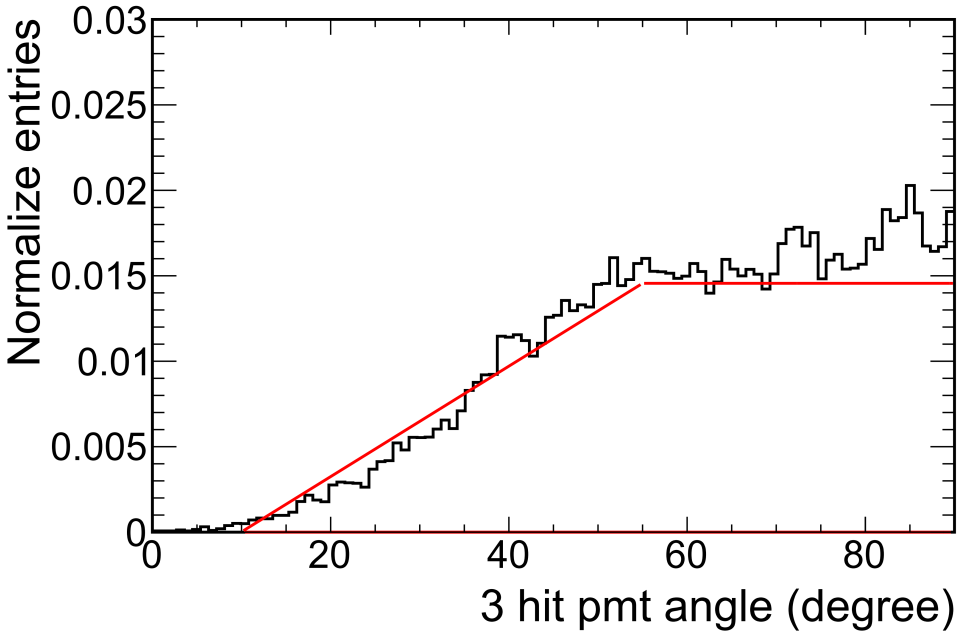

Figure I.9: The highland like pattern has the highest peak at about 90 degree. The black histogram shows the event with large Cherenkov angle. The red line is the fitting result using a highland function.

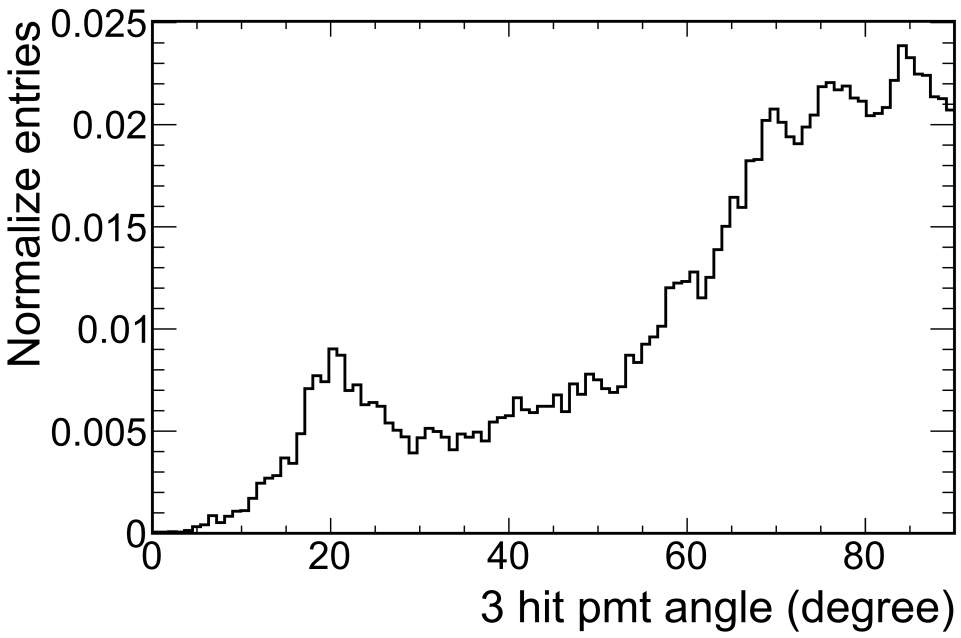

Figure I.10: The two-peak (multi-peak) like pattern has the highest peak at about 90 degree. The highest peak is located near 90 degree, and there is an alternative minor peak that locate below 42 degree.

photons are emitted from muon (or pion) produced in CC or NC-other reactions. Therefore, the minor peaks are used as an alternative selection (cut) to reduce the background, and the new selection is described in the next section.

The simulated events and the data candidate events are categorized into the three patterns by their 3 hit pmt angle histograms.

I.2.2 Likelihood method

Only $< 10\%$ faction of events are expected to have the two-peak (multi-peak) pattern of histogram. We categorize the γ-ray events into the linear like or the highland like using the likelihood values of the linear function and the highland function. Then, we select two-peak like from all the events using peak search method.

The categorization method is described as follows. As the number hit PMT in each event is different, we normalize the 3 hit pmt histogram to unit area for comparing the likelihood values easily.

The calculation of the likelihood value of linear pattern is described as follows: A linear function is used to fit the normalized angle histogram. The linear fitting function is given by.

$$y = a\theta_{angle} + b, \quad y \geq 0 \tag{I.7}$$

The fitting result is substituted into the linear function to obtain probability distribution function (p.d.f.). Then we use the p.d.f. to calculate likelihood value of linear pattern as below:

$$L_{linear} = \prod_i (a\theta_{i,angle} + b)^{y_i}, \quad y_i \geq 0 \tag{I.8}$$

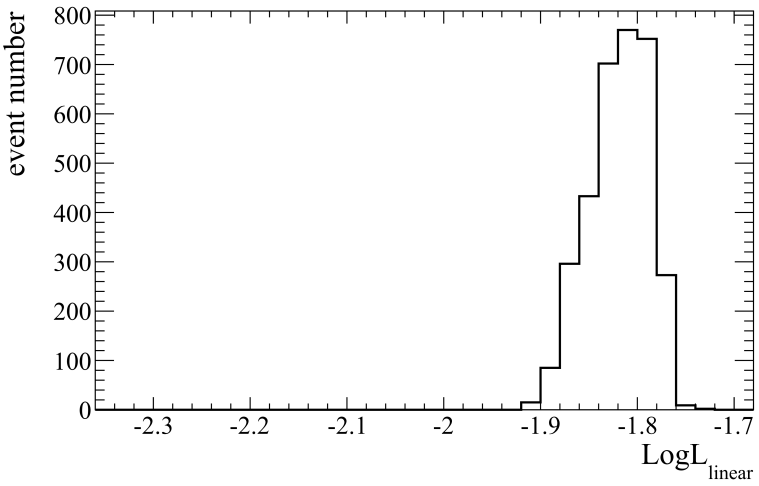

Figure I.11: The logarithm likelihood value distribution (linear) of the simulated events. The linear function is used as the probability distribution function. There is no obvious separation for linear like and linear unlike

where i means the i-th bin of the 3 hit pmt histogram, and $\theta_{i,angle}$ is the center angle of the i-th bin, and y_i is the normalized height of i-th bin of the histogram. A logarithm value of the likelihood value is used as below.

$$LogL_{linear} = \sum_i y_i Log(a\theta_{i,angle} + b) \tag{I.9}$$

The logarithm of likelihood value distribution of the simulated events is shown in Fig. I.11. The event with a larger likelihood value is expected to be more linear like, and there are no obvious separation for linear-like and linear-unlike in the figure.

The calculation of the likelihood value of highland pattern is described as follows: A highland function is given by

$$\begin{array}{rcll} y & = & a\theta_{i,angle} + b, & \theta_{angle} \leq \theta_t \,(\text{slant part}) \\ y & = & c = a\theta_t + b, & \theta_{angle} > \theta_t \,(\text{horizontal part}) \end{array} \tag{I.10}$$

where $\theta_{i,angle}$ is the center angle of the i-th bin, and c is constant that represents the height of the flat region. θ_t is the turning point from slant to horizontal, and the turning point is restricted in the region of $55^o \geq \theta_t \geq 40^o$. The fitting result is substituted into the highland function to obtain probability distribution function (p.d.f.). Then we use the p.d.f. to calculate likelihood value of highland pattern as below:

$$\begin{array}{rcll} L_{highland,slant} & = & \prod_i (a\theta_{i,angle} + b)^{y_i}, & y_i \geq 0, \quad \theta_{i,angle} \leq \theta_t \\ L_{highland,hori} & = & \prod_i c^{y_i}, & \theta_{i,angle} > \theta_t \\ L_{highland} & = & L_{highland,slant} \times L_{highland,hori} & \end{array} \tag{I.11}$$

Here the $LogL_{highland}$ values are also calculated as a logarithm of likelihood of highland pattern. Figure I.12 shows the logarithm of likelihood value distribution of simulated events, and there is no obvious separation for highland like and highland unlike events in the figure.

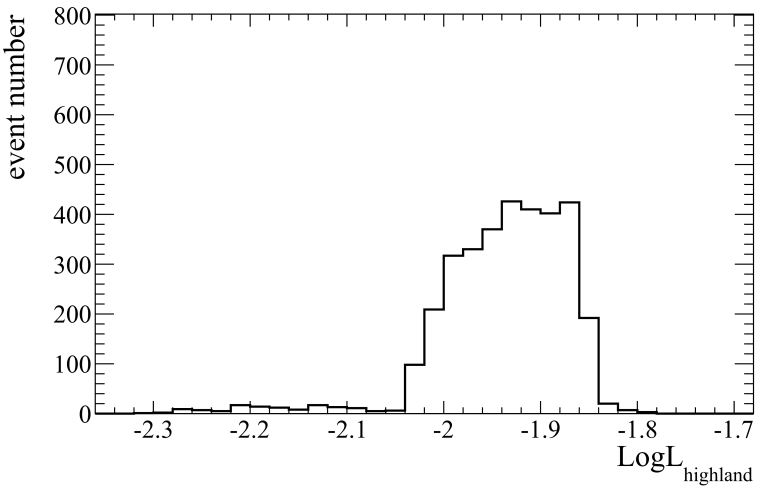

Figure I.12: The logarithm likelihood value distribution (highland) of the simulated events. The highland function is used as the probability distribution function. There is no obvious separation for highland like and highland unlike.

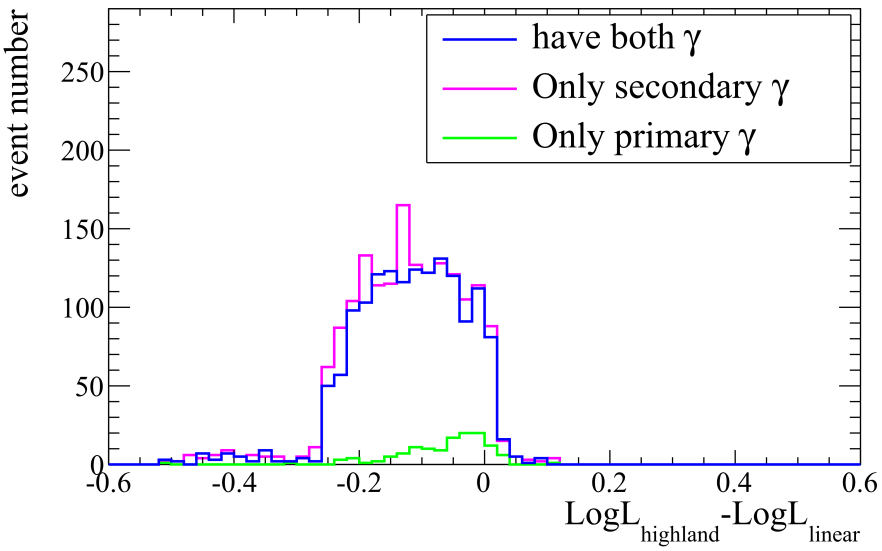

Figure I.13: The logarithm likelihood difference $LogL_{highland} - LogL_{linear}$ distribution of simulated γ-ray events. As the horizontal axis goes right side, the simulated events are more highland like and less linear like, while the left events are more linear like. The green line represents the distribution of the events with only primary γ-rays. highland like events. The pink line represents the distribution of the events with only secondary γ-rays. the blue line represent the distribution of events with bothe primary γ-ray and secondary γ-rays.

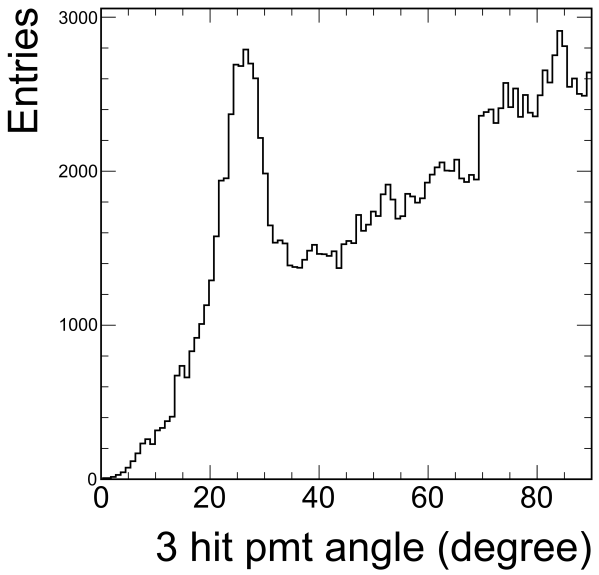

Figure I.14: The 3 hit pmt histogram of a CC event. The Cherenkov angle is found as 85 degree. There is a peak near 28 degree, and the peak results from the produced muon in the CC reaction.

I.2.3 Discussion

We try to find the correlation between the γ-ray production and the two patterns of histograms. The difference between the logarithm likelihood value of highland pattern and the logarithm likelihood value of linear pattern $LogL_{highland} - LogL_{linear}$ describes the relative degree of highland like or linear like. Figure I.13 shows that the $LogL_{highland} - LogL_{linear}$ distribution of different γ-ray production, such as events with only primary γ-rays, or events with only secondary γ-ray, or events with both γ-rays.

The events with only primary γ-ray are more linear like than highland like. For the events have secondary γ-rays, there is no obvious tendency toward linear like or highland like. The event categorizations by the pattern of the 3 hit pmt angle histogram don't have not enough information to know the details of γ-ray production. More information is needed to separate events with different production process.

I.3 Peak Search and Minor Peak Selection

I.3.1 Minor peaks

As described in the previous section, there are events with the two-peak pattern of 3 hit pmt histogram. The highest peak in the histogram is assigned to the Cherenkov angle value, and the other (minor) peaks have hidden information about produced particles. Figure I.14 shows the 3 hit pmt angle histogram of CC interaction, and the simulated event is selected as a de-excitation candidate event. Although photons from multi-γ rays dominate, there is the minor peak near 28 degree which is contributed from photons emitted by the muon with low momentum.

The information of the minor peaks reveals the heavy particles such as muons, pions which are are only produced from the background reactions. The minor peaks with angle

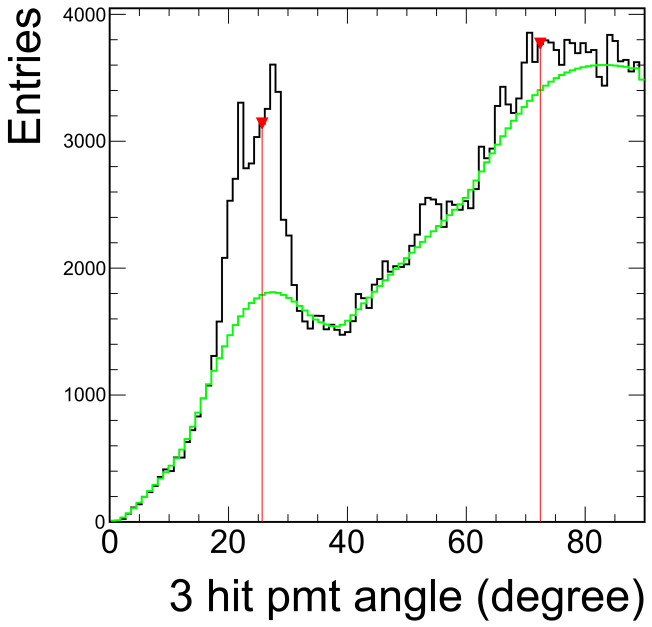

Figure I.15: The result of peak searching for a CC1π simulation events. A minor peak is found at near 28 degree. The black line represents the 3 hit pmt angle histogram. The smooth background is drawn as the green line that is base line. Two peaks are marked with red vertical lines. The higher one is near the highest peak that determines the Cherenkov angle value. The Cherenkov photons emitted from pion or the decayed muon contribute the minor peak in the figure.

value less than 34 degree are used to tag the background events.

I.3.2 Peak Search

We use the spectral processing tools TSpectrum class in ROOT to search minor peaks in 3 hit pmt angle histogram. The TSpectrum class is originally designed to process γ-ray peak in spectrum [149–151]. The peak search procedures for one-dimension histogram are as follows: The background function is estimated to subtract a base of the spectrum. Then, the locations of peaks are found using the discrete analog of the second derivative of 1-D histogram [152]. The found peaks are marked as minor peak candidates except the peaks near the highest peak. Figure I.15 shows the searching result of a CC1pi event, and the peak near 28 degree shows that there are Cherenkov photons emitted from pion or decayed muon.

I.3.3 Minor peak selection

As described previously, the TSpectrum searches the minor peaks in 3 hit pmt histogram. We choose the peak with minimum angle value among the found minor peaks for the minor peak selection (cut). The minimum angle of peaks distributions for reaction events are shown in Figure I.16. There is a clear peak which appearing near 30 degree in the distribution of CC events. Whereas in the distributions of other interactions, there is no peak with angle smaller than 34 degree. The minor peak cut remove CC events

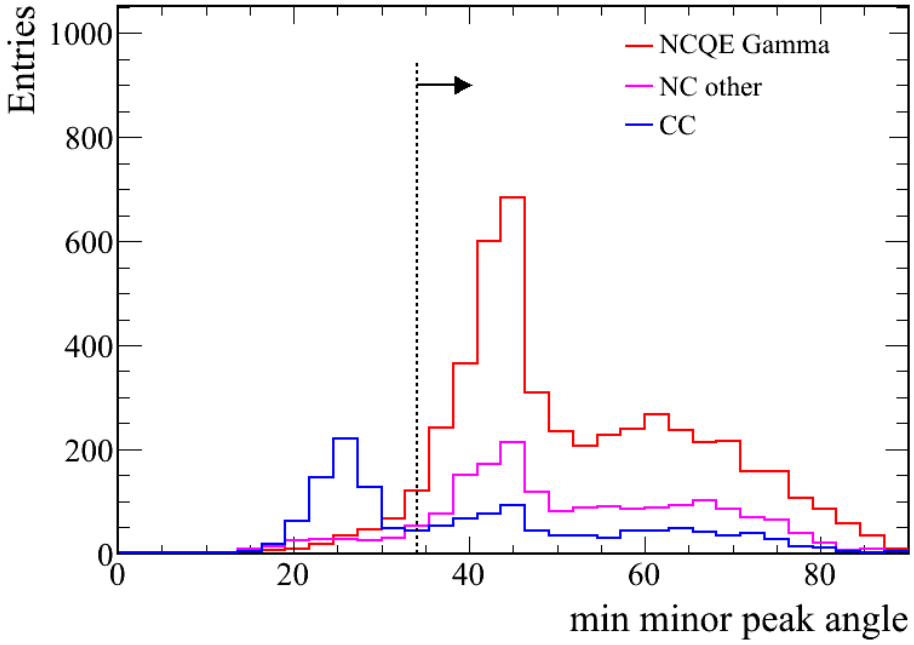

Figure I.16: The minimum angle distribution of found minor peaks. The distribution of CC events has a peak smaller than 34 degree.

efficiently.

Since the CC background events are expected only ∼4% fraction in γ-ray events. Using minor peak selection, the beam-related background events are removed by small amount. Table I.1 summarizes the expected number of events for T2K RUN1-4 with (without) using the minor peak cut. The number of total beam-related background (NCothers , CC) events decreased by 2.0. The number NCQE signal events decreased by 2.3, which is about the same amount with one of background events. Consequently, the minor peak cut is auxiliary to the Cherenkov angle selection in the future analysis.

Table I.1: Summaries of expected event number of T2K RUN1-4 that are before minor peak cut and after minor peak cut. The expected event numbers are listed before the cross-section correction.

neutrino reaction	No cut	With cut	Changing Ratio
NCQE	87.9	85.6	-2.6%
NCothers	25.5	24.37	-4.6%
CC	3.88	2.97	-23.4%
Total	117.3	112.98	-3.7%

I.4 Binning of 3-hit pmt angle plot

As mentioned in Appendix B.3, we separate the 3 hit pmt angle histogram into 100 bins, and the width of every angle bin is 0.9 degree. Therefore, the angle selection is 34.2 degree in practice. To find the suitable number of histogram bins, we attempt to change

the bin number to 90 that let the threshold value of the Cherenkov angle selection be 34.0 degree exactly.

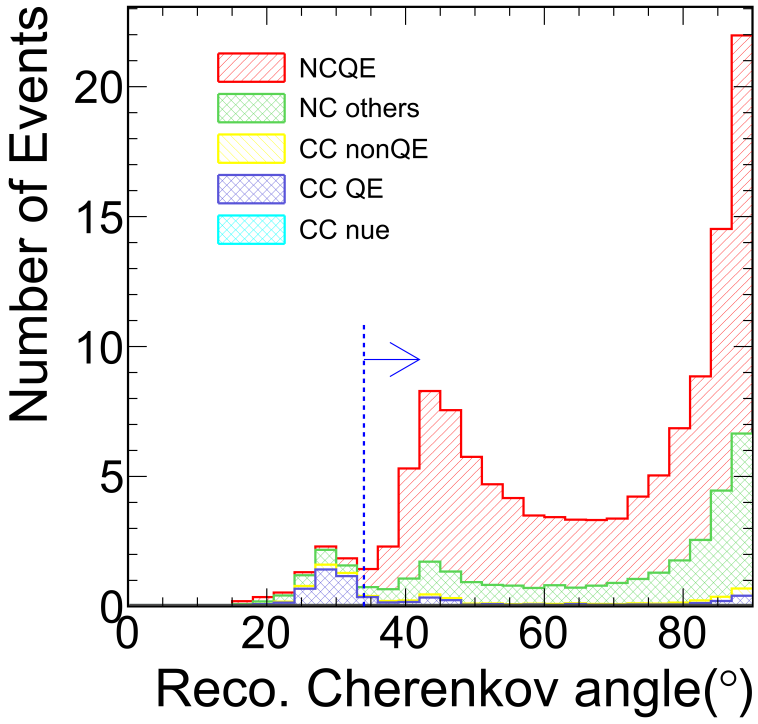

Figure I.17: The Cherenkov angle distribution for T2K RUN1-4 events is made from the 90 bins in 3 hit pmt histograms.

Then, the Cherenkov angle is reconstructed by the same method described in Appendix B.3. The Cherenkov angle distribution of T2K Run1-4 beam-related events for 90 bins of histogram is shown in Figure I.17, and the distribution using 90 bin of 3 hit pmt histogram is similar with the distribution using 100 bins of 3 hit pmt histogram. The expected number of events change by +0.18, and +0.15% fraction of events increased.

Let us try another binning number to see the effect of binning number after the Cherenkov angle selection. Now, we separate 1000 bins for the 3 hit pmt histogram. The procedures to determine Cherenkov angle are similar with one of 100 bins, but the sliding binning window is changed to 70 bins. Here, the Cherenkov angle distribution using 1000 bins of 3 hit pmt histogram is shown in Figure I.18. The expected number of events decreased by 0.25, and 0.21% fraction of events decreased. The variation is small, since there is no much change near 34.0 degree. The expected number for 90 binning and 1000 binning is summarized in Table I.2, and there are no large changes of the expected number of events for different binning number.

The 90 binning number is preferred for future analysis, since the Cherenkov angle selection is more precise.

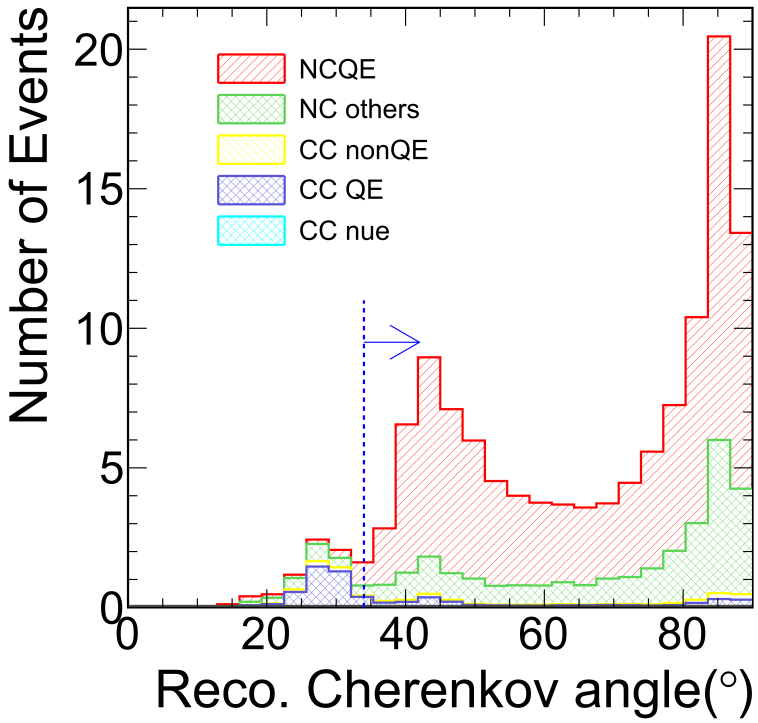

Figure I.18: The Cherenkov angle distribution fo T2K RUN1-4 is made from the 1000 bins in 3 hit pmt histograms.

Table I.2: Summary of expected number of events for different binning number of 3 hit pmt angle histograms. The expected numbers of events are listed before the cross-section correction.

binning number	100	90	1000
T2K RUN1-4 event number	117.31	117.49	117.06
changed ratio	–	+0.15%	-0.21%

List of Figures

List of Tables

Bibliography

[1] Sheldon L. Glashow, "Partial-symmetries of weak interactions", Nucl. Phys. **22**, 579-588(1961)

[2] Steven Weinberg, "A model of leptons", Phys. Rev. Lett. **19**, 1264-1266(1967)

[3] Abdus Salam, *Elementary particle Theory Proc. 8th Nobel Symp.: Relativistic Groups and Analyticity*, N. Svartholm, ed. Wiley-Interscience(1968)

[4] The ALEPH Collaboration, The DELPHI Collaboration, The L3 Collaboration, The OPAL Collaboration, The SLD Collaboration, "Precision electroweak measurements on the Z resonance", Phys. Rep. **427**, 257-454(2006)

[5] ATLAS Collaboration, "Observation of a new particle in the search for the Standard Model Higgs boson with the ATLAS detector at the LHC", Phys. Lett. B**716** 1-29(2012)

[6] CMS Collaboration, "Observation of a new boson at a mass of 125 GeV with the CMS experiment at the LHC", Phys. Lett. B**716**, 30-61(2012)

[7] Y. Fukuda, *et al.* (Super-Kamiokande Collaboration), "Evidence for Oscillation of Atmospheric Neutrinos", Phys. Rev. Lett. **81**, 1562-1567(1998)

[8] C. S. Wu, *et al.*, "Experimental Test of Parity Conservation in Beta Decay", Phys. Rev. **105**, 1413(1957)

[9] F. Reines and Clyde L. Cowan Jr., "Free Antineutrino Absrobtion Cross Section. I. Measurement of the Free Antineutrino Absorption Cross Section by Protons", Phys. Rev. **113**, 273(1959)

[10] F. J. Hasert, *et al.*, "Observation of neutrino-like interactions without muon or electron in the GARMELLE neutrino experiment", Phys. Lett. **46B** , 138(1973)

[11] Ziro Maki, Masami Nakagawa, and Shoichi Sakata, "Remarks on the Unified Model of Elementary Particles", Prog. of Theo. Phys. **28**, No. 5(1962)

[12] B. Pontecorvo, "Inverse beta process and nonconservation of lepton charge", Sov. Phys. JETP **7**, 172-173(1958)

[13] B. Pontecorvo, "Neutrino experiments and the problem of conservation of leptonic", Sov. Phys. JETP **26**, 984-988(1968)

[14] Burton Richter, "Conventional Beams or Neutrino Factories: The Next Generation of Accelerator-Based Neutrino Experiments", arXiv:hep-ph/0008222

[15] T. Yanagida, in *Proc. Workshop on the Unified theory and Baryon numer in the Universe*, ed. by Osawada, a. Sugamoto (KEK report 79-18, 1979), p.95

[16] L. Wolfenstein, "Neutrino oscillation in matter", Phys. Rev. D **17**, 2369(1978)

[17] S. P. Mikheev and A. Yu. Smirnov, "Neutrino oscillations in a variable-density medium and ν-bursts due to the gravitational collapse of stars", Zh. Eksp. Teor. Fiz. **91**, 7-13(1986)

[18] B. Zeitnitz, *et al.* (KARMEN collaboration), "KARMEN: Neutrino Physics at ISIS", Prog. Part. Nucl. Phys. **32**, 351-373(1994)

[19] B. Armbruster, *et al.* (KARMEN collaboration), "Measurement of the weak neutral current excitation $^{12}\mathrm{C}(\nu_\mu\nu_\mu^{'})^{12}\mathrm{C}^*(1+,1;15.1\mathrm{MeV})$ at $E_{\nu_\mu} = 29.8\mathrm{MeV}$", Phys. Lett. B **423**, 15-20(1998)

[20] J. Kameda, "Observation of de-excitation gamma rays from nuclei in 1kton detector in K2K experiment", Nucl. Phys. B(Proc. Suppl.) **159**, 44-49(2006)

[21] K.A. Olive, *et al.*, (Particle Data Group), Chin. Phys. C, **38**, 090001 (2014)

[22] B. Aharmim, *et al.*, "Combined analysis of all three phases of solar neutrino data from the Sudbury Neutrino Observatory", Phys. Rev. C **88**, 025501(2013)

[23] A. Gando, *et al.*, (KamLAND Collaboration), "Reactor on-off antineutrino measurement with KamLAND", Phys. Rev. D **88**, 033001(2013)

[24] Y. Fukuda, *et al.*, "Evidence for Oscillation of Atomspheric neutrinos" Phys. Rev. Lett. **81**, 1562(1998)

[25] P. Adamson, *et al.*, "Measurement of Neutrino and Antineutrino Oscillations Using Beam and Atmospheric Data in MINOS", Phys. Rev. Lett. **110**, 251801(2013)

[26] K. Abe, *et al.* (T2K collaboration), "Precise Measurement of the Neutrino Mixing Parameter θ_{23} from Muon Neutrino Disappearance in an Off-Axis Beam", Phys. Rev. Lett. **112**, 181801(2014)

[27] Aldo M. Serenelli, W.C. Haxton, and Carlos Pena-Garay, "Solar models with accretion I. application to the solar abudance problem", Astrophys. J. **743**, 24(2011)

[28] F. P. An, *et al.* (Daya Bay Collaboration), "Spectral Measurement of Electron antineutrino Oscillation amplitude and Frequency at Daya Bay", Phys. Rev. Lett. **112**, 061801(2014)

[29] J. K. Ahn, *et al.* (RENO Collaboration), "Observation of Reactor Electron Antineutrinos Disappearance in the RENO Experiment", Phys. Rev. Lett. **108**, 191802(2012)

[30] Y. Abe, *et al.* (Double Chooz Collaboration), "Reactor $\overline{\nu}_e$ disappearance in the Double Chooz experiment", Phys. Rev. D **86**, 052008(2012)

[31] A. Aguilar, *et al.* (LSND collaboration), "Evidence for neutrino oscillation from the observation of $\overline{\nu}_e$ appearance in a $\overline{\nu}_\mu$ beam", Phys. Pev. D **64**, 112007(2001)

[32] A. A. Aguilar-Arevalo, *et al.*, (MiniBooNE Collaboration), "Event Excess in the MiniBooNE Search for $\overline{\nu}_\mu \to \overline{\nu}_e$ Oscillations", Phys. Rev. Lett. **105**, 181801(2010)

[33] A. A. Aguilar-Arevalo, *et al.*, (MiniBooNE Collaboration), "Improved Search for $\overline{\nu}_\mu \to \overline{\nu}_e$ Oscillation in the MiniBooNE Experiment", Phys. Rev. Lett. **110**, 161801(2013)

[34] B. Armbruster, *et al.* (KARMEN collaboration), "Upper limits for neutrino oscillations $\overline{\nu}_\mu \to \overline{\nu}_e$ from muon decay at rest", Phys. Rev. D **65**, 112001(2002)

[35] K. Abe, *et al.* (Super-Kamikande collaboration), "Limits on sterile neutrino mixing using atmospheric neutrinos in Super-Kamiokande", Phys. Rev. D **91**, 052019(2015)

[36] P. Astier, *et al.* (NOMAD collaboration), "Search for $\nu_\mu \to \nu_e$ oscillations in the NOMAD experiment", Phys. Lett. B **570**, 19 (2003)

[37] M. Antonello, *et al.* (ICARUS collaboration), "Experimental search for the LSND anomaly with the ICARUS detector in the CNGS neutrino beam", Eur. Phys. J C**73**, 2345(2013)

[38] G. Mention, *et al.*, "Reactor antineutrino anomaly", Phys. Rev. D **83**, 073006(2011)

[39] Joachim Kopp, Pedro A. N. Machado, Michele Malton, and Thomas Schwetz, "Sterile neutrino oscillations: the global picture", JHEP **1305**, 050(2013)

[40] P. Adamson, *et al.* (The MINOS collaboration), "Search for sterile neutrino mixing in the MINOS long-baseline experiment", Phys. Rev. D **81** , 052004(2010)

[41] P. Adamson, *et al.* (The MINOS collaboration), "Active to Sterile Neutrino Mixing Limis from Neutral-Current Interactions in MIMOS", Phys. Rev. Lett. **107**, 011802(2011)

[42] H.-Th. Janka, *et al.*, "Theory of core-collapse supernovae", Phys. Repo. **442**, 38-74(2007)

[43] E. Cappellaro, R. Evans, and M. Turatto, "A new determination of supernova rates and a comparison with indicators for galactic star formation", Astron. Astrophys **351**, 459-466(1999)

[44] T. Tonani and K. Sato, "Spectrum of the relic neutrino background from past supernovae and cosmological models", Astropart. Phys. **3**, 367(1995)

[45] T. Totani, K. Sato and Y. Yoshi, "Spectrum of the Supernova Relic Neutrino Background and Evolution of Galaxies", Astropart. J. **460**, 303(1996)

[46] R. A. Malaney, "Evolution of the cosmic gas and the relic supernova neutrino background", Astropart. Phys. **7**, 125-136(1997)

[47] D. H. Hartmann and S. E. Woosley, "The cosmic supernova neutrino background", Astropart. Phys. **7**, 137-146(1997)

[48] M. Kaplinghat, G. Steigman and T. P. Walker, "Supernova relic neutrino background", Phys. Rev. D **62**, 043001(2000)

[49] L. Strigari, M. Kaplinghat, G. Steigman and T. Walker, "The supernova relic neutrino backgrounds at KamLAND and Super-Kamiokande", JCAP 0403:007(2004)

[50] S. Ando, K. Sato and T. Tonani, "Detectability of the supernova relic neutrinos and neutrino oscillation", Astropart. Phys. **18**, 307-318(2003)

[51] M. Fukugita and M. Kawasaki, "Constraints on the star formation rate from supernova relic neutrino observations", Mon. not. Roy. Astron. Soc. **340**, L7-L11(2003)

[52] C. Lunardini, "Diffuse Neutrino Flux from Failed Supernovae", Phys. Rev. Lett. **102**, 231101(2009)

[53] S. Horiuchi, J. F. Beacom and E. Dwek, "Diffuse supernova neutrino background is detectable in Super-Kamiokande", Phys. Rev. D **79**, 083013(2009)

[54] F. Vissani and G. Pagliaroli, "The diffuse supernova neutrino background: expectations and uncertainties derived from SN1987A", Astro. and Astrophys. **528**, L1(2011)

[55] K. Nakazato, "Imprint of explosion mechanism on supernova relic neutrinos", Phys. Rev. D **88**, 083012(2013)

[56] K. Bays, T. Ilda, *et al.* (Super-Kamikande collaboration), "Supernova relic neutrino search at Super-Kamiokande", Phys. Rev. D **85**, 052007(2012)

[57] H. Zhang, *et al.* (Super-Kamikande collaboration), "Supernova Relic Neutrino Search with Neutron Tagging at Super-Kamiokande-IV", Astropart. Phys. **60**, 41-46(2015)

[58] K. Abe, *et al.* (T2K collaboration), "The T2K Experiment", Nucl. Instr. Meth. A **659**, 106-135(2011)

[59] K. Abe, *et al.* (T2K collaboration), "Indication of Electron Neutrino Appearance from an Accelerator-produced Off-axis Muon Neutrino Beam", Phys. Rev. Lett. **107**, 041801(2011)

[60] F. P. An, *et al.* (The Daya Bay collaboration), "Observation of Electron-Antineutrino Disappearance at Daya Bay", Phys. Rev. Lett. **108**, 171803(2012)

[61] K. Abe, *et al.* (T2K collaboration), "Observation of Electron Neutrino Appearance in a Muon Neutrino Beam", Phys. Rev. Lett. **112**, 061802(2014)

[62] R. Wendell, *et al.* (Super-Kamikande collaboration), "Atmospheric neutrino oscillation analysis with subleading effects in Super-Kamiokande I, II, and III", Phys. Rev. D **81**, 092004(2010)

[63] K. Abe, *et al.* (T2K collaboration), "Measurement of Neutrino Oscillation Parameters from Muon Neutrino Disappearance with an Off-Axis Beam", Phys. Rev. Lett. **111**, 211803(2013)

[64] Patrick deNiverville, David McKeen, and Adam Ritz, "Signatures of sub-GeV dark matter beams at neutrino experiments", Phys. Rev. D **86**, 035022(2012)

[65] Brian Batell, Patrick deNiverville, David McKeen, Maxim Pospelov, and Adam Ritz, "Leptophobic dark matter at neutrino factories", Phys. Rev. D **90**, 115014(2014)

[66] Jorge S. Diaz, V. Alan Kostelecky, and Matthew Mewes, "Perturbative Lorentz and CPT violation for neutrino and antineutrino oscillations", Phys. Rev. D **80**, 076007(2009)

[67] V. Alan Kostelecky and Matthew Mewes, "Lorentz violation and short-baseline neutrino experiments", Phys. Rev. D **70**, 076002(2004)

[68] S. Bhadra, M. Cadabeschi, P. de Perio, *(*et al.), "Optical Transition Radiation Monitor for the T2K Experiment", Nucl. Instr. Meth. A **703**, 45-58(2013)

[69] A. K. Ichikawa, "Design concept of the magnetic horn system for the T2K neutrino beam", Nucl. Instr. Meth. A **690**, 27-33(2012)

[70] T. Sekiguchi *et al.*, "Development and operational experience of magnetic horn system for T2K experiment", Nucl. Instr. Meth. A **789**, 57-80(2015)

[71] K. Suzuki, *et al.*, "Measurement of the muon beam direction and muon flux for the T2K neutrino experiment", Prog. Theor. Exp. Phys. 053C01(2015)

[72] S. Assylbekkov, *et al.*, "The T2K ND280 Off-Axis Pi-Zero Detector", Nucl. Instr. Meth. A **686**, 48-63(2012)

[73] P.-A Amaudruz, *et al.*, "The T2K Fine-Grained Detectors", Nucl. Instr. Meth. A **696**, 1-31(2012)

[74] N. Abgrall, *et al.*, "Time Projection Chambers for the T2K Near Detectors", Nucl. Instr. Meth. A **637**, 25-46(2011)

[75] D. Allan, *et al.* (The T2K UK collaboration), "The electromagnetic calorimeter for the T2K near detector ND280", JINST **8**, P10019(2013)

[76] S. Aoki, *et al.*, "The T2K Side Muon Range Detector",Nucl. Instr. Meth. A **698**, 135-146(2013)

[77] K. Abe, *et al.* (T2K collaboration), "Measurements of the T2K neutrino beam properties using the INGRID on-axis near detector", Nucl. Instr. Meth. A **694**, 211-223(2012)

[78] S. Fukuda, *et al.* (Super-Kamikande collaboration), "The Super-Kamiokande detector", Nucl. Instr. Meth. A **501**, 418-462(2003)

[79] A. Suzuki, *et al.*, "Improvement of 20 in. diameter photomultiplier tubes", Nucl. Instr. Meth. A **329**, 299-313(1993)

[80] E. Blaufuss, *et al.* (Super-Kamikande collaboration), "^{16}N as a calibration source for Super-Kamiokande", Nucl. Instr. Meth. A **458**, 636-647(2001)

[81] M. Nakahata, *et al.* (Super-Kamikande collaboration), "Calibration of Super-Kamiokande using an electron LINAC", Nucl. Instr. Meth. A **421**, 113-129(1999)

[82] K. Abe *et al.* (Super-Kamikande collaboration), "Calibration of the Super-Kamiokande Detector", Nucl. Instr. Meth. A **737**, 253-272(2014)

[83] S. Yamada *et al.*, "Commissioning of the New Electronics and Online System for the Super-Kamiokande Experiment", IEEE Transactions on Nucl. Scie, 57 428(2010)

[84] D. R. Tilley, H. R. Weller, C. M. Cheves, "energy levels of light nuclei A=16-17", Nucl. Phys. A **564**, 1-183(1993)

[85] Michael Smy for the Super-Kamiokande Collaboration, "Low Energy Event Reconstruction and Selection in super-Kamiokande-III", *in Proceedings of 30TH International Cosmic Ray Conference*, Mexico city, Mexico, 2008, Vol.5 (HE part2), pages 1279-1282

[86] A. Abe *et al.*(SK Collaboration), "Solar neutrino results in Super-Kamiokande-III", Phys. Rev. D **83**, 052010(2011)

[87] A. Renshaw, *et al.*, "First Indication of Terrestrial Matter Effects on Solar Neutrino Oscillation", Phys. Rev. Lett. **112**, 091805(2014)

[88] Y. Hayato, Nucl. Phys. Proc. Suppl. **112** (2002) 171.

[89] A. Abe *et al.*(T2K Collaboration), "T2K neutrino flux prediction", Phys. Rev. D **87**, 019902(2013)

[90] N. Abgrall *et al.*(NA61/SHINE Collaboration),"Measurement of Cross Sections and Charged Pion Spectra in proton-carbon Interactions at 31GeV/c", Phys. Rev. C **84**, 034604(2011)

[91] N. Abgrall *et al.*(NA61/SHINE Collaboration),"Measurement of Production Properties of Positively Charged Kaons in Proton-Carbon Interactions at 31 GeV/c", Phys. Rev. C **85**, 035210(2012)

[92] A. A. Aguilar-Arevalo, *et al.* (MiniBooNE collaboration), "First measurement of the muon neutrino charged current quasielastic double differential cross section", Phys. Rev. D **81**, 092005(2010)

[93] A. A. Aguilar-Arevalo, *et al.* (MiniBooNE collaboration), "Measurement of ν_μ-induced charged-current neutral pion production cross sections on mineral oil at $E_\nu \in 0.52.0$GeV", Phys. Rev. D **83**, 052009(2011)

[94] A. A. Aguilar-Arevalo, *et al.* (MiniBooNE collaboration), "Measurement of neutrino-induced charged-current charged pion production cross sections on mineral oil at $E_\nu \sim 1$GeV", Phys. Rev. D **83**, 052007(2011)

[95] A. A. Aguilar-Arevalo, *et al.* (MiniBooNE collaboration), "Measurement of ν_μ and $\overline{\nu}_\mu$ induced neutral current single π^0 production cross sections on mineral oil at $E_\nu \sim \mathcal{O}(1$ GeV)", Phys. Rev. D **81**, 013005(2010)

[96] V. Lyubushkin, *et al.* (NOMAD collaboration), "A study of quasi-elastic muon neutrino and antineutrino scattering in the NOMAD experiment", Eur. Phys. J. C **63**, 355-381(2009)

[97] K. Hiraide, *et al.* (SciBooNE collaboration), "Search for charged current coherent pion production on carbon in a few-GeV neutrino beam", Phys. Rev. D **78**, 112004(2008)

[98] Y. Kurimoto, *et al.* (SciBooNE collaboration), "Improved measurement of neutral current coherent 0 production on carbon in a few-GeV neutrino beam", Phys. Rev. D **81**, 111102(2010)

[99] G. Battistoni, F. Broggi, M. Brugger, M. Campanella, M. Carboni *et al.*, "Applications of FLUKA Monte Carlo code for nuclear and accelerator physics", Nucl. Instr. Meth. B **269**, 2850(2011)

[100] R. Brun, F. Carminati, and S. Giani, "GEANT Detector Description and Simulation tool", CERN-W5013 (1994)

[101] C.H. Llewellyn Smith, "Neutrino Reactions at Accelerator Energies", Phys. Rept. **3**, 261-379(1972)

[102] M. Fukugita, T. Yanagida, *Physics of Neutrinos and Applications to Astrophysics*, (Springer: Springer-Verlag Berlin Heidelberg New York 2003)

[103] B. Bartoli, F. Felicetti, and V. Silvestrini, "Electromagnetic Structure of the Hadrons", Riv. Del Nuovo Cimento, **2**, 241-302(1972)

[104] M. Gourdin, "Weak and electromagnetic from factors of hadrons", Phys. Rept. **11**, 29-98(1974)

[105] Particle Data Group, Phys.Rev. D **66** (2002) 01001

[106] R. A. Smith and E. J. Moniz, "Neutrino reactions on nuclear targets", Nuclear Physics B **43** 605-622(1972)

[107] M. K. Jones *et al.*, "G_{E_p}/G_{M_p} Ratio by Polarization Transfer in $\vec{e}p \rightarrow e\vec{p}$", Phys. Rev. Lett. **84**, 1398(2000)

[108] R. Bradford, A. Bodek, H. Budd, and J. Arrington, "A New Parameterization of the Nucleon Elastic Form Factors", Nucl. Phys. Proc. Suppl. **159**, 127-132(2006)

[109] J. J. Kelly, "Simple parameterization of nucleon form factors", Phys. Rev. C **70**, 068202(2004)

[110] S. Riordan, *et al.*, "Measurements of the Electric Form Factor of the Neutron up to $Q^2 = 3.4$ GeV^2 Using the Reaction $^3\vec{H}e(\vec{e}, e^{'}n)pp$", Phys. Rev. Lett **105**, 262302(2010)

[111] S. Galster, H. Klein, J. Moritz, K.H. Schmidt, D. Wegener, J. Bleckwenn, "Elastic electron-deuteron scattering and the electric neutron form factor at four-momentum transfers 5 fm^{-2} <q^2 < 14 fm^{-2}", Nucl. Phys. B **32**, 221(1971)

[112] Omar Benhar *et al.*, "Electron- and neutrino-nucleus scattering in the impulse approximation regime", Phys. Rev. D **72**, 053005(2005)

[113] Omar Benhar, Davide Meloni, "Total neutrino and antineutrino nuclear cross sections around 1 GeV", Nucl. Phys. A **789**, (2007) 379-402

[114] C. Itzykson and J.B. Zuber, *Quantum Field Theory* (McGraw-Hill, New York, 1980)

[115] Artur M. Ankowski and Omar Benhar, "Analysis of γ-Ray Production in Neutral-Current Neutrino-Oxygen Interactions at Energies above 200 MeV", Phys. Rev. Lett. **108**, 052505(2012)

[116] Omar Benhar *et al.*, "Spectral function of finite nuclei and scattering of GeV electrons", Nucl. Phys. A **579**, 493-517(1994)

[117] M. Bernheim *et al.*, "The influence of bound state and optical potentials on 1p momentum distributions obtained from ^{12}C and ^{16}O$(e, e^{'}p)$ reactions", Nucl. Phys. A **375** (1982) 381-404

[118] D. Rohe *et al.*(E97-006 Collaboration), "Correlated Strength in the Nuclear Spectral Function", Phys. Rev. Lett. **93**, 182501

[119] *Table of Isotopes: 1999 Update with CD-ROM*, edited by R.B. Firestone, C. M. Baglin, and S. Y. F. Chu (Wilay, New York, 1999), 8th ed.

[120] Koh Ueno, "Study of neutral-current de-excitation gamma-rays with T2K neutrino beam", PhD thesis, University of Tokyo, Feb. 2012

[121] Takaaki Yokozawa, "Precision solar neutrino measurements with Super-Kamiokande-IV", PhD thesis, University of Tokyo, Dec. 2012

[122] H. Ejiri, "Nuclear deexcitations of nucleon holes associated with nucleon decays in nuclei", Phys. Rev. C **48**, 48(1993)

[123] M. Leuschner *et al.*, "Quasielastic proton knockout from ^{16}O", Phys. Rev. C **49**, 955(1994)

[124] F. Ajzenberg-Selove. "Energy Level of Light Nuclei", Nucl. Phys. A **523**, 1(1991)

[125] K. Kobayashi, *et al.*, "De-excitation γ-rays from the s-hole state in ^{15}N associated with proton decay in ^{16}O", arXiv:nucl-ex/0604006 [nucl-ex].

[126] M. Yosoi, "Structures and fragmentations of the deep-hole states in ^{11}B and ^{15}N", PhD thesis, Kyoto Univ., 2003

[127] M. Yosoi, *et al.*, "Cluster fragmentations of deep(1s)-hole states in light nuclei", Nucl. Phys. A **738**, 451(2004)

[128] M. Yosoi, *et al.*, "Structures and decay of deep-hole states in light nuclei populated by the (p,2p) reactions", Phys. Atom. Nucl. **67**, 1810(2004)

[129] K. Abe, *et al.* (T2K Collaboration), "Measurements of neutrino oscillation in appearance and disappearance channels by the T2K experiment with 6.6×10^{20} protons on target", Phys. Rev. D **91**, 072010(2015)

[130] E. Kolbe, K. Langanke, and P. Vogel, "Estimates of weak and electromagnetic nuclear decay signatures for neutrino reactions in Super-Kamiokande", Phys. Rev. D **66**, 013007(2002)

[131] E. Kolbe, K. Langanke, S. Krewald and F.-K. Thielemann, "Inelastic neutrino scattering on ^{12}C and ^{16}O above the particle emission threshold", Nucl. Phys. A **540**, 599-620(1992)

[132] D. Ashery, I. Navon, G. Azuelos, H. Walter, H. Pfeiffer, *et al.*, "True absorption and scattering of pions on nuclei", Phys. Rev. C **23**, 2173(1981)

[133] M. Jones, R. Ransome, V. Cupps, R. Fergerson, C. Morris, *et al.*, "Pion absorption above the $\Delta(1232)$ resonance", Phys. Rev. C **48**, 2800(1993)

[134] R. Giannelli, B. Ritchie, J. Applegate, E. Beck, J. Beck, *et al.*, "Multiproton final states in positive pion absorption below the $\Delta(1232)$ resonance", Phys. Rev. C **61**, 054615(2000)

[135] C. Zeitnitz and T. Gabriel, "The GEANT - CALOR interface and benchmark calculations of ZEUS test calorimeters", Nucl. Instr. Meth. A **349**, 106-111(1994)

[136] H. Engelhardt, C. Lewisw, and H. Ullrich, "The absorption of π^- at rest on complex nuclei", Nucl. Phys. A **258**, 480(1976)

[137] T. A. Gabriel, *Proceedings of the Workshop on Simulating Accelerator Radiation Environments*, "The CALOR93 Code system", 1994

[138] K. Matsuoka, "Measurement of the Neutrino Beam with the Muon Monitor and the First Result of the T2K Long-Baseline Neutrino Oscillation Experiment", PhD thesis, Kyoto Univ., 2011

[139] Chakravarti, Laha, and Roy, *Handbook of Methods of Applied Statistics, Volume I*, John Wiley and Sons, 392-394.

[140] Yuri Kamyshkov and Edwin Kolbe, "Signatures of nucleon disappearance in large underground detectors", Phys. Rev. D **67**, 076007(2003)

[141] N. Smirnov, *Table for estimating the goodness of fit of empirical distributions.* Annals of Mathematical Statistics **19** 279281.

[142] Q. R. Ahmad, *et al.*,(SNO Collaboration) "Direct Evidence for Neutrino Flavor Transformation from Neutral-Current Interactions in the Sudbury Neutrino Observatory", Phys. Rev. Lett. **89**, 011301(2002)

[143] Arthur M. Ankowski, *et al.*, "Estimate of the theoretical uncertainty of the cross sections for nucleon knockout in neutral-current neutrino-oxygen interactions", C **92**, 025501(2015)

[144] John F. Beacom and Mark R. Vagins, "Antineutrino Spectroscopy with Large Water Cerenkov Detectors", Phys. Rev. Lett. **93**, 171101(2004)

[145] H. Watanabe, H. Zhang, et al.(SuperKamiokande Collaboration), "First Study of Neutron Tagging with a Water Cherenkov Detector", Astropart. Phys. **31**, 320-328 (2009)

[146] D. Cokinos and E. Melkonian, "Measurement of the 2200 m/sec neutron-proton capture cross section", Phys. Rev. C **15** 1636(1977)

[147] T. J. Irvine, "Development of Neutron-Tagging Techniques and Application to Atmospheric Neutrino Oscillation Analysis in Super-Kamiokande", PhD thesis, University of Tokyo, 2014

[148] Lee Ka Pik, "Study of the neutrino mass hierarchy with the atmospheric neutrino data observed in Super-Kamiokande", PhD thesis, University of Tokyo, 2012

[149] Miroslav Morhac, *in Proceedings of XII Advanced Computing and Analysis Techniques in Physics Research Erice, Italy*, PoS(ACAT08)077

[150] Miroslav Morhac, *et al.*, "Efficient one- and two-dimensional Gold deconvolution and its application to gamma-ray spectra decomposition", Nucl. Instr. and Meth. A **401**, 385-408(1997)

[151] Miroslav Morhac, *et al.*, "Background elimination methods for multidimensional coincidence gamma-ray spectra", Nucl. Instr. and Meth. A **401**, 113-132(1997)

[152] Z.K. Silagadze, "A new algorithm for automatic photopeak searches", Nucl. Instr. and Meth. in Physics Research A **376**, 451-454(1996)